

5th Hellenic Institute of Nuclear Physics Workshop

12-13 April 2019

Physics Department, Aristotle University of Thessaloniki

HINPw5 Proceedings

Recent advances and prospects for Nuclear Theory
Nuclear Structure and Reactions
Nuclear Astrophysics and Nucleosynthesis
Super-heavy elements and Nuclear Fission
Hadronic Physics

Organized by
Hellenic Institute of Nuclear Physics

Organizing Committee:

G. Lalazissis (AUTH)

Ch. Moustakidis (AUTH)

D. Bonatsos (NCSR)

T. Gaitanos (AUTH)

A. Ioannidou (AUTH)

A. Pakou (UOI)

G. Souliotis (NKUA)



Sponsored by AUTH
Research Committee

hinpw5.physics.auth.gr

HELLENIC INSTITUTE OF NUCLEAR PHYSICS

PROCEEDINGS
of the
5th WORKSHOP (HINPw5)
12-13 APRIL 2019



DEPARTMENT OF PHYSICS
ARISTOTLE UNIVERSITY OF THESSALONIKI

ORGANIZING COMMITTEE

G. LALAZISSIS (AUTH)

CH. MOUSTAKIDIS (AUTH)

D. BONATSOS (NCSR)

T. GAITANOS (AUTH)

A. IOANNIDOU (AUTH)

A. PAKOU (UOI)

G. SOULIOTIS (NKUA)

EDITOR

CH. MOUSTAKIDIS (AUTH)

<http://hinpw5.physics.auth.gr>

FOREWORD

The 5th Workshop on new Aspects and Perspectives in Nuclear Physics (HINPW5) was held in Thessaloniki from April 12 to 13, 2020. This series of symposia, organized by the Hellenic Institute of Nuclear Physics since 2012, provides a lively forum not only for leading scientists of the Greek Universities and Institutes but also for fresheners in the field of Nuclear Physics to share the most recent advancements on various topics, thus offering a unique platform to exchange ideas and keep track of new aspects and perspectives in the area.

This year, more than 230 participants, mostly young scientists and post-graduate students attended the lectures of the Workshop. A total of 25 oral contributions were included in the agenda, in addition to 9 lectures delivered by distinguished colleagues invited from abroad. We are grateful to all the speakers and participants and especially to the invited speakers for their overwhelming response and participation in the Workshop.

The Workshop sessions covered the topics of Recent advances and prospects for Nuclear Structure and Reactions, Nuclear Astrophysics and Nucleosynthesis, Super-heavy elements and Nuclear Fission, Hadronic Physics, Challenges at the interface of Atomic and Nuclear Physics and Interdisciplinary studies and societal. All invited and contributed talks were of high quality and the articles based on the talks are collected in the present volume.

We would like to thank the Aristotle University of Thessaloniki for hosting the Workshop. Financial support by the A.U.T.H. Research Committee is warmly acknowledged. To Dr. V. Psonis, we express our thankfulness for providing us with the Workshop webpage and preparation of the proceedings. Would like to cordially thank N. Alamanos, P. Ring and F. Cappuzzello for their continuous support on most of the Workshops of the Hellenic Institute of Nuclear Physics.

Charalampos Moustakidis

on behalf of the Organizing Committee

Thessaloniki, October 2020

Nicolas Alamanos

Research Director at the CEA

Deputy Director of IRFU (Institute of Research into the Fundamental Laws of the Universe)

Title: “Nuclear Physics today - installations in perspective or under construction”.

Abstract: Taking the cosmological model as a time line, nuclear physics is an integral part of this model that describes the evolution of our universe from the Big Bang to nowadays, I would present nuclear physics facilities in perspective or under construction around the world.

The fundamental questions that animate hadronic physics at high temperature and temperature $T=0$ will be discussed and the installations in perspective will be presented. Special attention will be given to installations under construction or in perspective, which addresses the synthesis of super-heavy elements and the physics of exotic nuclei.

On the ab-initio derivation of covariant density functionals.

Peter Ring*

Physics Department, Technical University of Munich, 85748 Garching, Germany

Contact e-mail: ring@ph.tum.de

The successes of covariant density functional theory, that start from effective Lagrangians, to describe nuclear ground and excited-state properties all over the nuclear chart are confronted with the fact, that the parameters of such density functionals are determined in a completely phenomenological way. The challenges and ambiguities of predictions for unstable nuclei without data or for high-density nuclear matter, arising from covariant density functionals are discussed. The basic ideas in building an ab initio covariant density functional for nuclear structure from ab initio calculations with realistic bare nucleon-nucleon interactions for both nuclear matter and finite nuclei are presented. The current status of fully self-consistent relativistic Brueckner-Hartree-Fock (RBHF) calculations for both finite nuclei and neutron drops is presented. The guidances and perspectives towards an ab initio covariant density functional for nuclear structure derived from RBHF results are discussed

* Work supported by the DFG (Germany) cluster of excellence “Origin and Structure of the Universe” (www.universe-cluster.de).

The nuclear matrix elements of $0\nu\beta\beta$ decay and the NUMEN project at INFN-LNS

F. Cappuzzello^{1,13,17,*}, L. Acosta², P. Adsley^{3,4}, C. Agodi¹, C. Altana¹, P. Amador-Valenzuela⁵, N. Auerbach⁶, J. Barea⁷, J. I. Bellone¹, R. Bijker⁸, T. Borello-Lewin⁹, I. Boztosun¹⁰, V. Branchina¹¹, S. Brasolin¹², G. A. Brischetto^{1,13}, O. Brunasso¹², S. Burrello¹, L. Campajola^{14,15}, S. Calabrese^{1,2}, L. Calabretta¹, D. Calvo¹², V. Capirossi^{12,16}, D. Carbone¹, M. Cavallaro¹, L. E. Charon Garcia², E. R. Chávez Lomeli², R. Chen¹⁸, I. Ciraldo^{1,13}, M. Colonna¹, M. Cutuli^{1,13}, G. D'Agostino¹, F. Delaunay^{12,19}, N. Deshmukh²⁰, H. Djapo²¹, D. Gambacurta¹, G. De Geronimo²², K. De Los Rios², C. Eke¹⁰, C. Ferraresi²³, J. L. Ferreira²⁴, J. Ferretti^{25,26}, P. Finocchiaro¹, S. Firat¹⁰, M. Fisichella¹, D.C. Flechas Garcia⁹, A. Foti¹¹, E. Gandolfo^{14,15}, H. Garcia-Tecocoatzi^{25,27}, A. Hacisalihoglu²⁸, A. Huerta-Hernandez², J. Kotila²⁹, Y. Kucuk¹⁰, F. Iazzi^{12,16}, H. Jivan⁴, G. Lanzalone^{1,30}, J. A. Lay³¹, L. La Fauci^{1,13}, F. La Via³², H. Lenske³³, R. Linares²⁴, J. Lubian²⁴, J. Ma¹⁸, D. Marin-Lámbarri², J. Mas Ruiz², N. H. Medina⁹, D. R. Mendes²⁴, P. Mereu¹², M. Morales³⁴, L. Neri¹, R. Neveling³, J. R. B. Oliveira⁹, A. Pakou³⁵, L. Pandola¹, L. Pellegrini^{3,4}, H. Petrascu³⁶, N. Pietralla³⁷, F. Pinna^{12,16}, P. C. Ries³⁷, A. D. Russo¹, G. Russo^{11,13}, E. Santopinto²⁵, R. B. B. Santos³⁸, O. Sgouros¹, M. A. G. da Silveira³⁸, S. O. Solakci¹⁰, G. Souliotis³⁹, V. Soukeras¹, A. Spatafora^{1,13}, D. Torresi¹, S. Tudisco¹, H. Vargas Hernandez², R. I. M. Vsevolodovna^{25,27}, J. Wang^{18,40}, V. Werner³⁷, Y. Yang¹⁸, A. Yildirim¹⁰, V. A. B. Zagatto²⁴

for the NUMEN Collaboration

¹Istituto Nazionale di Fisica Nucleare, Laboratori Nazionali del Sud, Catania, Italy

²Instituto de Física, Universidad Nacional Autónoma de México - México City, México

³iThemba Laboratory for Accelerator Based Sciences (iThemba LABS), South Africa

⁴School of Physics, University of the Witwatersrand, Johannesburg, South Africa

⁵Instituto Nacional de Investigaciones Nucleares - Ocoyoacac, México

⁶School of Physics and Astronomy, Tel Aviv University - Tel Aviv, Israel

⁷Universidad de Concepción - Concepción, Chile

⁸Instituto de Ciencias Nucleares, Universidad Nacional Autónoma de México - México City, México

⁹Instituto de Física, Universidade de São Paulo - São Paulo, Brazil

¹⁰Department of Physics, Akdeniz University - Antalya, Turkey

¹¹Istituto Nazionale di Fisica Nucleare, Sezione di Catania, Italy

¹²Istituto Nazionale di Fisica Nucleare, Sezione di Torino, Italy

¹³Dipartimento di Fisica e Astronomia "Ettore Majorana", Università di Catania, Italy

¹⁴Dipartimento di Fisica, Università di Napoli Federico II, Italy

¹⁵Istituto Nazionale di Fisica Nucleare, Sezione di Napoli, Italy

¹⁶DISAT, Politecnico di Torino, Italy

- ¹⁷Centro Siciliano di Fisica Nucleare e Struttura della Materia, Italy
¹⁸Institute of Modern Physics, Chinese Academy of Sciences - Lanzhou, China
¹⁹LPC Caen, Normandie Universite, ENSICAEN, UNICAEN, CNRS/IN2P3 Caen, France
²⁰Nuclear Physics Division, Saha Institute of Nuclear Physics - Kolkata, India
²¹Ankara University, Institute of Accelerator Technologies, Turkey
²²Stony Brook University - Stony Brook, NY, USA
²³DIMEAS, Politecnico di Torino - Torino, Italy
²⁴Instituto de Fisica, Universidade Federal Fluminense - Niteroi, Brazil
²⁵Istituto Nazionale di Fisica Nucleare, Sezione di Genova - Genova, Italy
²⁶Department of Physics, Yale University - New Haven, CT, USA
²⁷Dipartimento di Fisica, Università di Genova - Genova, Italy
²⁸Institute of Natural Sciences, Karadeniz Teknik University - Trabzon, Turkey
²⁹University of Jyväskylä - Jyväskylä, Finland
³⁰Università degli Studi di Enna “Kore” - Enna, Italy
³¹Departamento de FAMN, Universidad de Sevilla - Sevilla, Spain
³²CNR-IMM, Sezione di Catania - Catania, Italy
³³Department of Physics, University of Giessen - Giessen, Germany
³⁴Instituto de Pesquisas Energeticas e Nucleares IPEN/CNEN - Sao Paulo, Brazil
³⁵Department of Physics and HINP, University of Ioannina - Ioannina, Greece
³⁶IFIN-HH - Magurele, Romania
³⁷Institut für Kernphysik, Technische Universität Darmstadt - Darmstadt, Germany
³⁸Centro Universitario FEI - Sao Bernardo do Campo, Brazil
³⁹Department of Chemistry, National and Kapodistrian University of Athens, Athens, Greece
⁴⁰Huzhou University, Huzhou, Zhejiang Province, China

cappuzzello@lns.infn.it

Abstract. Neutrinoless double beta decay of nuclei, if observed, would have important implications on fundamental physics. In particular, it would give access to the effective neutrino mass. In order to extract such information from $0\nu\beta\beta$ decay half-life measurements, the knowledge of the Nuclear Matrix Elements (NME) is of utmost importance. In this context the NUMEN and the NURE projects aim to extract information on the NME by measuring cross sections of Double Charge Exchange reactions in selected systems which are expected to spontaneously decay via $0\nu\beta\beta$. In this work an overview of the experimental challenges that NUMEN is facing in order to perform the experiments with accelerated beams and the research and development activity for the planned upgrade of the INFN-LNS facilities is reported.

1. Introduction

Neutrinoless double beta decay ($0\nu\beta\beta$) of atomic nuclei is a predicted but still unobserved spontaneous decay which is attracting a deep interest in the physics community. The main reason is that its observation would establish the Majorana nature of neutrino and would shed light on the absolute neutrino mass and hierarchy. In addition, this phenomenon could provide precious information to interpret key problems of fundamental physics as the unification of the fundamental forces and the matter-antimatter balance in the Universe [1].

A critical aspect of $0\nu\beta\beta$ physics is associated to the determination of the Nuclear Matrix Elements (NME) entering in the expression of the decay half-life. These quantities must be known with good accuracy, despite the intrinsic many-body nature of the parent and daughter nuclei makes this task particularly hard. There are no experimental methods to directly measure $0\nu\beta\beta$ NMEs and state of the

art theoretical calculations lead to discrepancy factors larger than two. In addition, some assumption common to different nuclear structure approaches could cause overall systematic uncertainties. Thus experimentally driven inputs are very useful to help evaluate the $0\nu\beta\beta$ NMEs and to constrain the existing calculations.

In this context, the NUMEN [2], [3] and NURE [4] projects at INFN-LNS Catania aim to study heavy-ion induced single (SCE) and double (DCE) charge exchange reactions in a systematic approach, aiming at extracting information on NMEs for single and double charge exchange processes and to identify the possible connections with $0\nu\beta\beta$.

Despite $0\nu\beta\beta$ decays and DCE reactions are mediated by different interactions, they present several similarities. Among those, the key aspects are that initial and final nuclear states are the same and the transition operators in both cases present a superposition of short-range isospin, spin-isospin and rank-two tensor components with a sizeable available momentum (≈ 100 MeV/c).

2. The NUMEN phases

The NUMEN (NUclear Matrix Elements for Neutrinoless double beta decay) project is conceived in the view of a comprehensive study of many candidate systems for $0\nu\beta\beta$ decay. Moreover, this project promotes and is strictly connected with the upgrade of the INFN-LNS research infrastructure (POT-LNS) and with a specific R&D activity on detectors, materials and instrumentation.

NUMEN is structured into four phases:

- Phase 1: “*The pilot experiment*” - In 2013, the $^{40}\text{Ca}(^{18}\text{O}, ^{18}\text{Ne})^{40}\text{Ar}$ DCE reaction was measured at INFN-LNS together with the competing processes: $^{40}\text{Ca}(^{18}\text{O}, ^{18}\text{F})^{40}\text{K}$ SCE, $^{40}\text{Ca}(^{18}\text{O}, ^{20}\text{Ne})^{38}\text{Ar}$ two-proton transfer and $^{40}\text{Ca}(^{18}\text{O}, ^{16}\text{O})^{42}\text{Ca}$ two-neutron transfer [5]. This work showed for the first time high resolution and statistically significant experimental data on DCE reactions in an wide range of transferred momenta. The measured angular distribution is characterized by an oscillating shape, well described by an $L = 0$ Bessel function, indicating that in the DCE reaction a simple mechanism should be dominant. This is confirmed by the observed suppression of the multi-nucleon transfer routes. DCE NMEs were extracted under the hypothesis of a two-step charge exchange process. Despite the approximations used in our model, which determine an uncertainty of $\pm 50\%$, the obtained results are compatible with the values known from literature, indicating that the main physics content has been kept.
- Phase 2: “*From the pilot experiment toward the hot cases*” – Based on the feasibility studies of Phase 1, during Phase 2 (presently on going) a few selected isotopes of interest for $0\nu\beta\beta$ are being studied by DCE reactions and competing quasi-elastic reactions, as reported in Section 3. The experimental activity with accelerated beams of Phase 2 is part of a project funded by European Research Council named NURE (NUclear REactions for neutrinoless double beta decay).

The results of experiments performed in Phase 1 and 2 indicate that suitable information from DCE reactions can be extracted. However, the low yields of the measured data and the long beam time needed (typically one month) suggest that the DCE experiments should be performed with higher beam current, two orders of magnitude higher than the present. Therefore, the present limits of beam power for the cyclotron accelerator (~ 100 W) and of acceptable rate for the MAGNEX focal plane detector (few kHz) [6] must be sensibly revised. This goal will be achieved by a substantial change in the technologies implemented in the beam extraction [7], in the detection of ejectiles and in target cooling systems [8], [9]. During Phase 2, such R&D activities is being performed, as introduced in Section 4. The development of the theory necessary to describe nuclear cross sections of DCE, SCE, transfer, elastic and inelastic channels is also pursued during Phase 2 [10], [11], [12] but is not the topic of this work.

- Phase 3: *The Facility Upgrade* - During Phase 3 the old MAGNEX set-up will be disassembled and the new one assembled. During this period, the data analysis of the NUMEN Phase 2 experiments will continue. In addition, tests of the new detectors and selected experiments will be performed in other laboratories in order to provide possible missing information.

- Phase 4: “*The Experimental Campaign with Upgraded Facility*” - The Phase 4 will consist of an experimental campaign at high beam intensities (particle- μA) and integrated charge of hundreds of mC up to C, spanning all the $0\nu\beta\beta$ decay candidate isotopes, such as: ^{48}Ca , ^{76}Ge , ^{76}Se , ^{82}Se , ^{96}Zr , ^{100}Mo , ^{106}Cd , ^{110}Pd , ^{116}Cd , ^{110}Sn , ^{124}Sn , ^{128}Te , ^{130}Te , ^{136}Xe , ^{130}Xe , ^{148}Nd , ^{150}Nd , ^{154}Sm , ^{160}Gd , ^{198}Pt . Hopefully, the use of improved theoretical analyses will give access to the NMEs, thus fulfilling the most ambitious goal of NUMEN.

3. The experimental activity with accelerated beams during Phase 2

Important experimental challenges must be addressed to measure heavy ion induced DCE reactions.

Such challenges are related to the request to detect heavy ions with good isotopic separation and energy resolution in a wide angular range, including zero-degree, in order to distinguish transitions to individual states and explore a wide momentum transfer range.

In addition, the need to measure small DCE cross sections (few nb) requires a challengingly high experimental sensitivity, which strongly depend on the rejection capability against unwanted events generated by competing reaction processes [13]. For this reason, high resolution particle identification is a prerequisite for the experiment.

Experimentally, the main tools for this project are the high resolution Superconducting Cyclotron beams and the MAGNEX magnetic spectrometer [14], [15]. The latter is a large acceptance magnetic system able to provide high resolution in energy, mass and angle and an accurate control of the detection efficiency. The implementation of trajectory reconstruction technique is the key feature of MAGNEX, which guarantees the above mentioned performance and its relevance in the research for heavy-ion physics [16], [17], [18], [19], [20], [21], [22], [23], [24], [25], [26], also taking advantage of its coupling to the EDEN neutron detector array [27], [28].

The experimental activity with accelerated beams presently in progress consists of two main classes of experiments, corresponding to the exploration of the two directions of isospin lowering $\tau^- \tau^-$ and rising $\tau^+ \tau^+$, characteristic of $\beta^- \beta^-$ and $\beta^+ \beta^+$ decays, respectively [29].

In particular, the $\beta^+ \beta^+$ direction in the target is investigated using an $^{18}\text{O}^{8+}$ beam and measuring the (^{18}O , ^{18}Ne) DCE transitions, together with other reaction channels involving same beam and target. Similarly, the $\beta^- \beta^-$ direction is explored via the (^{20}Ne , ^{20}O) reaction, using a $^{20}\text{Ne}^{10+}$ beam and detecting the reaction products of the DCE channel and of the other open channels characterized by same projectile and target.

Exploratory investigations of the two classes of experiments and for the competing quasi-elastic channels have been already performed, highlighting the strengths and the limiting aspects of the adopted technique and establishing the best working conditions [29], [30], [31], [32].

3.1. Experiments with ^{18}O projectiles ($\beta^+ \beta^+$ direction)

For the experiments of this class, the reaction channels of interest are listed below:

- Elastic and inelastic scattering (^{18}O , ^{18}O)
- DCE reaction (^{18}O , ^{18}Ne)
- Charge-exchange reaction (^{18}O , ^{18}F)
- Two-proton pickup reaction (^{18}O , ^{20}Ne)
- One-proton pickup reaction (^{18}O , ^{19}F)
- Two-neutron stripping reaction (^{18}O , ^{16}O)
- One-neutron stripping reaction (^{18}O , ^{17}O)

One of the main challenges of such experiments is the measurement at very forward angles, including zero-degree. This is performed by placing the spectrometer with its optical axis at $+3^\circ$ with respect to the beam axis. Thanks to its large angular acceptance, a range $0^\circ < \theta_{\text{lab}} < +9^\circ$ is thus covered. The MAGNEX quadrupole and dipole magnetic fields are set in order that the incident beam, after passing through the magnets, reaches a region besides the FPD where it stops in a specifically designed Faraday Cup, which measures the incident charge in each run.

^{116}Sn , ^{76}Se and ^{48}Ti are the targets already explored via ($^{18}\text{O}, ^{18}\text{Ne}$) reaction at 15 and 22 AMeV in order to study the $^{116}\text{Sn} \rightarrow ^{116}\text{Cd}$, $^{76}\text{Se} \rightarrow ^{76}\text{Ge}$ and $^{48}\text{Ti} \rightarrow ^{48}\text{Ca}$ transitions, respectively, and the competing channels. The reduction and analysis of the collected data is presently in progress.

3.2. Experiments with ^{20}Ne projectiles ($\beta^-\beta^-$ direction)

In the class of experiments with $^{20}\text{Ne}^{10+}$ beams, the reaction channels we are interested are the following:

- Elastic and inelastic scattering ($^{20}\text{Ne}, ^{20}\text{Ne}$)
- DCE reaction ($^{20}\text{Ne}, ^{20}\text{O}$)
- Charge Exchange reaction ($^{20}\text{Ne}, ^{20}\text{F}$)
- Two-proton stripping reaction ($^{20}\text{Ne}, ^{18}\text{O}$)
- One-proton stripping reaction ($^{20}\text{Ne}, ^{19}\text{F}$)
- Two-neutron pickup reaction ($^{20}\text{Ne}, ^{22}\text{Ne}$)
- One-neutron pickup reaction ($^{20}\text{Ne}, ^{21}\text{Ne}$)

For these experiments, the spectrometer optical axis is typically placed at -3° , thus the covered angular range is $0^\circ < \theta_{\text{lab}} < +8^\circ$. The quadrupole and dipole magnetic fields of MAGNEX are set in order that the $^{20}\text{Ne}^{10+}$ beam reaches the low-B ρ region besides the FPD where a specific Faraday cup is located.

A peculiarity of these experiments concerns the treatment of the different charge states of the beam emerging out of the target. The beam components characterized by charge states lower than 10^+ , mainly $^{20}\text{Ne}^{9+}$ and $^{20}\text{Ne}^{8+}$, produced by the interaction of the beam with the electrons of the target material, have a magnetic rigidity which is similar to the ions of interest. Therefore, they enter in the FPD acceptance, causing a limitation in the rate tolerable by the detector. In order to stop these unwanted ^{20}Ne particles, two aluminium shields are mounted upstream the sensitive region of the focal plane detector. Moreover, a specific study of different materials to be used as post-stripper foil downstream of the target foil to conveniently minimize the amount of $^{20}\text{Ne}^{9+}$ and $^{20}\text{Ne}^{8+}$ has been recently performed [30].

The systems already explored using the ($^{20}\text{Ne}, ^{20}\text{O}$) reaction at 15 AMeV are the ^{116}Cd target (to study the $^{116}\text{Cd} \rightarrow ^{116}\text{Sn}$ transition), the ^{130}Te (for the $^{130}\text{Te} \rightarrow ^{130}\text{Xe}$) and the ^{76}Ge (for the $^{76}\text{Ge} \rightarrow ^{76}\text{Se}$), together with the elastic, inelastic, SCE and transfer reactions involving same beams and targets. The data reduction and analysis are in progress.

4. The R&D activity during Phase 2

The main foreseen upgrades for the spectrometer whose R&D activities are being performed within Phase 2 are:

- The substitution of the present focal plane gas tracker, based on multiplication wire technology, with a tracker system based on micro patterned gas detector [33];
- The substitution of the wall of silicon pad stopping detectors with telescopes of SiC-CsI detectors [34], [35];
- The introduction of an array of scintillators for measuring the coincident γ -rays [36], [37];
- The enhancement of the maximum accepted magnetic rigidity, preserving the geometry and field uniformity of the magnetic field in order to keep the high-precision of the present trajectory reconstruction;
- The design and installation of a beam dump to stop the high-power beams, keeping the generated radioactivity under control [38].
- The development of the technology for suitable nuclear targets to be used in the experiments. Here the challenge is to produce and cool isotopically enriched thin films able to resist to the high power dissipated by the interaction of the intense beams with the target material [8], [9].

5. Conclusions

A systematic study of heavy-ion induced double charge exchange reactions and of the other reaction channels characterized by the same projectile and target is in progress at INFN-LNS. The main goal is to investigate the nuclear response to DCE reactions for all the isotopes candidate for $0\nu\beta\beta$ decay to give experimentally driven indication towards the determination of $0\nu\beta\beta$ NMEs.

In the present document, the focus was on the techniques adopted to set up the MAGNEX spectrometer for the challenging measurements of such suppressed reaction channels. The strategy used to perform the zero-degree measurement, based on an accurate simulation of the ion trajectories along the spectrometer and on the use of two Faraday cups properly designed for each category of experiments was described. The R&D activities presently on going on the beam lines and MAGNEX spectrometer were also briefly sketched.

Acknowledgments

This project has received funding from the European Research Council (ERC) under the European Union's Horizon 2020 research and innovation program (grant agreement No 714625).

References

- [1] H. Ejiri, J. Suhonen, K. Zuber, *Physics Reports* 797, 1 (2019).
- [2] F. Cappuzzello et al., *J. Phys.: Conf. Ser.* 630, 012018 (2015).
- [3] F. Cappuzzello et al., *Eur. Phys. J. A* 54, 72 (2018).
- [4] M. Cavallaro et al., *Proceedings of Science, PoS(BORMIO2017)* 015 (2017).
- [5] F. Cappuzzello et al., *Eur. Phys. J. A* 51,145 (2015).
- [6] M. Cavallaro et al., *Eur. Phys. J. A* 48 (2012) 59.
- [7] L. Calabretta et al., *Modern Physics Letters A* 32, 17 (2017).
- [8] F. Iazzi et al., *WIT Transactions on Engineering Science* 116, 206 (2017).
- [9] F. Pinna et al., *J. Phys. Conf. Ser.* 1056, 012046 (2018).
- [10] H. Lenske et al., *Phys. Rev. C* 98, 044620 (2018).
- [11] E. Santopinto et al., *Phys. Rev. C* 98 061601(R) (2018).
- [12] H. Lenske et al., *Prog. Part. Nucl. Phys.* 109 (2019) 103716.
- [13] S. Calabrese et al., *Nucl. Instr. and Meth. A* (submitted).
- [14] F. Cappuzzello et al. *Eur. Phys. J. A* 52, 167 (2016).
- [15] F. Cappuzzello et al., *Nucl. Instr. and Meth. A* 763 (2014) 314.
- [16] J.R.B. Oliveira et al., *J. Phys. G. Nucl. Part. Phys.* 40 (2013) 105101.
- [17] D. Carbone et al., *Phys. Rev. C* 90, 064621 (2014).
- [18] F. Cappuzzello et al., *Nature Communications* 6, 6743 (2015).
- [19] F. Cappuzzello et al., *Eur. Phys. J. A* 52 (2016) 169.
- [20] M.J. Ermamatov et al., *Phys. Rev. C* 94 (2016) 024610.
- [21] M.J. Ermamatov et al., *Phys. Rev. C* 96 (2017) 044603.
- [22] B. Paes et al., *Phys. Rev. C* 96 (2017) 044612.
- [23] E. N. Cardozo et al., *Phys. Rev. C* 97 (2018) 064611.
- [24] V.A.B. Zagatto et al., *Phys. Rev C* 97 (2018) 054608.
- [25] R. Linares et al., *Phys. Rev. C* 98 (2018) 054615.
- [26] M. Cavallaro et al., *Eur. Phys. J. A* 55 (2019) 244.
- [27] M. Cavallaro et al., *Phys. Rev. C* 93, 064323 (2016).

- [28] M. Cavallaro et al., Nucl. Instr. and Meth. A 700, 65 (2013).
- [29] M. Cavallaro et al., Nucl. Instr. and Meth. B 463 (2020) 334.
- [30] M. Cavallaro et al., Results in Phys. 13 (2019) 102191.
- [31] A. Spatafora et al., Phys. Rev. C 100 (2019) 034620.
- [32] S. Calabrese et al., Acta Phys. Pol. 49 (2018) 275.
- [33] M. Cortesi et al., Review of Scientific Instruments 88, 013303 (2017).
- [34] S. Tudisco et al., Sensors 18, 2289 (2018).
- [35] A. Muoio et al., EPJ Web of Conferences 117, 10006 (2016).
- [36] J. R. B. Oliveira et al., J. Phys. Conf. Ser. 18, 012040 (2018).
- [37] J.R.B. Oliveira et al., Eur. Phys. J. A (2020) 56:153.
- [38] A.D.Russo et al., J. Phys. Conf. Ser. 1056 (2018) 012051.

Theory of Heavy Ion Charge Exchange Reactions as Probes for Beta-Decay

Horst Lenske^{1,2a}, Jessica Bellone^{2,3}, Stefano Burello^{2,3}, Maria Colonna^{2,3}, and José-Antonio Lay⁴

¹ Institut für Theoretische Physik, Justus-Liebig-Universität Gießen, D-35392 Gießen, Germany

² NUMEN Collaboration, LNS Catania, Italy

³ INFN-LNS, I-95123 Catania, Italy

⁴ Department de FAMN, Universidad de Sevilla, Apartado 1065, E-41080 Sevilla, Spain

Abstract. The theory of peripheral heavy ion single (SCE) and double (DCE) charge reactions by quantum mechanical distorted wave and microscopic nuclear structure methods is discussed. Two distinct classes of DCE reactions are identified: Double single charge exchange (DSCE) reactions are conventional two-step processes given by a pair of sequential SCE reactions. Of special interest are hadronic Majorana-type DCE reactions (MDCE) where the DCE process is achieved in a reaction of formal one-step character, accompanied by intrinsic nuclear second order processes leading to the coherent exchange of two charged mesons. It is shown that DCE reactions cover processes resembling both $2\nu 2\beta$ and $0\nu 2\beta$ nuclear matrix elements. As such, they may serve the same role for probing double-beta decay matrix elements as SCE reactions for single beta-decay matrix elements. First results show that ion-ion DCE reactions are the ideal testing grounds for investigations of rare second order nuclear processes, giving insight into nuclear in-medium two-body correlation.

PACS. PACS-key describing text of that key – PACS-key describing text of that key

1 Introduction

Single charge exchange reactions (SCE) are a widely used tool for studying the isospin and spin-isospin response of nuclei. The discovery of the giant Gamow-Teller resonance by the pioneering experiments at IUCF [1] initiated widespread experimental and theoretical research activities, continuing until today with even increasing intensity. Over the years, a wealth of data has been accumulated and has served to understand the isovector charge exchange response of nuclei. Comprehensive reviews of the experimental and theoretical methods and achieved results are found in [2] for light ion reactions and in [3] for heavy ion-induced reactions. Peripheral heavy ion collisions, corresponding to direct reactions, are as useful for spectral studies as light ion scattering. An especially appealing aspect is the broad range of projectile-target combinations which, for example, allow to project out selectively specific features, e.g. spin flip and non-spin flip transitions. In a recent paper, the physics potential of heavy ion double charge reactions proceeding as a second order sequential process was investigated theoretically in Ref. [4]. From that work, it is evident that Double Single Charge Exchange (DSCE) reactions are well suited as strong interaction surrogate reactions for the weak interaction $2\nu 2\beta$ processes. Two-neutrino beta-decay ($2\nu 2\beta$) is under scrutiny since the work of Maria Goepfert-Maier [11] the late 1930ies. It is a second-order process, perfectly well al-

lowed by the standard model [12]. A few nuclei are known to decay by this already rather rare process, see Ref. [13].

The relation of DCE reactions to $0\nu 2\beta$, however, is not immediately clear. One purpose of this paper is to clarify that issue and establish a link to $0\nu 2\beta$. As discussed in breadth in the literature, e.g. [5–10], the interest on such a connection is manifold in view of the important implications on physics beyond the standard model, if $0\nu 2\beta$ decay will ever be observed. While the $2\nu 2\beta$ nuclear matrix elements (NME) are accessible experimentally, such a check against data does not yet exist for $0\nu 2\beta$ processes, but searches are a central topic of contemporary nuclear physics. Estimates of life times and transition probabilities are relying on theoretical investigations, notoriously showing an uncomfortably large spread of values. Independent tests of the nuclear models underlying the calculations of $0\nu 2\beta$ NME are highly necessary and desirable by obvious reasons because they will allow to evaluate and gauge the theoretical results independently. That role may be occupied by heavy ion DCE reactions.

While single charge exchange (SCE) reactions with light and heavy ions have been studied intensively, see e.g. [2, 3], close to nothing is known about double charge exchange reactions. Only very recently, the NUMEN project has been initiated [14], using heavy ion reactions to explore that unknown territory, also aiming at establishing the relation to double beta decay. Clearly, to establish that connection requires additional efforts in our theoretical understanding of nuclear multi-step re-

^a e-mail: horst.lenske@physik.uni-giessen.de

actions. In section 2 we start with a summarizing introduction into the theoretical background for single and double single charge exchange reactions. In section 3 the physical concepts of Majorana DCE reactions are introduced. First numerical results are discussed in section 4 and in section 5 an outlook will be given.

2 Single and Double Single Charge Exchange Reactions

As discussed in detail in Ref. [15], the SCE reaction amplitudes are expressed as DWBA matrix elements of transition form factors obtained with the nucleon-nucleon T-matrix:

$$K_{\alpha\beta}^{(ST)}(\mathbf{p}) = (4\pi)^2 \left(V_{ST}^{(C)}(p^2) F_{ST}^{(ab)\dagger}(\mathbf{p}) \cdot F_{ST}^{(AB)}(\mathbf{p}) + \delta_{S1} \sqrt{\frac{24\pi}{5}} V_{ST}^{(Tn)}(p^2) Y_2^*(\hat{\mathbf{p}}) \cdot \left[F_{ST}^{(ab)\dagger}(\mathbf{p}) \otimes F_{ST}^{(AB)}(\mathbf{p}) \right]_2 \right) \quad (1)$$

including spin-isospin elements of tensorial rank 0 with form factors $V_{ST}^{(C)}$, and rank-2 tensor components with form factors $V_{ST}^{(Tn)}$. We denote the initial channel by $\alpha = a + A$ and the final channel by $\beta = b + B$. The SCE reaction kernel is given by products of nuclear form factors, for example ($S = 0, 1, T = 1$)

$$F_{ST}^{(AB)}(\mathbf{p}) = \langle B | e^{i\mathbf{p}\cdot\mathbf{r}} \boldsymbol{\sigma}^S \boldsymbol{\tau}^T | A \rangle. \quad (2)$$

The rank-2 tensorial coupling relates to the spin degrees of freedom only. Through the form factors $F_{ST}^{(ab),(AB)}$, the kernels contain the spectroscopic information on the nuclear transitions, and the dynamics by the interaction form factors $V_{ST}^{(C),(Tn)}$. In the central interaction part, the scalar product indicates the contraction of the projectile and target form factor with respect to the spin and isospin degrees of freedom. The isospin degrees of freedom are of course projected by the nuclear transitions to the proper combination of τ_{\pm} operators. The one-step SCE reaction amplitude is obtained as

$$M_{\alpha\beta}(\mathbf{k}_\alpha, \mathbf{k}_\beta) = \sum_{ST} \int d^3 p N_{\alpha\beta}(\mathbf{p}) \langle bB | K_{\alpha\beta}^{(ST)}(\mathbf{p}) | aA \rangle. \quad (3)$$

Initial and final state interactions are contained in the distortion coefficient [15, 16]

$$N_{\alpha\beta}(\mathbf{p}) = \frac{1}{(2\pi)^3} \langle \chi_\beta^{(-)} | e^{-i\mathbf{p}\cdot\mathbf{r}} | \chi_\alpha^{(+)} \rangle. \quad (4)$$

The distortion coefficient $N_{\alpha\beta}$ is closely related to the elastic scattering amplitude: For $p \rightarrow 0$ and $k_\beta \rightarrow k_\alpha$ the definition of the elastic S-matrix is recovered. Thus, in leading order, the above equation corresponds to the folding of the nuclear transition form factors with the ion-ion elastic scattering amplitude. Because of the strong absorption, the distortion coefficient acts mainly as a scaling factor, typically reducing the forward cross section by several orders of magnitudes compared to the plane wave limit. Only at momentum transfers exceeding 100 MeV/c $N_{\alpha\beta}$ leads to modifications of the momentum structure of cross sections. Theory and applications of SCE reactions are reviewed in depth in [3].

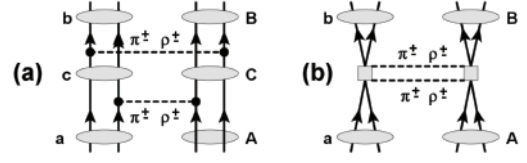


Fig. 1. Diagrams representing schematically the DSCE mechanism. The diagram on the right indicates the DSCE process as described by the effective second-order interaction, Eq.(6).

As discussed in detail in [4], the DSCE reaction matrix element is readily written down as a quantum mechanical second order amplitude in distorted wave approximation (DWA):

$$\mathcal{M}_{\alpha\beta}^{DSCE}(\mathbf{k}_\alpha, \mathbf{k}_\beta) \approx \langle \chi_\beta^{(-)} | bB | \mathcal{T}_{NN} \mathcal{G} \mathcal{T}_{NN} | aA, \chi_\alpha^{(+)} \rangle, \quad (5)$$

corresponding to second order perturbation theory in the residual isovector interaction T_{NN} but being non-perturbative in the initial state (ISI) and final state (FSI) ion-ion interactions, taken care of by the distorted waves $\chi_{\alpha,\beta}^{(\pm)}(\mathbf{r})$ with asymptotically outgoing and incoming spherical waves, respectively. Formally, we can assign the DSCE transition potential

$$\mathcal{U}_{\alpha\beta}^{(DSCE)} = \langle bB | \mathcal{T}_{NN} \mathcal{G} \mathcal{T}_{NN} | aA \rangle \quad (6)$$

After projection of the $a + A$ many-body Green function \mathcal{G} onto the intermediate channel states $|\gamma\rangle = |cC\rangle$ and taking into account the bi-orthogonality of distorted waves leading to the dual S-matrix \tilde{S}^\dagger , the channel propagator becomes [4]

$$G_\gamma(\omega_\alpha) = \int \frac{d^3 k_\gamma}{(2\pi)^3} |\chi_\gamma^{(+)}\rangle \frac{\tilde{S}_\gamma^\dagger(\mathbf{k}_\gamma)}{\omega_\alpha^{(+)} - \omega_\gamma} \langle \chi_\gamma^{(-)}|. \quad (7)$$

Inserting Eq.(7) into Eq.(5), the DSCE transition matrix element reads

$$\mathcal{M}_{\alpha\beta}^{DSCE}(\mathbf{k}_\alpha, \mathbf{k}_\beta) = \sum_{\gamma=c,C} \int \frac{d^3 k_\gamma}{(2\pi)^3} \times \mathcal{M}_{\gamma\beta}^{SCE}(\mathbf{k}_\gamma, \mathbf{k}_\beta) \frac{\tilde{S}_\gamma^\dagger(\mathbf{k}_\gamma)}{\omega_\alpha^{(+)} - \omega_\gamma} \mathcal{M}_{\alpha\gamma}^{SCE}(\mathbf{k}_\alpha, \mathbf{k}_\gamma) \quad (8)$$

showing that the DCE transition amplitude can be expressed as superposition of reaction amplitudes $\mathcal{M}_{\alpha\gamma}^{SCE}$ and $\mathcal{M}_{\beta\gamma}^{SCE}$, into and out of the intermediate channels γ , respectively.

In Fig. 1 the DSCE mechanism is illustrated by its diagrammatic structure. The reactions is driven by a sequence of two uncorrelated SCE processes as the exchange of isovector mesons between projectile and target, thereby altering cumulatively the isospin of either ion by two units.

3 Majorana Double Charge Exchange Reactions

Second order quantal processes like heavy ion DCE are of genuine theoretical interest, albeit rarely studied. Indeed, until recently heavy ion DCE reactions have not been studied systematically as a spectroscopic tool, see e.g. [3] for a review covering also earlier pionic DCE reactions. Our work of Ref. [4] is in

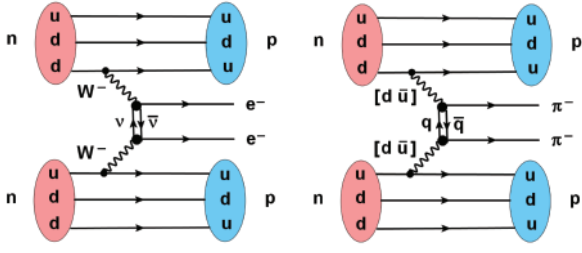


Fig. 2. The elementary weak interaction process mediating the yet to be discovered nuclear $0\nu 2\beta$ decay (left) and the corresponding strong interaction process (right) are depicted schematically. The QCD counterpart is given by the simultaneous emission of two $[d\bar{u}]$ pairs in an $J^\pi = 1^-$ isovector configuration (wavy lines), decaying into π^- -like $[d\bar{u}]$ state and a charge-neutral $q\bar{q}$ pair of π^0 character. Note that all mesonic states are of highly virtual nature.

fact the first theoretical study on fully microscopic grounds, utilizing a quantal description with microscopic reaction-theoretical and structure methods. Double charge exchange reactions with heavy ions are well suited for explorations of weakly populated transitions by several reasons, not to the least by the availability of a large variety of projectile and target combinations and the options for varying beam energies. Here, we consider collisional charge exchange processes given by elementary interactions between target and projectile nucleons. As confirmed by the explicit transfer calculations discussed in [4], the mean-field driven transfer contributions can safely be neglected. Thus, in accordance with the spectroscopic purposes, only processes changing the charge partitions but leaving the projectile-target mass partition unaltered will be discussed.

A central question is whether we can identify on the elementary level a correspondences between strong and weak interaction processes. The answer is yes, as illustrated in Fig. 2. Under nuclear structure aspects, the $0\nu 2\beta$ decay of a nucleus is nothing but a special class of two-body correlation, sustained by the exchange of a (pair of) Majorana neutrino(s) between two nucleons, initiated by the emission of virtual W^\pm gauge bosons. The strong interaction counterpart is initiated by a pair of highly virtual vector mesons $\sim d\bar{u}$, decaying into pairs of neutral and charged pions. This is a two-nucleon process where the participating nucleons are correlated by the virtual charge-neutral quark-antiquark ($q\bar{q}$) pair. Two units of charge (and isospin) are carried away by the emission of the charged component $\sim d\bar{u}$. At the end, the highly off-shell $q\bar{q}$ compounds will materialize into mesons, preferentially into pions but also multi-pion configurations given by isovector scalar and vector mesons.

Either of the weak and the strong processes becomes of interest if the existence and nature is revealed in observable signals. In this respect, we encounter a fundamental difference between $0\nu 2\beta$ decay and the hadronic analogue: Only the weak process may occur in an isolated nucleus while the hadronic one is inhibited – fortunately – by energy conservation. Thus, in order to observe the double-meson emission by a nucleon pair a partner nucleus is required which takes care of the virtuality of the process by absorbing the two charged virtual mesons. For that purpose, heavy ion double charge exchange reactions

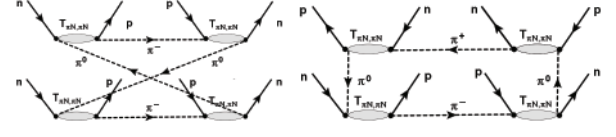


Fig. 3. Crossed-box (left) and box (right) diagrams representing the hadronic MDCE surrogate process for $0\nu 2\beta$ decay. The LHS diagram describes the coherent exchange of pions of equal charge, while the one at the RHS corresponds to a virtual (π^+ , π^-) reaction.

are the ideal tool. The diagrammatic structure of such a reaction is indicated in Fig. 3. Clearly, hadronic DCE will involve processes beyond the one depicted in Fig. 2. The full set of pion-nucleon interactions is taken care of by the well-studied pion-nucleon T-matrix, as indicated in Fig.3. The double- π^- process is contained in the crossed-box diagram which in fact implies a π^0 -supported correlation between projectile and target nucleons. The box (lower) diagram is the off-shell analogue of a pionic DCE reaction. Mesons other than pions will contribute as well.

As an example the box diagrams of Fig. 3 is evaluated here, choosing the $A \rightarrow B$ nuclear transition. Following Fig.3, only the pionic components will be considered. The pion-nucleon T-matrix, given by the resummation of the elementary pion-nucleon (chiral) vertices, may be projected to a variety of operators of scalar, vector, pseudo-scalar and pseudo-vector character. For simplicity, we consider pseudo-vector vertices only, given non-relativistically by the operator $m_\pi \Gamma_v(\mathbf{q}) \sim \boldsymbol{\sigma} \cdot \mathbf{q}\boldsymbol{\tau}$, but additional vertex structures are easily implemented.

The intermediate states are given by π^0 -nucleon configurations, leading to the $A \rightarrow B$ vertex form factor

$$\mathcal{W}_{AB}(\mathbf{p}_1, \mathbf{p}_2, \omega) = \int \frac{d^3k}{(2\pi)^3} \oint \frac{d\omega'}{2i\pi} \Pi_{AB}(\mathbf{p}_1, \mathbf{p}_2, \mathbf{k}, \omega - \omega') \times \frac{1}{2\varepsilon_\pi} T_{\pi^+ n, \pi^0 p}(\mathbf{p}_2, \mathbf{k}) [G_+^\pi(\omega') + G_-^\pi(\omega')] T_{\pi^0 n, \pi^- p}(\mathbf{p}_1, \mathbf{k}). \quad (9)$$

The (retarded) π^0 propagator has been decomposed into its positive and negative frequency contributions, $G_\pm^\pi(\omega) = \pm 1/(\omega \pm \varepsilon_\pi + i\eta)$ where $\varepsilon_\pi(k) = \sqrt{k^2 + m_\pi^2}$. Nuclear spectroscopy is contained in the polarization tensor:

$$\Pi_{AB}(\mathbf{p}_1, \mathbf{p}_2, \mathbf{k}, \omega) = \sum_C \frac{\mathcal{F}_{BC}(\mathbf{p}_2, -\mathbf{k}) \mathcal{F}_{CA}(\mathbf{p}_1, \mathbf{k})}{\omega - (E_C - E_A)} \quad (10)$$

which for $\omega \rightarrow 0$ becomes the inversely energy weighted polarization sum rule. The excitation energies of the intermediate states are denoted by $E_C - E_A$ and the excitation probabilities are described by the nuclear transition form factors

$$\mathcal{F}_{CA}(\mathbf{p}_1, \mathbf{k}) = \langle C | e^{i(\mathbf{p}_1 - \mathbf{k}) \cdot \mathbf{r}} \Gamma_v(\mathbf{p}_1 - \mathbf{k}) | A \rangle. \quad (11)$$

$\mathcal{F}_{BC}(\mathbf{p}_2, -\mathbf{k})$ and the corresponding quantities describing the $a \rightarrow b$ transition are defined accordingly. The ω' -integral is performed on a path in the complex plane picking up only the pion poles. The sum of the two pion propagators leads finally to

$$\Pi_{AB}(\mathbf{p}_1, \mathbf{p}_2, \mathbf{k}, \omega) = \sum_C \frac{\mathcal{F}_{BC}(\mathbf{p}_2, \mathbf{k}) \mathcal{F}_{CA}(\mathbf{p}_1, \mathbf{k})}{(\omega - (E_C - E_A))^2 - \varepsilon_\pi^2 + i\eta}. \quad (12)$$

In the energy denominator we replace $E_C - E_A \sim \bar{\omega}_c$ where $\bar{\omega}_c$ is an average excitation energy. Thus, the propagator becomes independent of the states C and closure can be used:

$$\begin{aligned} \Pi_{AB}(\mathbf{p}_1, \mathbf{p}_2, \mathbf{k}, \omega) &\simeq \frac{-1}{k^2 + m_\pi^2 - (\omega - \omega_C)^2} \\ &\times \langle B | \Gamma_v(\mathbf{p}_1 - \mathbf{k}) \Gamma_v(\mathbf{p}_2 + \mathbf{k}) e^{i(\mathbf{p}_1 \cdot \mathbf{r}_1 + \mathbf{p}_2 \cdot \mathbf{r}_2)} e^{-i\mathbf{k} \cdot (\mathbf{r}_1 - \mathbf{r}_2)} | A \rangle \end{aligned} \quad (13)$$

which is a two-body operator. Hence, in leading order of $1/m_\pi^2$ a NME of 2 particle–2 hole structure is obtained. That result establishes an important connection to $0\nu 2\beta$ decay. The MDCE energy denominator, however, differs from one found in double beta decay because of the bosonic nature of the exchanged mesons. Deeper insight into MDCE dynamics is obtained by evaluating the product of vertices:

$$\begin{aligned} \Gamma_v(\mathbf{p}_1 - \mathbf{k}) \Gamma_v(\mathbf{p}_2 + \mathbf{k}) &= [\boldsymbol{\tau}_1 \otimes \boldsymbol{\tau}_2]_2 \left(-\frac{k^2}{3} (\boldsymbol{\sigma}_1 \cdot \boldsymbol{\sigma}_2 + S_{12}(\hat{\mathbf{k}})) \right. \\ &\left. + \boldsymbol{\sigma}_1 \cdot \mathbf{p}_1 \boldsymbol{\sigma}_2 \cdot \mathbf{p}_2 + \boldsymbol{\sigma}_1 \cdot \mathbf{p}_1 \boldsymbol{\sigma}_2 \cdot \mathbf{k} - \boldsymbol{\sigma}_1 \cdot \mathbf{k} \boldsymbol{\sigma}_2 \cdot \mathbf{p}_2 \right), \end{aligned} \quad (14)$$

where the first term indicates the rank-2 isotensor structure and S_{12} denotes the usual rank-2 spin-tensor. Further reductions and approximations are possible as practised frequently in double-beta decay theory, see e.g. [5,6].

The transition potential, entering as kernel into the MDCE reaction amplitude of formal one-step DWBA structure is

$$\begin{aligned} \mathcal{U}_{\alpha\beta}^{(MDCE)}(\mathbf{r}) &= \int \frac{d^3 p_1}{(2\pi)^3} \int \frac{d^3 p_2}{(2\pi)^3} D_{\pi^q}(p_1^2) D_{\pi^{q'}}(p_2^2) \quad (15) \\ &\times e^{i(\mathbf{p}_1 + \mathbf{p}_2) \cdot \mathbf{r}} \mathcal{W}_{AB}(\mathbf{p}_1, \mathbf{p}_2, \omega_A) \mathcal{W}_{ab}(\mathbf{p}_1, \mathbf{p}_2, \omega_a) \end{aligned}$$

where \mathbf{r} is the channel coordinate $D_{\pi^q}(p^2) = 1/(p^2 + m_\pi^2)$.

The two-nucleon character of the MDCE mechanism is emphasized by the correlation between nucleon pairs within the same nucleus – described by the effective vertices of the kind of Eq.(9) – and of mutual pairs with partners in projectile and target. Each MDCE vertex is of second order in the pion-nucleon T-matrix, i.e. the full MDCE reaction amplitude is of fourth order in $T_{\pi N' \pi N}$. That assures full coverage of pion-nucleon dynamics up to the excitation of nucleon resonances. With respect to isospin, the transition potential corresponds to an effective rank-2 iso-tensor projectile-target interaction. The polarization tensors, Eq.(10), contain a rich content of multipolarities. The pseudo-vector vertex couples to nuclear spin-modes of which Gamow-Teller and spin-dipole excitations are of primary importance. The complete set of operators, however, involves also effective pseudo-scalar and scalar vertices, inducing Fermi-type transition. Even for a double- $0^+ \rightarrow 0^+$ transition in target and projectile, in principle the whole spectrum of multipolarities is allowed as intermediate states, constrained only by the requirement that the modes can be coupled to total angular momentum transfer $J_A = 0 = J_a$ which still allows orbital angular momentum and spin transfers of $L_{A,a} = 0, S_{A,a} = 0$ and $L_{A,a} = 2, S_{A,a} = 2$, respectively, independently in either ion. The similarity in structure to the nuclear matrix element of $0\nu 2\beta$ decay is easily recognized, justifying the naming Majorana-DCE.

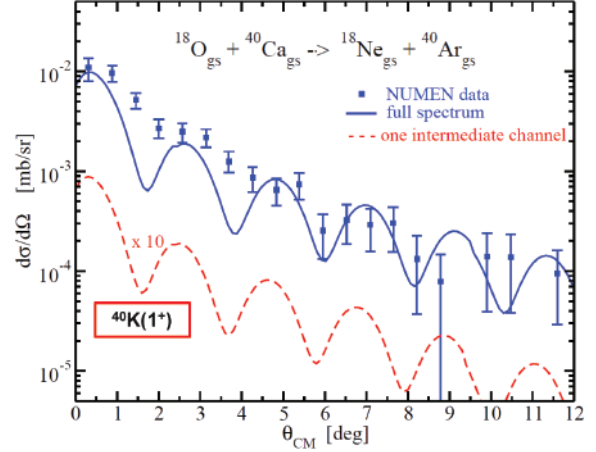


Fig. 4. (Color online) Experimental angular distribution for the DCE reaction $^{18}\text{O}_{gs} + ^{40}\text{Ca}_{gs} \rightarrow ^{18}\text{Ne}_{gs} + ^{40}\text{Ar}_{gs}$ at 15 AMeV [17] compared with DSCE calculation performed with only one intermediate state (red dashed line), and considering the full virtual intermediate state integration up to $J^\pi = 5^\pm$ (blue full line). Both cross sections are folded with the experimental angular resolution ($\Delta\theta_{exp} = 0.6^\circ$) (see Ref. [4]).

4 DCE Theory and Data

The results discussed below were obtained by second order DWBA calculations for the DSCE amplitudes and DWBA calculations for the MDCE amplitudes, respectively. The full DCE reaction amplitude is given by the coherent sum of the MDCE and the DSCE amplitudes:

$$M_{\alpha\beta} \sim \langle \chi_\beta^{(-)} | \mathcal{U}_{\alpha\beta}^{(DSCE)} + \mathcal{U}_{\alpha\beta}^{(MDCE)} | \chi_\alpha^{(+)} \rangle \quad (16)$$

but for the present exploratory studies we use instead the incoherent superposition

$$d\sigma_{\alpha\beta}^{(DCE)}/d\Omega = d\sigma_{\alpha\beta}^{(DSCE)}/d\Omega + d\sigma_{\alpha\beta}^{(MDCE)}/d\Omega. \quad (17)$$

The reaction theoretical aspects of SCE and DCE reactions are discussed in breadth in Refs. [15,4]. One of the major results is that in grazing ion-ion collisions the strong absorption is acting at small momentum transfer predominantly as a scaling factor, allowing to extract from the forward angle cross sections the nuclear transition potentials. Thus, in principle spectroscopic information can be deduced from the data, provided the elastic interactions are known to the necessary precision. In the present calculations, double folding potentials have been used.

In Fig.4 results of the recent theoretical DSCE study [4] are compared to the DCE data of the NUMEN collaboration for the reaction $^{18}\text{O} + ^{40}\text{Ca} \rightarrow ^{18}\text{Ne} + ^{40}\text{Ar}$ at $T_{lab} = 15$ AMeV [17]. Second-order DWBA calculations with QRPA transition strengths have been performed [4]. The measured angular distribution is surprisingly well described without adjustments of the model parameters. Although in total the angular distribution shows features typical for a $L = 0$ transition, intrinsically a rich structure of multipolarities is hidden in the so deceivingly simple looking distribution: Convergence is achieved only if nuclear transitions up to $J^\pi = 5^\pm$ are taken into account. Hence,

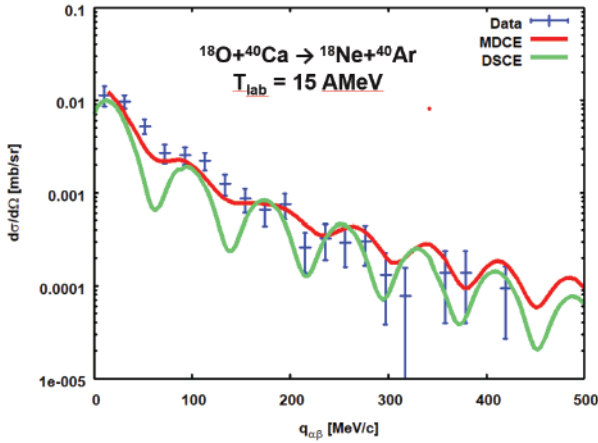


Fig. 5. Angular distribution of the DCE reaction $^{18}\text{O} + ^{40}\text{Ca} \rightarrow ^{18}\text{Ne} + ^{40}\text{Ar}$ at $T_{\text{lab}} = 270$ MeV. The one-step MDCE and the two-step DSCE cross sections are shown separately in comparison to the data of Ref. [17].

the selectivity claimed for $2\nu 2\beta$ NME is not found in the same manner in a DSCE reaction – which is not an unexpected result for a short range strong interaction process. Although the magnitude is almost perfectly well reproduced, obviously the DSCE calculations lead to a somewhat too pronounced diffraction structure, which may be taken to signal a missing component. A detailed discussion is found in [4].

DSCE and MDCE results are shown together in Fig.5. The MDCE results are preliminary because they do not include the full set of diagrams but only the pionic contributions were included. This leaves open an overall scaling factor which was fixed by normalizing the MDCE cross section to the data point at the smallest scattering angle. The cross section is a coherent superposition of $L = S = 0$ and $L = S = 2$ amplitudes, as discussed above. The forward peak of the angular distribution is dominated, in fact, by the MDCE component of total $L = S = 0$, but at larger scattering angles the $L = S = 2$ component approaches a comparable magnitude. Overall, the shape of the measured angular distribution is described decently well in view of the exploratory character of the calculations.

In Fig. 5, DSCE and MDCE cross sections are displayed and compared to data as a function of the momentum transfer $q_{\alpha\beta} = |\mathbf{k}_\alpha - \mathbf{k}_\beta|$. Remarkably, the measured angular range ($\theta \lesssim 12^\circ$) covers a momentum range of up to 400 MeV/c. The angular distribution show a typical $L = 0$ forward structure and the main body of the angular distribution hovering around a mean-value of a few times of 10^{-4}mb/sr .

5 Summary and Outlook

A new theoretical approach to heavy ion double charge exchange reactions was presented, emphasizing the competition of DWBA-type MDCE and second-order DSCE components. Elastic ion-ion interactions were taken into account by microscopic optical potentials. It was pointed out that DCE reactions are unique in their rich and demanding reaction-theoretical and

spectroscopical structure. They are determined by NME resembling those of $2\nu 2\beta$ and $0\nu 2\beta$ decay, respectively, for the DSCE and the MDCE mechanisms. These first results are very promising by indicating a new way of accessing second order DCE nuclear matrix elements. Together with the much better studied SCE reactions and their established usefulness for spectroscopic work, heavy ion DCE reactions are opening a new window to high-precision spectroscopy. Although it will not be possible to insert the extracted matrix elements directly into a double-beta decay analysis, DCE reactions provide an unique way to validate nuclear structure models under controllable laboratory conditions by comparison to data on processes of comparable physical content. New impact on theoretical investigations in both reaction and nuclear structure theory is demanded for a quantitative understanding of these special reactions. Although the present calculations do not yet include the full spectrum of contributions, they are establishing the hadronic Majorana-DCE reaction mechanism. The refinements may lead to changes in detail but will not alter the overall picture.

Acknowledgements

This work was supported by DFG contract Le439/16, Alexander-Humboldt Foundation, and INFN. H.L. acknowledges gratefully the hospitality of LNS Catania.

References

1. C. D. Goodman, C. A. Gouling, M. B. Greenfield, J. Rapaport, D. E. Bainum, C. C. Foster, W. G. Love, and F. Petrovich. *Phys. Rev. Lett.*, 44:1755–1759, 1980.
2. D. Frekers and Alanssari M. *Eur. Phys. J.*, A 54:177, 2018.
3. H. Lenske, F. Cappuzzello, M. Cavallaro, and M. Colonna. *Prog. Part. Nucl. Phys.*, 109:103716, 2019.
4. Jessica I. Bellone, Stefano Burrello, Maria Colonna, Jose-Antonio Lay, and Horst Lenske. *Phys. Lett. B*, 807:135528, 2020.
5. W. G. Haxton and G. J. Stephenson. *Prog. Part. Nucl. Phys.*, 12:409, 1984.
6. T. Tomoda. Double beta-decay. *Rept. Prog. Phys.*, 54:53, 1991.
7. J. Suhonen and O. Civitarese. *Phys. Rept.*, 300:123, 1998.
8. J. D. Vergados, H. Ejiri, and F. Šimkovic. *Rep. Prog. Phys.*, 75:106301, 2012.
9. O. Cremonesi and M. Pavan. *Adv. High Energy Phys.*, 2014:951432, 2014.
10. H. Ejiri, J. Suhonen, and K. Zuber. *Phys. Rept.*, 797:1–102, 2019.
11. M. Goepfert-Mayer. *Phys. Rev.*, 48:512–516, 1935.
12. D. Stefanik, F. Simkovic, and A. Faessler. *Phys. Rev. C*, 91:064311, 2015.
13. A. S. Barabash. *Nucl. Phys.*, A935:52–64, 2015.
14. F. Cappuzzello et al. *Eur. Phys. J.*, A54(5):72, 2018.
15. Horst Lenske, Jessica I. Bellone, Maria Colonna, and Jose-Antonio Lay. *Phys. Rev.*, C98:044620, 2018.
16. Horst Lenske. *J. Phys. Conf. Ser.*, 1056(1):012030, 2018.
17. F. Cappuzzello et al. *Eur. Phys. J.*, A51(11):145, 2015.

Nuclear symmetry energy and its components at zero and finite temperatures

A.N. Antonov¹, M.K. Gaidarov¹, D.N. Kadrev¹, P. Sarriguren², and E. Moya de Guerra³

¹ Institute for Nuclear Research and Nuclear Energy, Bulgarian Academy of Sciences, Sofia 1784, Bulgaria

² Instituto de Estructura de la Materia, IEM-CSIC, Serrano 123, E-28006 Madrid, Spain

³ Departamento de Estructura de la Materia, Física Térmica y Electrónica, and IPARCOS, Facultad de Ciencias Físicas, Universidad Complutense de Madrid, Madrid E-28040, Spain

Abstract. We derive the volume and surface components of the nuclear symmetry energy (NSE) and their ratio in finite nuclei within the coherent density fluctuation model (CDFM). The estimations use the results for the NSE in nuclear matter based on the Brueckner and Skyrme energy-density functionals. The obtained values of these quantities for the Ni, Sn, and Pb isotopic chains are compared with estimations of other approaches which have used available experimental data on binding energies, neutron-skin thicknesses, and excitation energies to isobaric analog states (IAS). Apart from the density dependence investigated in our previous works, we study also the temperature dependence of the symmetry energy in finite nuclei in the framework of the local density approximation combining it with the self-consistent Skyrme-HFB method using the cylindrical transformed deformed harmonic oscillator basis. The results for the thermal evolution of the NSE in the interval $T = 0 - 4$ MeV show that its values decrease with temperature. The same formalism is applied to obtain the values of the volume and surface contributions to the NSE and their ratio at finite temperatures. We confirm the existence of "kinks" of these quantities as functions of the mass number at $T = 0$ MeV for the double closed-shell nuclei ^{78}Ni and ^{132}Sn and the lack of "kinks" for the Pb isotopes, as well as the disappearance of these kinks as the temperature increases.

PACS. 21.60.Jz Nuclear Density Functional Theory and extensions – 21.65.Ef Symmetry energy – 21.10.Gv Nucleon distributions and halo features – 21.30.Fe Forces in hadronic systems and effective interactions

1 Introduction

The study of the nuclear symmetry energy and particularly, its density (ρ) and temperature (T) dependence is an important task in nuclear physics. This quantity is related to the energy connected with the conversion of the isospin asymmetric nuclear matter (ANM) into a symmetric one. It is an important ingredient of the nuclear equation of state (EOS) in a wide range of densities and temperatures (see, e.g., [1–3]). Using approaches like the local-density approximation (LDA) [4–7] and the coherent density fluctuation model [8–10], the knowledge of EOS can give information about the properties of finite systems. As noted in [11] information about NSE from laboratory experiments can be obtained from quantities that are sensitive to it, such as static properties, nuclear excitations, collective motions, and heavy-ion reactions.

The method of the CDFM [12,13] allowed us to make the transition from nuclear matter to finite nuclei in the studies of the NSE for spherical [8] and deformed [9] nuclei, as well as for Mg isotopes [10] using the Brueckner energy-density functional (EDF) of ANM [14,15].

One of the aims of the present work (see also [16,17]) is to evaluate the volume and surface contributions to the NSE and their ratio within the CDFM using Brueckner and Skyrme EDFs in the cases of Ni, Sn, and Pb isotopic chains at zero and finite temperatures. The obtained results in the case of $T = 0$ MeV are compared with results of other theoretical methods and with those from other approaches which used experimental data on binding energies, excitation energies to isobaric analog states, and neutron-skin thicknesses. In addition, we study the sensitivity of the calculated T -dependent quantities on different available forms of the density dependence of the symmetry energy. Another focus of the work (see also [18]) is following the LDA to determine the symmetry energy coefficient and its thermal evolution in the interval $T = 0 - 4$ MeV using different model temperature-dependent local density distributions for the same nuclei. The latter are calculated within a self-consistent Skyrme-HFB method using the cylindrical transformed deformed harmonic-oscillator basis (HFBTHO densities) [19,20]. The effect of temperature on the rms radii of protons and neutrons and the formation of neutron skin in hot nuclei is also analyzed and discussed.

2 The CDFM calculations of the temperature-dependent volume and surface components of the nuclear symmetry energy

We start with the expression for the nuclear energy in the droplet model [21]

$$E(A, Z) = -BA + E_S A^{2/3} + S^V A \frac{(1 - 2Z/A)^2}{1 + S^S A^{-1/3}/S^V} + E_C \frac{Z^2}{A^{1/3}} + E_{dif} \frac{Z^2}{A} + E_{ex} \frac{Z^{4/3}}{A^{1/3}} + a\Delta A^{-1/2}. \quad (1)$$

The symmetry energy [the third term on the right-hand side of Eq. (1)] can be rewritten in the form

$$S(T) \frac{(N - Z)^2}{A}, \quad (2)$$

where

$$S(T) = \frac{S^V(T)}{1 + \frac{S^S(T)}{S^V(T)} A^{-1/3}} = \frac{S^V(T)}{1 + A^{-1/3}/\kappa(T)} \quad (3)$$

with

$$\kappa(T) \equiv \frac{S^V(T)}{S^S(T)}. \quad (4)$$

S^V is the volume symmetry energy parameter and S^S is the modified surface symmetry energy parameter in the liquid model. In the case of nuclear matter, where $A \rightarrow \infty$ and $S^S/S^V \rightarrow 0$, we have $S(T) = S^V(T)$. From Eq. (3) follow the relations of $S^V(T)$ and $S^S(T)$ with $S(T)$:

$$S^V(T) = S(T) \left(1 + \frac{1}{\kappa(T) A^{1/3}} \right), \quad (5)$$

$$S^S(T) = \frac{S(T)}{\kappa(T)} \left(1 + \frac{1}{\kappa(T) A^{1/3}} \right). \quad (6)$$

We use essentially the CDFM scheme to calculate the NSE and its components (see Refs. [12,13,16]). The T -dependent NSE $S(T)$ is calculated by the expression:

$$S(T) = \int_0^\infty dx |\mathcal{F}(x, T)|^2 S[\rho(x, T)], \quad (7)$$

where the symmetry energy for the asymmetric nuclear matter $S[\rho(x, T)]$ has to be determined using a chosen EDF (in [16] Brueckner and Skyrme EDFs have been used for temperature $T = 0$ MeV). In Eq. (7) the weight function $|\mathcal{F}(x, T)|^2$, the key ingredient of the CDFM, depends on the temperature through the temperature-dependent total density $\rho_{total}(r, T)$:

$$|\mathcal{F}(x, T)|^2 = -\frac{1}{\rho_0(x)} \left. \frac{d\rho_{total}(r, T)}{dr} \right|_{r=x}, \quad (8)$$

where

$$\rho_{total}(r, T) = \rho_p(r, T) + \rho_n(r, T), \quad (9)$$

$\rho_p(r, T)$ and $\rho_n(r, T)$ being the proton and neutron T -dependent densities. Following Refs. [16,22–24] an approximate expression for the ratio $\kappa(T)$ can be written within the CDFM:

$$\kappa(T) = \frac{3}{R\rho_0} \int_0^\infty dx |\mathcal{F}(x, T)|^2 x \rho_0(x) \left\{ \frac{S(\rho_0)}{S[\rho(x, T)]} - 1 \right\}, \quad (10)$$

where $|\mathcal{F}(x, T)|^2$ is determined by Eq. (8), $R = r_0 A^{1/3}$ [24] and $S(\rho_0)$ is the NSE at equilibrium nuclear matter density ρ_0 and $T = 0$ MeV. For instance, the values of $S(\rho_0)$ for different Skyrme forces in the Skyrme EDF are given in Table II of Ref. [16]. In what follows we use the commonly employed power parametrization for the density dependence of the symmetry energy (e.g., [23–25])

$$S[\rho(x, T)] = S^V(T) \left[\frac{\rho(x, T)}{\rho_0} \right]^\gamma. \quad (11)$$

Studying the T -dependence of the mentioned quantities we observed (as can be seen below) a certain sensitivity of the results to the value of the parameter γ in Eq. (11). In order to make a choice of its value we imposed the following physical conditions: (i) the obtained results for the considered quantities at $T = 0$ MeV to be equal or close to those obtained for the same quantities in our previous works for the NSE, its components and their [16,18]; and (ii) their values for $T = 0$ MeV must be compatible with the available experimental data (see, e.g., the corresponding references in [16]).

In Fig. 1 the results for $S(T)$, $S^V(T)$, $S^S(T)$, and $\kappa = S^V(T)/S^S(T)$ are given as functions of the mass number A for the Ni isotopic chain for temperatures $T = 0$ –3 MeV calculated using the SkM* and SLy4 Skyrme forces. The results are presented for two values of the parameter $\gamma = 0.3$ and 0.4 . The reason for this choice is related to the physical criterion mentioned above. It can be seen that at $T = 0$ MeV and $\gamma = 0.4$ the value of κ is around 2.6. This result is in agreement with our previous result obtained in the case of the Brueckner EDF in Ref. [16], namely $2.10 \leq \kappa \leq 2.90$. The latter is compatible with the published values of κ extracted from nuclear properties presented in Ref. [24] from the IAS and skins [25] ($2.6 \leq \kappa \leq 3.0$) and from masses and skins [22] ($2.0 \leq \kappa \leq 2.8$). In the case of $\gamma = 0.3$ our result for $T = 0$ MeV is $\kappa = 1.65$ that is in agreement with the analyses of data in Ref. [24] ($1.6 \leq \kappa \leq 2.0$).

It can be seen in Fig. 1 that the quantities $S(T)$, $S^V(T)$, and $S^S(T)$ decrease with increasing temperatures ($T = 0$ –3 MeV), while $\kappa(T)$ slowly increases when T increases. This is true for both Skyrme forces (SkM* and SLy4) and for the three isotopic chains of the Ni, Sn, and Pb nuclei. Here we would like to note that the values of γ between 0.3 and 0.4 that give an agreement of the studied quantities with data, as well as with our previous results for $T = 0$ MeV, are in the lower part of the estimated limits of the values of γ (e.g., in the case of $\gamma = 0.5 \pm 0.1$ [24]).

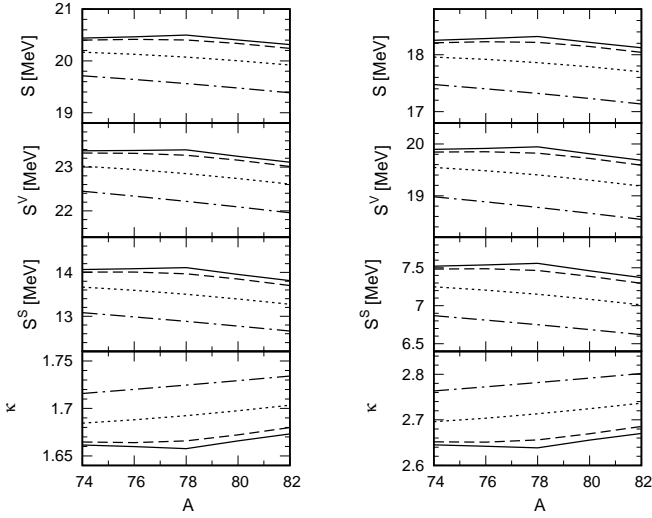


Fig. 1. Mass dependence of the NSE $S(T)$, its volume $S^V(T)$ and surface $S^S(T)$ components and their ratio $\kappa(T)$ for nuclei from the Ni isotopic chain at temperatures $T = 0$ MeV (solid line), $T = 1$ MeV (dashed line), $T = 2$ MeV (dotted line), and $T = 3$ MeV (dash-dotted line) calculated with SkM* Skyrme interaction for values of the parameter $\gamma = 0.3$ (left panel) and $\gamma = 0.4$ (right panel).

Also, it can be seen that there are “kinks” in the curves of $S(T)$, $S^V(T)$, $S^S(T)$, and $\kappa(T)$ for $T = 0$ MeV in the case of double closed-shell nucleus ^{78}Ni . The same is valid for ^{132}Sn and no “kinks” in the Pb chain are observed (see also [16,18]).

In Fig. 2 we give the results for the T -dependence of $S(T)$, $S^V(T)$, $S^S(T)$, and $\kappa(T)$ for the double-magic ^{132}Sn nucleus obtained using both SkM* and SLy4 Skyrme forces. The results are presented by grey areas between the curves for the values of the parameter $\gamma = 0.3$ and $\gamma = 0.4$. It can be seen that $S(T)$, $S^V(T)$, and $S^S(T)$ decrease, while $\kappa(T)$ slowly increases with the increase in temperature for both Skyrme forces.

3 Temperature dependence of the symmetry energy coefficient in finite nuclei and other properties (nucleon densities, rms radii, neutron skins)

For finite systems, different definitions of the symmetry energy coefficient and its temperature dependence are considered in the literature. In the present paper we develop an approach to calculate the symmetry energy coefficient for a specific nucleus starting with the LDA expression given in [4,5]:

$$e_{sym}(A, T) = \frac{1}{I^2 A} \int \rho(r) e_{sym}[\rho(r), T] \delta^2(r) d^3 r. \quad (12)$$

In Eq. (12) $I = (N - Z)/A$, $e_{sym}[\rho(r), T]$ is the symmetry energy coefficient at temperature T of infinite nuclear matter at the value of the total local density $\rho(r) =$

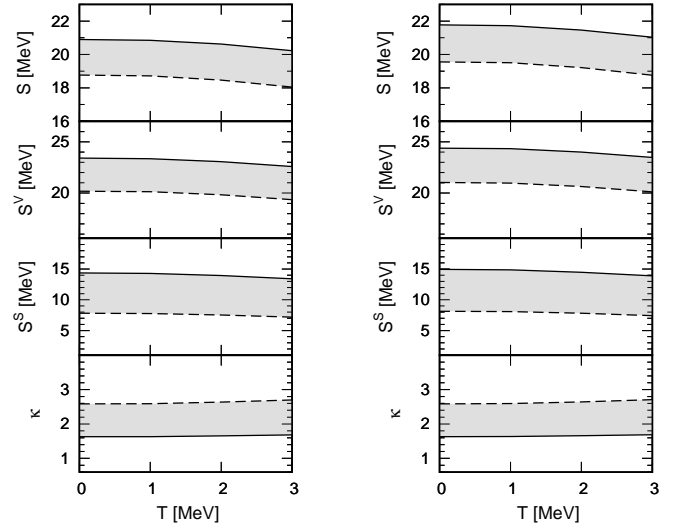


Fig. 2. Temperature dependence of the NSE $S(T)$, its volume $S^V(T)$ and surface $S^S(T)$ components, and their ratio $\kappa(T)$ obtained for values of the parameter $\gamma = 0.3$ (solid line) and $\gamma = 0.4$ (dashed line) with SkM* (left panel) and SLy4 (right panel) forces for ^{132}Sn nucleus.

$\rho_n(r) + \rho_p(r)$, $\delta(r) = [\rho_n(r) - \rho_p(r)]/\rho(r)$ is the ratio between the isovector and the isoscalar parts of $\rho(r)$, with $\rho_n(r)$ and $\rho_p(r)$ being the neutron and proton local densities. The symmetry energy coefficient $e_{sym}(\rho, T)$ can be evaluated in different ways. Following Refs. [4,7], we adopt in this work the definition

$$e_{sym}(\rho, T) = \frac{e(\rho, \delta, T) - e(\rho, \delta = 0, T)}{\delta^2}, \quad (13)$$

where $e(\rho, \delta, T)$ is the energy per nucleon in an asymmetric infinite matter, while $e(\rho, \delta = 0, T)$ is that one of symmetric nuclear matter. These quantities are expressed by $e = \mathcal{E}(r, T)/\rho$, where $\mathcal{E}(r, T)$ is the total energy density of the system (in our case we use the Skyrme EDF [26]).

There exist various methods to obtain the kinetic energy density $\tau_q(r, T)$ (with $q = (n, p)$ referring to neutrons or protons). One of them is, as mentioned above, to use the HFBTHO code. Another way is to use the Thomas-Fermi (TF) approximation adopted in Ref. [4], or an extension of the TF expression up to T^2 terms [27]:

$$\tau_q(r, T) = \frac{2m}{\hbar^2} \varepsilon_{K_q} = \frac{3}{5} (3\pi^2)^{2/3} \times \left[\rho_q^{5/3} + \frac{5\pi^2 m_q^2}{3\hbar^4} \frac{1}{(3\pi^2)^{4/3}} \rho_q^{1/3} T^2 \right]. \quad (14)$$

In Eq. (14) the first term in square brackets is the degenerate limit at zero temperature and the T^2 term is the finite-temperature correction. By using the approximate expression (14) for the kinetic energy density, Lee and Mekjian performed calculations of the volume and surface symmetry energy coefficients for finite nuclei in Ref. [27] showing that the surface symmetry energy term is the most sensitive to the temperature while the bulk energy

term is the least sensitive. In the present work we calculate the kinetic energy density using the self-consistent Skyrme-HFB method and the HFBTHO code [19]. Also, for a comparison we present the results when using $\tau_q(\mathbf{r}, T)$ from Eq. (14).

The T -dependent proton and neutron densities $\rho_q(\mathbf{r}, T)$ normalized by

$$\int \rho_q(\mathbf{r}, T) d\mathbf{r} = Q, \quad Q = Z, N \quad (15)$$

determine the corresponding mean square radii

$$\langle R_q^2 \rangle = \frac{\int r^2 \rho_q(\mathbf{r}, T) d\mathbf{r}}{\int \rho_q(\mathbf{r}, T) d\mathbf{r}}, \quad (16)$$

the rms radii

$$R_q = \langle R_q^2 \rangle^{1/2}, \quad (17)$$

and the neutron skin thickness which is usually characterized by the difference of the neutron and proton rms radii:

$$\Delta R = R_n - R_p. \quad (18)$$

We perform a comparative analysis of e_{sym} for several isotopes from the same Ni, Sn, and Pb chains applying a modified LDA. The symmetric nuclear matter part of Eq. (13) $e(\rho, \delta = 0, T)$ is obtained approximately with densities $\rho_n = \rho_p = \rho/2$, where ρ is the total density calculated with the HFBTHO code. The kinetic energy density is from the TF method with T^2 term [27] in Eq. (14) calculated with the above densities. So, in this case $\tau_n \approx \tau_p$. The results are presented in Fig. 3. It illustrates the isotopic evolution of the symmetry energy coefficient on the examples of Ni ($A=64-82$), Sn ($A=124-152$), and Pb ($A=202-214$) chains in the case of both SLy4 and SkM* Skyrme interactions used in the calculations. A smooth decrease of e_{sym} is observed with the increase of the mass number. Unfortunately, it is difficult to compare our results with other theoretical calculations of e_{sym} of nuclei from the mass range covered in the present work except from the results for ^{208}Pb shown in Refs. [4, 28] and for the mass number $A = 120$ presented in Fig. 5 of Ref. [7].

As an example, we show in Fig. 4 the neutron and proton rms radii [Eq. (17)] and their difference known as the neutron-skin thickness [Eq. (18)] as a function of the mass number A for Sn ($A=124-152$) isotopic chain calculated by using the SLy4 force. First, it can be seen that the proton rms radii increase more slowly than the neutron ones, which is valid also for Ni and Pb isotopic chains and temperatures. This is naturally expected in isotopic chains where the number of protons remains fixed. In addition, while the results of both radii at $T = 0$ and $T = 2$ MeV are close to each other with increasing A , one can see a steep increase of their values when the nucleus become very hot ($T=4$ MeV). As can be seen from Fig. 4(c), the neutron-skin thickness exhibits the same trend as the rms radii. It grows significantly with the increase of T being much larger at $T=4$ MeV than at lower temperatures $T=0$ and 2 MeV.

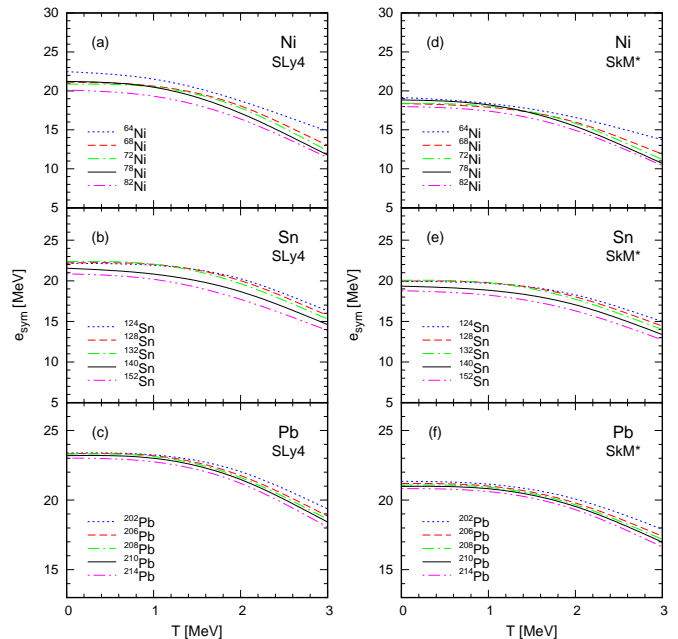


Fig. 3. Temperature dependence of the symmetry energy coefficient e_{sym} obtained for several nuclei from Ni ($A=64-82$) [(a) and (d)], Sn ($A=124-152$) [(b) and (e)], and Pb ($A=202-214$) [(c) and (f)] isotopic chains in HFB method with SLy4 (left panel) and SkM* (right panel) forces. The results of e_{sym} are obtained by applying a modified LDA version with HFBTHO densities and T^2 -approximation for the kinetic energy density [Eq. (14)].

The mechanism of the formation of the neutron skin in tin isotopes has been studied in Ref. [29], where the changes in the neutron skin was attributed mainly to the effect of the temperature on the occupation probabilities of the single-particle states around the Fermi level. In [29] a more limited Sn isotopic chain up to ^{120}Sn was considered. Our results for larger A in this chain (from $A = 124$ to $A = 152$) also show a slow increase of the neutron skin size. The enhancement of the proton and neutron radii at high temperatures leads to a rapid increase of the neutron skin size. We would like to note that at zero temperature, the use of HFBTHO temperature-dependent densities in the present approach confirms the observation in our previous work [30] (where the densities were calculated within a deformed Skyrme HF+BCS approach), namely that a pronounced neutron skin can be expected at $A > 132$ in Sn and $A > 74$ in Ni isotopes.

4 Conclusions

The main results of the present work can be summarized as follows:

(i) With increasing T , the quantities S , S^V , and S^S decrease, while κ slightly increases for all the isotopes in the three chains for both Skyrme forces and for all used density dependences of the symmetry energy.

(ii) The results for $S(T)$, $S^V(T)$, $S^S(T)$, and $\kappa(T)$ are sensitive to the choice of the density dependence of the

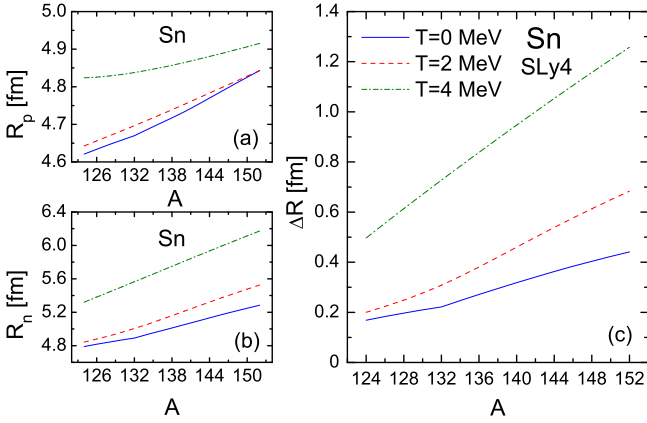


Fig. 4. Mass dependence of the proton R_p (a) and neutron R_n (b) radius of the Sn isotopes ($A=124-152$) calculated with SLy4 interaction at $T = 0$ MeV (solid line), $T = 2$ MeV (dashed line), and $T = 4$ MeV (dash-dotted line). Neutron skin thickness ΔR as a function of A (c) for the Sn isotopes.

symmetry energy $S[\rho(x, T)]$ in Eqs. (7) and (10). The results obtained with values of γ between 0.3 and 0.4 agree better with the experimental information.

(iii) In the cases of double-magic ^{78}Ni and ^{132}Sn nuclei we observe “kinks” for $T = 0$ MeV in the curves of $S(T)$, $S^V(T)$, $S^S(T)$, and $\kappa(T)$, but not in the case of Pb isotopes. It is also worth mentioning how the kinks are blurred and eventually disappear as T increases, demonstrating its close relationship with the shell structure.

(iv) A theoretical approach within the LDA is developed to study the T -dependence of the symmetry energy coefficient in finite nuclei, as well as T -dependent nuclear densities, rms radii, and the formation of neutron skins. The densities $\rho(r, T)$ decrease with T in the central region of nuclei. The neutron skin thickness grows with the increase of T for a given chain.

(v) A comparative analysis of $e_{sym}(A, T)$ is performed using kinetic energy densities $\tau(r, T)$ from TF method up to T^2 term and density distributions $\rho(r, T)$ from HF-BTHO method. The values of $e_{sym}(A, T)$ decrease smoothly with temperature. This is observed also in the case of ^{208}Pb with different model densities $\rho(r, T)$.

A.N.A., M.K.G., and D.N.K. are grateful for the support of the Bulgarian Science Fund under Contract No. KP-06-N38/1. P.S. acknowledges support from Ministerio de Ciencia, Innovación y Universidades MCIU/AEI/FEDER, UE (Spain) under Contract No. PGC2018-093636-B-I00.

References

1. *Topical issue on Nuclear Symmetry Energy*. Guest editors: Bao-An Li, Angels Ramos, Giuseppe Verde, Isaac Vidaña. Eur. Phys. J. A **50**, (2014) 2.
2. J.M. Lattimer, M. Prakash, Phys. Rep. **442**, (2007) 109.
3. B.A. Li *et al.*, Phys. Rep. **464**, (2008) 113.
4. B.K. Agrawal, J.N. De, S.K. Samaddar, M. Centelles, X. Viñas, Eur. Phys. J. A **50**, (2014) 19.

5. S.K. Samaddar, J.N. De, X. Viñas, M. Centelles, Phys. Rev. C **76**, (2007) 041602(R).
6. S.K. Samaddar, J.N. De, X. Viñas, M. Centelles, Phys. Rev. C **78**, (2008) 034607.
7. J.N. De, S.K. Samaddar, Phys. Rev. C **85**, (2012) 024310.
8. M.K. Gaidarov, A.N. Antonov, P. Sarriguren, E. Moya de Guerra, Phys. Rev. C **84**, (2011) 034316.
9. M.K. Gaidarov, A.N. Antonov, P. Sarriguren, E. Moya de Guerra, Phys. Rev. C **85**, (2012) 064319.
10. M.K. Gaidarov, P. Sarriguren, A.N. Antonov, E. Moya de Guerra, Phys. Rev. C **89**, (2014) 064301.
11. Bao-An Li, Nucl. Phys. News **27**, (2017) 7.
12. A.N. Antonov *et al.*, Bulg. J. Phys. **6**, (1979) 151; Z. Phys. A **297**, (1980) 257 (1980); *ibid* **304**, (1982) 239; Nuovo Cimento A **86**, (1985) 23; A.N. Antonov *et al.*, *ibid* 102, (1989) 1701; A.N. Antonov, D.N. Kadrev, P.E. Hodgson, Phys. Rev. C **50**, (1994) 164.
13. A.N. Antonov, P.E. Hodgson, and I.Zh. Petkov, *Nucleon Momentum and Density Distributions in Nuclei* (Clarendon Press, Oxford 1988); *Nucleon Correlations in Nuclei* (Springer-Verlag, Berlin-Heidelberg-New York 1993).
14. K.A. Brueckner, J.R. Buchler, S. Jorna, R.J. Lombard, Phys. Rev. **171**, (1968) 1188.
15. K.A. Brueckner, J.R. Buchler, R.C. Clark, R.J. Lombard, Phys. Rev. **181**, (1969) 1543.
16. A.N. Antonov, M.K. Gaidarov, P. Sarriguren, E. Moya de Guerra, Phys. Rev. C **94**, (2016) 014319.
17. A.N. Antonov, D.N. Kadrev, M.K. Gaidarov, P. Sarriguren, and E. Moya de Guerra, Phys. Rev. C **98**, (2018) 054315.
18. A.N. Antonov, D.N. Kadrev, M.K. Gaidarov, P. Sarriguren, E. Moya de Guerra, Phys. Rev. C **95**, (2017) 024314.
19. M.V. Stoitsov, N. Schunck, M. Kortelainen, N. Michel, H. Nam, E. Olsen, J. Sarich, S. Wild, Comp. Phys. Comm. **184**, (2013) 1592.
20. M.V. Stoitsov, J. Dobaczewski, W. Nazarewicz, P. Ring, Comput. Phys. Comm. **167**, (2005) 43.
21. A.W. Steiner, M. Prakash, J.M. Lattimer, P.J. Ellis, Phys. Rep. **411**, (2005) 325.
22. P. Danielewicz, Nucl. Phys. A **727**, (2003) 233.
23. P. Danielewicz, arXiv: 0607030 [nucl-th] (2006).
24. A.E.L. Dieperink, P. Van Isacker, Eur. Phys. J. A **32**, (2007) 11.
25. P. Danielewicz, arXiv: 0411115 [nucl-th] (2004).
26. N. Wang, M. Liu, L. Ou, Y. Zhang, Phys. Lett. B **751**, (2015) 553.
27. S.J. Lee, A.Z. Mekjian, Phys. Rev. C **82**, (2010) 064319.
28. Z.W. Zhang, S.S. Bao, J.N. Hu, H. Shen, Phys. Rev. C **90**, (2014) 054302.
29. E. Yüksel, E. Khan, K. Bozkurt, G. Colò, Eur. Phys. J. A **50**, (2014) 160.
30. P. Sarriguren, M.K. Gaidarov, E. Moya de Guerra, A.N. Antonov, Phys. Rev. C **76**, (2007) 044322.

The new facilities and devices at Mexico for low energy nuclear reactions studies.

L. Acosta¹, E. Chávez-Lomelí¹, L. Barrón-Palos¹, M.E. Ortiz¹, E. Andrade¹, J. Miranda¹, D. Marín-Lambarri¹, F. Favela², K. de los Ríos¹, S. Murillo¹, J. García¹, L.E. Charón¹, J. Mas¹, L.R. Ríos¹, F. Morales¹, G. Reza¹, C. Flores-Vázquez¹ and A.M. Sánchez-Benítez³.

¹Instituto de Física, Universidad Nacional Autónoma de México, Mexico City, Mexico.

²Instituto de Ciencias Nucleares, Universidad Nacional Autónoma de México, Mexico City, Mexico.

³Departamento de Ciencias Integradas, Universidad de Huelva, Huelva, Spain.

Since 2013 a new investment in facilities and devices occurred at Instituto de Física, UNAM (IFUNAM), promoted by a Program to implement National Laboratories placed at different research Institutions around the country. One of this National facilities is the Mass Spectrometer Accelerator Laboratory (LEMA), inaugurated 6 years ago [1]. The main equipment at LEMA is a high precision 1 MV accelerator performed by HVE, where different radioisotopes can be produced and analyzed by using AMS technique. Presently, ¹⁴C, ¹⁰Be and ²⁶Al concentrations can be well established with the LEMA isotope separator. In such direction, we have developed experiments related with the measure of reaction cross sections using AMS, taking some interesting reactions related with the radioisotopes mentioned. First of all, to produce the radionuclei, we used other Mexican older facilities, such as a Van de Graaff accelerators from IFUNAM and Instituto de Ciencias Nucleares (ININ), where as well slow neutrons can be produced at a TRIGA-III reactor. Many other reactions are presently under study.

Recently a beam line was included at LEMA accelerator, where high current beams with a good precision low energy of many isotopes can be produced. The new line is equipped with a multipurpose reaction chamber where besides nuclear studies, IBA measurements (as RBS and PIXE) can be carried out.

From the Nuclear Physics point of view, a special detection system is under construction: the so called SIMAS array, which will be composed of DSSSD-PAD telescopes (20 + 130 micron thickness) and small PIPS-Surface barrier telescopes (10 + 300 micron thickness) in order to measure low energy channels by using $\Delta E-E$ technique. The readout will be made with commercial Mesytec preamplifiers and the very recent FEBEX3 digitizer data acquisition system. SIMAS is thought to be used as well for experiments abroad.

Other interesting devices at Mexico for low energy physics, are the Super Sonic Jet Gas Target, SUGAR and the Neutron wall, MONDE which could be coupled to different beamlines and thus to be used along with detection array as the mentioned before [2].

This Projects are been partially funded by CONACyT-LN294537, PAPIIT-DGAPA IA103218, IG101616, IA101016 and PIIF-2018 Projects.

[1] C. Solís et al.: Nucl. Inst. Meth. Phys. B 331, (2014).

[2] F. Favela, et al.: Phys. Rev. ST-AB, 18, (2015).

Strongly Resonating Bosons in Hot Nuclei

S. Zhang¹, A. Bonasera^{2,3}, M. Huang¹, H. Zheng⁴, G. Zhang⁵, Z. Kohley^{2,6},
J.C. Wang¹, L. Lu¹, Y.G. Ma^{5,7}, S.J. Yennello^{2,6}

¹College of Physics and Electronics information, Inner Mongolia University for Nationalities, China. ²Cyclotron Institute, Texas A&M University, USA. ³Laboratori Nazionali del Sud, INFN, Italy. ⁴School of Physics and Information Technology, Shaanxi Normal University, China. ⁵Shanghai Advanced Research Institute, Chinese Academy of Sciences, China. ⁶Chemistry Department, Texas A&M University, USA. ⁷Key Laboratory of Nuclear Physics and Ion-beam Application (MOE), Institute of Modern Physics, Fudan University, China.

When two heavy ions near the Fermi energy collide, a warm and low-density region can form in which fragments appear. This region is mainly dominated by proton (p) and alpha (α) particles. In such an environment, the α s interact with each other, and especially through strong resonances, form complex systems such as ^8Be and ^{12}C . Our experimental data analysis results show that in the reactions $^{70(64)}\text{Zn}(^{64}\text{Ni})+^{70(64)}\text{Zn}(^{64}\text{Ni})$ at $E/A=35$ MeV/nucleon levels of ^8Be appear around relative energies $E_{ij}=0.092$ MeV, 3.03 MeV as well as above 10 MeV and 100 MeV. We propose a different method to derive the correlation function based on the relative transverse energy distribution to minimize the experimental uncertainties. For the 3α systems, multi resonance processes give rise to excited levels of ^{12}C . The interaction between any two of the 3 particles provides events with one, two or three ^8Be . Their interfering levels are clearly seen in the minimum relative energy distributions. Events of three couple α relative energies consistent with the ground state of ^8Be are observed with the decrease of the instrumental error at the reconstructed 7.458 MeV excitation energy of ^{12}C , which was suggested as the Efimov (Thomas) state [1]. Also, the Hoyle state at 7.654 MeV excitation energy shows a decay component through the ground state of ^8Be and also components where two different α couples are at relative energies consistent with the ground state of ^8Be at the same time [2].

References

- [1] S. Zhang et al., Chinese Phys. C (to be published); arXiv:1903.09772 (2019)
- [2] S. Zhang et al., Phys. Rev. C (to be published); arXiv:1810.01713 (2019)

Borromean topology in Nuclei; a clear signature of the breakup modes for ${}^9\text{Be}$

A. Pakou¹, O. Sgouros^{1,2}, V. Soukeras^{1,2}, F. Cappuzzello^{2,3}, L. Acosta^{4,5}, C. Agodi², A. Boiano⁶, C. Calabrese^{2,3}, D. Carbone², M. Cavallaro², N. N. Deshmukh², A. Foti^{2,3}, A. Haciosalihoglu², N. Keeley⁷, M. La Commara^{6,8}, I. Martel⁹, M. Mazzocco^{10,11}, A. Muoio², C. Parascandolo⁶, D. Pierroutsakou⁶, K. Rusek¹², A. M. Sanchez-Benitez¹³, G. Santagati², G. Souliotis¹⁴, A. Spatafora², E. Strano¹⁰, D. Torresi², and A. Trzcinska¹²

¹ Department of Physics and HINP, The University of Ioannina, 45110 Ioannina, Greece

² INFN Laboratori Nazionali del Sud, via S. Sofia 62, 95125, Catania, Italy

³ Dipartimento di Fisica e Astronomia, Università di Catania, via S. Sofia 64, 95125, Catania, Italy

⁴ Instituto de Física, Universidad Nacional Autónoma de México, México D. F. 01000, México

⁵ INFN - Sezione di Catania, via S. Sofia 64, 95125, Catania, Italy

⁶ INFN - Sezione di Napoli, via Cinthia, I-80126, Napoli, Italy

⁷ National Centre for Nuclear Research, ul. Andrzejki Sołtana 7, 05-400, Otwock, Poland

⁸ Dipartimento di Scienze Fisiche, Università di Napoli "Federico II", via Cintia, I-80126 Napoli, Italy

⁹ Departamento de Ciencias Integradas, Facultad de Ciencias Experimentales, Campus de El Carmen, Universidad de Huelva, 21071, Huelva, Spain

¹⁰ Dipartimento di Fisica e Astronomia, Università di Padova, via Marzolo 8, I-35131, Padova, Italy

¹¹ INFN - Sezione di Padova, via Marzolo 8, I-35131, Padova, Italy

¹² Heavy Ion Laboratory, University of Warsaw, ul. Pasteura 5a, 02-093, Warsaw, Poland

¹³ Departamento de Ciencias Integradas, Facultad de Ciencias Experimentales, Campus de El Carmen, Universidad de Huelva, 21071, Huelva, Spain

¹⁴ Department of Chemistry, National and Kapodistrian University of Athens and HINP, 15771 Athens, Greece

Abstract. The breakup of the Borromean nucleus ${}^9\text{Be}$ incident on a proton target at 5.67 MeV/nucleon was studied with a triple coincidence requirement between the two breakup α fragments and the recoiling proton. A clear signature of the three configuration modes : $\alpha + \alpha + n$, ${}^8\text{Be} + n$, and ${}^5\text{He} + {}^4\text{He}$ was observed in the recoiling proton spectra, reconstructed in a full kinematics approach, and the rates of these configurations were quantified.

PACS. 25.70Mn Aa – 24.10.Eq bb – 27.20.+n vv PACS-keydescribing text of that key

1 Introduction

With the advent of radioactive beam facilities, studies with weakly bound nuclei either radioactive or the stable ones, the last to be used as predecessor cases, have been pursued in several laboratories. Breakup cross sections have been measured with the aim of extracting structure properties which have to do either with conventional models or clustering models, for providing information relevant to astrophysics, and for exploring coupling channel effects. Amongst the most interesting weakly bound nuclei, the Borromean nuclei attract a vivid interest in the nuclear physics community.

In mathematics the topology of the Borromean rings is found in knot theory as a Brunnian link, a non trivial link that becomes a set of trivial unlinked circles if any one component is removed. The realization of a Borromean rings assembly from DNA was reported in 1997 by biologists Chengde Mao and coworkers [1]. In molec-

ular physics, in 2003 the chemist Fraser Stoddart and coworkers utilized coordination chemistry to construct a set of rings in one step from 18 components [2]. In Nuclear Physics the quantum-mechanical analog of the Borromean rings is a halo or Efimov state, predicted in 1970 [3].

The ${}^9\text{Be}$ nucleus is a stable Borromean nucleus, which attracts a vivid interest due to its role in astrophysical problems [4–7] and is an excellent example in clustering structure theories [8]. In fact the strength of any three-body $\alpha + \alpha + n$, and the two body ${}^8\text{Be}+n$ and ${}^5\text{He} + {}^4\text{He}$ cluster configuration has received renewed attention, since it is believed that in neutron-rich astrophysical environments, such as a core-collapse supernovae, the three-body reaction $\alpha + \alpha + n \rightarrow {}^9\text{Be}$ followed by ${}^9\text{Be}(\alpha, n){}^{12}\text{C}$ may provide a route for building up the heavy elements and triggering the r-process. Calculations in that direction are hampered by a severe lack of experimental information on the partial widths for the various channels, and therefore

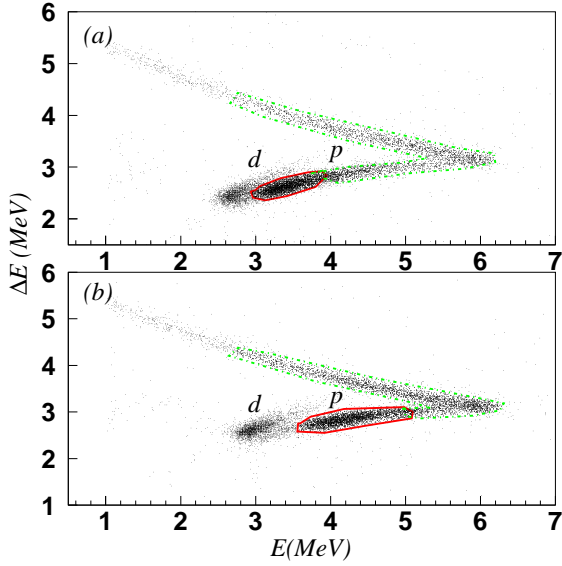


Fig. 1. $\Delta E - E$ spectrum obtained by the EXPADES module; (a): strip 16, corresponding to $\theta_{\text{lab}} = 14.6^\circ$ and (b): strip 8, corresponding to $\theta_{\text{lab}} = 20.2^\circ$, in coincidence with MAGNEX. Both panels present part of the spectra zoomed on protons. Some punched through deuterons are also distinguished. Gates related to the ${}^8\text{Be} + n$ mode and the ${}^5\text{He} + {}^4\text{He}$ mode are defined by the solid (red) and dot-dashed (green) curves, respectively.

an accurate determination of the decay rates of ${}^9\text{Be}$ to the three configurations : $\alpha + \alpha + n$, ${}^8\text{Be} + n$, ${}^5\text{He} + {}^4\text{He}$ is needed. Same should be important in clustering theories where ${}^9\text{Be}$ may be considered to be composed of two α - particles and a valence neutron, forming, at larger $\alpha + \alpha$ separations ${}^5\text{He}$ nuclei, where the neutron resides in a $p_{3/2}$ orbit. The linear combinations of two such orbits give rise to nuclear molecular σ - and π - bonds in ${}^9\text{Be}$.

The above theories either in astrophysics or in nuclear structure can be benefited from accurate determination of the decay rates of ${}^9\text{Be}$ to the three configurations : $\alpha + \alpha + n$, ${}^8\text{Be} + n$, ${}^5\text{He} + {}^4\text{He}$. While the breakup of ${}^9\text{Be}$ via the ${}^8\text{Be}$ s. has been measured for many of the low-lying excited states of ${}^9\text{Be}$, and is well established, the breakup branching via the first-excited 2^+ state of ${}^8\text{Be}$ and via ${}^5\text{He} + {}^4\text{He}$ remains uncertain while no attention has been given to the direct process $\alpha + \alpha + n$. Contradictory results are given for the above decay rates. Gete et al. [9] following a recent measurement of ${}^9\text{C}$ β -decay gives as predominant breakup mode the ${}^5\text{He} + {}^4\text{He}$ one while in a series of articles for breakup of ${}^9\text{Be}$ on light targets as ${}^6\text{Li}$ [10,11] or heavier as ${}^{208}\text{Pb}$ [12] and at similar center of mass energies, the predominant mode seems to be the ${}^8\text{Be} + n$ one.

In this direction we report in this paper breakup measurements of ${}^9\text{Be}$ on the simplest target, the proton, which guarantee us, as it will be shown later on, a clear signature of the three decay modes.

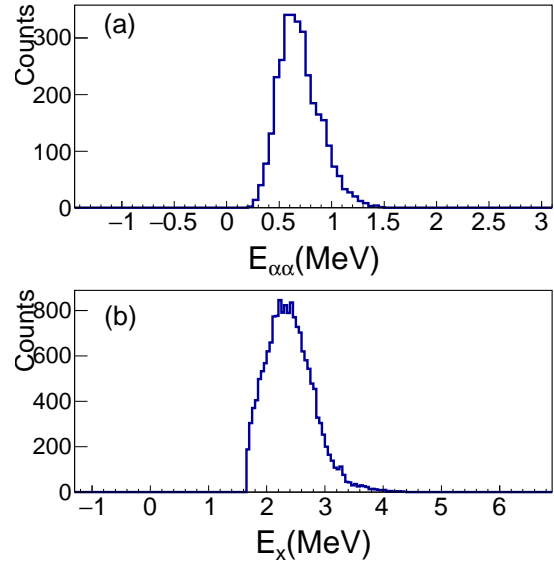


Fig. 2. (a) : reconstructed $\alpha - \alpha$ relative energy spectrum with $\alpha - \alpha - p$ triple coincidence event-by-event requirement. (b) : reconstructed excitation spectrum of ${}^9\text{Be}$

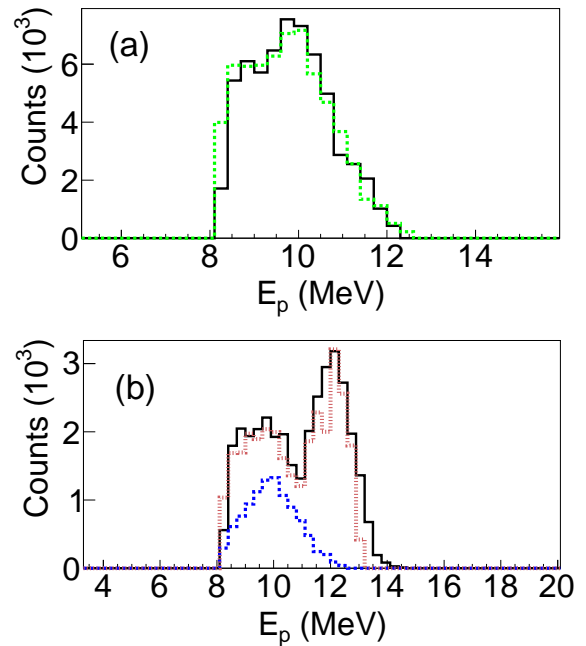


Fig. 3. Experimental energy spectrum of recoiling protons observed in the angular range 4.5 to 34° , reconstructed in a full kinematics approach. (a) : restricted to protons due to the ${}^5\text{He} + {}^4\text{He}$ mode. As an example the cut adopted for $\theta_{\text{lab}} = 20.2^\circ$ is designated in Fig. 1 by the green color. (b) : restricted to protons due to the ${}^8\text{Be} + n$ mode. An example cut for $\theta_{\text{lab}} = 20.2^\circ$ for this mode is designated in Fig. 1 by the red color. The dotted - dashed line (blue color) denotes our simulation for the ${}^5\text{He}$ mode in the specific angular range where a kinematical overlap between the two decay modes exists. The dotted curve (brown color) is the sum of both simulations.

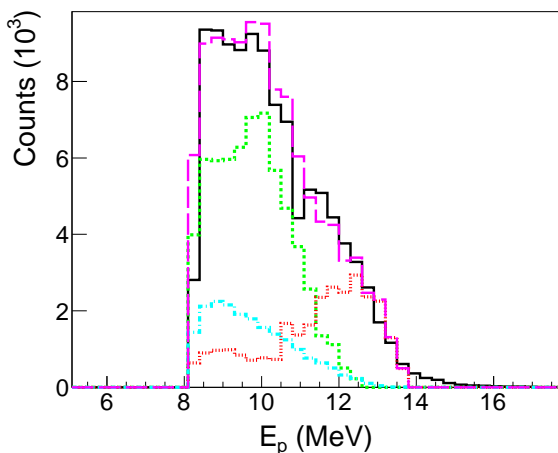


Fig. 4. Experimental energy spectrum of recoiling protons reconstructed in a full kinematics approach, observed in the angular range 4.5 to 34° , including all protons (cuts were applied to each of the $\Delta E - E$ spectra). The simulations of each of the three modes are designated by green and red lines for the ${}^5\text{He} + {}^4\text{He}$ and ${}^8\text{Be} + n$ sequential modes, respectively and the cyan line for the direct mode. Their sum is designated by the magenta line and is in excellent agreement with the data, represented by the black line.

2 Experimental Details

The experiment was designed to study the breakup of ${}^9\text{Be}$ from a proton target, by detecting the two alpha fragments and the recoiling proton. It is possible then to reconstruct the missing momentum of the undetected particle, the neutron fragment. In this respect, the reaction kinematics can be fully determined, allowing the complete reconstruction of the breakup events, providing identification of the populated ${}^9\text{Be}$ states and the type of the breakup procedure.

It was performed at the MAGNEX facility [13] of the Istituto Nazionale di Fisica Nucleare Laboratori Nazionali del Sud (INFN - LNS) in Catania, Italy. A ${}^9\text{Be}^{4+}$ beam was accelerated to 51 MeV by the LNS TANDEM Van de Graaff and impinged on a $450 \mu\text{g}/\text{cm}^2$ CH_2 target.

The MAGNEX [14] spectrometer was adopted to detect one of the alphas in an almost full angular range between $\sim 2.5^\circ$ to 12° . The elastically scattered ${}^9\text{Be}$ ions were most of them “masked” by appropriate magnetic fields, allowing the detection of alphas in an energy slice between 15 and 25 MeV corresponding, according to our simulation [15], to $\sim 70\%$ of our energy phase space. A small remainder of elastic scattering was rejected off line by the appropriate cuts in two dimensional ΔE vs. $(\Delta E + E)$ spectra, obtained from the focal plane gas and silicon detectors [13]. For the reduction of the MAGNEX data we followed the same techniques as in our previous studies [16,17] which is based on the ray reconstruction of the data, and is described in Refs. [18–21]. The other alpha breakup fragment and the proton recoil were detected in a $\Delta E - E$ silicon module of the EXPADES array [22,23] in coincidence with MAGNEX. It should be noted that sig-

nals were handled by the acquisition and in the reduction of the data such as the detector ΔE acting in an independent mode for acquiring α 's, and in a $\Delta E - E$ mode for acquiring the recoiling protons (two separate detectors). The EXPADES module was masked by a $49.6 \mu\text{m}$ thick tantalum foil to prevent deterioration from Rutherford scattering. This foil absorbed part of the α 's at the worse case in the order of 20% for combinations with alphas detected at the most forward angles of MAGNEX. Protons were passed through with a loss of the order of 35%, but due to the ΔE threshold the acquired phase space was reduced by 85%. Protons were well discriminated in most of the angles from deuterons originating from transfer reactions (${}^9\text{Be} + p \rightarrow {}^8\text{Be} + d$) as can be seen in Fig. 1. The $\alpha - \alpha - \text{proton}$ triple coincidence requirement, excluded all transfer events from carbon included in the CH_2 target (${}^9\text{Be} + {}^{12}\text{C} \rightarrow {}^8\text{Be} + {}^{13}\text{C}$), while the contamination from $\alpha - \alpha - d$ events was very small below 4% and only for the most forward or very backward angles, where some overlap of protons and deuterons occurred, since both light particles were punched through the second stage of the telescope.

3 Data reduction and results

An event-by-event analysis was adopted and a search within the appropriate energy regions was performed, looking for alpha particles detected in MAGNEX in coincidence with alpha particles stopped in the ΔE detector, identified via kinematics and energy loss algorithms, and protons identified by the $\Delta E - E$ technique (Fig. 1) in the EXPADES telescope in triple coincidence mode. This requirement gives clear evidence of a breakup event. When such an event was found, tagged by energy and angle (i.e. the momentum vector), the energy of the undetected neutron, E_n , was determined by applying the momentum conservation law.

Requesting only negative Q values for the breakup events, relative energy spectra between all outgoing particles were determined. It should be noted that, as was expected due to the available energy of our experiment, in the energy spectrum between the two α particles in a triple coincidence requirement only one obvious peak at ≈ 700 keV appeared. This is designated in Fig. 2 (a). No peak appears at 92 keV, since our setup does not include the breakup cone due to feeding of the ${}^8\text{Be}(\text{g.s.})$. The contribution of breakup via this state has been considered in the past [10,11] to be negligible. According to Refs. [10–12,24,25] the observed peak may be attributed to breakup either through the broad excited state of ${}^8\text{Be}(2^+)$ at 3.030 MeV with width $\Gamma = 1.5$ MeV (here we observe the tail of this broad resonance) and/or the broad ground state of ${}^5\text{He}$ with width $\Gamma = 648$ keV. These states are populated by the decay of the excited state in ${}^9\text{Be}$ at 2.429 MeV, as can be seen from our reconstructed excitation spectrum, displayed in Fig. 2 (b).

The big challenging question now is : to what extent are each of the two configurations involved in the breakup

process? The main problem is that the energy shared between the three particles is small and the energy correlations between the decay particles are the same irrespective of the intermediate step in the decay. In one of the previous [10] studies of ${}^9\text{Be}$ breakup on a lithium target an attempt was made at separation by adopting in simulations the angular distribution of the breakup fragments. No firm answer was given in this case either, since the authors were only able to do it for the ${}^8\text{Be}$ case. The fact that their experimental energy and angular distributions were understood using the ${}^8\text{Be}(2^+) + n$ channel alone is not in itself sufficient evidence that the ${}^5\text{He} + \alpha$ channel does not contribute. On the other hand, under the appropriate experimental conditions of the present experiment, the recoil kinematics could serve for this separation and for the first time a clear signature of the two sequential modes and finally of the direct mode was obtained.

An inspection of Fig. 1 discloses the existence of a intense signature for a process similar to that attributed to a two-body reaction. Indeed, a comprehensive investigation via our simulation code MULTIP [15] shows that in both sequential breakup channels our experimental conditions allow the involvement of a narrow part for the intermediate nucleus energy profile. This results in an energy “confinement” of events observed in the recoil proton two dimensional $\Delta E - E$ spectrum, see Fig. 1. Following the kinematics of the reaction through MULTIP, appropriate cuts as denoted by the red and green colors in Fig. 1 for the ${}^8\text{Be} + n$ and ${}^5\text{He} + {}^4\text{He}$ configurations, respectively, were applied to each strip of the telescope and therefore for each angle between 4.5 and 34° . We have assumed that the rest of the protons can be related to the direct three-body mode. The event-by-event reconstruction was therefore repeated three times, once with contours around just the protons designated in red in Fig. 1 then those designated in green as they appear in Fig. 1 and finally with a contour around all protons identified in the $\Delta E - E$ plot. The results are displayed in Figures 3a, 3b and 4 respectively. To evaluate the contribution of each mode to the breakup extensive simulations were performed with our code MULTIP [15]. For the sequential modes our simulation results are presented in Figs. 3 (a) and 3 (b), scaled according to the overall strength of the data and presenting an excellent description of them. The same simulations are also presented in Fig. 4 together with our simulation of the direct part. The sum of all three should represent the total breakup and apparently does so excellently. Finally, the efficiencies of each mode were extracted by dividing the obtained simulated areas restricted under the experimental conditions with the unrestricted ones, and the rate of each process was determined as: $29 \pm 8\%$, $22 \pm 4\%$ and $49 \pm 12\%$ for the $\alpha + \alpha + n$, ${}^8\text{Be} + n$ and ${}^5\text{He} + {}^4\text{He}$ modes, respectively. The source of the assigned errors is related mainly to the adopted angular distributions in our simulations. These assumptions based to either flat or CDCC angular distributions resulted on slightly different efficiencies and slightly different gates for the two sequential modes on the $\Delta E - E$ proton spectra. Although the resulting uncertainties are large, especially for the ${}^5\text{He} +$

α mode, it is obvious that this mode is strong, a result which agrees qualitatively with the findings from beta decay experiments such as those of of Gete *et al.* obtained from ${}^9\text{C}$ β -decay data [9]. It should be noted that our results exclude the observation of breakup decays via the ${}^8\text{Be}_{g.s}$ and also decays via the 1.684 MeV excited state of ${}^9\text{Be}$.

In summary, we have studied the breakup of the Borromean nucleus ${}^9\text{Be}$ incident on a proton target at 5.67 MeV/nucleon in inverse kinematics. The data analysis was based on a triple coincidence full kinematics approach. A clear signature of the three breakup modes of ${}^9\text{Be}$ was tagged in our recoiling proton spectra. The three modes were quantified after applying efficiency corrections via a Monte Carlo simulation of our experimental system. It was found that the breakup of ${}^9\text{Be}$ occurs after excitation to its 2.429 MeV state. The strongest contribution to breakup is via the ${}^5\text{He} + {}^4\text{He}$ mode, quantified at 59% while lesser contributions are due to the direct and the ${}^8\text{Be} + n$ modes. Hopefully these results will make substantial impact in the fields of astrophysics and cluster structure as discussed in the introduction.

4 Acknowledgments

The research leading to these results has received funding from the European Union HORIZON2020 research and innovation programme under Grant Agreement n 654002 - ENSAR2. One of us (L. Acosta) acknowledges partial support by the CONACyT-LN294537 and PAPIIT-IA103218 Projects.

References

1. Chengde Mao et al., Nature **386**, 137 (1997).
2. K. S. Chichak et al., Science **304**, 1308 (2004).
3. V. Efimov, Phys. Lett. **B 33**, 563 (1970).
4. S. E. Woosley and R. D. Hoffman ; Astrophys. J. **395**, 202 (1992).
5. B. S. Meyer et al. ; Astrophys. J. **399**, 656 (1992).
6. W. M. Howard et al. ; Astrophys. J. **417**, 713 (1993).
7. S. E. Woosley et al.; Astrophys. J. **433**, 229 (1994).
8. W. von Oertzen et al.; Physics Reports **432**, 43 (2006).
9. E. Gete et al., Phys. Rev. C **61**, 064310 (2000).
10. P. Papka et al., Phys. Rev C **75**, 045803(2007)
11. T. A. D. Brown et al., Phys. Rev C **76**, 054605(2007).
12. B. R. Fulton et al., Phys. Rev C **70**, 047602(2004).
13. M. Cavallaro et al.; Eur. Phys. J. A **48**, 59 (2012).
14. F. Cappuzzello et al.; Eur. Phys. J. **A 52**, 167 (2016).
15. O. Sgouros et al.; European Physical Journal A **53**, 165(2017).
16. V. Soukeras et al., Phys. Rev. C **95**, 054614(2017).
17. A. Pakou et al., Phys. Rev. C **95**, 044615 (2017)
18. F. Cappuzzello et al.; Nucl. Instruments and Methods in Phys. Research A **621**, 419 (2010).
19. F. Cappuzzello et al., Nucl. Instruments and Methods in Phys. Research A **638**, 74 (2011).
20. M. Cavallaro et al.; Nucl. Instruments and Methods in Phys. Research A **648**, 46 (2011).

21. M. Cavallaro et al. ; Nucl. Instr. and Meth. **A 637**, 77 (2011).
22. E. Strano et al.; Nucl. Instr. and Meth. **B317**, 657 (2013).
23. D. Pierrousakouet et al.; Nucl. Instr. and Meth. **A 834**, 46 (2016).
24. A. S. Denikin et al.; Phys. Part. Nucl. Lett. **12**, 703 (2015).
25. G. Nyman et al.; Nucl. Phys. **A 510**, 189 (1990).

Accessing the most neutron-rich nuclei: toward elucidating the nucleosynthesis of the elements beyond iron

George. A. Souliotis

Laboratory of Physical Chemistry, Department of Chemistry, National and Kapodistrian University of Athens, Athens 15771, Greece

The origin and distribution of the chemical elements are among the central topics of nuclear physics and chemistry today [1]. The light elements H, He and Li were formed at the late stages of the Big Bang, whereas heavier elements up to iron are products of thermonuclear fusion in the stars. Furthermore, elements beyond iron cannot be produced in fusion reactions. Instead, they are made by neutron capture reactions via the (slow) s-process and the (rapid) r-process, each contributing equally to their production. Whereas the details of the s-process are well understood [2], the precise site and conditions of the r-process remain elusive [3]. Supernova explosions and the merging of neutron stars are now believed to be the proper r-process sites [4]. The r-process takes place in astrophysical environments of extremely high neutron density (10^{20} neutrons/cm³) and involves nuclei that are extremely neutron rich, reaching the limits of nuclear binding (the so-called neutron drip line). The production and study of such nuclei is key in understanding and modeling the r-process and, thus, unveiling the origin of the chemical elements from iron all the way to uranium [5]. The main traditional avenues to produce and study neutron rich nuclei are spallation reactions, fission and high-energy projectile fragmentation. Surpassing the limits of these approaches and reaching out to the neutron drip line is nowadays highly desirable. Thus, the study of new synthesis routes constitutes a vigorous endeavor of the nuclear physics community.

Motivated by these developments, we have devoted a substantial part of our efforts to study the production of neutron rich nuclei in peripheral multinucleon transfer reactions in the beam energy range 15-25 MeV/nucleon. We have systematically studied the production of neutron rich projectile-like fragments from the reactions of a ⁸⁶Kr beam (15 and 25 MeV/nucleon) on ⁶⁴Ni and ¹²⁴Sn targets using the MARS recoil separator at the Cyclotron Institute of Texas A&M University [6], and have provided a detailed theoretical description of the measured distributions based on microscopic modeling of the involved reactions [7,8,9]. In parallel, we have experimentally and theoretically investigated the fission of an ²³⁸U (20 MeV/nucleon) beam interacting with a ²⁰⁸Pb target [10]. After an overview of these works, I will discuss recent work and plans to continue our efforts at LNS/Catania, at Texas A&M University, and, in the near future, at RISP/IBS, Korea.

[1] C.A. Bertulani and T. Kajino, Progress in Part. Nucl. Physics 89, 56 (2016).

[2] F. Kappeler et al., Review of Modern Physics 83, 157 (2011).

[3] M.R. Mumpower et al., Progress in Part. Nucl. Physics 86, 86 (2016).

[4] E. Pian et al., Nature 551, 67 (2017).

[5] Connecting Quarks with the Cosmos: Eleven Science Questions for the New Century. The National Academies Press, Washington, 2003.

[6] G.A. Souliotis et al., Phys. Rev. C 84, 064607 (2011).

[7] P.N. Fountas, G.A. Souliotis et al., Phys. Rev. C 90, 064613 (2014).

[8] A. Papageorgiou, G.A. Souliotis et al, Journal of Physics G 45, 095105 (2018).

[9] O. Fasoula, G.A. Souliotis et al, in preparation.

[10] N. Vonta, G.A. Souliotis et al, Phys. Rev. C 92, 064611 (2016).

Production cross sections and angular distributions of neutron-rich isotopes from Kr-induced collisions at 15 MeV/nucleon

O. Fasoula^a, G.A. Souliotis^{a,*}, Y.K. Kwon^b, K. Tshoo^b
M. Veselsky^c, S.J. Yennello^d and A. Bonasera^{d,e}

^a *Laboratory of Physical Chemistry, Department of Chemistry, National and Kapodistrian University of Athens, Athens, Greece*

^b *The Rare Isotope Science Project (RISP), Institute for Basic Science, Daejeon, Korea*

^c *Institute of Experimental and Applied Physics, Czech Technical University, Prague, Czech Republic*

^d *Cyclotron Institute, Texas A&M University, College Station, Texas, USA*

^e *Laboratori Nazionali del Sud, INFN, Catania, Italy*

* *Corresponding author. Email: soulioti@chem.uoa.gr*

Abstract

We present our recent study of cross sections and angular distributions of projectile fragments from heavy-ion reactions at beam energy of 15 MeV/nucleon. We studied the production cross sections and the angular distributions of neutron-rich nuclides from collisions of a ^{86}Kr (15 MeV/nucleon) beam with heavy targets (^{124}Sn and ^{238}U). Experimental data from our previous work at Texas A & M were compared with model calculations. Our calculations were based on a two-step approach: the dynamical stage of the collision was described with two models, the phenomenological Deep-Inelastic Transfer model (DIT) and with the microscopic Constrained Molecular Dynamics model (CoMD). The de-excitation of the hot heavy projectile fragments was performed with the Statistical Multifragmentation Model (SMM). An overall good description of the available data was obtained with the models employed. Furthermore, we performed calculations with a radioactive beam of ^{92}Kr (15 MeV/nucleon) interacting with a target of ^{238}U . We observed that the multinucleon transfer mechanism leads to extremely neutron-rich nuclides toward and beyond the astrophysical r-process path.

1 Introduction

The exploration of the nuclear landscape toward the astrophysical r-process path and the neutron drip-line are at the center of interest of the nuclear physics community [1]. Essential to this development is the efficient production of neutron-rich nuclides which constitutes a central issue in current and upcoming rare isotope beam facilities worldwide (see, e.g., [2–9]). Projectile fragmentation constitutes a general approach

to produce exotic nuclei at beam energies above 100 MeV/nucleon (see, e.g., [10,11]). Surpassing the limits of the traditional approaches and reaching out to the neutron dripline is highly desirable at present. Thus, the study of new synthesis routes constitutes a vigorous endeavor of the nuclear science community.

Our initial experimental studies of projectile fragments from 25 MeV/nucleon reactions of ^{86}Kr on ^{64}Ni [12] and ^{124}Sn [13] indicated substantial production of neutron-rich fragments. In this contribution, we present our study of the production cross sections and the angular distributions of projectile fragments from collisions of a ^{86}Kr (15 MeV/nucleon) beam with heavy targets. Data from our experimental work at Texas A&M are compared with calculations based on either the phenomenological Deep-Inelastic Transfer (DIT) model, or the microscopic Constrained Molecular Dynamics model (CoMD). A overall good description of the experimental data with DIT or CoMD was obtained, suggesting the possibility of using the present theoretical models to predict the production of exotic nuclei employing radioactive beams.

2 Outline of Results and Comparisons

A detailed presentation of our previously obtained experimental data appear in [16] in which the mass spectrometric measurements of production cross sections of neutron-rich projectile fragments from the reactions of a 15 MeV/nucleon ^{86}Kr beam with $^{64,58}\text{Ni}$ and $^{124,112}\text{Sn}$ targets were presented. We also mention that the experimental data of 25 MeV/nucleon ^{86}Kr -induced reactions are described in detail in our articles [12–16].

2.1 Study of Production Cross Sections

In Fig. 1.a), we present the experimental mass distributions of projectile-like fragments with $Z=37-30$ from the reaction ^{86}Kr (15 MeV/nucleon) + ^{124}Sn [16] and compare them with the calculations using the DIT code [17,18] (solid yellow line) and the CoMD code [20,21] (solid red line). Both dynamical codes were combined with the SMM model [19] for the de-excitation of the hot quasi-projectiles emerging after the dynamical stage of the reaction. The results of the calculations are in overall good agreement with the experimental data especially for isotopes close to the projectile with $Z=36-32$. We note that in some of the Kr isotopes ($A=86,89,90$), the experimental cross sections are especially high because of contamination from elastically scattered beam. The overestimation of the cross sections for n-rich products with $Z=31$ and 30 from the CoMD calculation may be related to issues of low excitation energy, as currently calculated in CoMD [22].

Furthermore, in Fig. 1.b) we show the DIT/SMM calculations of projectile-like fragments from the reaction ^{86}Kr (15 MeV/nucleon) + ^{238}U (solid yellow line). We have chosen the heaviest and most neutron-rich target available in order to explore how far in N/Z we can go with this reaction. Also, we chose to study the reaction with the ^{238}U target, but with a radioactive beam of ^{92}Kr (15 MeV/nucleon) (dashed yellow line). As there are no experimental data with the ^{238}U target, we used the data from ^{86}Kr (15 MeV/nucleon) + ^{124}Sn for reference. We observe that the distributions extend far to the neutron-rich side especially with radioactive beam. This tendency is pronounced for isotopes rather close to the projectile ($Z=34-36$).

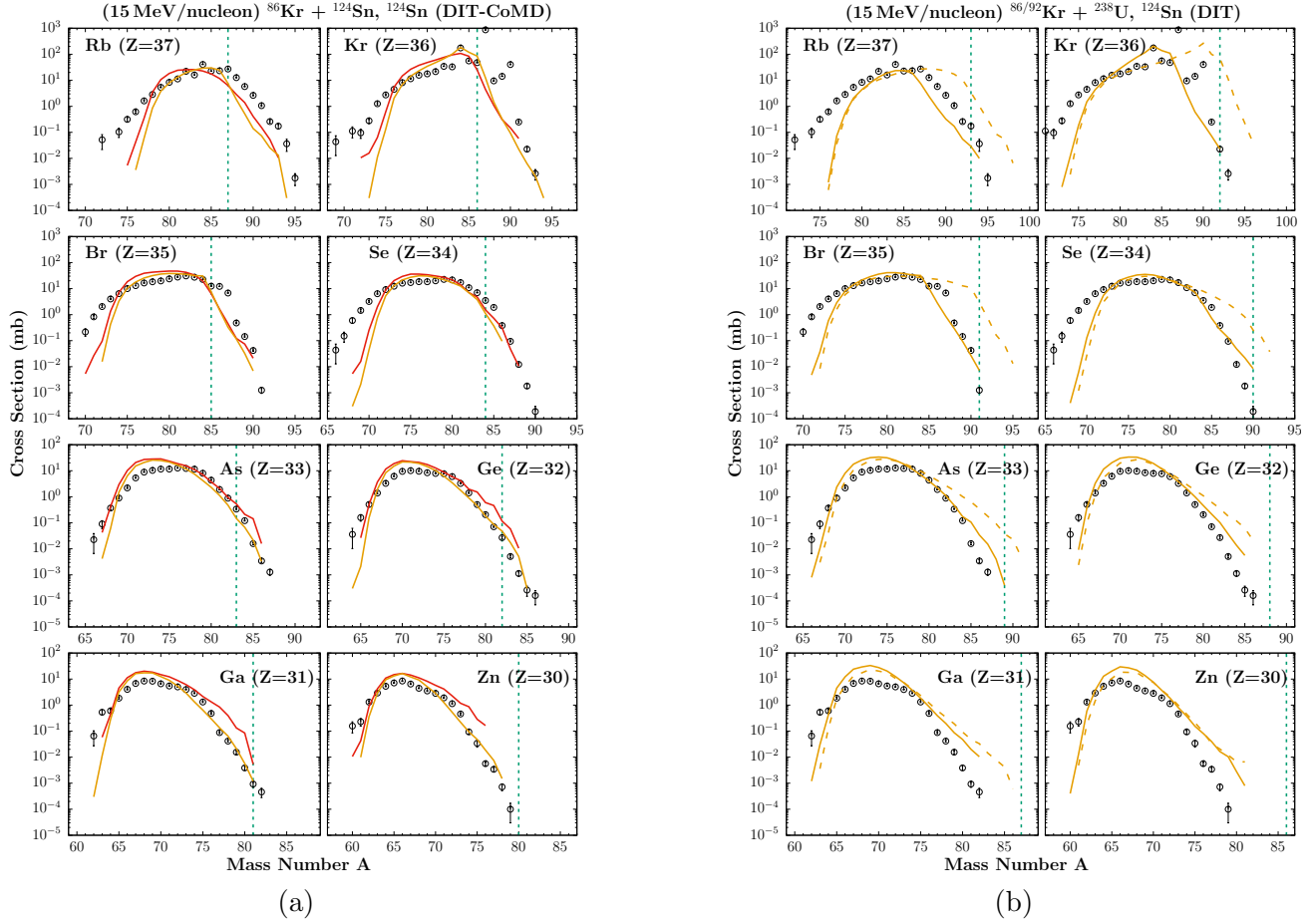


Fig. 1. a) Reaction of stable beam of ^{86}Kr (15 MeV/nucleon) with a ^{124}Sn target. b) Reaction of stable and radioactive beams of $^{86/92}\text{Kr}$ (15 MeV/nucleon) with a ^{238}U target. Open points: experimental mass distributions from ^{86}Kr (15 MeV/nucleon) + ^{124}Sn [16]. Red lines: CoMD/SMM calculations ($^{86}\text{Kr}+^{124}\text{Sn}$). Yellow lines: DIT/SMM calculations ($^{86}\text{Kr}+^{238}\text{U}$). Yellow dashed lines: DIT/SMM calculations ($^{92}\text{Kr}+^{238}\text{U}$).

We point out that, for, e.g., bromine ($Z=35$), isotopes that have up to 15 more neutrons ($A = 96$) than the corresponding stable isotope ($A = 81$) can be obtained. Thus, by using neutron-rich radioactive beams, and via the mechanism of peripheral multinucleon transfer, we have the possibility to produce extremely neutron-rich nuclides. We note that similar observations were made for the reaction with lighter projectiles (of Ar and Ca) on the ^{238}U target in our recent article [23]. We do not have experimental data for the $^{86}\text{Kr}+^{238}\text{U}$ reaction, but we have plans to study it in the near future.

A comprehensive presentation of the DIT/SMM calculated production cross sections of the projectile fragments from the above reaction on the Z vs N plane is given in Fig. 2. Stable isotopes are represented by closed squares, whereas fragments obtained by the $^{92}\text{Kr}+^{238}\text{U}$ reaction are given by the open circles, with sizes corresponding to cross-section ranges according to the figure key. Using this representation of the previous calculation, we clearly observe that the neutron pickup products from ^{92}Kr reach and even exceed the path of the r-process near $Z=30-36$.

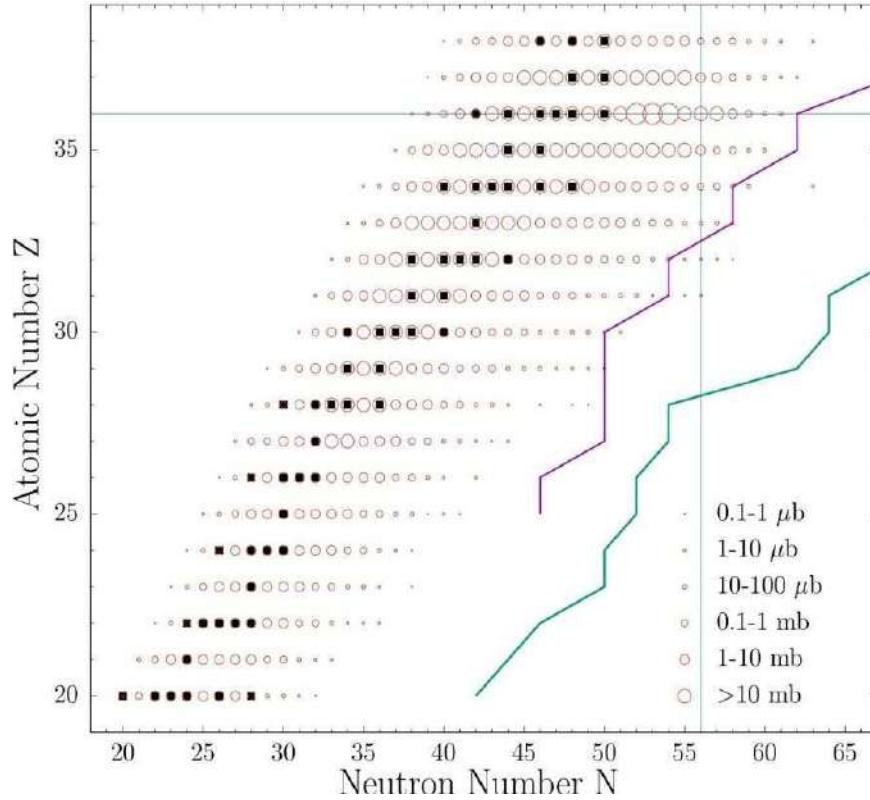
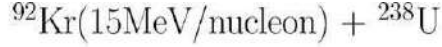


Fig. 2. Representation of DIT/SMM calculated production cross sections of projectile fragments from the radioactive-beam reaction ${}^{92}\text{Kr}$ (15 MeV/nucleon) + ${}^{238}\text{U}$ on the Z–N plane. Cross section ranges are shown by open circles according to the key. Closed squares show the stable isotopes. The purple line shows the astrophysical r-process path and the green line shows the neutron drip-line. The horizontal and vertical lines indicate, respectively, the Z and N of the ${}^{92}\text{Kr}$ projectile.

In Table 1, we summarize the calculated cross sections and production rates of several neutron-rich isotopes from the reaction of the radioactive beam of ${}^{92}\text{Kr}$ (15 MeV/nucleon) with the ${}^{238}\text{U}$ target. For the rate calculations, the ${}^{92}\text{Kr}$ beam with intensity of 1.0 pA (6.2×10^9 particles/sec) is assumed to interact with a ${}^{238}\text{U}$ target of 20 mg/cm² thickness. We see that it is possible to produce extremely neutron-rich isotopes in these reactions with the use of re-accelerated radioactive beams, such as ${}^{92}\text{Kr}$, that will become available in upcoming rare-isotope facilities (e.g. [7–9]). Along these lines, we wish to continue this work at the following facilities: a) the Cyclotron Institute of Texas A&M University using the MARS separator, b) the LNS/Catania using beams from the S800 Cyclotron and employing the MAGNEX spectrometer, and c) the RISP facility with stable and radioactive beams from the RAON accelerator complex using the KOBRA separator.

Table 1

Cross sections and rate estimates (last column) of very neutron-rich isotopes from the reaction ^{92}Kr (15 MeV/nucleon) + ^{238}U . For the rates, a radioactive beam of ^{92}Kr with intensity 1.0 particle nA (6.2×10^9 particles/s) is assumed to interact with a ^{238}U target of 20 mg/cm² thickness.

Rare Isotope	Reaction Channel	Cross Section (mb)	Rate (sec ⁻¹)
^{93}Kr	-0p+1n	12	3.6×10^3
^{94}Kr	-0p+2n	1.3	3.9×10^2
^{95}Kr	-0p+3n	0.3	90
^{96}Kr	-0p+4n	0.05	15
^{92}Br	-1p+1n	0.8	2.4×10^2
^{93}Br	-1p+2n	0.2	60
^{94}Br	-1p+3n	0.07	21
^{95}Br	-1p+4n	0.02	6
^{90}Se	-2p+0n	0.25	75
^{91}Se	-2p+1n	0.14	42
^{92}Se	-2p+2n	0.05	15
^{93}Se	-2p+3n	0.02	6

2.2 Study of Angular Distributions

After the description of the production cross sections, which have been the main focus of our work so far, we initiated a detailed study of the angular distributions of the projectile-like fragments. In regards to experimental data, we refer again to our previous work [16] with the MARS spectrometer. As described in [16], the data were obtained at two angle settings, by sending the beam on the target at the appropriate angle in the MARS target chamber. The angle settings were: the 4.0° setting and the 7.5° setting, covering the polar angular ranges of $\Delta\theta=2.2^\circ\text{--}5.8^\circ$, and $\Delta\theta=5.6^\circ\text{--}9.2^\circ$, respectively. We remind that appropriate integration of these data provided the total production cross sections that are reported in [16] and presented in Figs 1.a) and 1.b).

We present the angular distributions of selected projectile fragments from the reaction of $^{86}\text{Kr}+^{124}\text{Sn}$ at 15 MeV/nucleon (Figures 3.a) and 3.b)). For this system, the grazing angle is $\theta_{gr} \simeq 9.0^\circ$. (A vertical dashed line indicates this angle in the figures.) So it is expected that the 7.5° angle setting is the appropriate one to efficiently collect the quasi-elastic products, as has been discussed in [16,22].

The experimental data of the differential cross sections for each nuclide consist of two points: one at

$\theta=4.0^\circ$ and the other at $\theta=7.5^\circ$, each plotted with horizontal error bars indicating the polar angular acceptance of $\Delta\theta = 3.6^\circ$. (The vertical error bars indicate, as usual, the statistical uncertainties). The data are compared with calculations employing the DIT model (yellow symbols) and the CoMD model, both followed by the SMM model, as also shown in the previous comparisons for the cross sections. The calculations were binned and presented in angular steps of two degrees. Three different of calculations were performed with the CoMD model. a) The "standard" calculation (red symbols) using standard parameters of the CoMD code, as in our previous works [22,23]. b) A calculation with pairing (blue symbols). For this calculation, we introduced a phenomenological description of n-n and p-p pairing, according to the recent article [24]. In this description, for two neutrons (or protons) that have anti-parallel spins and energies near

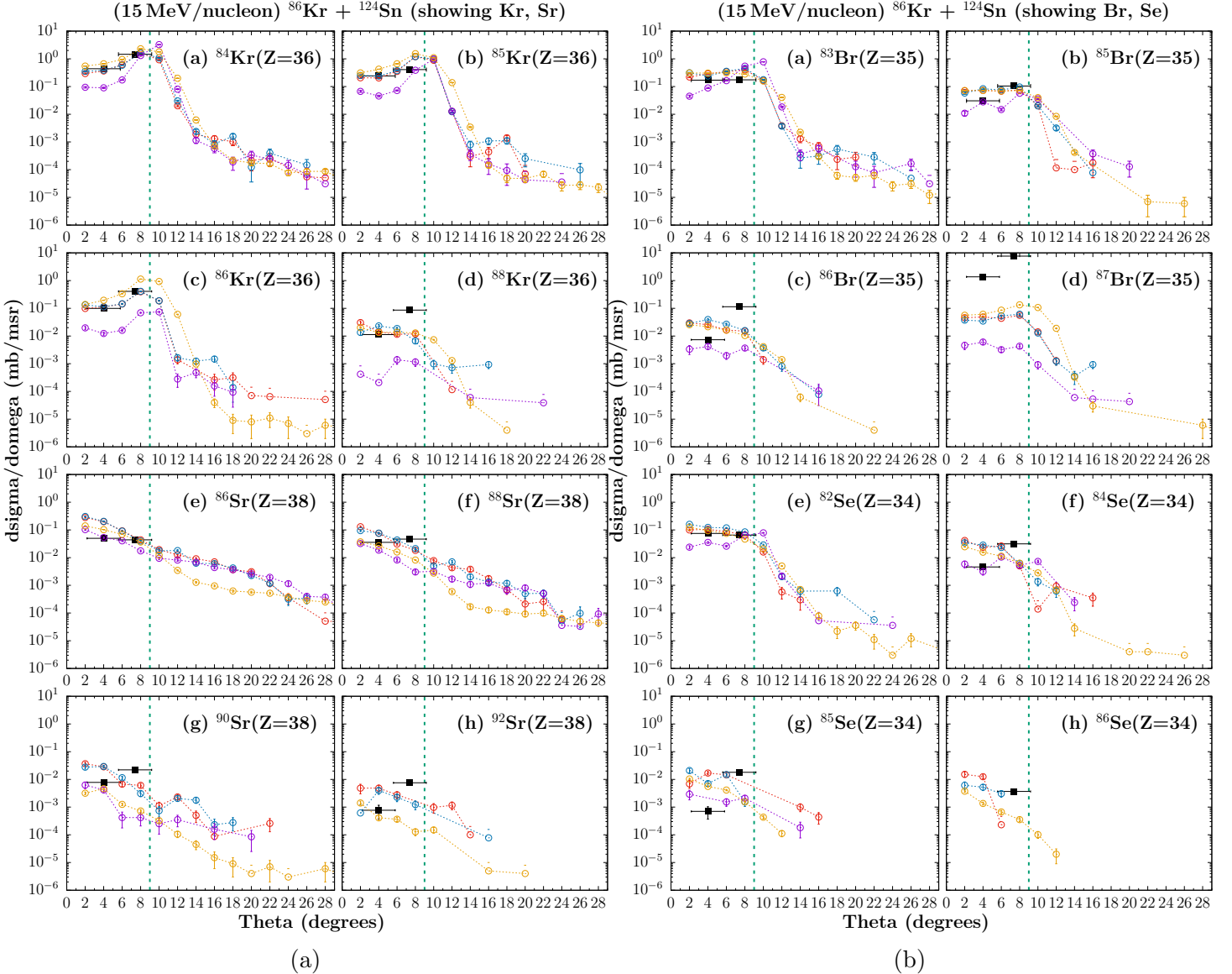


Fig. 3. a) Angular distributions of neutron rich isotopes of ^{36}Kr and ^{38}Sr from the reaction of ^{86}Kr (15 MeV/nucleon) with ^{124}Sn . b) Angular distributions of neutron rich isotopes of ^{35}Br and ^{34}Se from the reaction of ^{86}Kr (15 MeV/nucleon) with ^{124}Sn . Black squares (with horizontal errorbars): experimental data [16]. Symbols connected with dotted lines: calculations as follows. Yellow symbols: DIT. Red symbols: standard CoMD. Blue symbols: CoMD with pairing. Purple symbols: CoMD with compressibility $K=272$ MeV.

the Fermi energy, an additional attractive interaction was introduced with strength adjusted to reproduce the empirical pairing energy of the Bethe-Weizsacker equation. c) a calculation in which the compressibility of cold symmetric nuclear matter was increased to $K=272$ MeV (purple symbols). We remind that in the "standard" CoMD calculation, the parameters of the effective interaction correspond to a compressibility of $K=200$ MeV.

In the upper half of Fig. 3.a), we show the angular distributions for Krypton ($Z=36$). For $A=86$, we see that the data point at $\theta=7.5^\circ$ is higher than that at $\theta=4.0^\circ$, as expected. This step seems to be described by the DIT calculation, despite the larger value of the latter at $\theta=8^\circ$ and $\theta=10^\circ$. The CoMD calculations (in all three variations) appear to describe the shape of the angular distribution rather well; the CoMD calculation with $K=272$ is however lower than the other calculations. For $A=85$ and $A=84$, there is some agreement of the calculations with the data. However, for $A=88$ (+2n channel) the calculations cannot describe the step in the data. This may be related to enhanced neutron-pair transfer, possibly beyond our tentative pairing calculation.

In the lower half of Fig. 3.a), we show the angular distributions for Strontium ($Z=38$, +2p channels). For $A=88$, we note that the +2p channel does not peak at the grazing angle as the +2n channel (Fig. 8d). Moreover, for $A=86$, the removal of neutrons leads to a flat distribution in the data. The addition of neutrons, however, leads to angular distributions peaked at θ_{gr} . This feature cannot be described by DIT or CoMD, and requires further investigation.

In the upper half of Fig. 3.b), we show the angular distributions of several isotopes of bromine ($Z=35$). For $A=85$ (-1p channel), the calculations describe rather well the $\theta=7.5^\circ$ data point, but are higher than the $\theta=4.0^\circ$ data point. Interestingly, the CoMD calculation with $K=272$ MeV appears to describe both data points well. Again, the removal of neutrons ($A=83$, -1p-2n) results in a nearly flat angular distribution that seems to be described by the calculations. Concerning the neutron pickup nuclides ($A=86$, -1p+1n) and ($A=87$, -1p+2n), the experimental data are peaked at θ_{gr} and cannot be described by the DIT and CoMD calculations. We think that for $A=87$ (-1p+2n), the experimental data may be contaminated from background of elastically scattered beam. Moreover, especially for $A=86$, we speculate that part of the discrepancy may be due to a contribution of a single charge exchange (SCE) process that, of course, cannot be described by DIT or CoMD.

In the lower half of Fig. 3.b), we show the angular distributions of several isotopes of Selenium ($Z=34$) (-2p channels). Observations similar to those of the previous figure pertain here. For $A=82$ (-2p-2n), the experimental angular distribution is rather flat and is well described by the calculations. However, for $A=84$ (-2p), the experimental angular distribution is again peaked at θ_{gr} and cannot be adequately described by the calculations. The situation for the angular distributions of $A=85$ (-2p+1n) and $A=86$ (-2p+2n) is similar to the previous ones. We may attribute the discrepancy for $A=85$ in part to a contributing SCE process along with a +1n process. For $A=86$ (-2p+2n), we speculate that, a DCE (double charge exchange) process might also contribute, along with two successive SCE processes. The subject of potential contributions of SCE and DCE processes in these heavy-ion reactions below the Fermi energy is currently under investigation by our group via systematic studies of the momentum distributions of the relevant nuclides, and may shed light to interesting aspects of the reaction mechanism(s).

As a general remark of the angular distribution study, we point out that a rather satisfactory overall agreement of the calculations with the experimental data was achieved. Several discrepancies were noticed

and are the subject of further investigation.

Referring to the Kr+Sn system, the DIT calculations are rather similar in most cases to the CoMD calculations, especially to the standard CoMD calculation and the CoMD calculation with the pairing. Specifically, the CoMD calculation with the pairing seems to be slightly higher than the standard CoMD calculation for large angles (where, of course, there are no experimental data). Finally, the effect of the compressibility in the CoMD code was investigated by performing calculations with $K=272$ MeV, along with the standard value of $K=200$ MeV in the other CoMD calculations. We observed that with $K=272$, the CoMD calculated angular distributions are peaked more toward the θ_{gr} , as compared to those with the "standard" value of $K=200$ MeV, and are thus in better agreement with the data. However, they have the tendency to be lower than the other CoMD calculations.

3 Summary and Conclusions

In this contribution, we presented our recent studies of production cross sections and angular distributions of projectile fragments from $^{86}\text{Kr}/^{92}\text{Kr}$ -induced reactions at 15 MeV/nucleon with targets of ^{124}Sn and ^{238}U . Experimental data from our previous work at Texas A&M were compared with calculations which were based on a two-step approach: the dynamical stage of the collision was described with either the DIT model, or with various modes of the CoMD model. The de-excitation of the hot heavy projectile fragments was performed with the SMM model.

We studied the production cross sections of neutron-rich nuclides from collisions of a ^{86}Kr (15 MeV/nucleon) beam with ^{124}Sn and ^{238}U targets and from collisions of a radioactive beam of ^{92}Kr (15 MeV/nucleon) with a ^{238}U target. Subsequently, we initiated a study of the angular distributions of projectile fragments from the reactions of ^{86}Kr (15 MeV/nucleon) with the ^{124}Sn target. We compared our experimental data at the two angle settings of the MARS spectrometer, namely at 4.0° and at 7.5° , with detailed calculations using the models mentioned. A rather satisfactory agreement of the calculations with the experimental data was obtained. Several discrepancies were noticed and are the subject of further investigation.

Our current studies indicate that heavy-ion reactions below the Fermi energy can be exploited as an effective route to access extremely neutron-rich isotopes toward the r-process path and the neutron drip-line. In this vein, future experiments in several accelerator facilities may be planned that will enable a variety of nuclear studies in unexplored regions of the nuclear chart.

References

- [1] J. Erler et al, Nature **486**, 509 (2011).
- [2] D. F. Geesaman, C. K. Gelbke, R. V. F. Janssens, B. M. Sherrill, Ann. Rev. Nucl. Part. Sci. **56**, 53 (2006)
- [3] FRIB main page: www.frib.msu.edu
- [4] GANIL main page: www.ganil.fr

- [5] GSI main page: www.gsi.de
- [6] RIBF main page: www.rarf.riken.go.jp/Eng/facilities/RIBF.html
- [7] RISP main page: www.risp.re.kr/eng/pMainPage.do
- [8] K. Tshoo, Y. K. Kim, Y. K. Kwon et al, Nucl. Instrum. Methods B **317**, 242 (2013).
- [9] K. Tshoo, H. Chae, J. Park, J.Y. Moon, Y.K. Kwon, G.A. Souliotis et al, Nucl. Instrum. Methods B **376**, 188 (2016).
- [10] O. B. Tarasov et al., Phys. Rev. C **80**, 034609 (2009).
- [11] S. Lukyanov et al., Phys. Rev. C **80**, 014609 (2009).
- [12] G. A. Souliotis et al., Phys. Lett. B **543**, 163 (2002).
- [13] G. A. Souliotis et al., Phys. Rev. Lett. **91**, 022701 (2003).
- [14] G. A. Souliotis et al., Nucl. Instrum. Methods **B 204** 166 (2003).
- [15] G. A. Souliotis et al., Nucl. Instrum. Methods **B 266**, 4692 (2008).
- [16] G. A. Souliotis et al., Phys. Rev. C **84**, 064607 (2011).
- [17] L. Tassan-Got and C. Stephan, Nucl. Phys. **A 524**, 121 (1991).
- [18] M. Veselsky and G.A. Souliotis, Nucl. Phys. **A 765**, 252 (2006).
- [19] J. Bondorf et al., Phys. Rep. **257**, 133 (1995).
- [20] M. Papa et al., Phys. Rev. **C 64**, 024612 (2001).
- [21] M. Papa et al, J. Comp. Phys. **208**, 403 (2005).
- [22] P.N. Fountas, G.A. Souliotis, M. Veselsky and A. Bonasera, Phys. Rev. C **90**, 064613 (2014).
- [23] A. Papageorgiou, G.A. Souliotis et al., Journal of Physics G **45**, 095105 (2018).
- [24] C. Agodi, G. Giuliani, F. Cappuzzello, A. Bonasera, et al., Physical Review C **97**, 034616 (2018).

Non-conventional radionuclides produced by particle accelerators for theranostic applications

F. Groppi¹, F. Bianchi¹, G. Haki^{1,2}, and S. Manenti¹

¹LASA, Physics Department, Università degli Studi di Milano, and INFN, Milano, Italy,

²Physics Department, Salahaddin University, Erbil, Iraq

The use of High Specific Activity Radionuclides HSARNs, obtained by either proton, deuteron or alpha cyclotron irradiation, followed by selective radiochemical separation from the irradiated target in No Carrier Added (NCA) form, is a powerful analytical tool for plenty applications in pure and applied sciences and technologies. The main applications of these RNs are in medical radiodiagnosics and metabolic radiotherapy in addition to toxicological, environmental and industrial studies. Nowadays the new challenge in Nuclear Medicine is the so called theranostic medicine, a relatively novel paradigm that involves specific individual ‘dual-purpose’ radionuclides or radionuclide pairs with emissions that are suitable for both imaging, therapy and monitor the response to therapy. The theranostic radionuclides would potentially bring us closer to the age-long dream of personalized medicine [1]. A subchapter is the multifunctional nanoplatform that is an emerging highlight in nanomedicine, in which a suitable radionuclide is encapsulated in nanocarriers. Many of the “neutron-rich” radionuclides suitable for metabolic radiotherapy are produced by nuclear reactor with a very low specific activity (A_s). In selected cases, they can be produced by bombardment of targets by charged particle beams in NCA with very high A_s . If the irradiations are made with deuteron beams some more advantages are obtained as reported, as an example, in ref [2] for ^{186}gRe production.

At the Radiochemistry Laboratory of LASA, a wide range of high specific activity accelerator-produced radionuclides have been produced since the 70-ties in NCA form. Presently, nuclear activations are carried out at the cyclotron IBA K=70 of ARRONAX Center in Nantes France. The experimental measurements for the excitation functions determination are carried out at the Physics Measurements Laboratory in LASA, Italy. The experimental cross-sections were determined with the well-known staked foil technique and compared with the data present in literature and the curves of theoretical calculations obtained with suitable computer codes like EMPIRE-II, EMPIRE-3.2.2 and TENDL.

We will present some examples [2,3] of the more recent results in order to study and to obtain the optimal conditions for the production in NCA form of radionuclides with high A_s , highlighting the irradiation, measurements and data analysis techniques used by our research group.

- [1] S.C. Srivastava; Semin. in Nucl. Med. 42(3), 151 (2012).
- [2] F. Groppi et al.; J. Rad. Nucl. Chem. 305, 179 (2015).
- [3] S. Manenti et al.; Nucl. Med. Biol. 49, 30 (2017).

A Sparse and Ergonomic Tomographic Image Reconstruction Technique based on Artificial Neural Networks

M.-E. Tomazinaki^{1,2}, I. Lytrosyngounis¹, and E. Stiliaris^{1,3}

¹ Department of Physics, National and Kapodistrian University of Athens, Athens, Greece

² Medical School, National and Kapodistrian University of Athens, Athens, Greece

³ IASA, Institute of Accelerating Systems & Applications, Athens, Greece

Abstract. The recent advances in Artificial Intelligence (AI) and Machine Learning (ML) have affected Medical Physics and inevitably have set new frontiers in Medical Image Reconstruction. Hence, the aim of this study focuses on new approaches in Tomographic Image Reconstruction exploiting Radon Transform symmetries and novel training structures based on Artificial Neural Networks (ANNs). Exploiting Tensorflow library, fully-connected architectures seem to predict pixel-wise reconstructions of both software and clinical phantoms when they are fed with a symmetric transformation of the standard sinogram information.

1 Introduction

Nowadays modalities of tomography, such as SPECT, make use of software novelties since the current hardware have reach an upper limit even the rapidly changing field. While there has been a steady progress on reconstruction algorithms, new processing algorithms have become commercially available that promise to provide substantial reductions in SPECT acquisition time without degrading diagnostic quality. To this direction, the recent advances in Machine Learning (ML) have affected Medical Physics and Image Reconstruction. However, the reconstruction part of newly released algorithms is still in dire straits. In order to counterbalance this one-sided progress, we propose a new method in SPECT Imaging.

2 Artificial Neural Networks Implementation in SPECT Reconstruction

2.1 Problem Definition

In Single Photon Emission Tomography (SPECT), the available data during scanning is the density of the measured photons $p(\theta)$ at different angles along an axis defined by the length r of the detectors. The rotating detectors obtain for different angles (projections) the emitted photons, that have not been absorbed during passing through matter, coming from the radioactive object. The distribution of the incident photons among the also rotating r axis for each projection consists the only useful information in order to reconstruct the original object [1]. The acquired data about a set of projection profiles could be

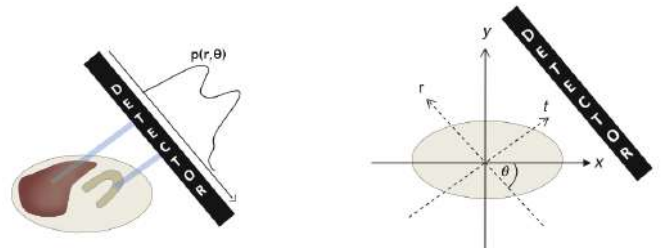


Fig. 1. Detected Photons distribution along rotating axis r for different angles θ

displayed in a two-dimensional (2-D) plot, known as sinogram [5].

The Image Reconstruction process relies on the inversion of this 2-D plot in order to define the distribution of the source that causes the emission. The obtained result is often reached with various algorithms, analytical, iterative or even learning ones. In this study, we focus on the learning reconstruction algorithms and how ML could contribute to this purpose.

2.2 Data Processing & ANN Implementation

While the mathematical transform of the tomographic process must be preserved, the following conditions, concerning the network architecture, should be fulfilled: The input data has to be characterized by the sinogram of the image while the output has to predict information about the images representation [1]. Instead of using the conventional sinogram technique [2] prone to memory effects depending on the size of the depicted objects (Fig. 2), a new approach is introduced.

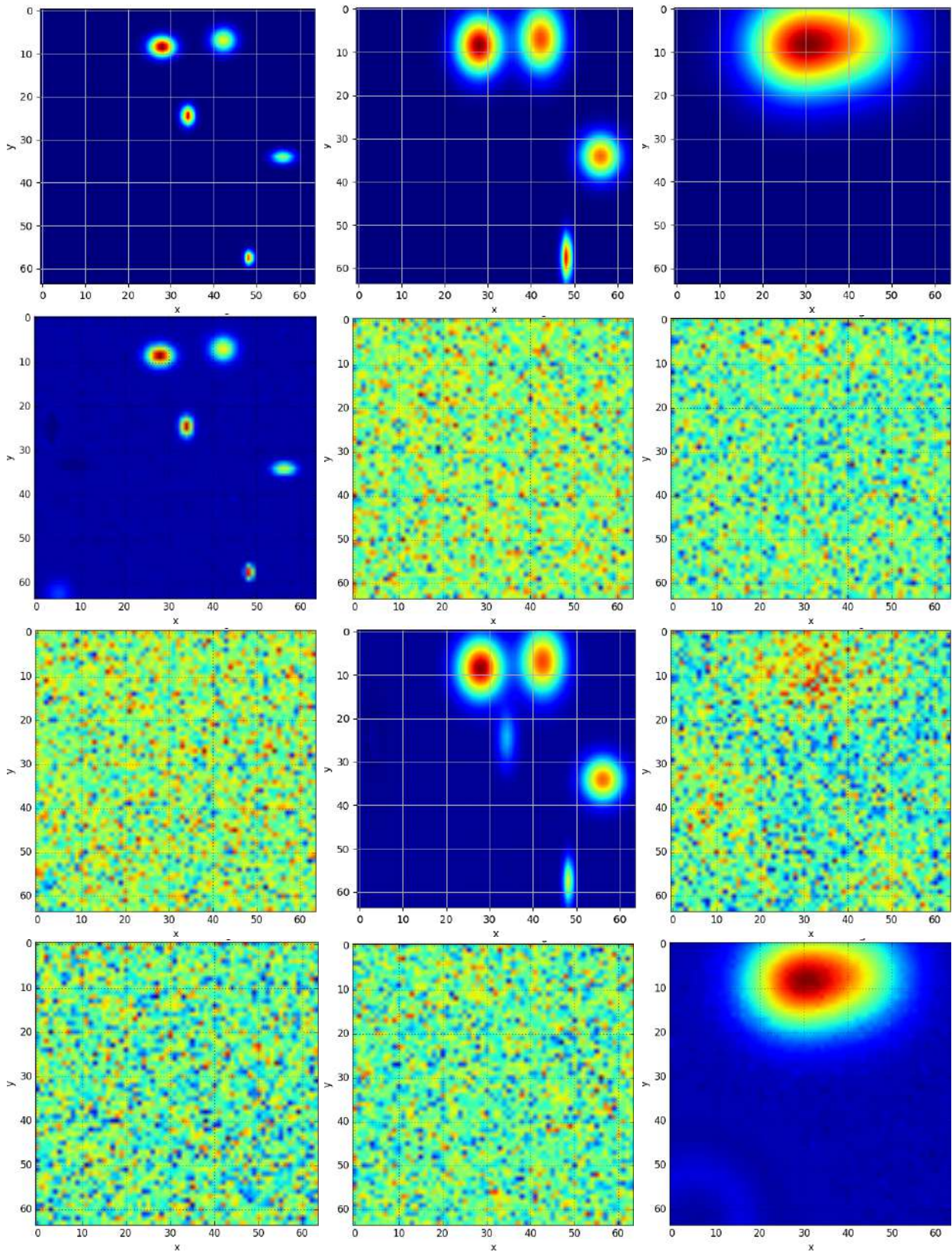


Fig. 2. Control Images and Reconstructed images via ANNs based on size classes

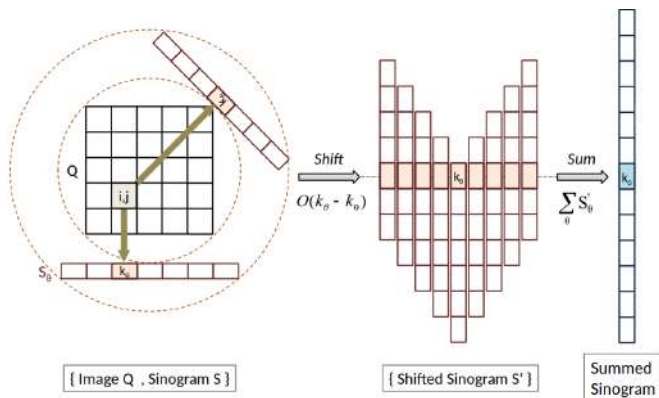


Fig. 3. Shifted and Summed Sinogram reflected about the center of the detector. The original form of the sinogram is now delineated by the outer margins of the sinograms.

A simple remapping of the well-known sinogram free of dependencies of the images features could lead to reconstructed images of diagnostic power and low time cost at real time processes. In this study, each pixel of the grid is treated the same with the others and it is characterized by a unique transformed sinogram. The pixel value consists the desirable prediction of the ANN and thus the output.

Based on the aforementioned, we exploit an underlying symmetry of Radon Transform and accomplish position independence. Thus, we shift the reconstructed object Q_{ij} such that the pixel that it is currently reconstructed, x_i, y_j , is at the origin. In this case, the center of pixel (x_i, y_j) is situated in row j and column i of the pixel grid, with $i \in 0, 1, \dots, N-1$ and $j \in 0, 1, \dots, N-1$, and $x_i = y_j = i - \frac{N-1}{2}$. In other words, as input for the neural network, we use projection data of the shifted pixel, which could be obtained by shifting the original one by $-x_i$ horizontally and $-y_j$ vertically[3]. The original sinogram ma-

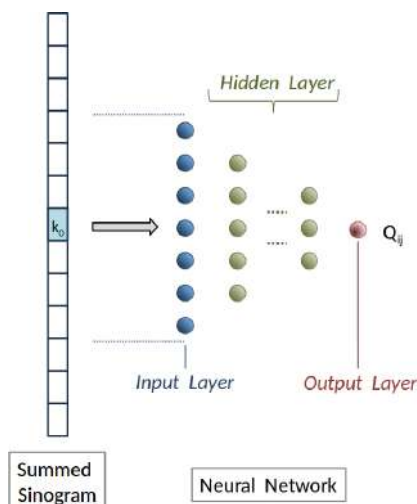


Fig. 4. Shifted and Summed Sinogram vector is fed to a single-layer, fully-connected architecture. The output of the newtwork predicts the pixel intensity of the given sinogram.

	Control Image I	Control Image II
ANN Reconstructed I	0.0167	0.1690
ANN Reconstructed II	0.0259	0.0203

Table 1. Chi-square index calculated for each reconstructed image based on image dimension for the cross test.

trix S undergoes a transformation procedure summarized in the following scheme[1]:

$$Q_{ij} \rightarrow S_k(\theta) \rightarrow S'_l = O(k_\theta - k_0)S_k \rightarrow \sum_M S'_l$$

where $(i, j) \in \{1 \dots N\}$, $k = k_\theta(i, j) \in \{1 \dots M\}$ and $l \in \{1 \dots 2M\}$. Each pixel has a set of sinograms for all projections in which the highest density of photons is located in the middle. The produced sinograms are summed, reflected about the detector's center and saved in a doubled vector (Fig. 1).

The transformed vector is then fed to a multilayer perceptron based on one hidden layer structure (Fig. 2) and the optimization phase is based on minimizing the chi-square value of the original and predicted output. The output of this ANN is capable of predicting one pixel value at a time. This modified sinogram, as described previously, characterizes each pixel of the image and has a special waveform symmetric to the center always correlated with the other pixels within the image grid. The algorithm of the proposed method is summarized in Fig.5.

Shifted and Summed Sinogram Algorithm:

1. Copy the existing sinograms in the extended ones
2. Move the selected pixel in the middle of the detector vector
3. Sum the moved sinograms in one and reflect the vector about the center
4. Repeat for all pixels in the image

3 Results

3.1 Software Phantoms

At this level, we focus on full image reconstruction (64x64 pixels, 36 projections) and an ANN architecture of one hidden layer consisted of 36 nodes with respect to the number of projections. The cost function that has to be minimized is, again, the chi-square value of the image.

Various experiments were conducted to study the efficiency and the stability of the algorithm. Here we choose to present a cross-test within a set of known or not sample images for the ANN. For this test, two images are needed to be generated via simulations. At this point, the validation phase has to be divided in two main levels: First, two images are generated, cross-validated with themselves and consequently with each other. The results of the cross test are quantified and represented in table 1 and Figure 6.

3.2 Clinical Cases

A challenge arises, when clinical data have to be reconstructed i.e. in brain SPECT. By decoding DICOM files

from brain scans in emission tomography, it is easy to detect long-term degenerative disorders, such as Parkinson disease. In general, during a DaTSCAN in a Nuclear Medicine Department, if the patient has Parkinsons disease, then the isotope that is injected will be deficient in certain areas of the brain. For the purposes of this study, the DICOM files from brain SPECT are anonymized and then several slices of the scan are selected for single or multiple image training (total number of slices: 128), as before[1]. Each gray slice is converted into a coloured image with respect to the original pixel values. The red spots are depicting the hot spots in the selected plane. The patient SPECT scan is tested for Parkinsons disease based on the two lobes size, shape and general view of the brain.

The proposed technique could be implemented in an extended version of image reconstruction combining ART with Newton-Raphson acceleration (NR-ART) and ANN pre-editing. The proposed method consists of two main steps: First, the shifted and summed sinogram for each pixel is constructed in order to predict the initial pixel values for the full image and secondly the ANN reconstructed image is given to NR-ART as the initial matrix to complete the reconstruction process. The ANN archi-

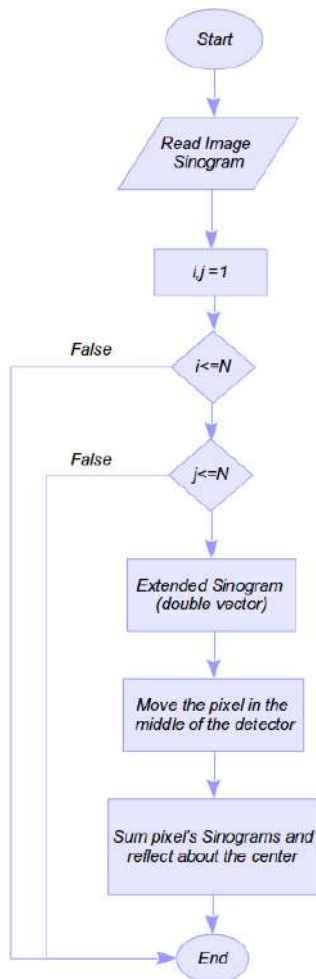


Fig. 5. Shifted and Summed Sinogram Algorithm

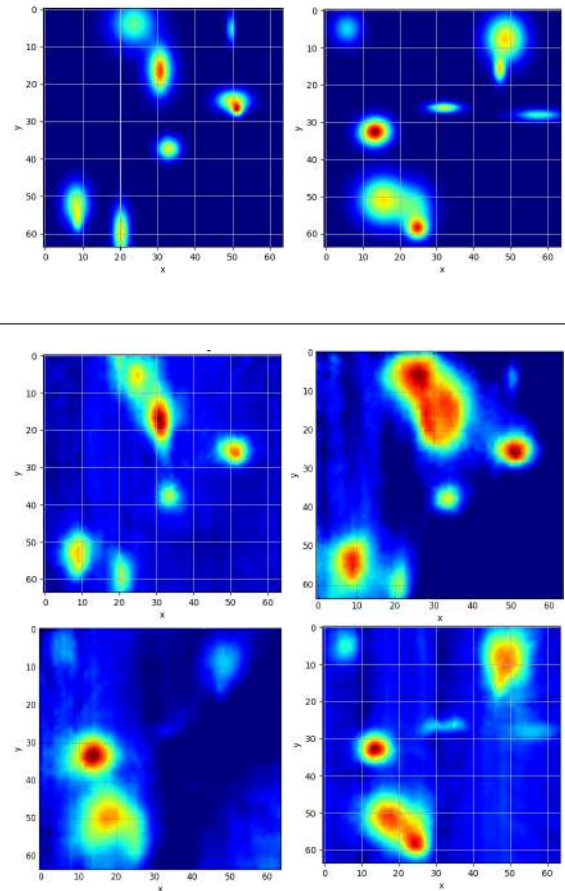


Fig. 6. Cross Test

Initial Matrix Origin	None	36-node ANN	72-node ANN
Total CPU Time(sec)	586.720	606.420	559.940
Reconstruction Time(sec)	500.400	580.190	533.810
Time per Grand Iteration(sec)	280.189	290.084	266.895
Time per Iteration(msec)	21.382	22.137	20.367

Table 2. Reconstruction statistics about the combined process of ANN pre-editing and ART Newton-Raphson method introducing the extended Cost Function and two grand iterations.

ture consists of one hidden layer with 36 and 72 nodes respectively to test two different ANN structures. The results of reconstruction time and mean squared error index with respect to grand iterations are shown in Table 2 and Fig. 8, while the corresponding reconstructions are shown in Fig. 7.

4 Conclusions

In this study, a sparse and ergonomic reconstruction technique for tomography has been proposed. Artificial Neural Networks are implemented in order to resolve the inverse problem of reconstruction, but always keeping the original mathematical process preserved. With respect to the original problem, the input and output of the ANN architecture is clearly fixed. The input data corresponds to the sinogram of the image while the output reflects information about the image matrix. For this purpose, a simple

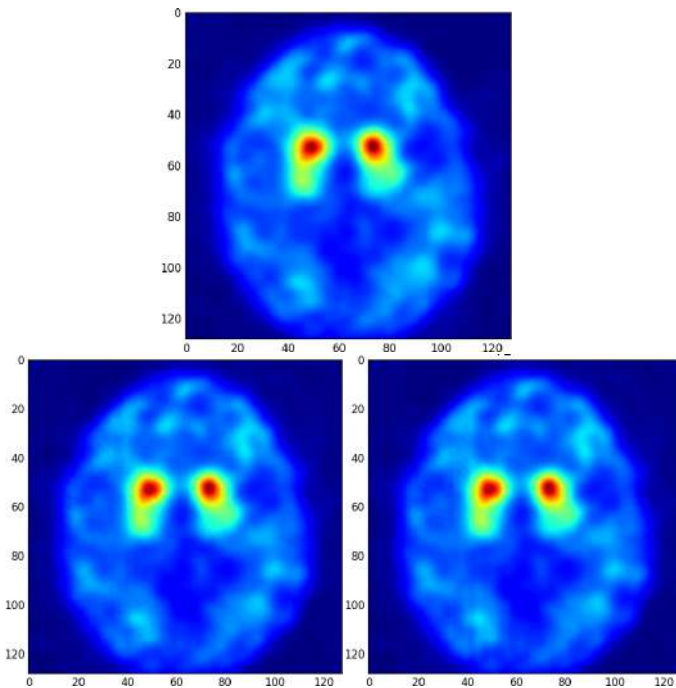


Fig. 7. Combined process of ANN pre-editing and NR-ART reconstruction with the full extended Cost Function

feed-forward ANN is selected instead of a more complicated structure with a minimization function defined by the chi-square value of the image.

However, the above-mentioned structure is designed to import transformed data, different from the original sinogram information. Each pixel of the image is related to its own shifted and summed sinogram. The sinogram vectors are centered and reflected according to the nominal position of the selected image pixel. The result of this process ends with a sum of all the shifted sinogram vectors so that the selected image pixel is always projected in the middle of the detector. This altered sinogram constitutes the new input data for the network and the so developed ANN could predict only a single pixel at a time and it is repeatable for the full image reconstruction. The proposed method is trained and tested with various software phantoms.

In addition, when clinical data have to be reconstructed, the network is capable of accelerating the reconstruction process by giving preliminary results about the equal (or not) radioactivity of several spots in the brain makes the method powerful to eliminate the time drawbacks of the reconstruction process. The ANN output is fed to NR-ART to accelerate and boost the reconstruction process. Even with a few grand iterations the system is capable of providing diagnostic images of high quality characterized by low chi-square values within short time. This sophisticated technique is tested with Parkinson's scans in order to evaluate the systems acceleration and efficiency.

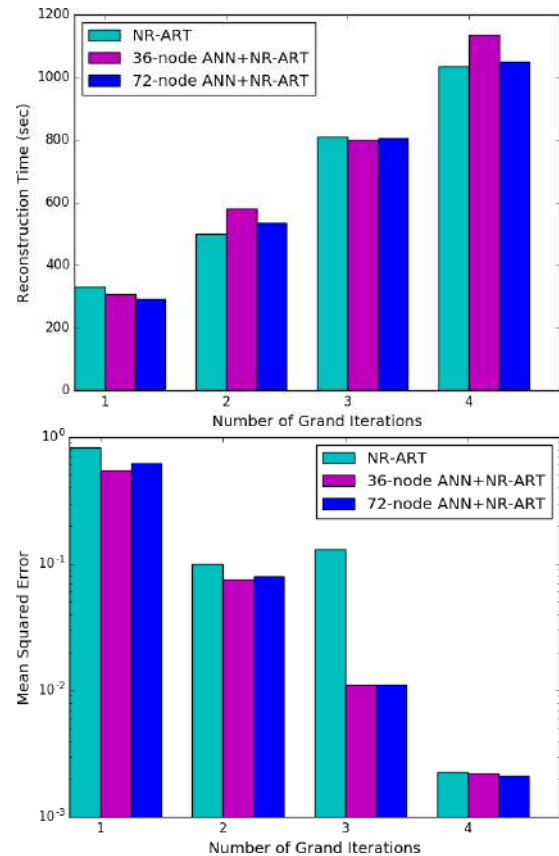


Fig. 8. (top) Reconstruction time depending on the number of grand iterations. The combined technique of ANN+NR-ART results in reduced total time of reconstruction than the NR-ART. (bottom) Upgraded mean quadratic error compared to the NR-ART with minimum number of grand iterations based on sinogram.

References

1. M.-E. Tomazinaki: *Artificial Neural Networks in Single Photon Emission Tomography* (MSc Thesis), National and Kapodistrian University of Athens, (2018).
2. M. Argyrou, D. Maintas, Ch. Tsoumpas and E. Stiliaris: Tomographic Image Reconstruction based on Artificial Neural Network (ANN) Techniques, *IEEE Medical Imaging Conference Record M1712* (2012) 3324-3327.
3. D.M. Pelt and K.J. Batenburg: Fast Tomographic Reconstruction from Limited Data using Artificial Neural Networks, *IEEE Transactions on Image Processing* **22** (2013) 5238-5251.
4. S. Angeli and E. Stiliaris: An Accelerated Algebraic Reconstruction Technique based on Newton-Raphson Scheme, *IEEE Medical Imaging Conference Record M09323* (2009) 3382-3387.
5. Magdy M.Khalil. *Basic Sciences in Nuclear Medicine*. Springer, 2011.

The use of mosses as biomonitors of trace elements in Greece

Ch. Betsou¹, M. Frontasyeva², E. Tsakiri³, N. Kazakis⁴, K. Eleftheriadis⁵, E. Diapouli⁵, and A. Ioannidou¹

¹ Physics Department, Nuclear Physics Lab., Aristotle University of Thessaloniki, Thessaloniki, 54124, Greece

² Frank Laboratory of Neutron Physics, Joint Institute for Nuclear Research, Dubna, Moscow Region 141980, Russia

³ Biology Department, Division of Botany, Aristotle University of Thessaloniki, Thessaloniki, 54124, Greece

⁴ Aristotle University of Thessaloniki, Geology Department, Division of Hydrogeology, Thessaloniki, Greece

⁵ Institute of Nuclear & Radiological Sciences and Technology, Energy & Safety, NCSR “Demokritos”, Greece

Abstract. Mosses are used as biomonitors for assessing the atmospheric deposition of trace elements. Due to the lack of roots, they absorb the elements and water from wet and dry deposition, using their entire surface. The low cost and the simplicity of the sampling can provide data even from remote areas. Ninety-five samples of *Hypnum cupressiforme* Hedw. were collected in the region of Northern Greece under the auspice of the ICP Vegetation Protocol. Samples were analysed to the content of trace elements by means of Neutron Activation Analysis (NAA). The elemental concentrations of the moss samples were further used for the application of source apportionment by Positive Matrix Factorization (PMF), and specifically by the EPA PMF 5.0 model. In total 30 species were used for source apportionment (Na, Mg, Al, Si, Cl, K, Ca, Sc, Ti, V, Cr, Mn, Fe, Co, Ni, As, Br, Rb, Sr, Mo, Cd, Sb, Cs, Ba, La, Ce, Tb, Hf, Ta and Th), revealing the contribution from five sources: Soil Dust, Aged Sea Salt, Vehicular Traffic, Heavy Oil Combustion and Mining Activities, with the Soil Dust contributing the most to the measured metal concentrations among all other sources.

1 Introduction

Biomonitoring is a well-established technique for monitoring different air pollutants, such as the particulate matter (PM), trace elements and persistent organic compounds [1,2]. Mosses are ideal biomonitors for studying the trace elements atmospheric deposition [3,4,5]. They have been used as biomonitors since the late 1960s in the Scandinavian countries [3,4,5,6,7]. Mosses obtain most of their nutrient supply directly from precipitation and dry deposition [6,7,8,9]. The absence of an elaborate rooting system allows the easy uptake from the atmosphere, while the uptake from the substrate is normally not significant [10]. Supplementary to the above properties, moss biomonitoring technique provides a simple and non-expensive sample collection as well as a higher sampling density compared to those provided by the conventional precipitation analysis method and the air sampling [10,11,12]. Additionally, the slow growth rate of mosses can provide information about the accumulation of trace elements over a large period of time [2,10] while revealing the temporal trends of air quality both in urban and remote areas [11,12].

Studying the concentrations of trace elements was considered crucial as the exposure to elevated levels of them might have significant impact on human health and the environment [13]. Thus, every five years and since the 90's

the European moss survey provides information about the elemental concentrations in natural growing mosses [10]. The latest moss survey was performed in 2015/2016 and was coordinated by the Joint Institute of Nuclear Research (JINR; Dubna, Russian Federation), under the auspice of the ICP Vegetation Programme (United Nations Economic Commission for Europe Convention on Long-Range Transboundary Air Pollution, Monitoring of Atmospheric Deposition of Heavy Metals, Nitrogen and POPs in Europe using Bryophytes) [13,14,15].

The aim of this study is to measure the elemental concentrations in natural growing mosses in Northern Greece using Neutron Activation Analysis and to find out their possible sources by applying the source apportionment Positive Matrix Factorization model.

2 Sampling and measurements

Ninety five (95) samples of *Hypnum Cupressiforme* Hedw. were collected in the region of Northern Greece during the end of summer 2016. Mosses were collected from different altitudes, from 30 m to 1450 m above the mean sea level. There was no rain during the sampling and all the regions from where samples were collected were open regions far from treetops in most of the sampling sites. All the moss samples were collected according to the instructions of the Protocol of the European Survey ICP Vegetation [13,14], in which Greece is the first time that is included.

Correspondence to: chbetsou@physics.auth.gr

Table 1. The descriptive analysis of the most frequently analyzed and published in studies elements that were determined in the moss samples from Northern Greece, by means of Neutron Activation Analysis (NAA).

	Mg	Al	Ti	V	Cr	Mn	Fe	Co	Ni	Zn	As	Sb
Mean	4432	7886	440	10.08	24.04	269	5.974	3.02	12.83	56.56	2.45	0.27
Median	3600	5840	327	8.17	11.50	219	3770	1.69	7.26	37.60	1.44	0.20
Min	705	1350	97	2.61	2.04	34	1010	0.43	1.72	14.60	0.52	0.02
Max	17800	46100	1760	33.4	222	1090	28700	20.30	90.20	282	17.90	3.23
St. Dev.	2813	6812	327	6.12	35.60	200	5182	3.25	12.77	52.74	2.99	0.39

After sampling, mosses were air-dried, homogenized and pelletized by means of a pneumatic press. Then they were irradiated at the pulsed fast IBR-2 reactor of the Joint Institute for Nuclear Research (JINR) in Dubna, Russia. The irradiation time varied from 180 sec to 4-5 days for the determination of the short lived and the long lived isotopes respectively. After their irradiation, they were measured on HPGe detectors with relative efficiency 40% and 1.74 keV FWHM at the 1332 keV line of ^{60}Co .

The obtained gamma spectra were analysed using the Genie-2000 software by Canberra. Then the elemental concentrations were calculated by means of a special software that was developed in the Frank Laboratory of Neutron Physics of the JINR [16]. High quality certified reference materials (SRM) were used for the quality control of the NAA results. All the reference materials were packed and irradiated simultaneously with the moss samples. The results that were obtained were compared with the certified values. The reference material that presented the least deviation between the measured and the certified values of each elemental concentration was chosen.

3 Results and discussion

The elemental concentrations of forty-four elements were determined using the NAA. The descriptive statistical analysis (mean, median, min, max and standard deviation) of the most frequently analyzed and studied elements in the literature is presented in Table 1.

In order to determine the sources of the measured elements in mosses, the Positive Matrix Factorization (PMF) analysis by means of the PMF 5.0 model was applied. In total 30 species were used for source apportionment (Na, Mg, Al, Si, Cl, K, Ca, Sc, Ti, V, Cr, Mn, Fe, Co, Ni, As, Br, Rb, Sr, Mo, Cd, Sb, Cs, Ba, La, Ce, Tb, Hf, Ta and Th). The uncertainties of the concentrations of all chemical species were calculated based on the sampling and analytical uncertainties. Extra modelling uncertainty in the order of 10% was put in the model. The model was run 100 times for each possible number of sources in order to ensure that the solution which was achieved was based on a universal minimum [17]. Solutions with different number of factors (4 to 10) were checked. The best solution included five sources: *The Soil Dust*, *the Aged Sea Salt*, *the Road Dust*, *the Lignite Power Plant* and *the Mn-rich source*.

The Soil Dust source includes the elements Mg, Al, Ti, Si, Ca, Th, Ba, La, K and Fe, and all the elements were transferred to mosses through the resuspension of the soil. The Aged sea salt factor includes the elements Na, Rb, Sr, Hf and Ta, with Na contributing the most. The Road Dust source contains high contribution of Sb and As, while the Lignite Power Plant source has high contribution of Ni, Cr and Co. This last factor is also related to heavy oil combustion emissions. The Mn-rich source is connected with mining activities. The soil dust source contributes more than 50% to almost all the moss samples. The areas of Ptolemaida and Skouries are distinguished according to the relative source contribution for each sampling site. The first one is characterized by the lignite power plant source, while the second one by the Mn-rich source and the lignite power plant source.

This is the first time that the atmospheric deposition of trace elements in mosses is studied in such a big territory in Greece during a five years' interval. There were some other surveys that were conducted in specific areas in Greece. For example, in Athens, close to an industrial area, moss bags were used for studying the elemental atmospheric deposition [18]. According to the results of this study, the concentrations of the elements Al, Zn, Fe, Cr, Ni, V were higher in the sites that were closer to the industrial zone. According to another more detailed biomonitoring study in Northern Greece [19], high concentrations of As, Cr, Fe, Ni and V were due to old mines, soil contamination by windblown dust and road transportation. In the current study as well as in the aforementioned one, the pollutants' chemical composition in the region of Northeastern part of Greece, next to the Bulgarian borders presents a lot of similarities especially for the Al, As, Fe and V elements. Additionally, two other studies [20, 21] were performed in the Region of West Macedonia, close to the lignite power plants and the lignite mining ores, in the concentrations of Fe, Mn, Cr and Ni elements were studied. A reduction of the order of 30% in the elemental concentrations of Cr, Mn and has been observed.

Furthermore, there are differences between the concentrations of the current study and those the other countries that participated in the 2005/2006 and 2010/2011 European Moss Surveys [22, 23]. The maximum concentrations of Zn, Mn, Co in Greece are lower than in Norway, in contrast to the max elemental concentrations of Bulgaria and Switzerland. Ni max concentrations are similar to those of Bulgaria, but lower than those of Norway and Albania. Fi-

nally, the concentrations of V and Zn elements are similar both in Greece, Serbia and Croatia.

4 Conclusions

Mosses are ideal bioindicators of trace elements. They are widely used for monitoring their deposition from the atmosphere, as they do not have roots and all the nutrients and water they need, are taken directly from wet and dry deposition. The current survey was conducted at the end of summer 2016 under the auspice of the ICP Vegetation Programme. Ninety-five moss samples of *Hypnum cupressiforme* Hedw. were collected from the Region of Northern Greece. They were analyzed by the NAA method and the elemental concentrations were defined. In order to identify the sources of the elements in mosses, the Positive Matrix Factorization (PMF) analysis was performed by means of the PMF 5.0 model. Five different factors-sources were extracted: The Soil Dust, the Aged Sea Salt, the Road Dust, the Lignite Power Plant and the Mn-rich source. The Soil Dust source is the one that contributes the most in almost all the moss samples. Two areas are distinguished based on the relative source contribution for each sampling site, the areas of Ptolemaida and Skouries. The first one is characterized by the Lignite Power Plant source while the second one is mainly characterized by the Mn-rich source and the Lignite Power Plant Source. The concentrations of Al, As, Fe and V of this study are similar to those presented by an earlier study next to the Bulgarian borders. According to the previous Moss Surveys results, the maximum concentrations of Zn, Mn, Co in Greece are lower than in Norway, while the concentrations of V and Zn elements are similar both in Greece, Serbia and Croatia. Finally, this survey consists the first attempt for capturing the atmospheric deposition of trace elements in mosses in such a big territory in a short time interval, while fulfilling the gap of the European Moss Database.

References

1. L. Thinova, M. Frontasyeva, K. Vergel, E. Bayushkina, *Radiation Physics and Chemistry* **104**, (2014) 432-435.
2. I. Vučković, Z. Špirić, T. Stafilov, V. Kušan, *Geologica Macedonica* **26**, (2012) 11-19.
3. H. Lippo, J. Poikolainen, E. Kubin, *Water, Air and Soil Pollution* **85**, (1995) 2241-2246.
4. A. Rühling and G. Tyler, *Water, Air and Soil Pollution* **2**, (1973) 445-455.
5. P. Adamo, S. Giordano, S. Vingiani, R. Castaldo Cobianchi, P. Violante, *Environmental Pollution* **122**, (2003) 91-103.
6. J. Poikolainen, E. Kubin, J. Piispanen, J. Karhu, *The Science of the Total Environment* **318**, (2004) 171-185.
7. E. Lequy, S. Sauvage, X. Laffray, S. Gombert-Courvoisier, A. Pascaud, L. Galsomiès, S. Leblond, *Ecological Indicators* **71**, (2016) 20-31.
8. L. Yurukova, E. Tsakiri, A. Ayir, *Cross-Border Response of Moss*, *Bulletin of Environmental Contamination and Toxicology* **83**, (2009) 174-179.
9. S. Loppi, I. Bonini, *Chemosphere* **41**, (2000) 1333-1336.
10. H. Harmens, D.A. Norris, E. Steinnes, E. Kubin, J. Piispanen, R. Alber, Y. Aleksiyenak, O. Blum, M. Coşkun, M. Dam, L. De Temmerman, J.A. Fernández, Frolova, M. Frontasyeva, L. Gonzalez-Miqueo, K. Grodzińska, Z. Jeran, S. Korzekwa, M. Krmar, K. Kvietskus, S. Leblond, S. Liiv, S.H. Magnússon, B. Maňková, R. Pesch, A. Rühling, J.M. Santamaria, W. Schröder, Z. Spiric, I. Suchara, L. Thöni, V. Urumov, L. Yurukova, H.G. Zechmeister, *Environ. Pollut.* **158**, (2010) 3144-3156.
11. R. Gerdol, R. Marchesini, P. Iacumin, L. Brancaleoni, *Chemosphere* **108**, (2014) 388-395.
12. P. Adamo, S. Giordano, A. Sforza, R. Bargagli, *Environ. Pollut.* **159**, (2011) 1620-1628.
13. M. Frontasyeva, H. Harmens, and the participants of the ICP Vegetation Programme, *International Cooperative Programme on Effects of Air Pollution on Natural Vegetation and Crops*. 1-26, (2015). <http://icpvegetation.ceh.ac.uk>
14. M. Frontasyeva, H. Harmens, *Heavy metals, nitrogen and POPs in European mosses: 2020 survey - Monitoring Manual*, (Bangor, UK, ICP Vegetation, 2020). <https://icpvegetation.ceh.ac.uk/sites/default/files/ICP%20Vegetation%20moss%20monitoring%20manual%202020.pdf>
15. C. Meyer, M. Diaz-de-Quijano, F. Monna, M. Franchi, M. Toussaint, D. Gilbert, N. Bernard, *Atmos. Environ.* **101**, (2015) 286-293.
16. A.Y. Dmitriev, S.S. Pavlov, *Phys. Part. Nucl. Lett.* **10**(1), (2013) 33-36.
17. C.J. Saitanis, M.V. Frontasyeva, E. Steinnes, M.W. Palmer, T.M. Ostrovskaya, S.F. Gundorina, *Environ. Monit. Assess.* (2012). <https://doi.org/10.1007/s10661-012-2606-0>
18. E. Diapouli, M. Manousakas, S. Vratolis, V. Vasilatou, Th. Maggos, T. Saraga, Th. Grigoratos, G. Argyropoulos, D. Voutsas, C. Samara, K. Eleftheriadis, *Atmospheric Environment* **164**, (2017) 416-430.
19. L. Yurukova, E. Tsakiri, A. Hayir, *Bull Environ. Contam. Toxicol.* **83**, (2009) 174-179.
20. K. Tsigaridas. *Study of heavy metal and radionuclide contamination in Kozani-Ptolemais basin with the use of bioindicators, water and microorganisms*. Doctoral dissertation, Faculty of Sciences, School of Biology, Aristotle University of Thessaloniki, Thessaloniki, (2014).
21. L. Tsikritzis. *Study of the bioaccumulation of heavy metals and radionuclides of plants in West Macedonia*. Doctoral dissertation, Technical University of Thessaloniki, Aristotle University of Thessaloniki, Thessaloniki, (2002), ISSN 1101-5049.
22. H. Harmens, D. A. Norris, *The Participants of the Moss Survey. Spatial and Temporal Trends in Heavy Metal Accumulation in Mosses in Europe (1990-2005)*, ICP Vegetation, (2008).
23. H. Harmens, D. A. Norris, G. Mills, *The Participants of the Moss Survey, Heavy Metals and Nitrogen in Mosses: Spatial Patterns in 2010/2011 and Long-term Temporal Trends in Europe*. ICP Vegetation Programme Coordination Centre, Centre for Ecology and Hydrology, (Bangor, UK, 2013).

Resolution Study of a γ -Camera System for SPECT at Preclinical Level

D. Zarketan^{1,2}, L. Koutsantonis³, M.-E. Tomazinaki^{1,2}, and E. Stiliaris^{1,4}

¹ Department of Physics, National and Kapodistrian University of Athens, Athens, Greece

² Medical School, National and Kapodistrian University of Athens, Athens, Greece

³ The Cyprus Institute, Nicosia, Cyprus

⁴ Institute of Accelerating Systems & Applications (IASA), Athens, Greece

Abstract. One of the most important imaging systems in Medical Physics is the γ -Camera, mainly used for Single Photon Emission Computed Tomographic (SPECT) scans. The present study focuses on the characterization at preclinical level of a small field, high resolution γ -Camera system developed in our laboratory with respect to its energy and spatial resolution. The system consists of a Position Sensitive PhotoMultiplier Tube (PSPMT) and is optimized for the ^{99m}Tc radiotracer. The intrinsic resolution of this tube is primarily checked with a series of measurements using LED pulses of variable duration, which are guided to the surface of the PSPMT. Accumulated charge from the wires of the anodic grid is then analyzed for various high voltage working values. The performance of the integrated system is further studied at planar and tomographic level by acquiring projective images of simple geometrical phantoms. For this purpose, a set of capillaries filled with ^{99m}Tc water solution was measured at different orientations and the obtained planar images were offline improved by implementing correction algorithms to eliminate spatial distortions. Further characterization of the system includes the tomographic reconstruction of more complicated geometrical phantoms. Finally, the performance of the γ -Camera system at preclinical level was tested by imaging specific organs of a small mouse targeted with ^{99m}Tc labelled pharmaceutical substances.

1 Introduction

A γ -Camera represents one of the most basic imaging systems in Medical Physics and the main instrument for Photon Emission Computed Tomographic (SPECT) scans. It is a common practice to use SPECT modality in preclinical studies, in order to optimize the spatial resolution and the energy response of the system. The present study focuses on the characterization of a small field γ -Camera system used at preclinical level, as a whole, through a number of various experiments. The process involves three different integration steps:

- Characterization of the **intrinsic resolution** of the main body of the small field γ -Camera system, the Position Sensitive Photomultiplier Tube (PSPMT).
- **Planar imaging** of a geometrical phantom with the use of our laboratory's small field γ -Camera system in order to check its spatial resolution and to define a correction algorithm for planar distortions.
- Use of the small field γ -Camera system for **tomographic reconstruction** of a complicated geometrical phantom and imaging of a labelled **small animal**.

2 Position Sensitive PhotoMultiplier Tube (PSPMT)

The main body of the small field γ -Camera system is the PSPMT. For every γ -ray that hits the scintillation crystal a few thousand photons are produced, each with a very low energy of a few electronvolts. These very low light signals need to be amplified and converted into an electrical current that can be digitized: Photomultiplier tubes are the devices used for this specific task; more specifically, a photomultiplier that preserves also the information of the photon's incident position is characterized as a Position Sensitive PhotoMultiplier Tube (PSPMT).

2.1 PSPMT Operating Principle

For the current study a cylindrical PSPMT is used with a circular 3"-diameter window. It is composed of a photocathode, a 12-stage coarse mesh dynode structure and a multi-wire anodic grid. This grid comprises 32 cross-wired anodes that are arranged into two orthogonal groups, so 16-X and 16-Y different signals can be individually recorded.

The information of the planar position (X_{pos}, Y_{pos}) and the energy E of each incident γ -ray is reconstructed by

using the traditional charge Center-of-Gravity Anger algorithm:

$$X_{pos} = \frac{\sum_{i=1}^N Q_i X_i}{\sum_{i=1}^N Q_i} \quad Y_{pos} = \frac{\sum_{i=1}^N Q_i Y_i}{\sum_{i=1}^N Q_i} \quad (1)$$

and

$$E = \sum_{i=1}^N Q_i \quad (2)$$

where X_i, Y_i is the running number of the wire that recorded Q_i charge signal and N the total number of wires in each direction. Based on the above equations, (X_{pos}, Y_{pos}) can be easily calculated in arbitrary units in the interval $X_{pos} \in (X_1, X_N)$ and $Y_{pos} \in (Y_1, Y_N)$. The transformation to physical units can be smoothly performed with a calibration procedure as explained in the next section.

2.2 PSPMT Characterization

The intrinsic resolution of this tube is primarily checked with a series of measurements using LED pulses of variable duration, which are guided to the surface of the PSPMT and supported by a 5×5 hole-matrix spacer. The recorded planar image is divided into slices (5 orientated in the X- and 5 in the Y-direction), the projection of which defines the PSPMT's spatial resolution; a typical projection is shown in Figure 1. After a careful analysis and taking into account all possible position combinations for the signal calibration, the final mean intrinsic spatial resolution for the tube is found to be [1]:

$$\Gamma_x = \langle FWHM \rangle_x = (0.124 \pm 0.009) \text{ mm}$$

$$\Gamma_y = \langle FWHM \rangle_y = (0.123 \pm 0.051) \text{ mm}$$

The energy response of the PSPMT is checked by the

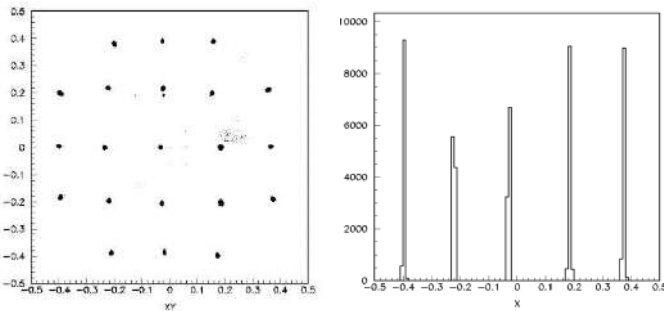


Fig. 1. *Left:* Final recorded planar image for controlled light pulses produced by a LED at different entrance positions. *Right:* A typical X-projection for a specific slice of the planar image from the analysis of which the PSPMT's spatial resolution is extracted.

variation of the accumulated charge for different applied high voltages (H.V.) and pulse durations (T). The charge

is an exponential function of the applied H.V. and the intrinsic charge distribution shows, as expected, a linear relationship with the pulse duration T [1].

3 Small Field γ -Camera System

Our laboratory small field, high-resolution γ -Camera is dedicated to radiopharmaceutical research and other clinical SPECT (Single Photon Emission Computed Tomography) applications. The main body of the system is the PSPMT equipped with a 4 mm pixelated CsI(Tl) scintillation crystal. Focus is achieved with a lead collimator, 28.8 mm of thickness optimized for the 140 keV ^{99m}Tc photons, with parallel holes of hexagonal geometry.

3.1 Spatial Resolution

The whole system characterization is based on experimental data that were collected from a simple geometrical phantom consisted of four identical capillaries with 1mm diameter and filled with ^{99m}Tc as shown in Figure 3. Each recorded planar image is divided in slices of

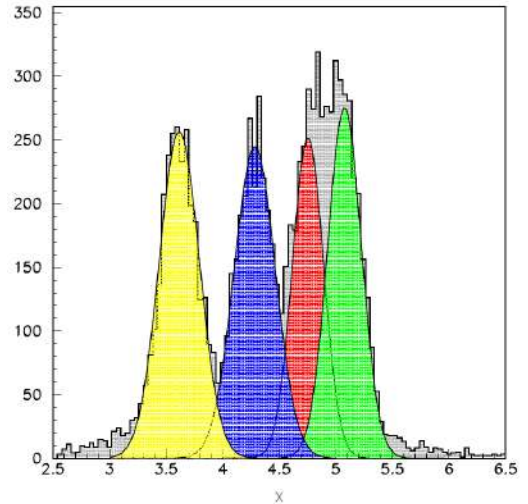


Fig. 2. The four different gaussian curves fitted on a slice of a vertical planar image. Position in the horizontal axis is measured in arbitrary units (a.u.), while the vertical axis shows the amount of the recorded events.

the same dimensions and by fitting four different gaussian-type curves, one for each filled capillary, the mean position and its sigma of each capillary is determined (Figure 2). With a series of such planar images the mean spatial resolution of the γ -Camera system is determined to be:

$$\langle \sigma_x \rangle = (1.49 \pm 0.08) \text{ mm}$$

$$\langle \sigma_y \rangle = (1.58 \pm 0.18) \text{ mm}$$

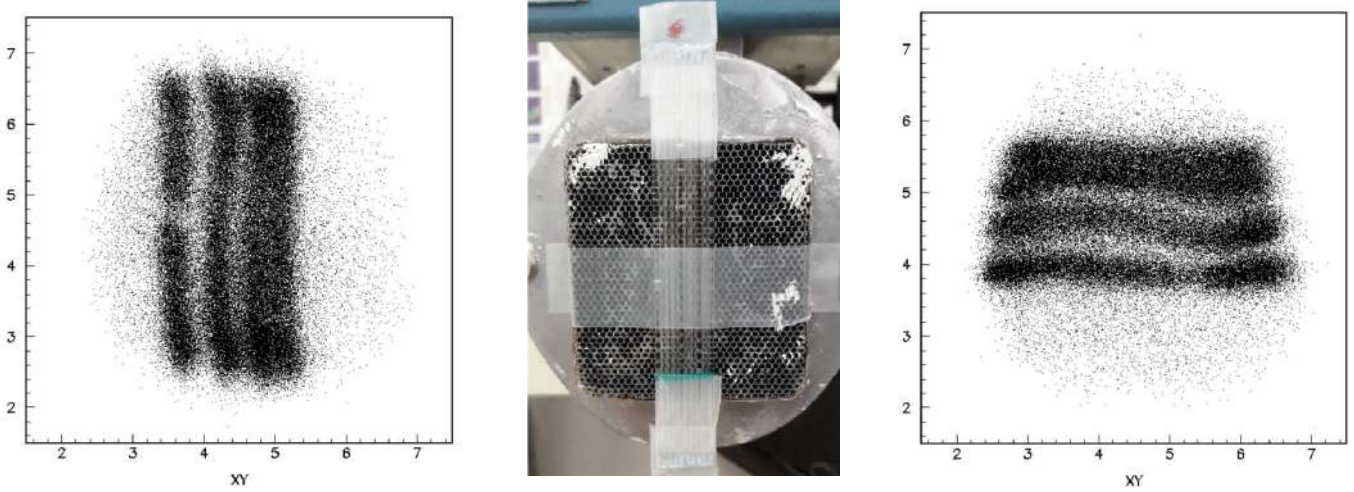


Fig. 3. *Left and Right:* Planar images recorded for the geometrical phantom oriented horizontally and vertically respectively. Position reconstruction was performed with the described Anger algorithm. *Middle:* The geometrical four-capillaries phantom in front of the γ -Camera system in the vertical orientation. The capillaries phantom has a configuration 1-000-1-00-1-0-1, where 1 represents a ^{99m}Tc filled and 0 an empty capillary normally used as a spacer.

3.2 Correction Algorithm for Spatial Distortions

All the recorded planar images seem to be systematically characterized by a spatial deformation mainly caused by the PSPMT for a given scintillation light distribution. This kind of spatial distortion observed at the edges of the images is referred as *barreloid deformation*.

The barreloid effect is mainly caused because the traditional Center-of-Gravity Anger algorithm for the charge distribution operates successfully in the case of centrally detected γ -rays but not satisfactorily in the case of an electron cloud positioned near the edge of the anode. In order to eliminate this distortion, a functional correction based on a first order interpolation technique [2] was used.

For the definition of the appropriate spline correction function, a phantom with three capillaries filled with ^{99m}Tc water solution was used and it was placed at different nominal positions. Along each capillary, recorded in the distorted planar image for a given phantom position, a family of supporting points has been formed, as shown in Figure 4. These supporting points are appropriately handled to build a first order interpolation/correction routine, which operates on each detected event and corrects the recorded position by shifting it to a nominal value. The applied algorithm is described in the following.

For each random event in the planar image (X_i, Y_i) the two neighbor levels Y_H and Y_L ($Y_L < Y_i < Y_H$) are determined from the j -th family of the supporting points. Then the following correction is applied:

$$\alpha_i = \frac{Y_i - Y_L}{Y_H - Y_L} \quad (3)$$

$$\Delta X_{ij} = \alpha_i(\Delta X_{Hj} - \Delta X_{Lj}) + \Delta X_{Lj} \quad (4)$$

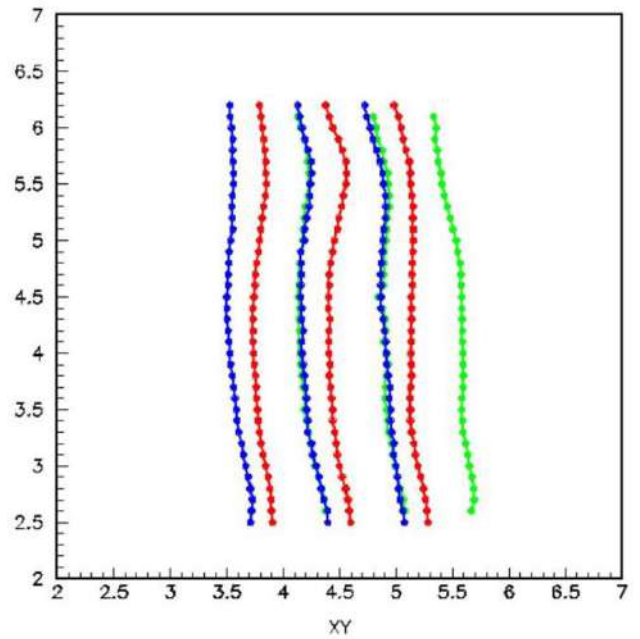


Fig. 4. Families of supporting points along each capillary of the phantom for the three different nominal positions of the phantom. Each phantom placement in front of the γ -Camera is indicated with different color.

where ΔX_{Hj} denotes the necessary X-shift required for the supporting point X_H to be moved to its nominal position and ΔX_{Lj} respectively the shift for the supporting point X_L . The nominal positions are calculated and stored in a lookup table after the calibration procedure has been performed with the parallel capillaries.

In order to smooth out the whole procedure from local discontinuities, the previous ΔX_{ij} correction is weighted with the ΔX_{ij+1} correction of the next family, according to:

$$\Delta X_{total} = \frac{D_{j+1} \times \Delta X_{ij} + D_j \times \Delta X_{ij+1}}{D_{j+1} + D_j} \quad (5)$$

Here D_j and D_{j+1} are the distances of the point from the nominal positions of the two neighbor families j and $j + 1$. All the above described correction procedure is equivalent to a two-dimensional linear interpolation. Results based on this technique are shown in Figure 5.

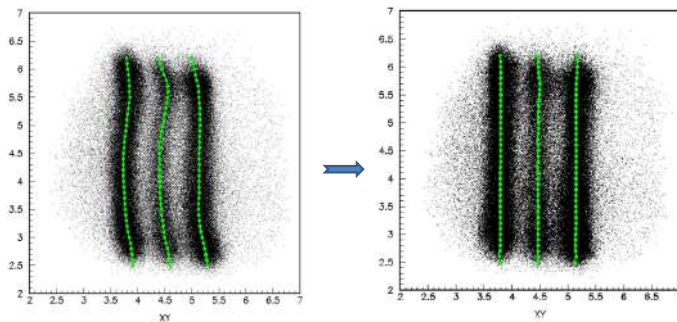


Fig. 5. *Left:* Uncorrected planar image and the supporting points for a specific position of the phantom. *Right:* The same image after the analytical (2D-linear interpolation) correction.

4 The γ -Camera System in Tomography

Finally the whole γ -Camera system and the above mentioned correction technique were checked at a tomographic level via a 3D reconstruction of a more complicated geometrical phantom and the imaging of a labelled small animal.

4.1 3D Reconstruction of a Complicated Phantom

In order to evaluate the γ -Camera system on the tomographic level with phantoms, a complicated geometrical phantom was used. It consisted of five different volumes (Figure 6) filled with ^{99m}Tc water solution with a specific activity of $0.73 \mu\text{Ci}/\mu\text{L}$. The protocol that was followed for the experimental process included accommodation of 24 planar images of the phantom with a fixed angular step of 15° , covering the full angle region ($0^\circ - 360^\circ$) and accumulated statistics of 100000 events per run. The planar information was further analyzed to reconstruct the tomographic images, taking into account all off-line corrections needed to remove barreloid deformations appearing at the edges of the Field of View (FoV).

Parallel to the analytical spline function technique described here, another correction procedure operating on the anodic wire charge distribution [1] was used for comparison. Both, the charge distribution model and the spline

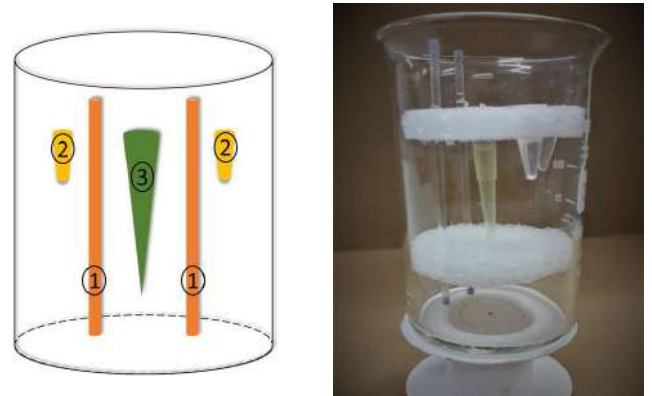


Fig. 6. A schematic depiction of the geometrical phantom (left) and a photograph of it (right).

function technique applied to the observed data to reproduce the corrected 3D images. The uncorrected tomogram obtained from planar images based on the Anger algorithm, as well as the corrected 3D images are shown in Figure 8. From the reconstructed image we conclude that volumes over 0.2 cm^3 at a specific activity of $0.73 \mu\text{Ci}/\mu\text{L}$ are easily detectable from our laboratory γ -Camera system. This result is also in full agreement with detectability limits obtained with the same apparatus in [3].

4.2 Small Animal Labelled Imaging

The final step of this study includes the imaging of specific organs of a targeted small mouse. More specifically, two different and similar-sized mice were used; the first injected with ^{99m}Tc -DTPA, used in radioisotope renography to evaluate function kidneys and the second with ^{99m}Tc -MAA (Macro-Aggregates of Albumin), used in lungs imaging.

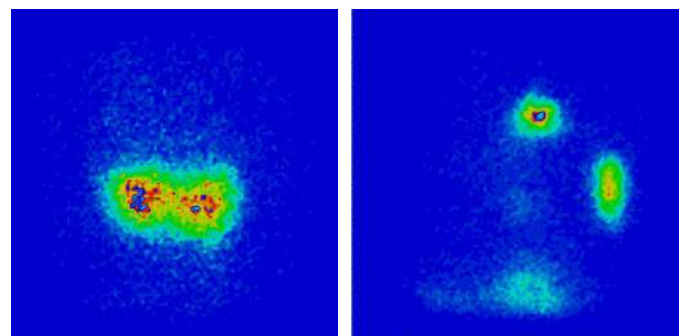


Fig. 7. Mouse's lungs imaging (left) and kidneys (right) with the small field γ -Camera.

The followed protocol included again 24 planar images, with a fixed angular step of 15° for the whole 2π range; 100000 events were recorded at each planar. The mouse was placed on a rotating table in the front of the camera

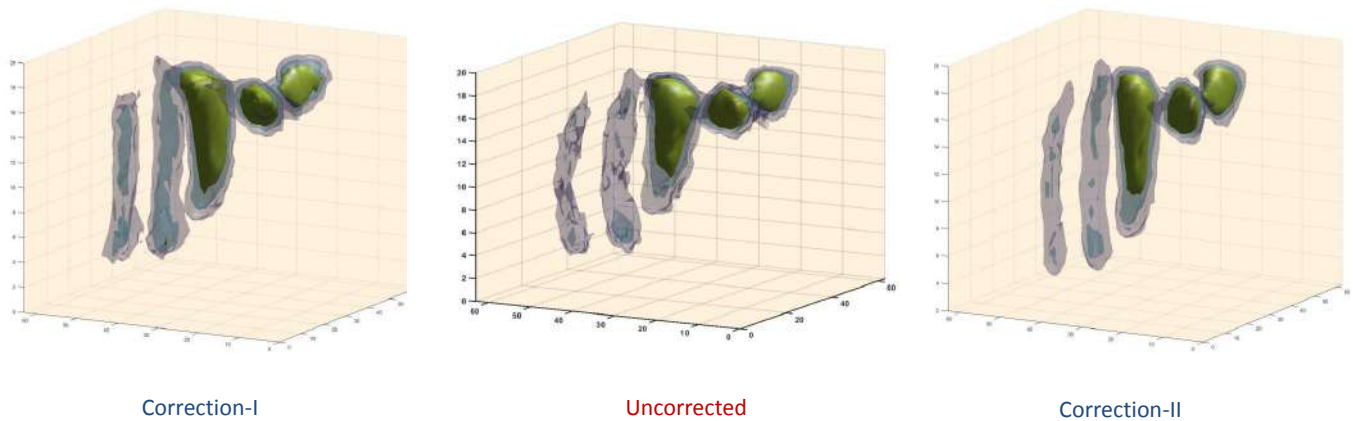


Fig. 8. A 3D reconstruction of the complicated geometrical phantom: *Center*: Uncorrected tomogram. *Left*: Corrected with the charge distribution model. *Right*: Corrected with the analytical 2D linear interpolation technique (spline function) described previously.

[4]. In order to achieve the highest spatial resolution, the distance between the animal and the front of the collimator was reduced to less than 1 cm. Two of the recorded planar images for the two different regions of interest are shown in Figure 7.

5 Concluding Results and Summary

The main purpose of the use of a small field γ -Camera system in preclinical studies is the optimization of its performance; spatial and energy resolution offered by such a system is in general superior compared with the respective clinical system.

A small field γ -Camera system equipped with modern PSPMTs can reach a spatial resolution better than 2mm at planar imaging, as the intrinsic PSPMT spatial resolution is better than 150 μ m. However, a spatial distortion is often noticed at the edges of a recorded image because of the followed conventional Anger algorithm and several defects in a canonical charge distribution. This effect can be eliminated in planar images by using analytical correction methods. A first order interpolation technique seems to be adequate and simple in implementation.

In the present study, it has been shown that a small field γ -Camera is an appropriate system for preclinical experiments and an optimal imaging instrument for sen-

sitivity tests with complicated geometrical phantoms and targeted organs of small animals labelled with specific radionuclides.

References

1. D. Zarketan: *Resolution Study of a γ -Camera System for Single Photon Emission Computed Tomography (SPECT) at Preclinical Level*, MSc Thesis, Department of Physics and Medical School, National and Kapodistrian University of Athens, (2019).
2. D. Thanasas, E. Georgiou, N. Giokaris, A. Karabarbounis, D. Maintas, C.N. Papanicolas, A. Polychronopoulou and E. Stiliaris: *A Correction Method of the Spatial Distortion in Planar Images from γ -Camera Systems*, Journal of Instrumentation **4** (2009) P06012.
3. I. Lytrosyngounis, D. Zarketan, M. Argyrou, D. Maintas, C. Mainta, M.-E. Tomazinaki and E. Stiliaris: *Cancer Lesions Detectability Limits in the SPECT Breast Imaging* IEEE Nuclear Science Symposium & Medical Imaging Conference Record **M03-160** (2018).
4. L. Koutsantonis: *Employing a Novel Analysis Method in Single Photon Emission Computed Tomography for Tomographic Image Reconstruction*, PhD Thesis, The Cyprus Institute, Nicosia, Cyprus, (2019).

Approximate SU(3) symmetries in heavy deformed nuclei

Dennis Bonatsos^{1,a}, Andriana Martinou¹, S. Sarantopoulou¹, I.E. Assimakis¹, S. Peroulis¹, and N. Minkov²

¹ Institute of Nuclear and Particle Physics, National Centre for Scientific Research “Demokritos”, GR-15310 Aghia Paraskevi, Attiki, Greece

² Institute of Nuclear Research and Nuclear Energy, Bulgarian Academy of Sciences, 72 Tzarigrad Road, 1784 Sofia, Bulgaria

Abstract. The rapid increase of computational power over the last several years has allowed detailed microscopic investigations of the structure of many nuclei in terms of Relativistic Mean Field theories as well as in the framework of the no-core Shell Model. In heavy deformed nuclei, in which microscopic calculations remain a challenge, algebraic models based on the SU(3) symmetry offer specific predictions directly comparable to experimental data. Two different approximate models for heavy deformed nuclei based on the SU(3) symmetry, the pseudo-SU(3) and the proxy-SU(3) schemes are discussed and the compatibility between their predictions for the nuclear deformation parameters is shown.

PACS. 21.60.Fw Models based on group theory – 21.60.Ev Collective models

When working in the pseudo-SU(3) framework [1] with a specific nucleus, the first task is to count how many of the valence protons and neutrons occupy normal parity orbitals and how many occupy intruder parity orbitals. This is done from the standard Nilsson diagrams [2], using as an estimate for the deformation parameter of the nucleus under discussion the value given by the D1S Gogny interaction [3]. It should be noticed that the deformation parameter ϵ of the Nilsson model is related to the β shape variable of the collective model [4] through the equation $\epsilon = 0.946\beta$ [5]. The results of this procedure for nuclei in the rare earth region are shown in Table 1.

Once the number of valence protons (neutrons) in the relevant shell is known, the SU(3) irrep (λ_p, μ_p) characterizing the protons and the SU(3) irrep (λ_n, μ_n) characterizing the neutrons can be found by looking at Table 2, in which the SU(3) irreps corresponding to the relevant particle number are given. The valence protons of this shell live within a U(10) pseudo-SU(3) shell, which can accommodate a maximum of 20 particles, while the valence neutrons live within a U(15) pseudo-SU(3) shell, which can accommodate a maximum of 30 particles. In Table 2 for each U(N) algebra and each particle number, two irreps are reported. One of them is the highest weight irrep, labeled by hw, while the other is the irrep possessing the highest eigenvalue of the second order Casimir operator $C_2^{SU(3)}(\lambda, \mu)$, labeled by hC. Both of them have been obtained using the code of Ref. [6].

We are going to produce results for two cases: a) both protons and neutrons live in shells in which the hw irreps are taken into account, b) both protons and neutrons live

in shells in which the hC irreps are taken into account. In both cases it will be assumed that the whole nucleus is described by the “stretched” SU(3) irrep $(\lambda_p + \lambda_n, \mu_p + \mu_n)$ [1]. The results for the former case are shown in Table 3, while the results for the latter case are shown in Table 4.

Numerical results for the collective deformation variables β and γ , calculated using the formulae given in Ref. [7], for several isotopic chains of rare earths are shown in Figs. 1 and 2 respectively.

In Fig. 1 it is clear that both the hw and C choices give identical predictions for β up to midshell, while above midshell the hw predictions for β lie systematically lower than the C predictions for all isotopic chains shown. In Fig. 2 it is clear that both the hw and C choices give identical predictions for γ up to midshell. Above midshell the C predictions jump up to oblate values immediately after midshell, while the hw predictions cross the prolate to oblate border of $\gamma = 30^\circ$ much later, at $N = 114-116$, and this only happens for the Hf, W, Os, and Pt isotopic chains, in agreement to existing experimental evidence, which has been extensively reviewed in Ref. [7] and needs not to be repeated here.

In what follows attention is focused on the hw predictions of pseudo-SU(3).

In Fig. 3 the predictions for β of the hw pseudo-SU(3) and of proxy-SU(3) [7, 8] are compared. In general, the predictions are very similar in the beginning of the neutron shell, while in the middle of the shell the proxy-SU(3) predictions are in general higher than the hw pseudo-SU(3) predictions. Finally, near the end of the shell, the hw pseudo-SU(3) predictions become higher than the proxy-SU(3) ones. In the same figure, predictions by Relativistic Mean Field (RMF) theory [9] are reported. In the begin-

^a e-mail: bonat@inp.demokritos.gr

ning of the neutron shell the RMF predictions are lower than the hw pseudo-SU(3) and proxy-SU(3) predictions, while near midshell the RMF and proxy-SU(3) predictions are closer to each other. Near the end of the neutron shell the agreement between the three theories is better than in the beginning of the shell.

In Fig. 4 the predictions for γ of the hw pseudo-SU(3) and of proxy-SU(3) are compared. Remarkable similarity between the results of the two theories is seen, despite the different approximations made and the different harmonic oscillator shells used in each of them. In particular, minima related to low values of μ in the (λ, μ) irrep appear for both theories around $N = 100-102$ and $N = 112$. Considerable disagreement is seen in the beginning of the neutron shell, where proxy-SU(3) predicts minima at $N = 88, 94$, while the hw pseudo-SU(3) shows a stabilized region around $N = 90$, related to the gradual filling of the abnormal parity neutron orbitals. It should be remembered that the $N = 90$ isotones ^{150}Nd , ^{152}Sm , and ^{154}Gd are the best examples of the X(5) critical point symmetry, characterizing the shape/phase transition between spherical and prolate deformed shapes [10].

Financial support by the Bulgarian National Science Fund (BNSF) under Contract No. KP-06-N28/6 is gratefully acknowledged.

References

1. J. P. Draayer and K. J. Weeks, Phys. Rev. Lett. **51**, 1422 (1983)
2. C. M. Lederer and V. S. Shirley (Eds.), *Table of Isotopes* (Wiley, New York, 1978)
3. J. -P. Delaroche, M. Girod, J. Libert, H. Goutte, S. Hilaire, S. Péru, N. Pillet, and G. F. Bertsch, Phys. Rev. C **81**, 014303 (2010)
4. A. Bohr and B. R. Mottelson, *Nuclear Structure, Vol. II: Nuclear Deformations* (Benjamin, New York, 1975)
5. S. G. Nilsson and I. Ragnarsson, *Shapes and Shells in Nuclear Structure* (Cambridge University Press, Cambridge, 1995)
6. J. P. Draayer, Y. Leschber, S. C. Park, and R. Lopez, Comput. Phys. Commun. **56**, 279 (1989)
7. D. Bonatsos, I. E. Assimakis, N. Minkov, A. Martinou, S. Sarantopoulou, R. B. Cakirli, R. F. Casten, and K. Blaum, Phys. Rev. C **95**, 064326 (2017)
8. D. Bonatsos, I. E. Assimakis, N. Minkov, A. Martinou, R. B. Cakirli, R. F. Casten, and K. Blaum, Phys. Rev. C **95**, 064325 (2017)
9. G. A. Lalazissis, S. Raman, and P. Ring, At. Data Nucl. Data Tables **71**, 1 (1999)
10. P. Cejnar, J. Jolie, and R. F. Casten, Rev. Mod. Phys. **82**, 2155 (2010)

Table 1. Distribution of valence protons and valence neutrons into normal and abnormal parity orbitals in the rare earth region, as obtained from the standard Nilsson diagrams [2], using for each nucleus the deformation parameter obtained from Ref. [3]. In each sum, the first number represents the normal parity nucleons, while the second number corresponds to the abnormal parity nucleons. The valence protons in normal parity orbitals live within a U(10) pseudo-SU(3) shell, while the valence neutrons in normal parity orbitals live within a U(15) pseudo-SU(3) shell.

N_{val}	Xe	Ba	Ce	Nd	Sm	Gd	Dy	Er	Yb	Hf	W	Os	Pt
2	2+0	2+0	2+0	2+0	2+0	2+0	2+0	2+0	2+0	2+0	2+0	2+0	2+0
4	4+0	4+0	4+0	4+0	4+0	4+0	4+0	4+0	4+0	4+0	4+0	4+0	4+0
6	6+0	6+0	6+0	6+0	6+0	6+0	6+0	6+0	6+0	6+0	6+0	6+0	6+0
8	8+0	6+2	6+2	6+2	6+2	6+2	6+2	6+2	6+2	8+0	8+0	8+0	8+0
10	8+2	6+4	6+4	6+4	6+4	6+4	6+4	6+4	6+4	8+2	8+2	8+2	10+0
12	8+4	8+4	8+4	8+4	8+4	8+4	8+4	8+4	8+4	10+2	8+4	8+4	10+2
14	10+4	8+6	8+6	8+6	8+6	8+6	8+6	8+6	8+6	10+4	10+4	8+6	10+4
16	10+6	10+6	10+6	10+6	10+6	10+6	10+6	10+6	10+6	12+4	10+6	10+6	10+6
18	12+6	12+6	12+6	12+6	12+6	12+6	12+6	12+6	12+6	12+6	12+6	12+6	12+6
20	12+8	12+8	12+8	12+8	12+8	12+8	12+8	12+8	14+6	14+6	12+8	12+8	12+8
22	14+8	14+8	14+8	14+8	14+8	14+8	14+8	14+8	14+8	16+6	14+8	14+8	14+8
24	16+8	16+8	16+8	16+8	16+8	16+8	16+8	16+8	16+8	16+8	16+8	14+10	16+8
26	16+10	16+10	16+10	16+10	16+10	16+10	16+10	16+10	18+8	16+10	16+10	16+10	16+10
28	18+10	18+10	18+10	18+10	18+10	18+10	18+10	18+10	18+10	18+10	18+10	18+10	18+10
30	20+10	20+10	20+10	20+10	20+10	20+10	20+10	20+10	20+10	20+10	20+10	20+10	20+10
32	22+10	22+10	22+10	22+10	22+10	22+10	22+10	22+10	22+10	22+10	22+10	22+10	22+10
34	24+10	24+10	24+10	24+10	24+10	24+10	24+10	24+10	24+10	24+10	24+10	24+10	24+10
36	24+12	26+10	24+12	24+12	24+12	24+12	24+12	24+12	24+12	24+12	24+12	26+10	24+12
38	24+14	26+12	24+14	24+14	24+14	24+14	24+14	24+14	24+14	24+14	24+14	26+12	24+14
40	26+14	26+14	26+14	26+14	26+14	26+14	26+14	26+14	26+14	26+14	26+14	26+14	26+14
42	28+14	28+14	28+14	28+14	28+14	28+14	28+14	28+14	28+14	28+14	28+14	28+14	28+14

Table 2. Highest weight irreducible representations (irreps), labeled by hw, and irreps possessing the highest eigenvalue of the second order Casimir operator of SU(3), labeled by hC, occurring in the decomposition of U(10) and U(15) for M particles, as obtained through the code of Ref. [6]. Oblate irreps are shown in boldface.

M	2	4	6	8	10	12	14
U(10) hw	(6,0)	(8,2)	(12,0)	(10,4)	(10,4)	(12,0)	(6,6)
U(10) hC	(6,0)	(8,2)	(12,0)	(10,4)	(10,4)	(4,10)	(0,12)
U(15) hw	(8,0)	(12,2)	(18,0)	(18,4)	(20,4)	(24,0)	(20,6)
U(15) hC	(8,0)	(12,2)	(18,0)	(18,4)	(20,4)	(24,0)	(20,6)

M	16	18	20	22	24	26	28
U(10) hw	(2,8)	(0,6)	(0,0)				
U(10) hC	(2,8)	(0,6)	(0,0)				
U(15) hw	(18,8)	(18,6)	(20,0)	(12,8)	(6,12)	(2,12)	(0,8)
U(15) hC	(6,20)	(0,24)	(4,20)	(4,18)	(0,18)	(2,12)	(0,8)

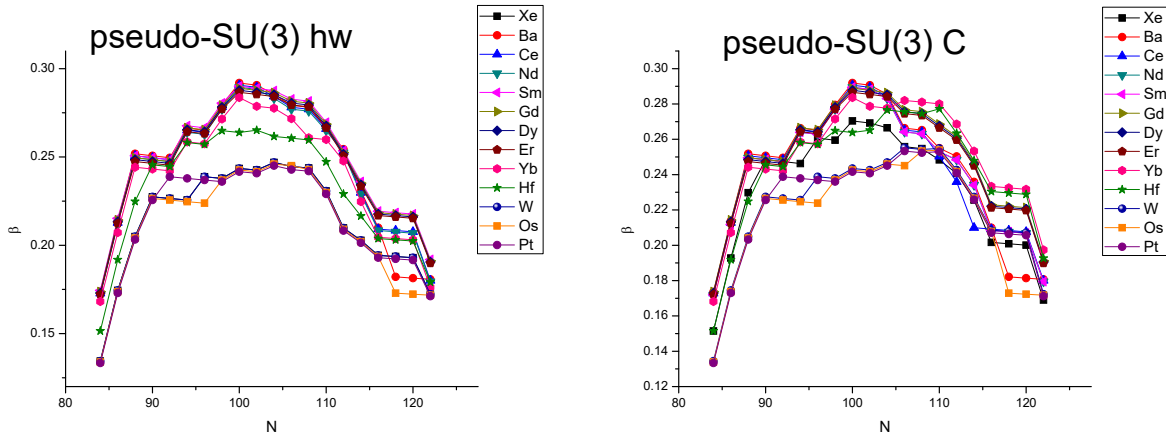


Fig. 1. Pseudo-SU(3) predictions for the collective deformation variable β for the Xe-Pt series of isotopes, obtained using the highest weight irreps of SU(3) (labeled by hw), and the irreps of SU(3) having the highest eigenvalue of the second order Casimir operator of SU(3), $C_2^{SU(3)}$ (labeled by C).

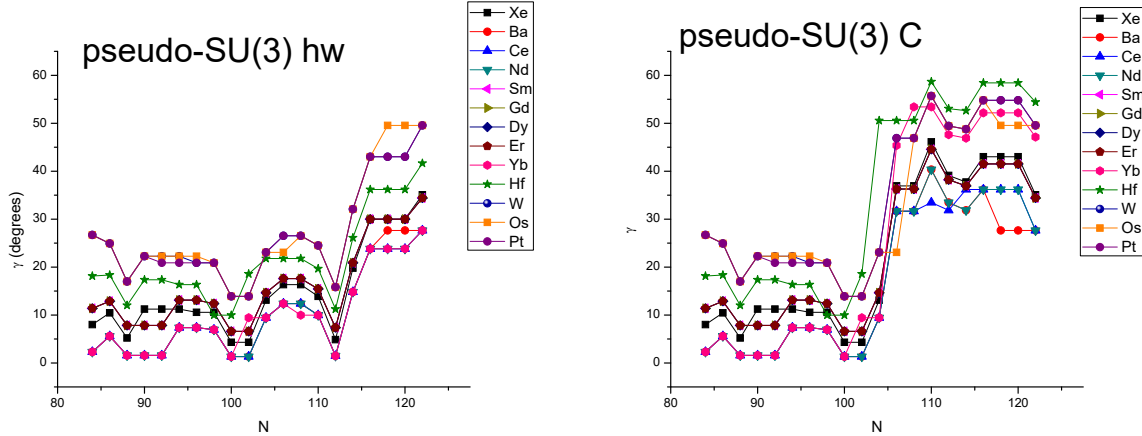


Fig. 2. Pseudo-SU(3) predictions for the collective deformation variable γ for the Xe-Pt series of isotopes, obtained using the highest weight irreps of SU(3) (labeled by hw), and the irreps of SU(3) having the highest eigenvalue of the second order Casimir operator of SU(3), $C_2^{SU(3)}$ (labeled by C).

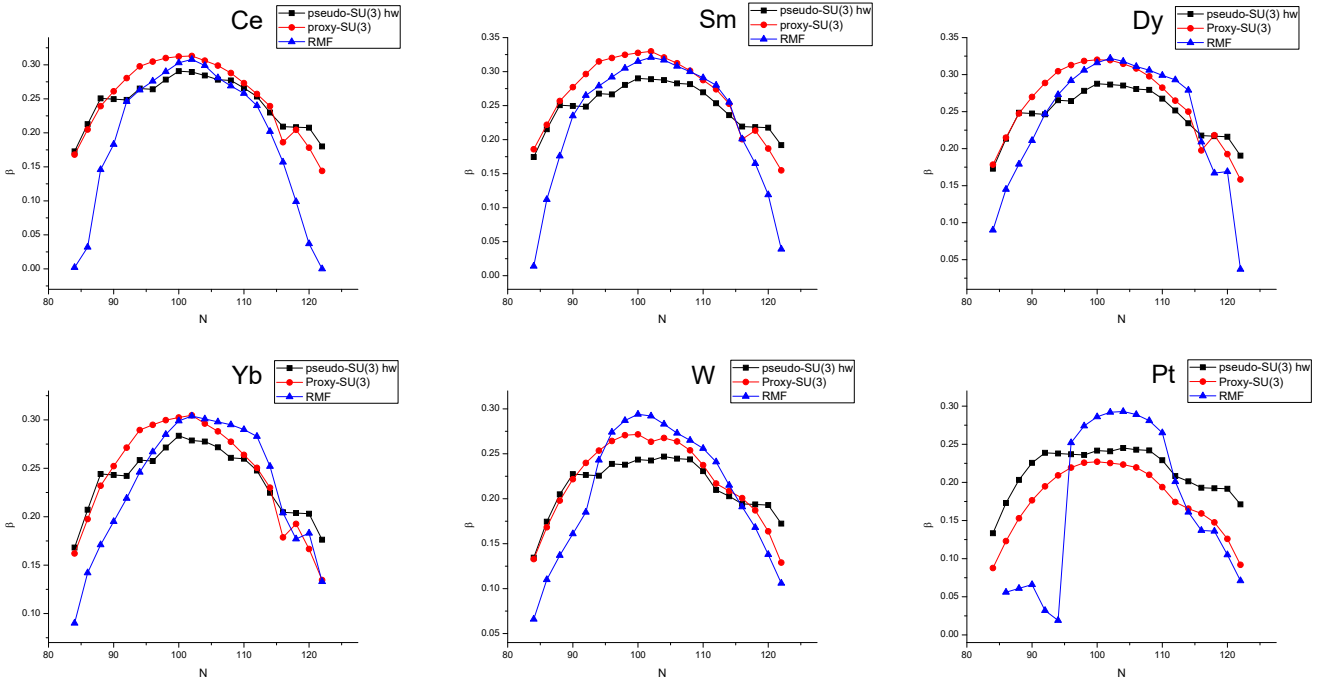


Fig. 3. Pseudo-SU(3) hw predictions for the collective deformation variable β for six series of isotopes in the rare earth region are compared to proxy-SU(3) results obtained as described in Ref. [7], as well as to relativistic mean field theory (RMF) predictions [9].

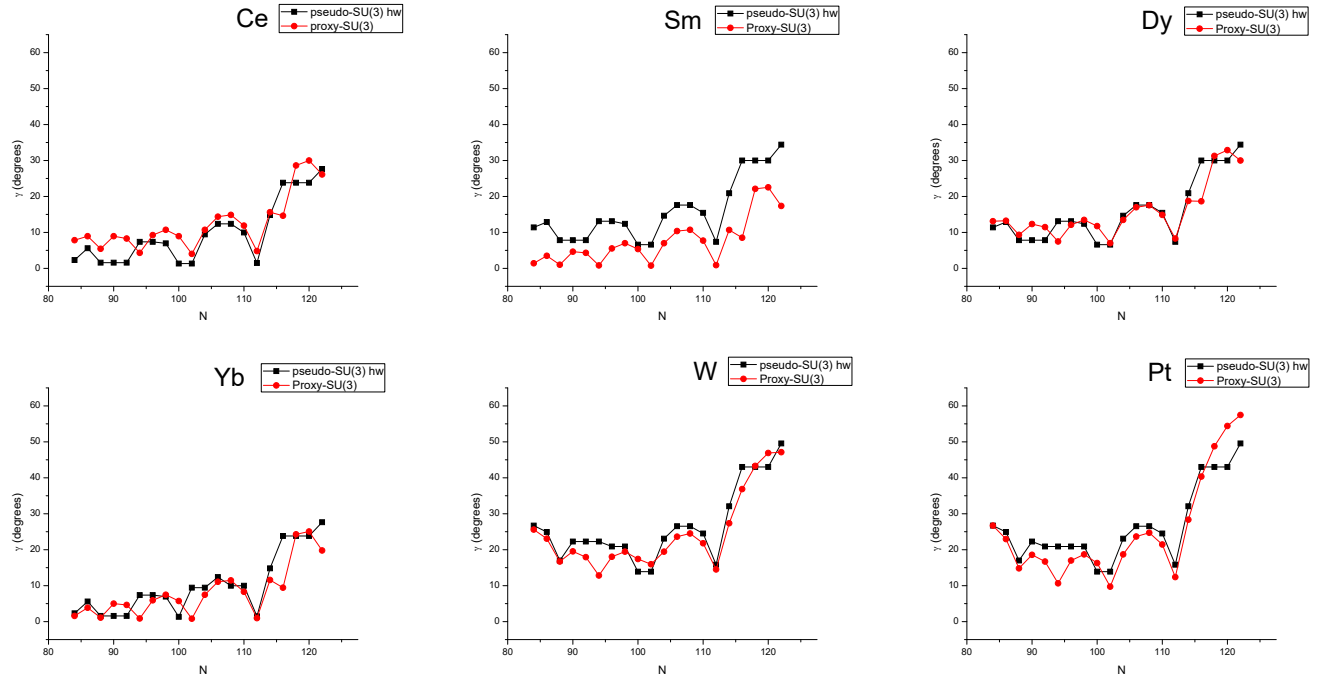


Fig. 4. Pseudo-SU(3) hw predictions for the collective deformation variable γ for six series of isotopes in the rare earth region are compared to proxy-SU(3) results obtained as described in Ref. [7].

Table 3. Total irreps corresponding to rare earth nuclei obtained when the highest weight irreps (hw) are used for both the valence protons and the valence neutrons. The irreps are taken from Table 2. Oblate irreps are shown in boldface.

N	Xe	Ba	Ce	Nd	Sm	Gd	Dy	Er	Yb	Hf	W	Os	Pt
84	16,2	20,0	20,0	20,0	18,4	18,4	18,4	18,4	20,0	14,6	10,8	10,8	10,8
86	20,4	24,2	24,2	24,2	22,6	22,6	22,6	22,6	24,2	18,8	14,10	14,10	14,10
88	26,2	30,0	30,0	30,0	28,4	28,4	28,4	28,4	30,0	24,6	20,8	20,8	20,8
90	26,6	30,0	30,0	30,0	28,4	28,4	28,4	28,4	30,0	24,10	20,12	20,12	20,12
92	26,6	30,0	30,0	30,0	28,4	28,4	28,4	28,4	30,0	24,10	20,12	20,12	20,12
94	26,6	30,4	30,4	30,4	28,8	28,8	28,8	28,8	30,4	26,10	20,12	20,12	20,12
96	28,6	32,4	32,4	32,4	30,8	30,8	30,8	30,8	32,4	30,6	22,12	22,12	22,12
98	28,6	32,4	32,4	32,4	30,8	30,8	30,8	30,8	32,4	30,6	22,12	22,12	22,12
100	32,2	36,0	36,0	36,0	34,4	34,4	34,4	34,4	36,0	26,8	26,8	26,8	26,8
102	32,2	36,0	36,0	36,0	34,4	34,4	34,4	34,4	36,0	26,12	26,8	26,8	26,8
104	28,8	32,6	32,6	32,6	30,10	30,10	30,10	30,10	32,6	24,14	22,14	22,14	22,14
106	26,10	30,8	30,8	30,8	28,12	28,12	28,12	28,12	30,8	24,14	20,16	22,14	20,16
108	26,10	30,8	30,8	30,8	28,12	28,12	28,12	28,12	30,6	24,14	20,16	20,16	20,16
110	26,8	30,6	30,6	30,6	28,10	28,10	28,10	28,10	30,6	24,12	20,14	20,14	20,14
112	28,2	32,0	32,0	32,0	30,4	30,4	30,4	30,4	32,0	26,6	22,8	22,8	22,8
114	20,10	24,8	24,8	24,8	22,12	22,12	22,12	22,12	24,8	18,14	14,16	14,16	14,16
116	14,14	18,12	18,12	18,12	16,16	16,16	16,16	16,16	18,12	12,18	8,20	8,20	8,20
118	14,14	14,12	18,12	18,12	16,16	16,16	16,16	16,16	18,12	12,18	8,20	4,20	8,20
120	14,14	14,12	18,12	18,12	16,16	16,16	16,16	16,16	18,12	12,18	8,20	4,20	8,20
122	10,14	14,12	14,12	14,12	12,16	12,16	12,16	12,16	14,12	8,18	4,20	4,20	4,20
124	8,10	12,8	12,8	12,8	10,12	10,12	10,12	10,12	12,8	6,14	2,16	2,16	2,16

Table 4. Total irreps corresponding to rare earth nuclei obtained when the irrep having the highest eigenvalue of the second order Casimir operator of SU(3) (hC) is used for both the valence protons and the valence neutrons. The irreps are taken from Table 2. Oblate irreps are shown in boldface.

N	Xe	Ba	Ce	Nd	Sm	Gd	Dy	Er	Yb	Hf	W	Os	Pt
84	16,2	20,0	20,0	20,0	18,4	18,4	18,4	18,4	12,10	8,12	10,8	10,8	10,8
86	20,4	24,2	24,2	24,2	22,6	22,6	22,6	22,6	16,12	12,14	14,10	14,10	14,10
88	26,2	30,0	30,0	30,0	28,4	28,4	28,4	28,4	22,10	18,12	20,8	20,8	20,8
90	26,6	30,0	30,0	30,0	28,4	28,4	28,4	28,4	22,10	18,16	20,12	20,12	20,12
92	26,6	30,0	30,0	30,0	28,4	28,4	28,4	28,4	22,10	18,16	20,12	20,12	20,12
94	26,6	30,4	30,4	30,4	28,8	28,8	28,8	28,8	22,14	20,16	20,12	20,12	20,12
96	28,6	30,4	30,4	30,4	28,8	28,8	28,8	28,8	22,14	20,16	22,12	20,12	22,12
98	28,6	32,4	32,4	32,4	30,8	30,8	30,8	30,8	24,14	24,12	22,12	22,12	22,12
100	32,2	36,0	36,0	36,0	34,4	34,4	34,4	34,4	28,10	24,12	26,8	26,8	26,8
102	32,2	36,0	36,0	36,0	34,4	34,4	34,4	34,4	24,16	20,18	26,8	26,8	26,8
104	28,8	32,6	32,6	32,6	30,10	30,10	30,10	30,10	24,16	6,32	22,14	22,14	22,14
106	14,22	18,20	18,20	18,20	16,24	16,24	16,24	16,24	10,30	6,32	8,28	22,14	8,28
108	14,22	18,20	18,20	18,20	16,24	16,24	16,24	16,24	4,34	6,32	8,28	8,28	8,28
110	8,26	12,24	12,24	12,24	10,28	10,28	10,28	10,28	4,34	0,36	2,32	2,32	2,32
112	12,22	16,20	16,20	16,20	14,24	14,24	14,24	14,24	8,30	4,32	6,28	6,28	6,28
114	12,20	16,18	16,18	16,18	14,22	14,22	14,22	14,22	4,28	4,30	6,26	6,26	6,26
116	8,20	12,18	12,18	12,18	10,22	10,22	10,22	10,22	4,28	0,30	2,26	2,26	2,26
118	8,20	14,12	12,18	12,18	10,22	10,22	10,22	10,22	4,28	0,30	2,26	4,20	2,26
120	8,20	14,12	12,18	12,18	10,22	10,22	10,22	10,22	4,28	0,30	2,26	4,20	2,26
122	10,14	14,12	14,12	14,12	12,16	12,16	12,16	12,16	6,22	2,24	4,20	4,20	4,20
124	8,10	12,8	12,8	12,8	10,12	10,12	10,12	10,12	4,18	0,20	2,16	2,16	2,16

Many-body wavefunctions in the Elliott SU(3) symmetry

Andriana Martinou
INPP “Demokritos”, Athens, Greece

The attractive nucleon-nucleon interaction has a short-range character, which favors the most symmetric spatial Elliott SU(3) irrep. The symmetry of the Elliott SU(3) irreps is investigated. It emerges, that in each (λ, μ) irrep the $\lambda + \mu$ harmonic oscillator quanta are symmetric upon their interchange, while the μ quanta are neither symmetric, nor antisymmetric.

I. INTRODUCTION

It is evident, that the nucleon-nucleon interaction has a short range [1, 2]. The special connection of the short-range character with the leading Elliott SU(3) irrep has been enunciated at [3], where the authors state, that “the short-range character of the nuclear force favors the most symmetric spatial SU(3) irrep, which allows the maximum spatial overlap among the fermions”. The understanding of the symmetrization mechanism in the Elliott SU(3) Model may clarify, which one is the most symmetric and thus the *leading* SU(3) irrep.

II. THE MANY-BODY SU(3) WAVEFUNCTIONS

The single-particle Hamiltonian in the Elliott SU(3) symmetry [4, 5] consists by the 3D isotropic harmonic oscillator mean field potential and by the spin-orbit term:

$$H = \frac{p^2}{2M} + \frac{1}{2}M\omega^2 r^2 + V_{ls}ls, \quad (1)$$

where p, r, M, ω are the momentum, spatial coordinate, mass and oscillation frequency respectively, while the last term is the spin-orbit interaction, with l, s being the angular momentum and spin. The V_{ls} is the potential of the spin-orbit coupling. The spatial, single-particle eigenstates of the 3D isotropic harmonic oscillator in the cartesian coordinate system are Hermite polynomials [6], which are labeled by the number of quanta in each cartesian direction $|n_z, n_x, n_y\rangle$. The spinor of each particle is $|s, m_s\rangle$, where $s = 1/2$ and the spin projection is $m_s = \pm 1/2$. The overall, single-particle wavefunction is $|n_z, n_x, n_y, m_s\rangle$, which are connected through a unitary transformation with the spherical Shell Model states [7].

The multi-particle wavefunction is simply a Slater determinant [1] of the $|n_z, n_x, n_y, m_s\rangle$ states [8]. The Slater determinant represents a totally antisymmetric multi-particle wavefunction, as dictated by the Pauli Principle for a fermion system. This complicated wavefunction combines both the spatial and the spinor information for all the valence nucleons. Fortunately the overall, antisymmetric wavefunction can be decomposed into a spatial and a spinor part for the many nucleon system:

$$\Psi = \Psi_{spatial} \cdot \Psi_{spinor}. \quad (2)$$

Each part may be nor totally symmetric, neither totally antisymmetric and thus may possess mixed symmetry, as long as combination of the two parts produces a totally antisymmetric Slater determinant. To this purpose the spinor has to be the conjugate of the spatial part and vice versa [9, 10].

The spatial wavefunction of the valence nucleons is represented by a Young pattern of the U(3) symmetry of the type [4, 5, 11]:

$$\begin{array}{|c|c|c|c|} \hline \square & \square & \square & \square \\ \hline \square & \square & \square & \\ \hline \square & & & \\ \hline \end{array} \quad (3)$$

Each row contains f_1, f_2 and f_3 boxes respectively, with $f_1 \geq f_2 \geq f_3$. The f_1, f_2, f_3 for the low-lying nuclear properties are the summations of the number of quanta in each cartesian axis for every valence nucleon [5, 12]:

$$f_1 = \sum n_z, f_2 = \sum n_x, f_3 = \sum n_y. \quad (4)$$

Each U(3) Young pattern is labeled as $[f_1, f_2, f_3]$. A column with three boxes may be deleted, so the Young pattern of Eq. (3) equivalents with the:

$$\begin{array}{|c|c|c|} \hline \square & \square & \square \\ \hline \square & \square & \\ \hline \end{array} \quad (5)$$

and is labeled as $[f_1, f_2, 0]$. The U(3) algebra contains an SU(3) algebra characterized by the Elliott quantum numbers (λ, μ) :

$$\lambda = f_1 - f_2, \quad (6)$$

$$\mu = f_2 \quad (7)$$

The spatial wavefunction of k particles in a harmonic oscillator shell with \mathcal{N} number of quanta is the result of the action of the creation operators of the oscillator well on the vacuum state [13] and is a tensor of rank $k\mathcal{N}$ [5]. The transformations among the three components of each single-particle creation operator are characterized by the group U(3) [5]. The U(3) wavefunction is a tensor of rank:

$$\lambda + 2\mu = f_1 + f_2, \quad (8)$$

which equals to the number of boxes of the U(3) Young pattern $[f_1, f_2, 0]$. The symmetry of this tensor is described by the partition:

$$[\lambda + \mu, \mu] = [f_1, f_2], \quad (9)$$

which means, that the $\lambda + \mu = f_1$ components of this tensor are symmetric among them, while the rest μ components are not symmetric, neither antisymmetric [5]. Therefore if $\mu = 0$ the tensor transforms as a totally symmetric tensor of rank λ , while for $\mu \neq 0$ the tensor is of mixed symmetry.

Let for instance three protons (neutrons) to be placed in the p nuclear shell: two are placed in the orbital $|n_z, n_x, n_y\rangle = |1, 0, 0\rangle$ and one in the $|0, 1, 0\rangle$. Therefore the $U(3)$ partition, which results from Eqs. (4), is $[2, 1, 0]$. This state may be represented by the $U(3)$ Young pattern:

$$\begin{array}{|c|c|} \hline & \\ \hline & \\ \hline \end{array} \quad (10)$$

and has an $SU(3)$ irreducible representation (irrep) $(\lambda, \mu) = (1, 1)$. If $a_\alpha^\dagger(i)$ is the creation operator, which gives to the i^{th} particle a quantum in the $\alpha = z, x, y$ cartesian direction [13], then the terms of the spatial many-body wavefunction of this example are of the type:

$$a_z^\dagger(1)a_z^\dagger(2)a_x^\dagger(3)|0\rangle, \quad (11)$$

with $|0\rangle$ being the vacuum state, namely the $1s$ Shell Model orbital. The particle-number Young tableaux, which represents the spatial, multi-particle wavefunction of this example is [11]:

$$\begin{array}{|c|c|} \hline z & z \\ \hline x & \\ \hline \end{array}, \quad \begin{array}{|c|c|} \hline 1 & 2 \\ \hline 3 & \\ \hline \end{array} \quad (12)$$

where the z, x, y represent one quantum in each cartesian direction, while the numbers 1, 2, 3 enumerate the quanta and can be placed in the Young pattern so as the numbers increase from the left to the right and downwards. The wavefunction of the particle-number Young tableaux (12) is [11]:

$$\Psi_{\text{spatial}} = \sqrt{\frac{1}{6}}(2y_z(1)y_z(2)y_x(3) - y_z(1)y_x(2)y_z(3) - y_x(1)y_z(2)y_z(3)), \quad (13)$$

where $y_\alpha(i)$ is an Hermite polynomial with one quantum in the $\alpha = z, x, y$ direction for the i^{th} particle [6]. Obviously this wavefunction is symmetric under the transposition $1 \leftrightarrow 2$, but there is no symmetry in the transpositions $1 \leftrightarrow 3$ and $2 \leftrightarrow 3$. Indeed only 2 out of the 3 quanta are symmetric among them. The number of symmetric quanta for the total wavefunction for the above example is $\lambda + \mu = 2$.

III. DISCUSSION

The number of symmetric quanta out of the total number of quanta may lead to a measure of the symmetry of each Elliott $SU(3)$ irrep. This symmetry is of utmost importance, due to the short range character of the nucleon-nucleon interaction. One may deduce from symmetry considerations, which irrep describes the nuclear low lying properties.

-
- [1] P. Ring, P. Schuck, *The Nuclear Many-Body Problem* (Springer-Verlag, New York, United States, 1980)
- [2] R.F. Casten, *Nuclear Structure from a Simple Perspective* (Oxford University Press, New York, United States, 1990)
- [3] P.V. Isacker, D.D. Warner, D.S. Brenner, *Physical Review Letters* **74**(23), 4607 (1995). DOI 10.1103/physrevlett.74.4607
- [4] J.P. Elliott, *Proceedings of the Royal Society of London. Series A. Mathematical and Physical Sciences* **245**(1240), 128 (1958). DOI 10.1098/rspa.1958.0072
- [5] J.P. Elliott, *Proceedings of the Royal Society of London. Series A. Mathematical and Physical Sciences* **245**(1243), 562 (1958). DOI 10.1098/rspa.1958.0101
- [6] C. Cohen-Tannoudji, B. Diu, F. Laloe, *Quantum Mechanics*, vol. 1, 1st edn. (Wiley, 1991)
- [7] A. Martinou, N. Minkov, S. Sarantopoulou, S. Peroulis, I. Assimakis, D. Bonatsos, *Bulgarian Journal of Physics* **46**(4), 337 (2019)
- [8] J.P. Elliott, M. Harvey, *Proceedings of the Royal Society of London. Series A. Mathematical and Physical Sciences* **272**(1351), 557 (1963). DOI 10.1098/rspa.1963.0071
- [9] V.K.B. Kota, *SU(3) Symmetry in Atomic Nuclei* (Springer Singapore, 2020). DOI 10.1007/978-981-15-3603-8
- [10] J.P. Draayer, *Algebraic approaches to nuclear structure: Interacting boson and fermion models, Contemporary Concepts in Physics*, vol. 6 (Harwood Academic Publishers, New York, United States, 1993)
- [11] P.O. Lipas, *Algebraic approaches to nuclear structure: interacting boson and fermion models, Contemporary Concepts in Physics*, vol. 6 (1993)
- [12] D. Bonatsos, I.E. Assimakis, N. Minkov, A. Martinou, S. Sarantopoulou, R.B. Cakirli, R.F. Casten, K. Blaum, *Physical Review C* **95**(6) (2017). DOI 10.1103/physrevc.95.064326
- [13] M. Harvey, *The Nuclear SU(3) Model, Advances in Nuclear Physics*, vol. 1, 1st edn. (Plenum Press, New York, United States, 1968)

Breaking SU(3) spectral degeneracies in heavy deformed nuclei

Dennis Bonatsos^{1,a}, I.E. Assimakis¹, Andriana Martinou¹, S. Peroulis¹, S. Sarantopoulou¹, and N. Minkov²

¹ Institute of Nuclear and Particle Physics, National Centre for Scientific Research “Demokritos”, GR-15310 Aghia Paraskevi, Attiki, Greece

² Institute of Nuclear Research and Nuclear Energy, Bulgarian Academy of Sciences, 72 Tzarigrad Road, 1784 Sofia, Bulgaria

Abstract. Symmetries are manifested in nature through degeneracies in the spectra of physical systems. In the case of heavy deformed nuclei, when described in the framework of the Interacting Boson Model, within which correlated proton (neutron) pairs are approximated as bosons, the ground state band has no symmetry partner, while the degeneracy between the first excited beta and gamma bands is broken through the use of three-body and/or four-body terms. In the framework of the proxy-SU(3) model, in which an approximate SU(3) symmetry of fermions is present, the same three-body and/or four-body operators are used for breaking the degeneracy between the ground state band and the first excited gamma band. Experimentally accessible quantities being independent of any free parameters are pointed out in the latter case.

PACS. 21.60.Fw Models based on group theory – 21.60.Ev Collective models

Proxy-SU(3) is an approximate symmetry appearing in heavy deformed nuclei [1,2]. The foundations of proxy-SU(3) [3], its parameter-free predictions for the collective deformation parameters β and γ [4,5], as well as for $B(E2)$ ratios [5], have been discussed and its usefulness in explaining the dominance of prolate over oblate shapes in the ground states of even-even nuclei [6] and the point of the prolate to oblate shape transition in the rare earths region [6] has been demonstrated. In the present contribution, preliminary calculations for the spectra of heavy deformed nuclei, in which three-body and four-body operators are needed, will be discussed.

Since Elliott demonstrated the relation of SU(3) symmetry to nuclear deformation [7,8], several group theoretical approaches to rotational nuclei have been developed. In theories approximating correlated valence nucleon pairs by bosons, like the Interacting Boson Model (IBM) [9], the ground state band (gsb) is sitting in the lowest-lying irreducible representation (irrep) alone, while the γ_1 band and the β_1 band belong to the next irrep, therefore being degenerate to each other if only one-body and two-body terms are included in the Hamiltonian. Actually this degeneracy has been used as a hallmark of the appearance of SU(3) symmetry in atomic nuclei [9]. Higher order (three- and four-body terms) have been introduced in the IBM Hamiltonian mostly in order to accommodate triaxial shapes [10,11]. A particular class of higher order terms consists of the symmetry-preserving three-body operator Ω and the four-body operator Λ (their mathemati-

cal names being the O_l^0 and Q_l^0 shift operator respectively) [12–15], the role of which in breaking the degeneracy between the β_1 and the γ_1 band [16,17], as well as in producing the correct odd-even staggering within the γ_1 band [18] has been considered.

A different picture emerges within algebraic models employing fermions, like the pseudo-SU(3) [19,20] and the proxy-SU(3) [1,2] models. In these cases the lowest lying irrep accommodates both the gsb and the γ_1 band, and possibly higher- K bands with $K = 4, 6, \dots$, while the β_1 and γ_2 bands, and possibly higher bands with $K = 4, 6, \dots$ belong to the next irrep. In these cases, the three- and/or four-body terms are absolutely necessary from the very beginning, in order to break the degeneracy between the gsb and the γ_1 bands. In the framework of pseudo-SU(3) this program has been successfully carried out both by using general three- and four-body terms [21], as well as by using a specific K -band splitting operator [22], containing the Ω and Λ operators with appropriate coefficients. Numerical solutions have been produced in both cases, in the second case because the Λ and Ω operators are diagonal in different bases [16].

The K -band splitting operator used in [22] has the interesting property of being diagonal for values of the angular momentum L which are low in relation to the Elliott quantum numbers λ, μ characterizing the irreducible representations (λ, μ) of SU(3) [7,8]. In lowest order approximation, in what follows we are going to use the K operator as a diagonal operator.

In the present work we would like to consider the breaking of the degeneracy of the gsb and γ_1 band within the

^a e-mail: bonat@inp.demokritos.gr

proxy-SU(3) scheme, using the same Λ , Ω , and K -band splitting operators mentioned above. Before attempting any fittings, we would like to focus attention on physical quantities which exhibit some characteristic behavior. For example, if we consider Hamiltonians of the form [16]

$$H^{(3)} = aL^2 + bK + c\Omega - dL^4, \quad (1)$$

or

$$H^{(4)} = aL^2 + bK + cA - dL^4, \quad (2)$$

one can easily realize that the behavior of the differences of the energies of the gsb and the γ_1 bands for the same angular momentum L , $E(L_{\gamma_1}) - E(L_g)$, normalized to their first member, $E(2_{\gamma_1}) - E(2_g)$, will depend only on the relative parameter c/b , since only the second and the third term in the above Hamiltonians would contribute to them. Essentially parameter-independent predictions would also occur for the odd-even staggering [23,24] within the γ -bands, which is essentially determined by the third term in the above Hamiltonians, while the first and fourth term have a minimal influence. It is interesting that while for the odd-even staggering detailed studies exist, pointing out the different behavior of this quantity in vibrational, rotational, γ -unstable or triaxial nuclei [23,24], no similar study exists for the behavior of the energy differences between the gsb and the γ_1 band in the different regions, thus we will first attempt such a study.

In Fig. 1 experimental values of $E(L_{\gamma}^+) - E(L_g^+)$ are plotted as a function of the angular momentum L for several series of isotopes. For all isotopes normalization to $E(2_{\gamma}^+) - E(2_g^+)$ has been used. The following observations can be made.

1) In most of the deformed nuclei reported in these figures, the “distance” between the gsb and the γ_1 band is decreasing, the actinides been a clear example.

2) Several examples of increasing “distance” are seen in the Os-Pt region, in which the O(6) symmetry is known to be present [9].

3) Increasing “distance” is also seen in a few nuclei (^{170}Er , ^{192}Os , ^{192}Pt , which are expected to be triaxial, based on the staggering behavior exhibited by their γ_1 bands [24].

4) No effort has been made to exclude levels which are obviously due to band-crossing, like the last point shown in ^{188}Pt .

It should be noticed at this point, that the odd-even staggering in γ_1 bands, defined as

$$\Delta E(L) = E(L) - \frac{E(L-1) + E(L+1)}{2}, \quad (3)$$

is also known to exhibit different behavior in various regions [23,24]. In particular, staggering of small magnitude is seen in most of the deformed nuclei in the rare earths and in the actinides region, while strong staggering is seen in the Xe-Ba-Ce region.

The present systematics of the energy differences between the gsb and the γ_1 band can be combined with the systematics of odd-even staggering in the γ_1 -bands, which should be calculated and compared to the data. Since the

sign in front of the three- or four-body term in the Hamiltonian has to be fixed in order to guarantee that the γ_1 band will lie above the gsb, the sign of the change of the “distance” between the γ_1 band and the gsb, as well as the form of the staggering within the γ_1 bands (minima at even L and maxima at odd L , or vice versa) are also be fixed by this choice, offering consistency checks of the symmetry.

Preliminary proxy-SU(3) predictions for four deformed nuclei, obtained with the Hamiltonian of Eq. (2) with the parameters of Table 1, are shown in Fig. 2 for the “distance” between the γ_1 band and the gsb. In all cases decrease is predicted. Notice that the slope of the theoretical curve is determined by the parameter ratio c/b , while the parameter b can be considered as a scale parameter for the energy differences under consideration. Parameters a and d do not influence these energy differences.

Results for the odd-even staggering within the γ_1 band for the same nuclei are shown in Fig. 3, in which the small energy scale should be noticed. In the results labeled “2-terms”, only the second and the third terms of Eq. (2) are taken into account, in analogy to Fig. 2, while in the results labeled “4-terms” all four terms of Eq. (2) are considered. It is seen that the two extra terms have little effect on the staggering quantity and certainly do not affect its overall shape, exhibiting minima at even values of L and maxima at odd values of L .

The spectra obtained for two of these nuclei are shown in Table 2. Details of the calculations will be given in a longer publication.

In a series of papers [26,27], Jolos and von Brentano have shown, based on experimental data, that different mass coefficients should be used in the Bohr Hamiltonian for the ground state band and the γ_1 band. In order to show this, they use Grodzins products [28] of excitation energies and B(E2) transition rates. The relation of the above findings to the work of Jolos and von Brentano should be considered in a next step, in which B(E2) transition rates will be included in the study.

Financial support by the Bulgarian National Science Fund (BNSF) under Contract No. KP-06-N28/6 is gratefully acknowledged.

Table 1. Parameters (in units of keV) of the Hamiltonian of Eq. (2) for four nuclei. Data were taken from Ref. [25]. L_g (L_{γ}) denotes the maximum angular momentum for the ground state band (γ -band) included in the fit.

nucleus	10^{-2} a	b	10^{-7} c	10^{-5} d	L_g	L_{γ}
^{162}Er	1443	408	440	1258	20	12
^{160}Dy	1025	445	578	412	28	23
^{166}Yb	540	483	2992	533	24	13
^{178}Hf	1225	588	748	890	20	15

Table 2. Spectra of ^{162}Er and ^{178}Hf in keV, taken from Ref. [25], fitted by the Hamiltonian of Eq. (2). The parameter values used are given in Table 1. The rms deviations in keV are 34 and 58 respectively.

L	^{162}Er	^{162}Er	^{178}Hf	^{178}Hf	L	^{162}Er	^{162}Er	^{178}Hf	^{178}Hf
	exp	th	exp	th		exp	th	exp	th
2	102	93	93	85	2	901	895	1175	1198
4	330	309	307	291	3	1002	987	1269	1282
6	667	640	632	615	4	1128	1107	1384	1372
8	1097	1073	1059	1044	5	1286	1259	1533	1529
10	1603	1588	1570	1566	6	1460	1428	1691	1651
12	2165	2162	2150	2161	7	1669	1638	1890	1876
14	2746	2766	2777	2809	8	1873	1846	2082	2038
16	3292	3364	3435	3484	9	2134	2107	2316	2295
18	3847	3920	4119	4157	10	2347	2344	2538	2519
20	4463	4388	4837	4795	11	2656	2647	2798	2782
22		4719		5361	12	2911	2901	3053	3073
24		4859		5814	13		3224	3336	3316
26					14		3488	3625	3680
28					15		3810	3928	3874

References

1. D. Bonatsos, I.E. Assimakis, N. Minkov, A. Martinou, R.B. Cakirli, R.F. Casten, and K. Blaum, Phys. Rev. C **95**, 064325 (2017)
2. D. Bonatsos, I.E. Assimakis, N. Minkov, A. Martinou, S. Sarantopoulou, R.B. Cakirli, R.F. Casten, and K. Blaum, Phys. Rev. C **95**, 064326 (2017)
3. I.E. Assimakis, D. Bonatsos, N. Minkov, A. Martinou, R.B. Cakirli, R.F. Casten, and K. Blaum, Bulg. J. Phys. **44**, 398 (2017)
4. D. Bonatsos, I.E. Assimakis, N. Minkov, A. Martinou, S.K. Peroulis, S. Sarantopoulou, R.B. Cakirli, R.F. Casten, and K. Blaum, Bulg. J. Phys. **44**, 385 (2017)
5. A. Martinou, D. Bonatsos, I.E. Assimakis, N. Minkov, S. Sarantopoulou, R.B. Cakirli, R.F. Casten, and K. Blaum, Bulg. J. Phys. **44**, 407 (2017)
6. S. Sarantopoulou, D. Bonatsos, I.E. Assimakis, N. Minkov, A. Martinou, R.B. Cakirli, R.F. Casten, and K. Blaum, Bulg. J. Phys. **44**, 417 (2017)
7. J. P. Elliott, Proc. Roy. Soc. Ser. A **245**, 128 (1958)
8. J. P. Elliott, Proc. Roy. Soc. Ser. A **245**, 562 (1958)
9. F. Iachello and A. Arima, *The Interacting Boson Model* (Cambridge University Press, Cambridge, 1987)
10. P. Van Isacker and J.-Q. Chen, Phys. Rev. C **24**, 684 (1981)
11. K. Heyde, P. Van Isacker, M. Waroquier, and J. Moreau, Phys. Rev. C **29**, 1420 (1984)
12. J.W.B. Hughes, J. Phys. A: Math., Nucl. Gen. **6**, 48 (1973)
13. J.W.B. Hughes, J. Phys. A: Math., Nucl. Gen. **6**, 281 (1973)
14. B.R. Judd, W. Miller, Jr., J. Patera, and P. Winternitz, J. Math. Phys. **15**, 1787 (1974)
15. H. De Meyer, G. Vanden Berghe, and J. Van der Jeugt, J. Math. Phys. **26**, 3109 (1985)
16. G. Vanden Berghe, H.E. De Meyer, and P. Van Isacker, Phys. Rev. C **32**, 1049 (1985)
17. J. Vanthournout, Phys. Rev. C **41**, 2380 (1990)
18. D. Bonatsos, Phys. Lett. B **200**, 1 (1988)
19. R. D. Ratna Raju, J. P. Draayer, and K. T. Hecht, Nucl. Phys. A **202**, 433 (1973)
20. J. P. Draayer, K. J. Weeks, and K. T. Hecht, Nucl. Phys. A **381**, 1 (1982)
21. J. P. Draayer and K. J. Weeks, Ann. Phys. (N.Y.) **156**, 41 (1984)
22. H.A. Naqvi and J.P. Draayer, Nucl. Phys. A **516**, 351 (1990)
23. N.V. Zamfir, and R.F. Casten, Phys. Lett. B **260**, 265 (1991)
24. E.A. McCutchan, D. Bonatsos, N.V. Zamfir, and R.F. Casten, Phys. Rev. C **76**, 024306 (2007)
25. Brookhaven National Laboratory ENSDF database <http://www.nndc.bnl.gov/ensdf/>
26. R. V. Jolos and P. von Brentano, Phys. Rev. C **74**, 064307 (2006)
27. R. V. Jolos and P. von Brentano, Phys. Rev. C **76**, 024309 (2007)
28. L. Grodzins, Phys. Lett. **2**, 88 (1962)

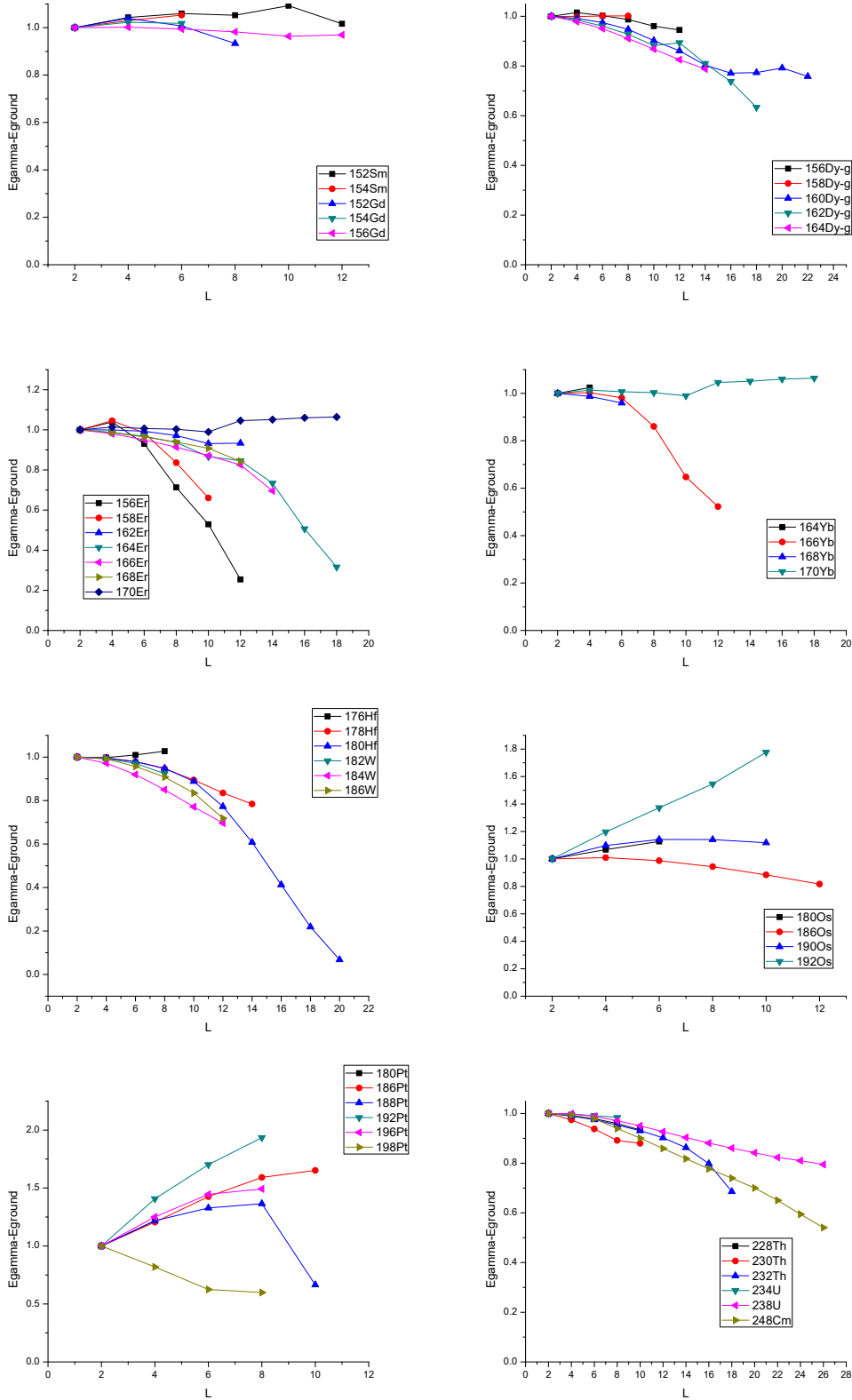


Fig. 1. Experimental values of $E(L_\gamma) - E(L_g)$, taken from Ref. [25], plotted as function of the angular momentum L for several series of isotopes. For all isotopes, normalization to $E(2_\gamma) - E(2_g)$ has been used.

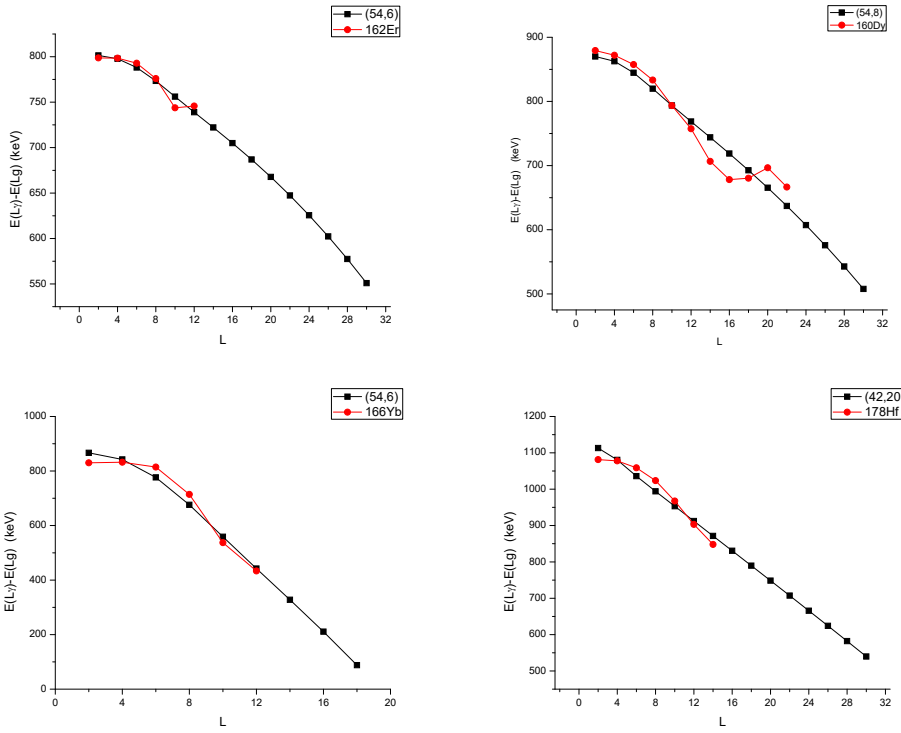


Fig. 2. Experimental values of $E(L_7) - E(L_g)$ [25] compared to proxy-SU(3) predictions from the Hamiltonian of Eq. (2) for four nuclei.

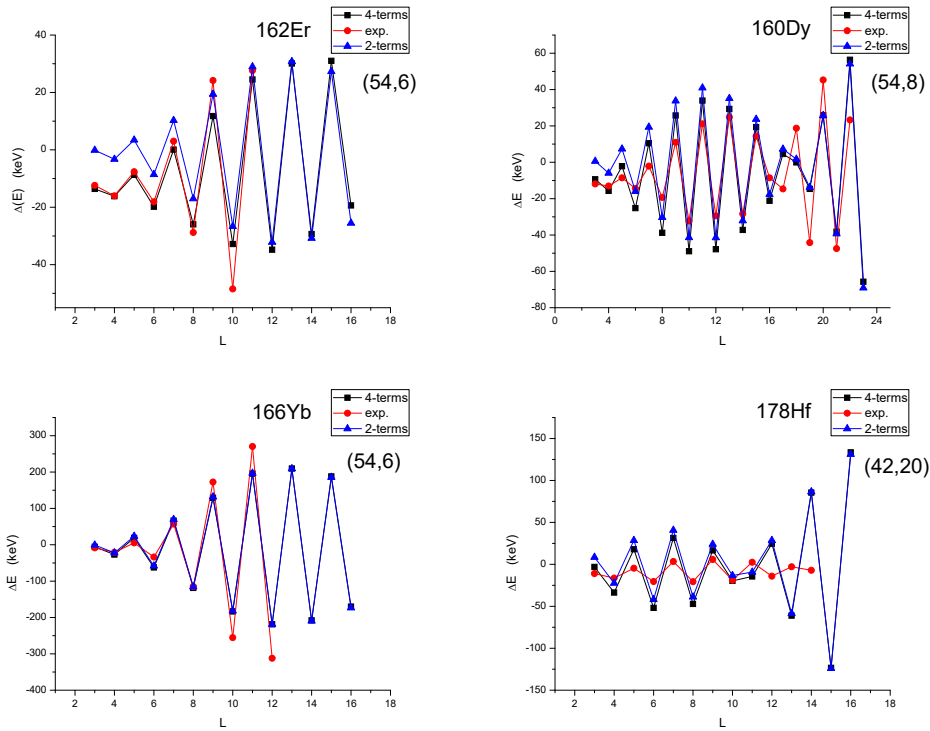


Fig. 3. Experimental values of odd-even staggering in the γ_1 bands, calculated from Eq. (3) using data from [25], compared to proxy-SU(3) predictions from the Hamiltonian of Eq. (2) for four nuclei.

Non-relativistic conformal symmetry in nuclear structure

Panagiotis E Georgoudis¹

¹Grand Accélérateur National d'Ions Lourds, CEA/IRFU, BP 55027, F-14076 Caen Cedex 5, France

The unitarity limit refers to infinite scattering length in a scattering problem of nucleons and manifests non-relativistic conformal symmetry [1]. A scheme is proposed [2] using group theoretical methods of the Interacting Boson Model [3] and techniques from Bose Einstein Condensates [4] for the introduction of the unitarity limit to nuclear collective states. In this talk I will present the $SO(2,1)$ conformal algebra along with some of its implications in nuclear structure and will discuss the scaling behavior of nuclear collective states at unitarity.

[1] T. Mehen, I. W. Stewart and M.B. Wise, Phys. Lett. B **474**, 145 (2000); D.T. Son, Phys. Rev. D **78**, 046003 (2008).

[2] P. E. Georgoudis, arXiv: 1903.05426, under review by the Physical Review Letters.

[3] F. Iachello and A. Arima (*The Interacting Boson Model*, Cambridge University Press, 1989).

[4] M. Randeria, W. Zwerger and M. Zwerlein in *BCS to BEC Crossover and the Unitary Fermi gas* (Springer-Verlag, Berlin, 2012), and references therein.

This work is funded by the European Union's H2020 program, Marie Skłodowska Curie Actions-Individual Fellowships, Grant Agreement No 793900 - GENESE 17.

Microscopic studies of fission dynamics based on energy density functionals

V. Prassa¹, H. Tao², J. Zhao^{3,4}, Z. P. Li², T. Nikšić⁴, and D. Vretenar⁴

¹ Department of Computer Science and Telecommunications, Faculty of Sciences, University of Thessaly, Greece

² School of Physical Science and Technology, Southwest University, China

³ Microsystem & Terahertz Research Center, China Academy of Engineering Physics, China

⁴ Physics Department, Faculty of Science, University of Zagreb, Croatia

Abstract. In this work we apply the self-consistent framework of relativistic energy density functionals (EDFs) and the corresponding collective Hamiltonian to an analysis of induced fission dynamics making use of a recent implementation of the time-dependent generator coordinate method in the Gaussian overlap approximation. Multidimensionally constrained mean-field calculations in the collective space based on the energy density functional PC-PK1 and a δ -force pairing, determine the potential energy surface of the fissioning nucleus, the scission line, the single-nucleon wave functions, energies, and occupation probabilities. A collective Schrödinger equation, determined entirely by the microscopic single-nucleon degrees of freedom, propagates adiabatically in time the initial wave packet built by boosting the ground-state solution of the collective Hamiltonian for ^{226}Th . The position of the scission line and the microscopic input for the collective Hamiltonian are analyzed as functions of the strength of the pairing interaction, as well as the effect of static pairing correlations on charge yields and total kinetic energy of fission fragments[1].

PACS. 24.75.+i, 25.85.Ec, 25.85.w Nuclear fission – 21.60.Jz Nuclear density functionals – 21.60.Ev Collective models – 27.90.+b A 220

1 Introduction

The theoretical description of nuclear fission remains one of the major challenges of quantum many-body dynamics. In order for fission to occur, nuclei have to overcome the fission barrier, which involves dissipative motion. The slow large-amplitude collective motion of the compound system that eventually leads to the formation of the final fragments can be described, in a first approximation, as an adiabatic process in which the intrinsic nucleonic degrees of freedom are decoupled from macroscopic collective degrees of freedom such as multipole moments (deformations) of the mass distribution and pairing fields [2, 3]. The spontaneous or induced fission process in which a heavy nucleus splits into fragments is out of reach for ab initio methods and, therefore, modern microscopic approaches are based on the framework of nuclear energy density functionals (NEDFs). Nuclear density functional theory (DFT) and its time-dependent (TD) generalization have enabled a self consistent treatment of both static and dynamic aspects of fission [4–12]. Numerous studies of spontaneous fission, based on NEDFs, have analyzed the effects of the choice of collective coordinates (shape degrees of freedom), approximations used to calculate the collective inertia, and coupling between shape and pairing degrees of freedom on fission half-lives [13–19]. A micro-

scopic approach capable of predicting both the low-energy collective excitation spectra in the deformed equilibrium minimum and the fission fragment distribution is the generator coordinate method (GCM). In the Gaussian overlap approximation (GOA) the GCM Hill-Wheeler equation reduces to a local Schrödinger-like equation in the space of collective coordinates. For a specific choice of collective coordinates, the essential inputs are the potential and inertia tensor that can be computed microscopically in a self-consistent mean-field deformation-constrained calculation. In particular, several recent studies have used the time-dependent generator coordinate method (TDGCM) [20] to compute the induced fission fragment charge and mass distributions [21, 25].

2 Theoretical framework

In the present study we consider the axial deformation parameters: quadrupole β_2 and octupole β_3 . A time-dependent Schrödinger-like equation describes low-energy fission dynamics, and this equation can be derived using the time dependent generator coordinate method (TDGCM) in the

Gaussian overlap approximation (GOA) [2,24]:

$$i\hbar \frac{\partial}{\partial t} g(\beta_2, \beta_3, t) = \left[-\frac{\hbar^2}{2} \sum_{kl} \frac{\partial}{\partial \beta_k} B_{kl}(\beta_2, \beta_3) \frac{\partial}{\partial \beta_l} + V(\beta_2, \beta_3) \right] \times g(\beta_2, \beta_3, t) \quad (1)$$

where $g(\beta_2, \beta_3, t)$ denotes the complex wave function of the collective variables (β_2, β_3) and time t . $V(\beta_2, \beta_3)$ and $B_{kl}(\beta_2, \beta_3)$ are the collective potential and mass tensor, respectively, and they completely determine the dynamics of the fission process in the TDGCM+GOA framework. These quantities will here be calculated in a self-consistent mean field approach based on relativistic energy density functionals. For the time-evolution we follow the method of Refs. [23,24] and make use of the software package FELIX [23] that solves the equations of the TDGCM in N dimensions under the Gaussian overlap approximation. From the Schrödinger-like Eq. (1) a continuity equation for the probability density $|g(\beta_2, \beta_3, t)|^2$ is obtained,

$$\frac{\partial}{\partial t} |g(\beta_2, \beta_3, t)|^2 = -\nabla \mathbf{J}(\beta_2, \beta_3, t) \quad (2)$$

where $\mathbf{J}(\beta_2, \beta_3, t)$ is the probability current defined by the relation:

$$\begin{aligned} J_k(\beta_2, \beta_3, t) &= \frac{\hbar}{2i} \sum_{l=2}^3 B_{kl}(\beta_2, \beta_3) \\ &\times \left[g^*(\beta_2, \beta_3, t) \frac{\partial g(\beta_2, \beta_3, t)}{\partial \beta_l} - g(\beta_2, \beta_3, t) \frac{\partial g^*(\beta_2, \beta_3, t)}{\partial \beta_l} \right] \end{aligned} \quad (3)$$

The collective space is divided into the inner region in which the nuclear density distribution is whole, and an external region that contains the two fission fragments. The set of scission configurations defines the hypersurface that separates the two regions. The flux of the probability current through this hypersurface provides a measure of the probability of observing a given pair of fragments at time t . For a surface element ξ on the scission hypersurface, the integrated flux $F(\xi, t)$ is defined as [23]:

$$F(\xi, t) = \int_{(t=0)}^t dt \int_{((\beta_2, \beta_3) \in \xi)} \mathbf{J}(\beta_2, \beta_3, t) d\mathbf{S} \quad (4)$$

For each scission point, (A_L, A_H) denote the masses of the lighter and heavier fragments, respectively. Therefore, the yield for the fission fragment with mass A can be defined by

$$Y(A) \propto \sum_{\xi \in A} \lim_{t \rightarrow \infty} F(\xi, t) \quad (5)$$

where A is the set of all elements ξ belonging to the scission hypersurface such that one of the fragments has mass A .

3 Results and Discussion

In this section we present the results of an illustrative study of induced fission of ^{226}Th , for which the charge

distribution of fission fragments exhibits a coexistence of symmetric and asymmetric peaks [26]. In the first step a large-scale deformation-constrained self-consistent RMF + BCS calculation is performed to generate the potential energy surface and single-nucleon wave functions in the (β_2, β_3) plane. The range of collective variables is $-0.83 - 6.01$ for β_2 with a step $\Delta\beta = 0.04$, and from $0.01 - 3.53$ for β_3 with a step $\Delta\beta_3 = 0.08$. The energy density functional PC-PK1 [27] is used for the effective interaction in the particle-hole channel, and a δ -force pairing with strengths parameters: $V_n = 360 \text{ MeV fm}^3$ and $V_p = 378 \text{ MeV fm}^3$ determined by the empirical pairing gap parameters of ^{226}Th , calculated using a five-point formula [28]. The self-consistent Dirac equation for the single-particle wave functions is solved by expanding the nucleon spinors in an axially deformed harmonic oscillator basis in cylindrical coordinates with 20 major shells. The computer code FELIX [23] is used for modeling the time evolution of the fissioning nucleus with a time step $\delta t = 5 \times 10^4$ zs. The parameters of the additional imaginary absorption potential that takes into account the escape of the collective wave packet in the domain outside the region of calculation [23] are: the absorption rate $r = 20 \times 10^{22} \text{ s}^{-1}$, and the width of the absorption band $w = 1.5$. The present RMF + BCS results for the potential energy surface (PES), scission line, and total kinetic energy of ^{226}Th can be compared to those obtained in Ref. [29] using the Hartree-Fock-Bogoliubov framework based on the Gogny D1S effective interaction. Figure 1 displays the self-consistent RMF+BCS quadrupole and octupole constrained energy surfaces, the static fission path, and density distributions for selected deformations along the fission path of ^{226}Th . The lowest minimum is located at $(\beta_2, \beta_3) \approx (0.20, 0.17)$, but is rather soft against octupole deformation. A triple-humped fission barrier is predicted along the static fission path, and the calculated heights are 7.10, 8.58, and 7.32 MeV from the inner to the outer barrier, respectively. At elongations $\beta_2 > 1.5$ a symmetric valley extends up to the scission point at $\beta_2 \approx 5.4$. The symmetric and asymmetric fission valleys are separated by a ridge from $(\beta_2, \beta_3) = (1.6, 0.0)$ to $(3.4, 1.0)$. One notices that the overall topography of the PES is similar to that calculated with the Gogny D1S interaction [29]. When describing fission in the $\beta_2 - \beta_3$ collective space, scission is characterized by a discontinuity between the two domains of pre-scissioned and post-scissioned configurations. Scission can be described using the Gaussian neck operator $Q_N = \exp[-(z - z_N)^2/a_N^2]$, where $a_N = 1 \text{ fm}$ and z_N is the position of the neck [30]. It is related to the number of particles in the neck, and here we follow the prescription of Ref. [24] to define the pre-scission domain by $\langle Q_N \rangle > 3$ and consider the frontier of this domain as the scission line. The total kinetic energy (TKE) for a particular pair of fragments can be evaluated from

$$E_{TKE} = \frac{e^2 Z_H Z_L}{d_{ch}} \quad (6)$$

where e is the proton charge, Z_H (Z_L) the charge of the heavy (light) fragment, and d_{ch} the distance between frag-

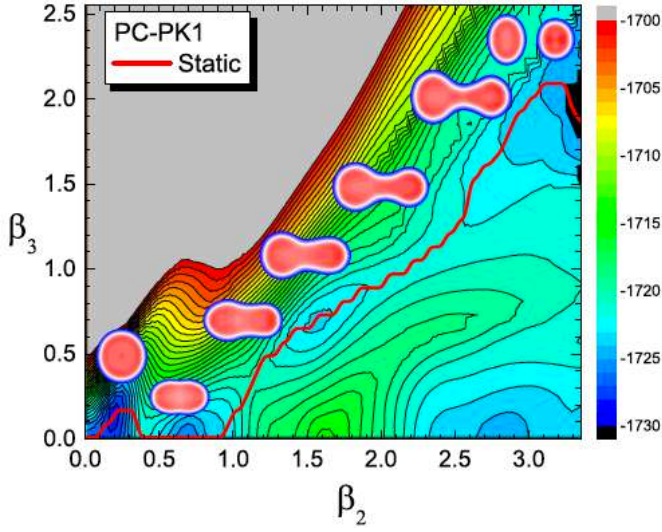


Fig. 1: Self-consistent RMF+BCS quadrupole and octupole constrained deformation energy surface (in MeV) of ^{226}Th in the $\beta_2 - \beta_3$ plane.

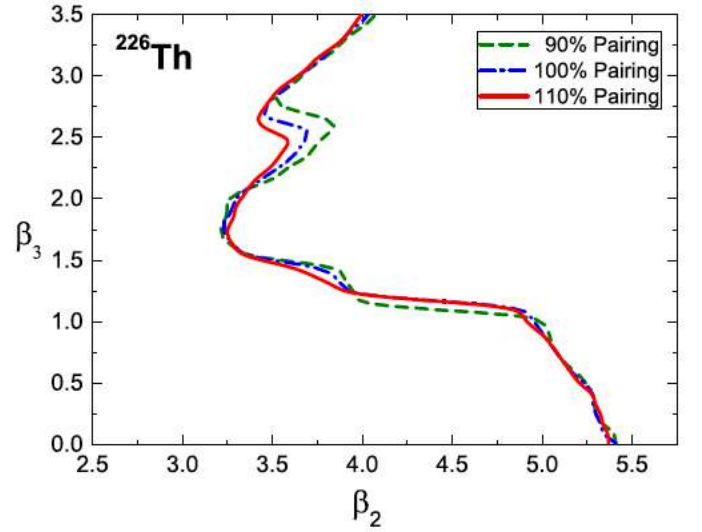


Fig. 3: The scission lines for ^{226}Th in the $\beta_2 - \beta_3$ plane, obtained in calculations with three different values of the pairing strength.

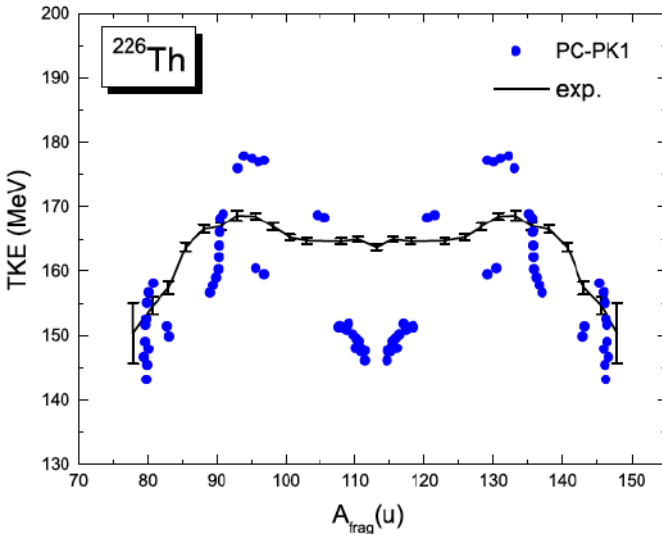


Fig. 2: The calculated total kinetic energy of the nascent fission fragments for ^{226}Th as a function of fragment mass, in comparison to the data [26].

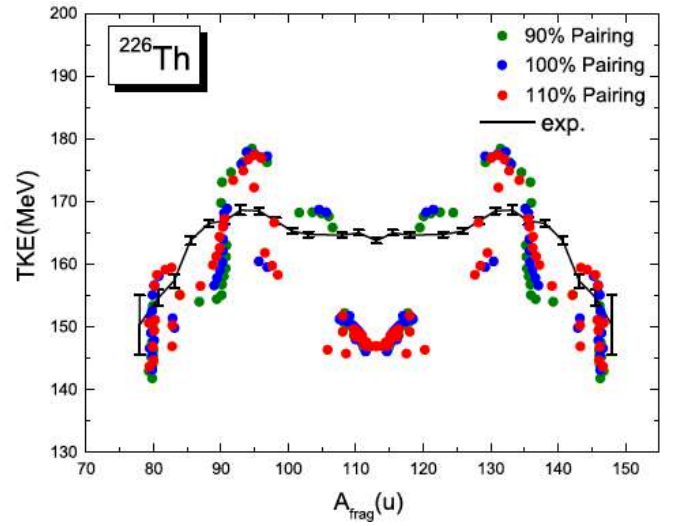


Fig. 4: Comparison between experimental and calculated total kinetic energy of nascent fission fragments for ^{226}Th , as a function of fragment mass and pairing strength

ment centers of charge at scission. Figure 2 displays the calculated total kinetic energies of the nascent fission fragments for ^{226}Th as a function of fragment mass. For comparison, the data obtained in photoinduced fission measurement [26] are also included in the figure. One notices that the theoretical results qualitatively reproduce the trend of the data, in particular the maxima for $A_{frag} \approx 132$ and $A_{frag} \approx 94$. On a quantitative level the calculation exhibits more structure when compared to experiment. This may be due to the fact that the experimental values correspond to an excitation energy of the fissioning nucleus of the order of 11 MeV, whereas formula (6) is valid only for low-energy fission. As it is well known,

the kinetic energy distribution is generally smoothed out as the fission energy increases. In particular, the kinetic energy in the symmetric mass region increases [31], which explains why experimental TKEs display only a very shallow minimum for $A_{frag} = A/2$. We note that the present theoretical results are consistent with those obtained using the Gogny D1S effective interaction in Ref. [29]. Figures 3 and 4 display the scission lines in the $\beta_2 - \beta_3$ plane and the TKEs of nascent fission fragments of ^{226}Th , respectively, for three different values of the pairing strength. The pattern of the scission line does not change significantly, except at the bending points and, overall, a smoother contour is obtained for stronger pairing. We also note that

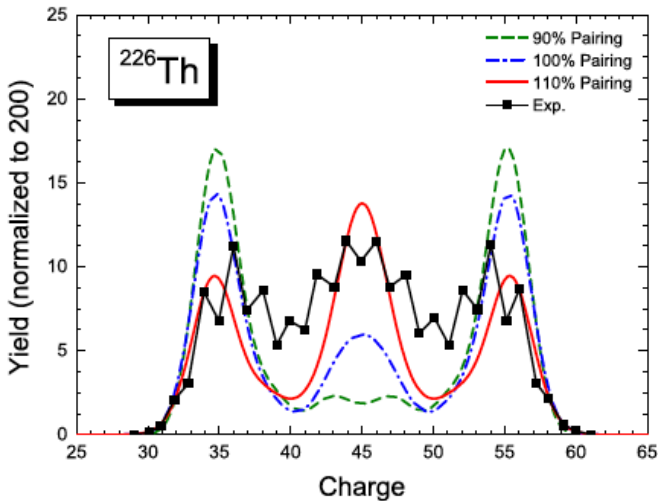


Fig. 5: Preneutron emission charge yields for photoinduced fission of ^{226}Th . The results of calculations for three different values of the pairing strength are compared to the data [26].

the scission points on the static fission path for three values of the pairing strength are very close to each other, at $(\beta_2, \beta_3) \approx (3.3, 2.0)$. This result differs from that in ^{240}Pu calculated using the HFB method with the Skyrme functional SkM [32], where the quadrupole deformation β_2 at the scission point changes by as much as ≈ 0.65 when the original pairing strength is varied from 90% to 110%. Since the TKEs in the present study are fully determined by the scission configurations, varying the pairing strength does not lead to marked differences in the TKE distribution. In Fig. 5 we compare the charge yields, obtained with three different pairing strengths, to the data for photoinduced fission of ^{226}Th . Following the procedure of Ref. [24], the initial state is prepared by boosting the collective ground state in the direction of increasing axial quadrupole deformation. The amplitude of the boost is determined so that the average energy of the initial state is ≈ 1 MeV above the corresponding asymmetric fission barrier B_{II}^{asy} of the collective potential energy surface. The calculation reproduces the trend of the data, except that obviously the model cannot describe the odd-even staggering of the experimental charge yields. For weak pairing correlations, that is, at 90% of the original pairing strength, the yields are dominated by asymmetric fission with peaks at $Z = 35$ and $Z = 55$. A broad peak corresponding to symmetric fission is also predicted but is too low compared to data. This is because the asymmetric fission barrier B_{II}^{asy} is ≈ 6 MeV lower than the symmetric one B_{II}^{sym} . The asymmetric peaks are reduced and the symmetric peak enhanced as pairing correlations increase, and we find that the data are best reproduced by a pairing strength between 100% and 110% of the original parameters. This can be attributed to a reduction of the ridge between asymmetric and symmetric fission valleys when increasing the pairing strength. Another important effect is that the wavelength becomes longer because of smaller collective masses for stronger

pairing, and this enhances the collective current in the symmetric fission valley beyond $\beta_2 > 2.5$.

4 Conclusions

The dynamics of induced fission of ^{226}Th has been analyzed in a theoretical framework based on covariant energy density functionals and the corresponding collective Hamiltonian, making use of a recently developed numerical implementation of the time-dependent generator coordinate method plus Gaussian overlap approximation [23]. The potential energy surface, scission line, and total kinetic energies have been calculated using the multidimensionally constrained relativistic mean-field model based on the energy density functional PC-PK1, and with pairing correlations taken into account in the BCS approximation. The fission process is described in a two-dimensional axially symmetric collective space (β_2, β_3) . We note that the overall topography of the PES, the total kinetic energies for a particular pair of fragments, and the general pattern of the scission line are consistent with previous studies based on the Gogny effective interaction [29, 30]. The TDGCM+GOA calculation reproduces the main characteristics of the fission charge and mass distributions, thus confirming the main conclusion of the analysis presented in Ref. [24]. In this study we have analyzed the influence of ground-state pairing on the preneutron emission charge yields. The increase of static pairing correlations reduces the asymmetric peaks and enhances the symmetric peak in charge yields distribution. Therefore a very interesting topic for future studies is dynamic pairing correlation in induced fission, possibly through the inclusion of pairing degrees of freedom in the space of TDGCM+GOA collective coordinates.

This research was conducted within the Call Fellowship for Postdoctoral research implemented by the University of Thessaly and funded by the Stavros Niarchos Foundation.

References

1. Jie Zhao, et al., Phys. Rev. C **99** 014618 (2019).
2. N. Schunck and L. M. Robledo, Rep. Prog. Phys. **79**, 116301 (2016).
3. Hans J. Krappe and K. Pomorski, **Theory of Nuclear Fission** (Springer-Verlag, Berlin, 2012).
4. G. Scamps, C. Simenel, and D. Lacroix, Phys. Rev. C **92**, 011602(R) (2015).
5. C. Simenel and A. S. Umar, Phys. Rev. C **89**, 031601(R) (2014).
6. P. Goddard, P. Stevenson, and A. Rios, Phys. Rev. C **92**, 054610 (2015).
7. B. Avez, C. Simenel, and P. Chomaz, Phys. Rev. C **78**, 044318 (2008).
8. A. Bulgac, P. Magierski, K. J. Roche, and I. Stetcu, Phys. Rev. Lett. **116**, 122504 (2016).
9. P. Goddard, P. Stevenson, and A. Rios, Phys. Rev. C **93**, 014620 (2016).

10. Y. Tanimura, D. Lacroix, and S. Ayik, *Phys. Rev. Lett.* **118**, 152501 (2017).
11. T. Nakatsukasa, K. Matsuyanagi, M. Matsuo, K. Yabana, *Rev. Mod. Phys.* **88**, 045004 (2016).
12. S. A. Giuliani, L.M. Robledo, and R. Rodriguez-Guzman, *Phys. Rev. C* **90**, 054311 (2014).
13. C. R. Chinn, J.-F. Berger, D. Gogny, and M. S. Weiss, *Phys. Rev. C* **45**, 1700 (1992).
14. A. Staszczak, A. Baran, and W. Nazarewicz, *Phys. Rev. C* **87**, 024320 (2013).
15. M. Warda and J. L. Egidio, *Phys. Rev. C* **86**, 014322 (2012).
16. J. W. Negele, *Rev. Mod. Phys.* **54**, 913 (1982).
17. J. Sadhukhan, et al., *Phys. Rev. C* **88**, 064314 (2013).
18. J. Sadhukhan, et al., *Phys. Rev. C* **90**, 061304 (2014).
19. R. Smolanczuk, J. Skalski, and A. Sobieczewski, *Phys. Rev. C* **52**, 1871 (1995).
20. J. F. Berger, M. Girod, and D. Gogny, *Comput. Phys. Commun.* **63**, 365 (1991).
21. H. Goutte, J. F. Berger, P. Casoli, and D. Gogny, *Phys. Rev. C* **71**, 024316 (2005).
22. W. Younes and D. Gogny, Lawrence Livermore National Laboratory Report No. LLNL-TR-586678, 2012 (unpublished).
23. D. Regnier, M. Verrire, N. Dubray, and N. Schunck, *Comput. Phys. Commun.* **200**, 350 (2016).
24. D. Regnier, N. Dubray, N. Schunck, and M. Verrire, *Phys. Rev. C* **93**, 054611 (2016).
25. A. Zdeb, A. Dobrowolski, and M. Warda, *Phys. Rev. C* **95**, 054608 (2017).
26. K.-H. Schmidt, et al., *Nucl. Phys. A* **665**, 221 (2001).
27. P. W. Zhao, Z. P. Li, J. M. Yao, and J. Meng, *Phys. Rev. C* **82**, 054319 (2010).
28. M. Bender, K. Rutz, P.-G. Reinhard, and J. A. Maruhn, *Eur. Phys. J. A* **8**, 59 (2000).
29. N. Dubray, H. Goutte, and J.-P. Delaroche, *Phys. Rev. C* **77**, 014310 (2008).
30. W. Younes and D. Gogny, *Phys. Rev. C* **80**, 054313 (2009).
31. S. Pomm, et al., *Nucl. Phys. A* **572**, 237 (1994).
32. N. Schunck, D. Duke, H. Carr, and A. Knoll, *Phys. Rev. C* **90**, 054305 (2014).

Two quasiparticle k-isomers within the covariant density functional theory

Konstantinos E Karakatsanis¹, G. A. Lalazissis¹, and P. Ring³

¹ Department of physics, Aristotle University of Thessaloniki, Thessaloniki GR-54124, Greece

² Department of physics, Technical University of Munich, Garching D-85747, Germany

Abstract. Relativistic density functionals provide a powerful phenomenological way to study nuclear structure phenomena. They have been mostly used in describing bulk nuclear properties of ground states and have been also very successful in the description of collective excitations. Nuclear excitations that form due to the inherent structure of nuclei and have a relatively long half-life are called isomers. They play a significant role in recent experimental and theoretical studies of nuclei far from stability, in nuclear fission and in the process of nucleosynthesis relative to astrophysics. In this study we concentrate on the single particle excitations of high K -level isomers that appear mainly at nuclei with well defined axial deformation. We employ the blocking effect to create two quasiparticle states within the relativistic hartree-Bogoliubov framework. We use the Equal filling approximation that respects the time-reversal symmetry breaking caused by blocking. We concentrate our interest in medium mass axially deformed nuclei where there have been several experimentally observed K -level isomers and we can compare directly our results.

PACS. PACS-key describing text of that key – PACS-key describing text of that key

1 Introduction

Nuclear isomers are metastable states of nuclei with half-lives 100 to 1000 times longer than normally excited states. As nuclear excited states, they can decay through γ -emission, β -decay, electron conversion, α -decay or fission. In general, for cases where the nuclear matrix elements of the transition operator are connected with large changes of particular quantum numbers, the corresponding direct decay to the ground state is significantly hindered.

K -isomers are a special case of such excitations. They occur in well deformed heavy nuclei where the angular momentum quantum number K along the symmetry axis plays an important role. More specifically, they are formed as configurations of multi-particle or multi-quasiparticle excitations with high K -values. The direct decay to the $K = 0$ ground state involves a large change in K and violates the K -selection rule $\Delta K \leq \lambda$. The actual de-excitation follows an alternative path through the rotational bands by an $E1$ or $M1$ transition and depending on the energy levels of the rotational states this leads to a metastable excited state.

The study of isomers in general, has been an active field of research for many decades. It is a wide subject related to nuclear structure phenomena as well as nuclear reactions. Recent reviews include: the list of all isomers with half-lives greater than 10 ns by Jain *et al* [1]; The connection of shape coexistence and shape isomers by Heyde and Wood [2]; the compilation of high- K isomers with

mass number $A > 100$ by Kondev *et al* [3]; the discussion by Walker and Xu [5] on K -isomers in rotational nuclei; The comprehensive review by Dracoulis *et al* on high-spin isomers for $A > 150$ [4]; The summary of recent experimental efforts studying K -isomers in superheavy nuclei by Ackermann and Theisen [6,7]; and the most recent historical outline of nuclear isomer research by Walker and Podolyák [8].

The first theoretical efforts to study isomeric states as multi-quasiparticle states in nuclei were based on the Nilsson model [9], with improvements including pairing through the BCS method [10,11], blocking [12,13] and residual interactions between quasiparticles [14,15]. This model proved to be very successful in the description of multi-quasiparticle states in well deformed nuclei [12,16–18]. With the acknowledgment that configuration dependence is important [19], the Nilsson-Strutinsky approach [20] was extended into configuration-constrained energy surfaces calculations of multi-quasiparticle nuclear states [21–28]. For more details on the historical evolution of these approaches and their extended application to K -isomers with rotational degrees of freedom, ref. [5] offers a great review. A recent application of the above, has been reported in [29] where the cranked shell model with particle number conservation has been employed for the study of 2-quasiparticle states in even-even Nd and Sm isotopes. Additionally the self-consistent mean field model with Skyrme functionals [30–36] and the Gogny interac-

tion [37–39] has been used for similar studies. Finally, the covariant density functional approach has also been applied for the investigation of two-quasiparticle excitations in transactinide nuclei in Ref. [40].

The present work focuses on the study of K -isomers, which arise as multi-quasiparticle excitations of the nuclear ground state. High- K isomers in well deformed axially symmetric even-even nuclei with $A > 100$ are investigated within the self-consistent Relativistic-Hartree-Bogoliubov (RHB) framework using the blocking approximation [41]. We focus on nuclei with well established K -isomers in the region of Hf-, Er- isotopes ($A \approx 180$) [43,44], where there has been great experimental effort to study their existence [3].

2 Isomer formation

K -isomers are a special case of single particle, low lying, nuclear excitations. They appear in many well deformed heavy nuclei, where the projection Ω on the symmetry axis of the total angular momentum J is a good quantum number. Their formation originates by the fact that orbitals with high values of total angular momentum j come closer to the Fermi surface. Thus, with a minimal amount of energy which is roughly equal as the energy required to break the required number of nucleon pairs, it is possible to create excited states of two or more quasiparticles, involving configurations of such orbitals. So formally, if we have a combination of n -quasiparticles the resulting nucleus is one of the 2^{n-1} multiplet excited states, with the total K and parity, determined by the combination of the individual quasiparticle orbitals as follows

$$K = |\pm K_1 \pm K_2 \pm \dots \pm K_n|, \quad \pi = \prod_i^n \pi_i \quad (1)$$

Typically among those states the one with the highest value of K , $K = \sum_i |K_i|$ has the lowest energy and is the best candidate for an actual K -isomer.

In order to study k -isomer excitations we use the blocking effect on the Hartree-Bogoliubov framework to create multi-quasiparticle states starting from the ground state $|\Phi_0\rangle$ of a system under investigation. As we have already stated, this ground state is defined as the quasiparticle vacuum i.e.

$$\alpha_k |\Phi_0\rangle = 0 \quad \text{for } E_k > 0 \quad \text{or} \quad |\Phi_0\rangle = \prod_{E_k > 0} \alpha_k |-\rangle, \quad (2)$$

where $|-\rangle$ is the bare vacuum of the configuration space defined by the original single particles. If $|\Phi_0\rangle$ describes an even system as is usually the case, one can study the neighbouring odd system by constructing a one quasiparticle state $|\Phi_1\rangle$,

$$|\Phi_1\rangle = \alpha_1^\dagger |\Phi_0\rangle = \alpha_1^\dagger \prod_k \alpha_k |-\rangle \quad (3)$$

by choosing to block the quasi-particle state with the lowest energy, which corresponds to the operator α_1^\dagger .

The same procedure can be extended for the low lying excitations of the system by constructing for example, two quasi-particle states,

$$|\Phi_2\rangle = \alpha_1^\dagger \alpha_2^\dagger |\Phi_0\rangle \quad (4)$$

Now, this new state is the vacuum of the set of quasiparticle operators $(\alpha'_1, \alpha'_2, \dots, \alpha'_N)$ where N is the dimension of the quasiparticle space with

$$\alpha'_1 = \alpha_1^\dagger, \alpha'_2 = \alpha_2^\dagger, \dots, \alpha'_N = \alpha_N. \quad (5)$$

This way a new quasiparticle basis is formed defined by the set of operators $(\alpha'_1, \dots, \alpha'_N, \alpha_1^\dagger, \dots, \alpha_N^\dagger)$, with the exchange of operators $\alpha_1^\dagger \leftrightarrow \alpha_1, \alpha_2^\dagger \leftrightarrow \alpha_2$. The operators α_1^\dagger and α_2^\dagger correspond to the quasi-particle states with the lowest energy, or in the single particle basis to the states that are closer to the Fermi surface. In other words, in order to study the lowest lying excitation applying the blocking effect, we have exchanged the annihilation operators α_1, α_2 with the corresponding creation operators $\alpha_1^\dagger, \alpha_2^\dagger$.

The solution of the RHB equations for the ground state of even-even nuclei is simplified by the time-reversal symmetry since no currents exist in that case and only the time-like components of the four vectors of the meson fields and the densities contribute in the equations of motion. This also implies that states with the same K value but opposite signs are degenerate and that the solution of the RHB equations can be solved only for the $+K$ subspace of the system and for each k block separately, significantly reducing the computational effort.

Now, in our case, where we construct two or more quasiparticle configurations by blocking certain quasiparticle states of different k -blocks in the $+k$ subspace, by definition, we block at the same time their conjugate states in the $-k$ subspace. The particular nucleon pair is broken and we have to remove its contribution from the pairing tensor. Furthermore, time-reversal symmetry is also broken and the degeneracy between states with opposite signs of k is removed. Thus, we have to solve the RHB equations additionally for the corresponding $-k$ block and to include currents in the formation of the meson fields. This is actually done **to some extent** in [40] where they studied the formation of two quasi-particle isomers in the transactinide nuclei close to $N = 162$. In the results of that investigation one can see that for a given two quasiparticle configuration one gets two slightly different excitation energies depending on whether the total K value corresponds to $K_{max} = K_1 + K_2$ or $K_{min} = |K_1 - K_2|$. One can also observe the fact that configurations with the K_{max} value always have lower energy than those with K_{min} , in agreement with the rule we mentioned above.

However, in the present study, our primary goal is to evaluate the description of K isomers within the RHB/CDFT, by comparing our theoretical results with well established experimental examples. Since the energy difference in [40] amongst the states with K_{max} and K_{min} is relatively small and around 0.1 MeV, we follow a different approach and conserve time-reversal symmetry for

the multi quasi-particle states we construct. This is done within the Equal Filling Approximation (EFA), which has been applied within the Skyrme HFB and in [34], where they studied one-quasiparticle states in the rare earth-region, it was shown that EFA is a reasonable approximation and it is actually equivalent with the actual blocking procedure when the time-odd fields are not taken into account. Practically, this means that in each step, we average the density matrix ρ and symmetrize the pairing tensor κ for the K subspaces where blocking takes place and replaced them by the equations

$$\rho' = \rho_{M \times M} + \frac{1}{2}(U_{k_b} U_{k_b}^{*T} - V_{k_b}^* V_{k_b}^T), \quad (6)$$

$$\kappa' = \kappa_{M \times M} - \frac{1}{2}(U_{k_b} V_{k_b}^{*T} + V_{k_b}^* U_{k_b}^T), \quad (7)$$

where U_{k_b} and V_{k_b} correspond to the bogoliubov coefficients U and V of the blocked quasiparticle level.

3 Results

In our calculation the 2qp-states are determined by blocking the lowest neutron or proton quasi-particle orbitals located in the vicinity of the Fermi energy that corresponds to the fully paired ground state solution. After performing the iterative minimization, the energy of the two-quasiparticle excitation is obtained as the difference between the energy of the self-consistent blocked RHB solution and the energy of the fully paired equilibrium minimum.

3.1 The 6^+ isomer in Hf isotopes and in $N = 104$ isotones

In this section, we present the systematics of the 6^+ high- K isomeric state in the even-even Hf isotopes with neutron number $98 \leq N \leq 108$ and in the $N = 104$ isotones with atomic number $68 \leq Z \leq 84$. The two-quasiparticle (2qp) configurations that form a 6^+ isomer are: $\nu 5/2^- [512] \otimes \nu 7/2^- [514]$ and $\nu 5/2^+ [642] \otimes \nu 7/2^+ [633]$ for neutrons and $\pi 5/2^+ [402] \otimes \pi 7/2^+ [404]$ for protons. This is in line with the configuration assignment given in Refs. [43, 4] and in the nuclear data table [3] for the six isotopes $^{170-180}\text{Hf}$ and the isotones $N = 104$ from ^{172}Er to ^{180}Os .

3.1.1 Hf isotopes

The formation of isomers in well deformed nuclei occurs when nucleons fill high- K orbitals coming close to the Fermi surface and the projections of their total angular momentum can couple to a large total value K , parallel to the symmetry axis. The excitation energy is roughly equal to the energy cost of breaking the respective pairs or equivalently equal to the sum of the quasiparticle energies E_k , i.e.

$$E^* \approx \sum_k \sqrt{(\epsilon_k - \lambda)^2 + \Delta_k^2} = \sum_k E_k \quad (8)$$

where $\epsilon_k = h_{k,k}$ and $\Delta_k = \Delta_{k,-k}$ are the single-particle energy and the pairing gap in the canonical basis. λ is the Fermi energy. Therefore the position of the lowest quasi-particle orbitals in the ground state of each nucleus under consideration provides information about the possible formation of low-energy two quasiparticle states.

In Fig. 1 we show the position of the quasiparticle states with energy less than 3 MeV for neutrons (Fig. 1a) and protons (Fig. 1b) in the even-even $^{170-180}\text{Hf}$ isotopes calculated with the relativistic density functional DD-ME2. In the neutron spectrum of Fig. 1a we see that the Fermi surface moves to higher energies with increasing neutron number. Here the neutron high- j orbitals that are candidates to form a low-lying 6^+ state are the 2qp configurations: $\nu 5/2^+ [642] \otimes \nu 7/2^+ [633]$ and $\nu 5/2^- [512] \otimes \nu 7/2^- [514]$. The relative energy difference $|\epsilon_k - \lambda|$ of the two orbitals $\nu 5/2^+ [642]$ and $\nu 7/2^+ [633]$ forming a 6^+ state increases gradually with neutron number and thus the sum of the two quasiparticle energies $\sum E_k$ of that state will increase. The relative position of the neutron orbitals $\nu 5/2^- [512]$ and $\nu 7/2^- [514]$ that create an alternative 6^+ isomer displays a different pattern. For the isotopes of $^{170-176}\text{Hf}$ their relative energy difference decreases gradually while around $^{178-180}\text{Hf}$ an abrupt raise shows up.

Fig. 2 displays the interplay between the excitation energies of these two quasineutron configurations $\nu 5/2^+ [642] \otimes \nu 7/2^+ [633]$ (black line) and $\nu 5/2^- [512] \otimes \nu 7/2^- [514]$ (red line). As we observe the $\nu 5/2^+ [642] \otimes \nu 7/2^+ [633]$ configuration is the lowest lying 2qp state for the isotopes of ^{170}Hf and ^{172}Hf with excitation energy ≈ 1.9 and 1.7 MeV respectively, while in ^{174}Hf and ^{176}Hf the favoured configuration is $\nu 5/2^- [512] \otimes \nu 7/2^- [514]$ with energies 1.5 and 1 MeV, respectively. In ^{178}Hf and ^{180}Hf both neutron configurations are predicted at excitation energies higher than 4 MeV. For these isotopes the favored 6^+ configuration predicted by our model appears to be a 2qp-state formed by two protons, as discuss below.

In Fig. 1b we show the structure of the proton quasi-particle spectrum for the $^{170-180}\text{Hf}$ isotopes. Since the number of protons is constant the relative position of the Fermi surface remains almost unchanged. Here the lowest lying 6^+ two quasiproton state corresponds to the configuration $\pi 5/2^+ [402] \otimes \pi 7/2^+ [404]$ as shown in Fig. 2 (green line). The excitation energy of the 6^+ occurs at around 2.6 – 2.7 MeV in all the isotopes $^{170-180}\text{Hf}$ under consideration.

In Fig. 3 the predictions of the lowest lying 6^+ 2qp states in $^{170-180}\text{Hf}$ isotopes are compared to data. Purple dots correspond to the DD-ME2 functional with EFA, filled turquoise squares to the DD-PC1 functional with EFA and open turquoise squares to the calculation with the DD-PC1 functional allowing for breaking of time reversal symmetry. The data taken from Refs. [43, 3] are shown as black crosses. In $^{170-172}\text{Hf}$ isotopes the predicted excitation energies correspond to the two quasineutron configuration $\nu 5/2^+ [642] \otimes \nu 7/2^+ [633]$, in $^{174-176}\text{Hf}$ to $\nu 5/2^- [512] \otimes \nu 7/2^- [514]$ and in $^{178-180}\text{Hf}$ to the two quasiproton configuration $\pi 5/2^+ [402] \otimes \pi 7/2^+ [404]$. We observe that the trend of the theoretical predictions repro-

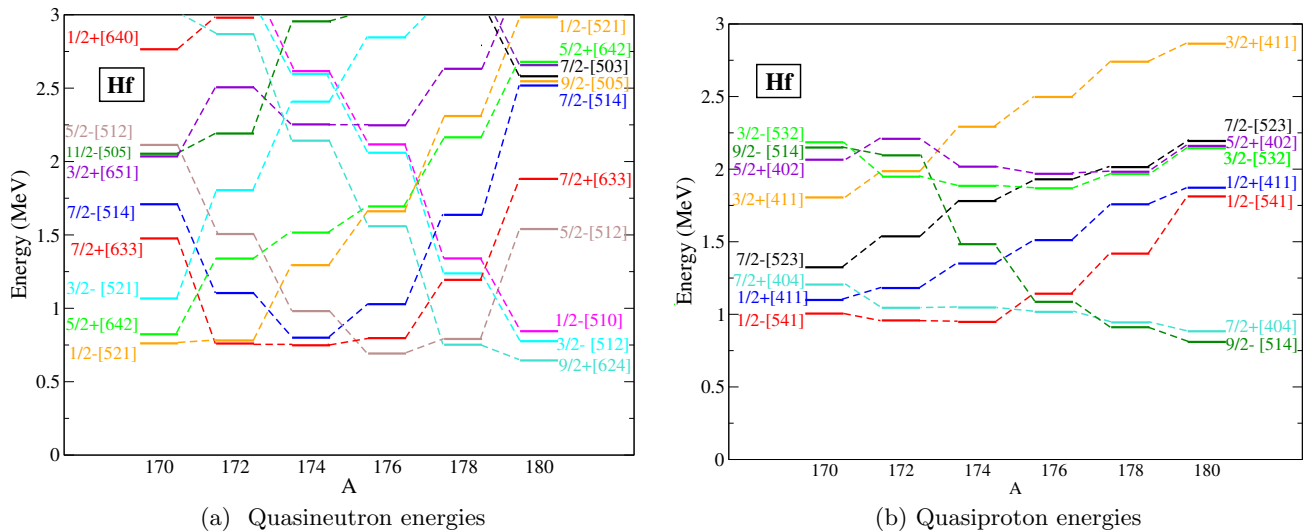


Fig. 1: Quasiparticle energies in even-even Hf isotopes with neutron number $170 \leq A \leq 180$ obtained with the relativistic functional DD-ME2 and the separable pairing force TMR

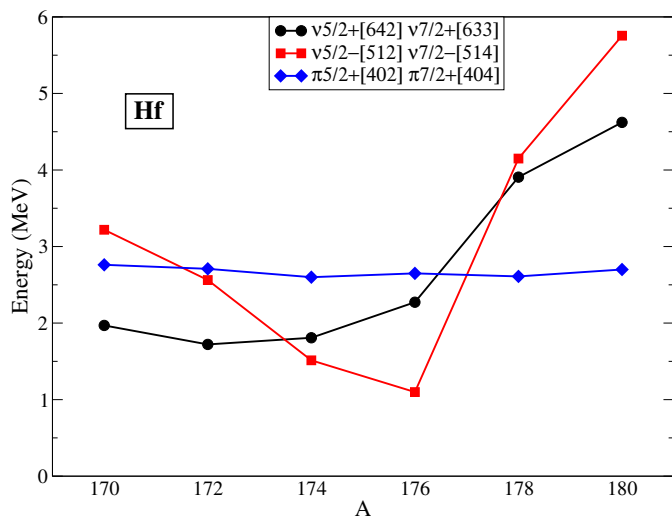


Fig. 2: Excitation energies of the 6^+ 2qp states coming from the configurations $\nu 5/2^+[642] \otimes \nu 7/2^+[633]$ (black dots), $\nu 5/2^-[512] \otimes \nu 7/2^-[514]$ (red squares), and $\pi 5/2^+[402] \otimes \pi 7/2^+[404]$ (green diamonds) in the $170-180$ Hf isotopes calculated with the relativistic functional DD-ME2 and the separable TRM pairing force.

duces the data. Quantitatively, the two functionals give similar results, with the DD-PC1 functional predicting slightly higher excitation energies for $170-176$ Hf and slightly lower values for $178-180$ Hf. The inclusion of currents leads, in each isotope, to a decreasing of the excitation energy by roughly 0.3 MeV. The predicted excitation energies that correspond to the two quasineutron configuration reproduce more accurately the experimental data. In the $178-180$ Hf isotopes where the lowest-lying 6^+ state originates from the two quasiproton configuration the difference between our theoretical calculations and the ex-

Table 1: 6^+ excitation energy in $170-180$ Hf calculated with the relativistic functionals DD-ME2 (first column), DD-PC1 (second column) and DD-PC1 with time-reversal symmetry breaking (third column). In all cases the separable pairing force TMR has been used. Experimental data [43,3] are given in column four.

	DD-ME2	DD-PC1	DD-PC1 + currents	Expt.
170 Hf	1.969	2.061	1.827	1.773
172 Hf	1.721	1.855	1.629	1.685
174 Hf	1.513	1.579	1.279	1.549
176 Hf	1.099	1.151	0.855	1.594
178 Hf	2.610	2.579	2.239	1.554
180 Hf	2.700	2.647	2.318	1.703

perimental assignments is approximately 1 MeV. Table 1 includes the predictions of the lowest lying 6^+ isomeric states in comparison with data. The first column contains the calculations with the DD-ME2 functional, in the second column are calculations with the DD-PC1 and in the third column are calculations with the DD-PC1 functional and with the inclusion of time reversal symmetry breaking. In the last column the experimental data are shown.

3.1.2 $N = 104$ isotones

In this section the formation of the 6^+ high- K isomer is studied in the five even-even $N = 104$ isotones with $68 \leq Z \leq 76$. The dominant high- j orbitals from which this 2qp state originates are $\nu 5/2^-[512]$ and $\nu 7/2^-[514]$. In Fig. 4 we show the quasiparticle energies up to 3 MeV of the neutron orbitals in the $N = 104$ isotones with $172 \leq A \leq 180$ calculated with the DD-ME2 functional. The relative energy difference between the two orbitals

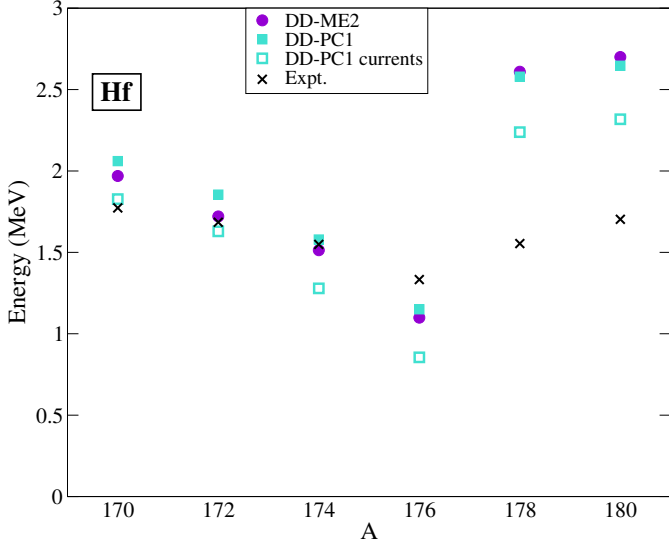


Fig. 3: Excitation energy of the 6^+ 2qp states in $^{170-180}\text{Hf}$ isotopes obtained with the relativistic functionals DD-ME2 (purple dots) and DD-PC1 (turquoise squares) and the separable pairing force TMR. Results with the inclusion of currents using the DD-PC1 functional are shown in turquoise open squares. Calculations are compared to the data [43,3].

increases gradually from 1.2 to 1.7 MeV. Fig. 5 displays the evolution of the excitation energy for the 6^+ high- K isomer in the $N = 104$ isotones with $172 \leq A \leq 180$. Purple dots correspond to the DD-ME2 functional, filled turquoise squares to the DD-PC1 functional and open turquoise squares to calculation with the DD-PC1 functional with the inclusion of time reversal symmetry breaking. The data taken from Refs. [43,3] are shown as black crosses. We observe that qualitatively we reproduce the trend of the data with the exception of ^{176}Hf where the data exhibit a downward kink, probably because of the strong mixing with an alternative two quasiproton 6^+ state as suggested in Ref. [43]. Calculations with the DD-ME2 functional reproduce better the data except from ^{176}Hf where the DD-PC1 functional gives a better prediction. Predictions with the inclusion of time reversal symmetry breaking lead to a constant decrease of roughly 0.3 MeV in the excitation energies of all isotones in the chain.

Table 2 includes the predictions of the excitation energy of the 6^+ state in the $N = 104$ isotones with $172 \leq A \leq 180$. The first column contains the calculations with the DD-ME2 functional, in the second column are calculations with the DD-PC1 and in the fourth column are calculations with the DD-PC1 functional and with the inclusion of time reversal symmetry breaking. In the last column the experimental data are shown.

Table 2: Same as Table 1 for the 6^+ excitation energy formed by the $\nu 5/2^- [512] \otimes \nu 7/2^- [514]$ 2qp configuration in $N = 104$ isotones with $172 \leq A \leq 180$.

	DD-ME2	DD-PC1	DD-PC1 currents	Expt.
172 Er	0.821	0.401	0.116	1.5
174 Yb	0.913	0.479	0.194	1.518
176 Hf	1.099	1.151	0.855	1.594
178 W	1.123	0.872	0.573	1.665
180 Os	1.308	1.046	0.744	1.878

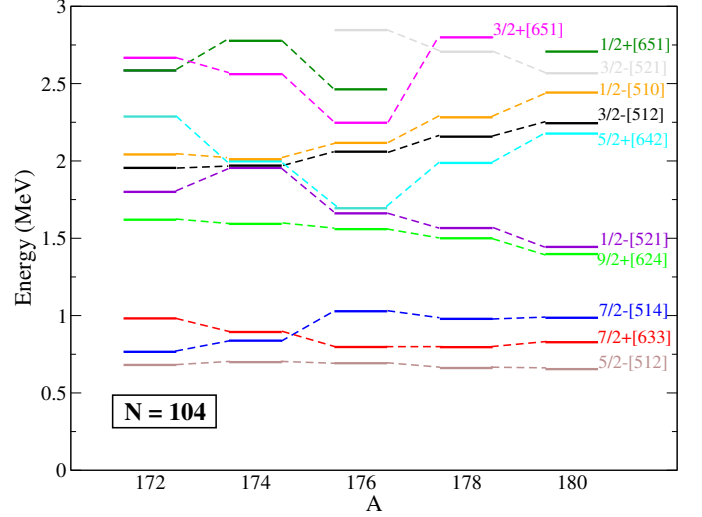


Fig. 4: Same as Fig. 1a but for $N = 104$ isotones with $172 \leq A \leq 180$.

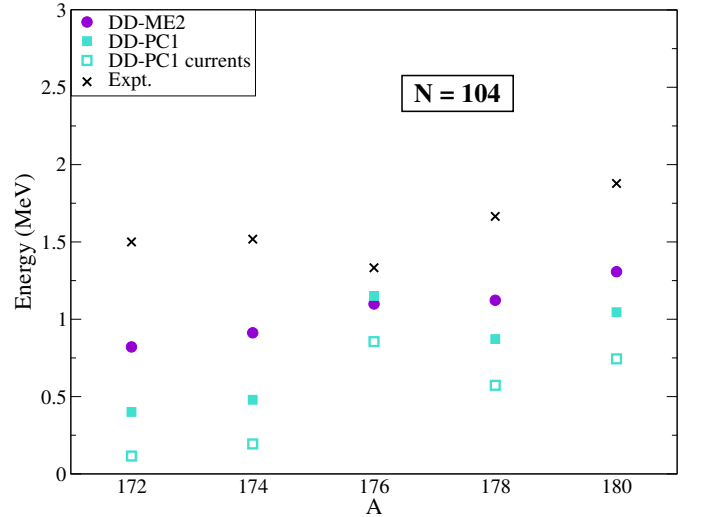


Fig. 5: Same as Fig. 2 but for $N = 104$ isotones with $172 \leq A \leq 180$.

3.2 8^- isomer in Hf isotopes and in $N=106$ isotones

3.2.1 Hf isotopes

Another case of a systematically occurring high- K isomer is the 8^- two quasiparticle excitation that has been

observed experimentally (see Ref. [3]) in the $^{170-184}\text{Hf}$ isotopes. This particular isomer originates from the two quasiproton configuration: $\pi 9/2^- [514] \otimes \pi 7/2^+ [404]$.

Fig. 6 is the same as Fig. 1b, but extended up to ^{186}Hf , to include the neutron quasiparticle energies of all nuclei in which an 8^- isomer occurs. We observe that the $\pi 9/2^- [514]$ orbital (dark green line) has a relatively high quasiparticle energy at nearly 2.3 MeV in ^{170}Hf . In the subsequent isotopes the orbital approaches the Fermi level, and eventually becomes the lowest quasiparticle state in ^{178}Hf up to ^{186}Hf . The second orbital of the configuration $\pi 7/2^+ [404]$ (turquoise line) has a very low quasiparticle energy throughout the isotopic chain, exhibiting only a slight decrease from the initial value of 1.4 MeV in ^{170}Hf .

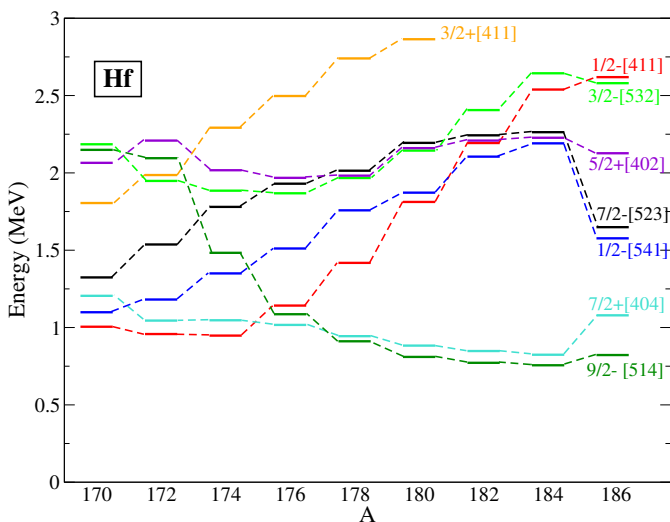


Fig. 6: Same as Fig. 1b but for the isotopic chain $^{170-186}\text{Hf}$.

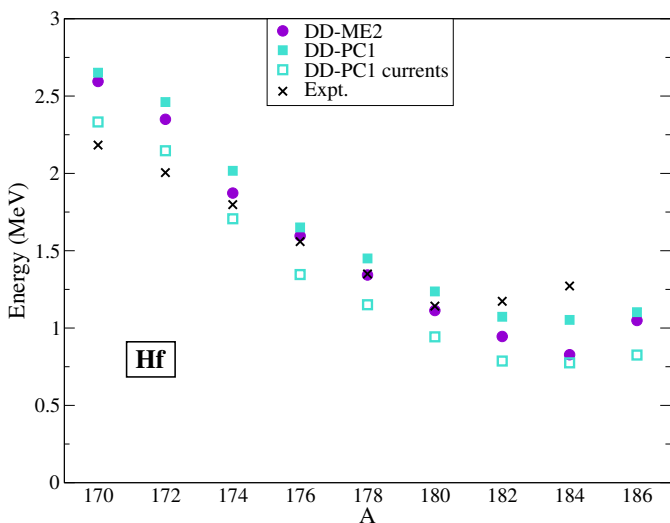


Fig. 7: Same as Fig. 2 but for the 8^- 2qp states in the isotopic chain $^{170-186}\text{Hf}$.

Applying the blocking approximation to the two quasineutron states we can examine how the energy of the 8^- isomer evolves along the isotopic chain. Table 3 includes the predicted excitation energy for each isotope calculated with the functionals DD-ME2 and DD-PC1 and compared to experimental data [3]. In Fig. 7 the results of Table 3 are schematically presented.

Table 3: Same as Table 1 for the excitation energy of the 8^- 2qp state formed by the configurations $\pi 9/2^- [514] \otimes \pi 7/2^+ [404]$ in the isotopic chain $^{170-186}\text{Hf}$.

	DD-ME2	DD-PC1	DD-PC1 currents	Expt.
^{170}Hf	2.595	2.651	2.333	2.183
^{172}Hf	2.350	2.461	2.146	2.005
^{174}Hf	1.873	2.017	1.707	1.798
^{176}Hf	1.596	1.651	1.346	1.559
^{178}Hf	1.343	1.450	1.151	1.350
^{180}Hf	1.113	1.237	0.943	1.142
^{182}Hf	0.945	1.073	0.787	1.173
^{184}Hf	0.827	1.053	0.775	1.272
^{186}Hf	1.049	1.103	0.826	-

Comparing the results in Fig. 7 with the neutron quasiparticle energies in Fig. 6 the predicted excitation energy of the 8^- 2qp state follows the trend of the two neutron orbitals $\pi 9/2^- [514]$ and $\pi 7/2^+ [404]$ which also explains the evolution of the experimentally observed excitation energies. The experimentally observed excitation energies start at 2.183 MeV for ^{170}Hf and decrease linearly losing about 0.2 MeV at each subsequent isotope, until ^{180}Hf where they reach a minimum and then increase for the two last nuclei ^{184}Hf and ^{186}Hf . Our calculations predict the 8^- excitation energy at around ≈ 2.5 MeV in ^{170}Hf and gradually lose energy approaching the data. The difference is that the minimum appears in ^{184}Hf and not in ^{180}Hf as in the experiment. The result in ^{186}Hf was included to show that the ^{184}Hf is the theoretical minimum. The two functionals give similar results and the inclusion of currents has the same effect of giving 0.3 MeV lower energy.

3.2.2 N=106 isotones

In this section the 8^- isomeric state in the $N = 106$ isotones with atomic number $68 \leq Z \leq 82$ is studied. In this isotonic chain not all nuclei are axially deformed, since ^{184}Pt is a transitional nucleus, ^{186}Hg exhibits oblate-prolate shape coexistence and ^{188}Pb is a rather neutron-deficient nucleus. Nevertheless, an 8^- isomer was experimentally observed in Ref. [43]. The configuration of the two neutron orbitals that create the particular isomer is: $\nu 7/2^- [514] \otimes \nu 9/2^+ [624]$.

In Fig. 8 the quasiparticle energies of the neutron orbitals with energies less than 3 MeV in the $N = 106$ isotones from Er to Pb calculated with the DD-ME2 functional are presented. The $\nu 7/2^- [514]$ orbital corresponds

to the orange line and the $\nu 9/2^+[624]$ to the turquoise one. We observe that the relative energy difference of the two orbitals is constantly increasing with proton number from Er to Os (with the exception of ^{176}Yb where the energy is almost the same as in ^{174}Er) and then remains stable from Pt to Pb.

In Fig. 9 and Table 4, the predictions of our model for the 8^- excitation energy in the above mentioned isotonic chain are presented in comparison to data. We observe that our theoretical calculations reproduce qualitatively the behavior of the data from ^{174}Er to ^{182}Os which are indeed the axially symmetric nuclei of the chain. However, quantitatively our calculations overpredict the data by about 0.8 – 1 MeV. The calculated excitation energy is ≈ 1.9 MeV in ^{174}Er and increases to 2.3 – 2.4 MeV in ^{182}Os . For the last three nuclei (Pt to Pb) the predicted excitation energy remains almost unchanged, in contrast to the experimental values. The predictions between the DD-ME2 and the DD-PC1 functionals are equivalent, while the inclusion of currents affects all the calculated energies by 0.3 MeV.

Table 4: Same as Table 1 for the 8^- excitation energy formed by $\nu 7/2^- [514] \otimes \nu 9/2^+ [624]$ 2qp configuration in $N = 106$ isotones with $172 \leq A \leq 188$.

	DD-ME2	DD-PC1	DD-PC1 currents	Expt.
174 Er	1.891	1.851	1.575	1.112
176 Yb	1.862	1.863	1.589	1.050
178 Hf	2.213	2.123	1.845	1.350
180 W	2.391	2.215	1.935	1.529
182 Os	2.422	2.252	1.971	1.831
184 Pt	2.380	2.302	2.020	1.839
186 Hg	2.405	2.378	2.096	2.217
188 Pb	2.431	2.418	2.137	2.578

4 Overview and conclusions

In this study, we have used the self-consistent mean field approach within the Relativistic Hartree-Bogoliubov framework based on relativistic energy density functionals, to calculate the two-quasiparticle excitations in heavy nuclei with axially deformed shapes. Throughout this work we used the meson exchange functional DD-ME2 and the point coupling functional DD-PC1, both with density depended coupling constants. Well-established experimental data of the systematic appearance of 6^+ and 8^- low-energy high- K isomers, in the region of Er to Pb ($68 \leq Z \leq 84$, $98 \leq N \leq 112$) and in nuclei with $A \approx 160 - 190$, were used for the evaluation of our method. The theoretical calculation of the corresponding excitation energies is based on the blocking approximation. The application of this approximation in the theoretical framework is implemented in two different ways. Firstly, the time-reversal symmetry of the unblocked state is preserved by

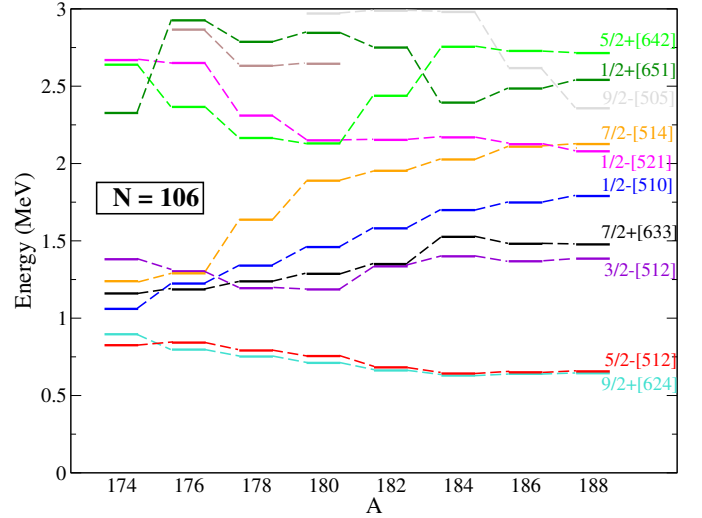


Fig. 8: Same as Fig. 4 but for $N = 106$ isotones with $174 \leq A \leq 188$.

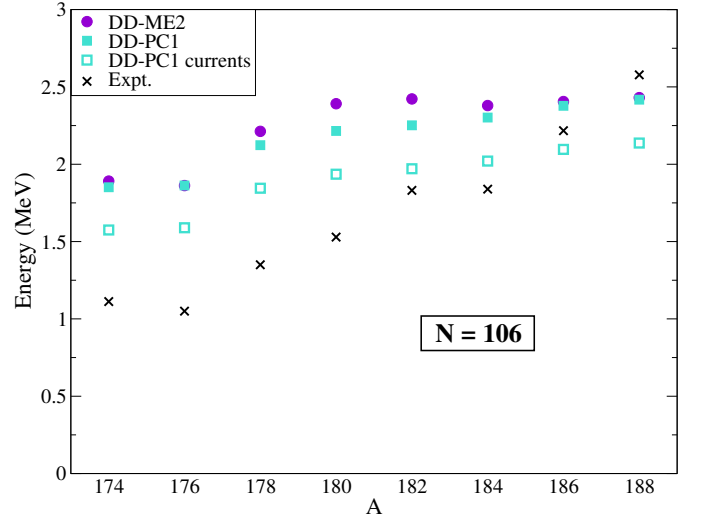


Fig. 9: Same as Fig. 7 but for $N = 106$ isotones with $174 \leq A \leq 188$.

the equal filling approximation (EFA). Second, the time-reversal symmetry is broken and the induced currents coming from the unpaired, blocked nucleons are taken into account in the calculation of the fields.

As a first step, using calculations with a quadrupole-constraint, we constructed Nilsson diagrams within the canonical basis of the RHB framework for the case of ^{176}Hf . We were thus able to demonstrate that in axially deformed nuclei in the region of interest, several neutron and proton orbitals with high- K values come close to the Fermi surface.

Satisfying this basic property our next step was to examine the effect of pairing correlations using the 6^+ and 8^- 2qp states in ^{176}Hf as a test case. It was shown that as the pairing strength increases so does the excitation energy. This is expected since the amount of energy needed

to break a pair of nucleons is larger for stronger pairing. This result shows that one could use the strength of pairing to fine tune the calculation of the excitation energy in order to reproduce the experimental data in a better way. However, in this work, the strength of the TMR separable pairing force was always set to its default value.

In the main part of this study, our microscopic self-consistent approach, provides a good qualitative description of the systematic appearance of the 6^+ and 8^- high- K isomers in the nuclear chains under consideration. This is true for both DD-ME2 and DD-PC1 functionals since they show equivalent results. The detailed examination of the underlying quasiparticle structure demonstrates its importance in the resulting excitation energy of high- K isomers. More specifically, the fact that the isomer energy is, to a first approximation, equal to the sum of the individual quasiparticle energies, provides an explanation of the trend followed by the experimental values in each nuclear chain. In addition, the 2qp configuration assignment for the creation of the specific isomers also agrees with the assignment given by other models, with few exceptions in the Hf isotopes.

On a quantitative level our results reproduce well the experimental values of the excitation energies in most cases. It is important to note that for the DD-PC1 functional, the full blocking scheme with the inclusion of currents via the breaking of time-reversal symmetry, provides a standard effect in the final excitation energies. Namely, in all cases it gives an extra binding of about 0.3 MeV in the 2qp state lowering by the same amount the corresponding excitation energy.

For a future work one could consider the inclusion of correlations beyond the mean field, that might provide a better qualitative description. An example could be the particle-vibration coupling that has been shown to provide a better picture of the single particle structure around the Fermi surface in spherical nuclei [70,69]. A more ambitious task is to develop a method of calculating the lifetimes of the proposed isomers by analyzing the rotational spectra of the nuclear ground states and finding possible de-excitation paths. Finally, the fact that in the case of $N = 106$ isotones, high- K isomers exist in the last four nuclei that are transitional or shape coexisting shows an interesting connection. A further theoretical examination can be achieved in our framework, by using multi-dimensional constraint calculations and investigating the energy surface of both ground and 2-quasiparticle states.

5 acknowledgments

This research was funded by the Greek State Scholarship Foundation (IKY), through the program “IKY Fellowships of excellence for postgraduate studies in Greece-SIEMENS program”, and by the DFG cluster of excellence “Origins” (www.origins-cluster.de). Important assistance has been provided by the it center of Aristotle University of Thessaloniki for accessing the computational hub of HellasGrid.

References

1. A. K. Jain, B. Maheshwari, S. Garg, M. Patial, and B. Singh, Nucl. Data Sheets **128**, 1 (2015).
2. K. Heyde and J. L. Wood, Rev. Mod. Phys. **52**, 725 (2011).
3. F. G. Kondev, G. D. Dracoulis, and T. Kibedi, At. Data Nucl. Data Tables **50**, 103 (2015).
4. G. D. Dracoulis, P. M. Walker, and F. G. Kondev, Rep. Prog. Phys. **79**, 076301 (2016).
5. P. M. Walker and F. R. Xu, Phys. Scr. **91**, 013010 (2016).
6. D. Ackermann, Nucl. Phys. A **944**, 736 (2015).
7. D. Ackermann and C. Theisen, Phys. Scr. **92**, 083002 (2017).
8. P. M. Walker and Z. Podolyák, Phys. Scr. **95** 044004 (2020).
9. S. G. Nilsson, Mat. Fys. Medd. Dan. Vid. Selsk. **29**, No. 16 (1955).
10. A. Bohr, B. R. Mottelson and D. Pines, Phys. Rev **110**, 936 (1958).
11. S. T. Belyaev and K. Dan, Vidensk. Selsk. Mat. Fys. Medd. **31**, 11 (1959).
12. K. Jain, O. Burglin, G. D. Dracoulis, B. Fabricius, N. Rowley and P. M. Walker, Nucl. Phys. A **591**, 61 (1995).
13. G. D. Dracoulis, P. M. Walker and F. G. Kondev, Phys. Lett. B **419**, 7 (1998).
14. C. J. Gallagher and S. A. Moszkowski, Phys. Rev. **111**, 1282 (1958).
15. C. J. Gallagher, Phys. Rev. **126**, 1525 (1962).
16. K. Jain, P. M. Walker, N. Rowley, Phys. Lett. B **322**, 27 (1994).
17. F. G. Kondev, G. D. Dracoulis, A. P. Byrne, T. Kibeédi, and S. Bayer, Nucl. Phys. A **617**, 97 (1997).
18. F. R. Xu, P. M. Walker, J. A. Sheikh, and R. Wyss, Phys. Lett. B **435**, 257 (1998).
19. W. Nazarewicz, M. Riley, and J. Garrett, Nucl. Phys. A **512**, 61 (1990).
20. V. M. Strutinsky, Nucl. Phys. A **95**, 420 (1967).
21. F. R. Xu, and P. M. Walker, Phys. Rev. C **60**, 051301 (1999).
22. F. R. Xu, P. M. Walker and R. Wyss, Phys. Rev. C **62**, 014301 (2000).
23. F. R. Xu, E. G. Zhao, R. Wyss and P. M. Walker, Phys. Rev. Lett. C **92**, 252501 (2004).
24. H. L. Liu, F. R. Xu, S. W. Xu, R. Wyss, and P. M. Walker, Phys. Rev. C **76**, 034313 (2007).
25. H. L. Liu, F. R. Xu, P. M. Walker, and C. A. Bertulani, Phys. Rev. C **83**, 011303(R) (2011).
26. H. L. Liu, F. R. Xu, P. M. Walker, and C. A. Bertulani, Phys. Rev. C **83**, 067303 (2011).
27. H. L. Liu and F. R. Xu, Phys. Rev. C **87**, 067304 (2013).
28. H. L. Liu, P. M. Walker, and F. R. Xu, Phys. Rev. C **89**, 044304 (2014).
29. Z.-H. Zhang, Phys. Rev. C **98**, 034304 (2018).
30. S. Ćwiok, J. Dobaczewski, P.-H. Heenen, P. Magierski, and W. Nazarewicz, Nucl. Phys. A **611**, 211 (1996).
31. S. Ćwiok, W. Nazarewicz, and P. H. Heenen, Phys. Rev. Lett. **83**, 1108 (1999).
32. T. Duguet, P. Bonche, and P.-H. Heenen, Nucl. Phys. A **679**, 427 (2001).
33. M. Bender, P. Bonche, T. Duguet, and P.-H. Heenen, Nucl. Phys. A **723**, 354 (2003).
34. N. Schunck, J. Dobaczewski, J. McDonnell, J. Moré, W. Nazarewicz, J. Sarich, and M. V. Stoitsov, Phys. Rev. C **81**, 024316 (2010).

35. M. Bender and P.-H. Heenen, *J. Phys. Conf. Ser.* (2013).
36. Y. Shi, J. Dobaczewski, and P. T. Greenlees, *Phys. Rev. C* **89**, 034309 (2014).
37. J. L. Egido and L. M. Robledo, *Phys. Rev. Lett.* **85**, 1198 (2000).
38. J.-P. Delaroche, M. Girod, H. Goutte, and J. Libert, *Nucl. Phys. A* **771**, 103 (2006).
39. M. Warda and J. L. Egido, *Phys. Rev. C* **86**, 014322 (2012).
40. V. Prassa, B.-N. Lu, T. Nikšić, D. Ackermann, and D. Vretenar, *Phys. Rev. C* **91**, 034324 (2015).
41. P. Ring and P. Schuck, *The Nuclear Many-Body Problem* (Springer-Verlag, Berlin, 1980).
42. G. Audi, F. G. Kondev, Meng Wang, W. J. Huang and S. Naimi, *Chin. Phys. C* **41**, No 3, 030001, (2017).
43. G. D. Dracoulis, G. J. Lane, F. G. Kondev, A. P. Byrne, R. O. Hughes, P. Nieminen, H. Watanabe, M. P. Carpenter, R. V. F. Janssens, T. Lauritsen, D. Seweryniak, S. Zhu, P. Chowdhury, and F. R. Xu, *Phys. Lett. B* **635**, 200 (2006).
44. S. K. Tandel, P. Chowdhury, F. G. Kondev, R. V. F. Janssens, T. L. Khoo, M. P. Carpenter, T. Lauritsen, C. J. Lister, D. Seweryniak, S. Zhu, A. Deacon, S. J. Freeman, N. J. Hammond, G. D. Jones, E. F. Moore, and J. F. Smith, *Phys. Rev. C* **94**, 064304 (2016).
45. B. D. Serot and J. D. Walecka, *Adv. Nucl. Phys.* **16**, 1 (1986).
46. P. Ring, D. Vretenar, and B. Podobnik, *Nucl. Phys. A* **598**, 107 (1996).
47. D. Vretenar, A. V. Afanasjev, G. A. Lalazissis, and P. Ring, *Phys. Rep.* **409**, 101 (2005).
48. *Lecture Notes in Physics*, edited by G. A. Lalazissis, P. Ring, and D. Vretenar (Springer-Verlag, Heidelberg, 2004), Vol. 641.
49. T. D. Cohen, R. J. Furnstahl, and D. K. Griegel, *Phys. Rev. Lett.* **67**, 961 (1991).
50. A. V. Afanasjev and P. Ring, *Phys. Rev. C* **62**, 031302(R) (2000).
51. U. Hofmann and P. Ring, *Phys. Lett. B* **214**, 307 (1988).
52. S. H. Shen, H. Z. Liang, W. H. Long, J. Meng, and P. Ring, *Prog. Part. Nucl. Phys.* **109**, 103713 (2019).
53. G. A. Lalazissis, T. Nikšić, D. Vretenar, and P. Ring, *Phys. Rev. C* **71**, 024312 (2005).
54. T. Nikšić, D. Vretenar, and P. Ring, *Phys. Rev. C* **78**, 034318 (2008).
55. P. W. Zhao, Z. P. Li, J. M. Yao, and J. Meng, *Phys. Rev. C* **82**, 054319 (2010).
56. T. Gonzalez-Llarena, J. Egido, G. Lalazissis, and P. Ring, *Phys. Lett. B* **379**, 13 (1996).
57. Y. Tian, Z. Y. Ma, and P. Ring, *Phys. Lett. B* **676**, 44 (2009).
58. Y. Tian, Z. Y. Ma, and P. Ring, *Phys. Rev. C* **80**, 024313 (2009).
59. H. Kucharek and P. Ring, *Z. Phys. A* **339**, 23 (1991).
60. T. Nikšić, N. Paar, D. Vretenar, and P. Ring, *Comp. Phys. Comm.* **185**, 1808 (2014).
61. L. Li, J. Meng, P. Ring, E.-G. Zhao, and S.-G. Zhou, *Chin. Phys. Lett.* **29**, 042101 (2012).
62. S. Perez-Martin and L. M. Robledo, *Phys. Rev. C* **78**, 014304 (2008).
63. W. Koepf and P. Ring, *Nucl. Phys. A* **511**, 279 (1990).
64. J. König and P. Ring, *Phys. Rev. Lett.* **71**, 3079 (1993).
65. A. V. Afanasjev, J. König, and P. Ring, *Phys. Rev. C* **60**, 051303(R) (1999).
66. A. Afanasjev, P. Ring, and J. König, *Nucl. Phys. A* **676**, 196 (2000).
67. A. V. Afanasjev, T. L. Khoo, S. Frauendorf, G. A. Lalazissis, and I. Ahmad, *Phys. Rev. C* **67**, 024309 (2003).
68. M. Bender, K. Rutz, P. G. Reinhard, J. A. Maruhn, and W. Greiner, *Phys. Rev. C* **60**, 034304 (1999).
69. K. Karakatsanis, G. A. Lalazissis, P. Ring, and E. Litvinova, *Phys. Rev. C* **95**, 034318 (2017).
70. E. Litvinova and P. Ring, *Phys. Rev. C* **73**, 044328 (2006).
71. E. V. Litvinova and A. V. Afanasjev, *Phys. Rev. C* **84**, 014305 (2011).
72. M. Serra and P. Ring, *Phys. Rev. C* **65**, 064324 (2002).
73. J. F. Berger, M. Girod, and D. Gogny, *Nucl. Phys. A* **428**, 23 (1984).
74. J. F. Berger, M. Girod, and D. Gogny, *Comp. Phys. Comm.* **63**, 365 (1991).
75. S. E. Agbemava, A. V. Afanasjev, D. Ray, and P. Ring, *Phys. Rev. C* **89**, 054320 (2014).
76. A. V. Afanasjev, T. L. Khoo, S. Frauendorf, G. A. Lalazissis, and I. Ahmad, *Phys. Rev. C* **2003**, 024309 (2003).

Relativistic Equations of State for hot matter and neutron star dynamics

A. Chorozidou¹ and T. Gaitanos¹

¹ Department of Physics, Aristotle University of Thessaloniki

Abstract. Compressed hadronic matter is studied in the framework of the Non-Linear Derivative (NLD) model. NLD model accounts for the momentum dependence of relativistic mean-fields. It is covariantly and thermodynamically-consistently formulated and it is shown that it is compatible with results from microscopic nuclear matter calculations and with Dirac phenomenology. It also reproduces the correct behaviour of the proton-nucleus potential as proton energy increases. Moreover, predictions of NLD approach are presented for hot matter, something important for both nuclear experimental (FAIR@GSI) and astrophysical (dynamic neutron star binary systems) purposes.

Key words. Equation of State, optical potential, hot matter

1 Introduction

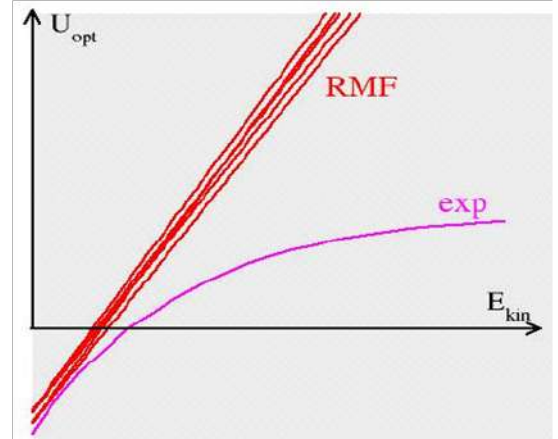
The theoretical physicists attempt to describe compressed nuclear matter is becoming more and more intense, as data from Heavy Ion Collisions may be available and the same time Neutron Stars have already started to give us invaluable information about high density nuclear matter.

In order to describe nuclear matter, one can start with the well-established Relativistic Hydrodynamics (RHD) and take the Relativistic Mean-Field approximation (RMF). In RMF approximation the meson field operators are replaced by their ground state expectation values, which are classical fields. Taking the standard RHD Lagrangian in RMF approximation, the nucleon self-energies become simple functions of density only and do not depend on momentum of the nucleon explicitly. Therefore the Schrödinger-equivalent optical potential, which is energy dependent (as a consequence of relativistic description), depends linearly on energy and at high energies does not agree with Dirac phenomenology (Figure 1). In order to solve this issue, we introduce the Non-linear derivative (NLD) model, where the nucleon self-energies depend not only on density, but explicitly on momentum of the nucleon [1]. It modifies the behavior of optical potential, eq. (1),

$$U_{opt} = \frac{E}{m} \Sigma_v - \Sigma_s + \frac{1}{2m} (\Sigma_s^2 - \Sigma_v^2) \quad (1)$$

where Σ_s and Σ_v scalar and vector self-energies respectively.

Fig. 1. In-medium proton Schrödinger-equivalent $Re(U_{opt})$



2 The Non-Linear Derivative (NLD) model

The Lagrangian is as in the conventional QHD, eq. (2)

$$\begin{aligned} \mathcal{L} = & \frac{1}{2} \left(\bar{\Psi} \gamma_\mu i \vec{\partial}^\mu \Psi - \bar{\Psi} i \overleftarrow{\partial}^\mu \gamma_\mu \Psi \right) + m \bar{\Psi} \Psi - \frac{1}{2} m_\sigma^2 \sigma^2 \\ & + \frac{1}{2} \partial_\mu \sigma \partial^\mu \sigma - U(\sigma) + \frac{1}{2} m_\omega^2 \omega_\mu \omega^\mu - \frac{1}{4} F_{\mu\nu} F^{\mu\nu} \\ & + \frac{1}{2} m_\rho^2 \vec{\rho}_\mu \vec{\rho}^\mu - \frac{1}{4} \vec{G}_{\mu\nu} \vec{G}^{\mu\nu} + \mathcal{L}_{int} \end{aligned} \quad (2)$$

but in the interaction term, eq. (3), we introduce the momentum dependence with the non-linear derivative operators $\vec{\mathcal{D}}$, $\overleftarrow{\mathcal{D}}$, which are assumed to be generic functions of partial derivative

operator and supposed to act on the nucleon spinors Ψ and $\bar{\Psi}$ respectively.

$$\begin{aligned} \mathcal{L}_{int} = & \frac{g_\sigma}{2} \left(\bar{\Psi} \overleftarrow{\mathcal{D}} \Psi \sigma + \sigma \bar{\Psi} \overrightarrow{\mathcal{D}} \Psi \right) \\ & - \frac{g_\omega}{2} \left(\bar{\Psi} \overleftarrow{\mathcal{D}} \gamma^\mu \Psi \omega_\mu + \omega_\mu \bar{\Psi} \gamma^\mu \overrightarrow{\mathcal{D}} \Psi \right) \\ & - \frac{g_\rho}{2} \left(\bar{\Psi} \overleftarrow{\mathcal{D}} \gamma^\mu \vec{\tau} \Psi \vec{\rho}_\mu + \vec{\rho}_\mu \bar{\Psi} \vec{\tau} \gamma^\mu \overrightarrow{\mathcal{D}} \Psi \right) \end{aligned} \quad (3)$$

The Taylor expansion of the operator functions (supposing that they are smooth functions) in terms of partial derivatives generates an infinite series of higher-order derivative terms

$$\overrightarrow{\mathcal{D}} := \mathcal{D}(\vec{\xi}) = \sum_{j=0}^{n=\infty} \frac{\partial^j}{\partial \vec{\xi}^j} \mathcal{D} \Big|_{\vec{\xi} \rightarrow 0} \frac{\vec{\xi}^j}{j!} \quad (4)$$

$$\overleftarrow{\mathcal{D}} := \mathcal{D}(\overleftarrow{\xi}) = \sum_{j=0}^{n=\infty} \frac{\overleftarrow{\xi}^j}{j!} \frac{\partial^j}{\partial \overleftarrow{\xi}^j} \mathcal{D} \Big|_{\overleftarrow{\xi} \rightarrow 0} \quad (5)$$

The expansion coefficients are given by the partial derivatives of \mathcal{D} with respect to the operator arguments $\vec{\xi}$ and $\overleftarrow{\xi}$ around the origin. The operators are defined as $\vec{\xi} = -\frac{v^\alpha i \partial_\alpha}{\Lambda}$ and $\overleftarrow{\xi} = \frac{i \partial_\alpha v^\alpha}{\Lambda}$, where Λ is a cut-off parameter (its value is supposed to be of natural hadronic scale of around 1 GeV) and v^α is an auxiliary vector [2]. Applying the generalized Euler-Lagrange equations to the full Lagrangian density with respect to the spinor field Ψ , leads to a Dirac equation with self-energies, which in the RMF approximation to infinite nuclear matter are

$$\Sigma_{vi}^\mu = g_\omega \omega^\mu \mathcal{D} + g_\rho \tau_i \rho^\mu \mathcal{D} \quad (6a)$$

and

$$\Sigma_{si} = g_\sigma \sigma \mathcal{D} \quad (6b)$$

The meson - fields equations are taken from the standard Euler - Lagrange equations.

$$m_\sigma^2 \sigma + \frac{\partial U}{\partial \sigma} = g_\sigma \sum_{i=p,n} \langle \bar{\Psi}_i \mathcal{D} \Psi_i \rangle = g_\sigma \rho_\sigma \quad (7)$$

$$m_\omega^2 \omega = g_\omega \sum_{i=p,n} \langle \bar{\Psi}_i \gamma^0 \mathcal{D} \Psi_i \rangle = g_\omega \rho_\omega \quad (8)$$

$$m_\rho^2 \rho = g_\rho \sum_{i=p,n} \tau_i \langle \bar{\Psi}_i \mathcal{D} \Psi_i \rangle = g_\rho \rho_I \quad (9)$$

It must be noticed that the cut-off Λ regulates both the density and momentum dependence of self-energies, and the density dependence of meson-fields sources (particularly for ω -field). Applying the Noether theorem for translational invariance to the NLD Lagrangian gives us the energy-momentum tensor, from which the energy density $\varepsilon \equiv T^{00}$ and the pressure P are

$$\varepsilon = \sum_{i=p,n} \frac{\kappa}{(2\pi)^3} \int_{|\vec{p}| \leq p_F} d^3 p E(\vec{p}) - \langle \mathcal{L} \rangle \quad (10)$$

$$P = \frac{1}{3} \sum_{i=p,n} \int_{|\vec{p}| \leq p_F} d^3 p \frac{\vec{\Pi}_i \vec{p}}{\Pi_i^0} + \langle \mathcal{L} \rangle \quad (11)$$

3 NLD results

3.1 Model Parameters

On table 1 there is the form of operator \mathcal{D} we choose (it's a monopole form) and on table 2 the values of parameters, which have been extracted from fit to known properties (saturation density, binding energy per nucleon, compressibility etc.), and on table 3 there are the values of these properties in comparison with values from other theoretical models.

Table 1. Form of \mathcal{D}

$\overrightarrow{\mathcal{D}}$	$\overrightarrow{\mathcal{D}}$ in NM
$\frac{1}{1 + \sum_{j=1}^4 \left(\frac{v_j^\alpha \delta_\alpha}{\Lambda} \right)^2}$	$\frac{\Lambda^2}{\Lambda^2 + p^2}$

Table 2. Parameters

Λ_s	Λ_v	g_σ	g_ω	g_ρ	b	c	m_σ	m_ω	m_ρ
[GeV]		[fm ⁻¹]				[GeV]			
0.95	1.125	10.08	10.13	3.50	15.341	-14.735	0.592	0.782	0.763

Table 3. Bulk saturation properties for NLD in comparison with other theoretical models

Model	ρ_{sat} [fm ⁻³]	E_b MeV/A	K [MeV]	α_{sym} [MeV]
NLD	0.156	-15.30	251	30
NL3*	0.150	-16.31	258	38.68
DD	0.149	-16.02	240	31.60
D ³ C	0.151	-15.98	232.5	31.90
DBHF	0.185	-15.60	290	33.35
	0.181	-16.15	230	34.20
empirical	0.167±0.019	-16±1	230±10	31.1±1.9

Model	L [MeV]	K_{sym} [MeV]	K_{asy} [MeV]	
NLD	81	-28	-514	
NL3*	125.7	104.08	-650.12	
DD	56	-95.30	-431.30	
D ³ C	59.30	-74.7	-430.50	
DBHF	71.10	-27.1	-453.70	
	71	87.36	-340	
empirical	88±25	-	-550±100	

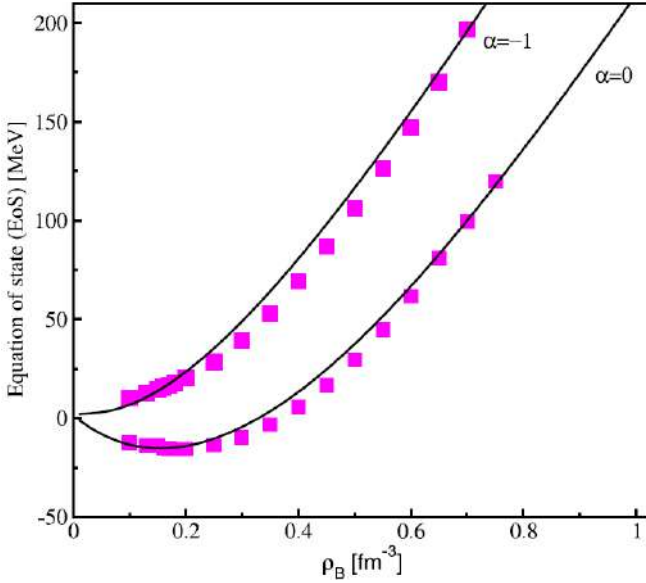
In our fit to bulk properties of nuclear matter we use different cut-off parameters Λ_s and Λ_v for the scalar and meson-nucleon vertices, respectively. The parameters of NLD are: the meson-nucleon couplings g_σ , g_ω and g_ρ , the parameters b and c of the self-interactions of the σ -meson, the mass m_σ of the σ -meson and the cut-offs Λ_s and Λ_v (for m_ω and m_ρ we take the

bare masses, because in all the calculations concerning the fit the results for these two masses turned out to be always around their free values).

3.2 The NLD equation of state

The density dependence affects the equation of state i.e. the binding energy per nucleon as function of nucleon density. In Figure 2 this is demonstrated for isospin-symmetric ($\alpha = 0$)¹ and pure neutron matter ($\alpha = -1$) in comparison with DBHF calculations. The momentum-dependent monopole form factor D regulates the high-density dependence of the fields such that the NLD EoS agrees with the DBHF calculations for both symmetric nuclear and pure neutron matter. It must be noted that the NLD parameters are not fitted to the calculations of DBHF models, but to the empirical data at ground state density only.

Fig. 2. EoS for isospin-symmetric ($\alpha = 0$) and pure neutron matter ($\alpha = -1$). NLD model (black solid curve) and DBHF calculations (filled squares).

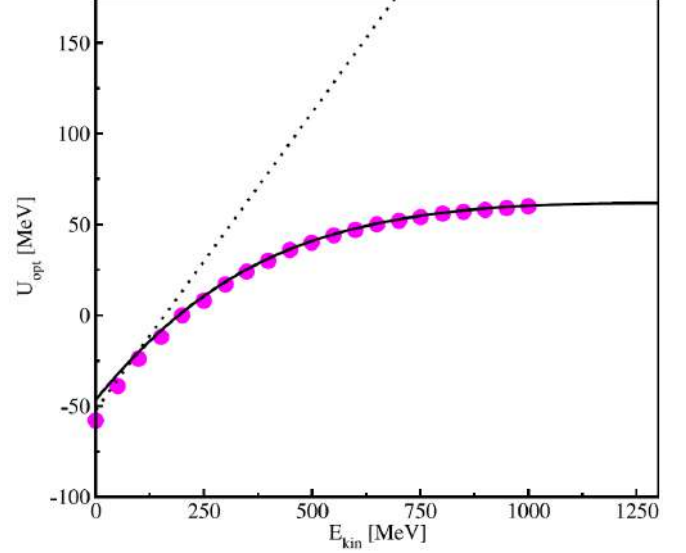


3.3 In-medium nucleon optical potential

Figure 3 shows the in-medium proton optical potential as function of the in-medium single particle kinetic energy for typical RMF models and NLD model in comparison with results of Dirac phenomenology [3]. Obviously NLD is consistent with Dirac phenomenology.

¹ The isospin-asymmetry parameter α is defined as $\alpha = \frac{J_p^0 - J_n^0}{J_p^0 + J_n^0}$, where $J_{p,n}^0$ denote the proton and neutron density, respectively.

Fig. 3. The in-medium proton optical potential as function of the in-medium single particle kinetic energy. Typical RMF models (dotted line), NLD model (black solid curve) and results of the Dirac phenomenology (filled circles).



3.4 Equation of state for hot matter

All the previous study was for temperature equal to zero. In Figures 4 and 5 are shown predictions of the NLD approach for hot hadronic matter for symmetric and pure neutron matter, respectively. The reason for this extrapolation is our willing to apply this model to dynamic systems, like binary Neutron Stars, where the temperatures are higher.

Fig. 4. EoS for different values of temperature. Symmetric matter ($\alpha = 0$). Starting from $T=0$ (black curve) the second curve is for $T=10$ MeV (red curve), the third for $T=20$ MeV (green curve) etc.

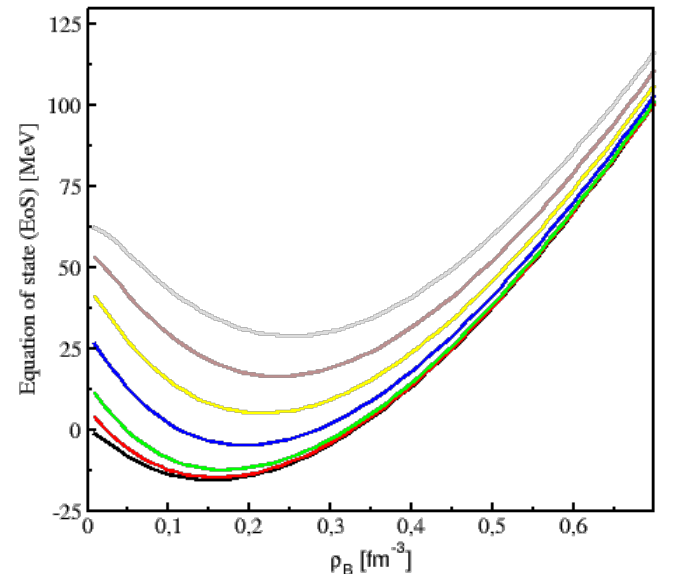
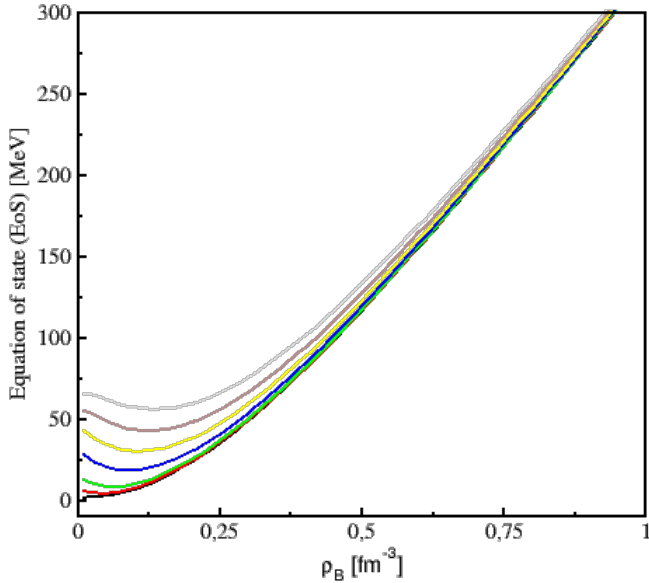


Fig. 5. EoS for different values of temperature. Pure neutron matter ($\alpha = -1$). Starting from $T=0$ (black curve) the second curve is for $T=10$ MeV (red curve), the third for $T=20$ MeV (green curve) etc.



4 Conclusions

The advantage of NLD model is that keeping the simplicity of RMF approximation, it can describe complex features (non-linear density and momentum dependences), only by introducing appropriate regulators on a Lagrangian level covariantly, which regulate the high density and momentum components of mean fields.

The equation of state we get is soft at low densities (the compressibility is around 250 MeV, Table 2), but becomes stiffer at high densities - a remarkable agreement with microscopic DBHF calculations (Figure 2). The momentum dependence we introduced seems to be correct, if we compare with results from Dirac phenomenology (Figure 3). All these are compatible with all recent observations of high density relevant equations of state (Neutron Stars).

Regarding future developments, we will apply our model to new experiments, which will be done at HADES collaboration for pion induced reactions. This will give us many experimental data not only for nucleons but for other particles as well, so we can expand this formalism to strangeness. Also we will do more systematic comparison with results from transport calculations.

References

1. T. Gaitanos et. al. *Nuclear Physics A* **828**, pages 9–28, 2009.
2. T. Gaitanos et al. *Nuclear Physics A* **828**, pages 133–169, 2013.
3. E. Cooper et al. *Physical Review C* **47**, pages 297–311, 1993.

Equation of state of cold rapidly rotating neutron stars and the effects of the Keplerian sequence

P.S. Koliogiannis and Ch.C. Moustakidis

Department of Theoretical Physics, Aristotle University of Thessaloniki, 54124 Thessaloniki, Greece

Abstract. Rapidly rotating neutron stars are considered to be the perfect laboratory for extreme density and gravity in general relativity. In the present work, we face two extreme configurations: the maximum mass and the maximum rotating frequency at the mass-shedding limit. We study the effects of the Keplerian sequence on the high density part of the equation of state of cold neutron star matter. We mainly focus on the dependence of the maximum rotation frequency from the macroscopic properties of neutron stars. We also study the dimensionless spin parameter (kerr parameter) of rotating neutron stars at the mass-shedding limit. In addition, supramassive time evolutionary rest mass sequences, which have their origin in general relativity, are explored. Supramassive sequences have masses exceeding the maximum mass of a non-rotating neutron star and evolve toward catastrophic collapse to a black hole. Important information can be gained from the astrophysical meaning of the kerr parameter and the supramassive sequences in neutron stars. Finally, the effects of the Keplerian sequence, in connection with the latter, may provide us constraints on the high density part of the equation of state of cold neutron star matter.

Key words. Equation of state, neutron stars, uniform rotation, Keplerian sequence

1 Introduction

Neutron stars, as one of the most extreme objects in Universe, probe excellent conditions for studying the constitution of matter at high densities, where the equation of state (EoS) remains an unsolved problem. Understanding the EoS is of critical meaning because it determines many of the bulk properties of neutron stars, including their mass, radius, moment of inertia, and spin parameter. While terrestrial experiments probe the EoS near to the nuclear saturation density, neutron stars astrophysical observations remain ideal for the implication of constraints in cold, dense nuclear matter.

Neutron stars observations provided us with several limits on their maximum mass and one for spin frequency. In particular, the EoS is constraint through the observations of a) the PSR J1614-2230 ($M = 1.908 \pm 0.016 M_{\odot}$) [1], b) the PSR J0348+0432 ($M = 2.01 \pm 0.04 M_{\odot}$) [2], c) the PSR J0740+6620 ($M = 2.14^{+0.10}_{-0.09} M_{\odot}$) [3] and d) the PSR J2215+5135 ($M = 2.27^{+0.17}_{-0.15} M_{\odot}$) [4], which referring to the maximum allowed mass and the PSR J1748-244ad with a spin frequency of 716 Hz [5], much lower than the theoretical predictions for hadronic matter.

A set of hadronic EoSs, based on various models (phenomenological, field theoretical and microscopic) [6], is employed for this study. These EoSs predict the upper bound of the maximum neutron star mass, while also re-

producing accurately the bulk properties of symmetric nuclear matter. Moreover, we construct two EoSs based on the Momentum Dependent Interaction model (MDI) and the microscopic data of Akmal *et al.* [7]. We refer to this model because among its advantages, it reproduces the results of microscopic calculations of symmetric nuclear matter and neutron star matter at zero temperature, with the advantage of its extension to finite temperature. Firstly, we explore the possibility for the existence of a relation between the properties of a non-rotating or a maximally rotating neutron star and the Keplerian frequency. We systematically study the role of the moment of inertia, eccentricity and kerr parameter on the bulk properties of neutron stars. These quantities are directly connected with the spin frequency of a neutron star and furthermore, the last one, can be a guide to distinguish the compact objects.

In addition, we construct the evolutionary sequences of constant rest mass and study the specific case where they considered to be progenitors of black holes. This type of sequences provide us with significant information about the collapse to a black hole by the spin up trail of the neutron star. Finally, we study the previous limit on central energy density [8] based on analytical solutions and provide a new one extracted from the set of realistic EoSs that are under consideration in this paper.

The article is organized as follows. In Section 2 we briefly present the EoSs and the rotating configuration for neutron stars. Section 3 is dedicated to the discussion

Correspondence to: pkoliogi@physics.auth.gr

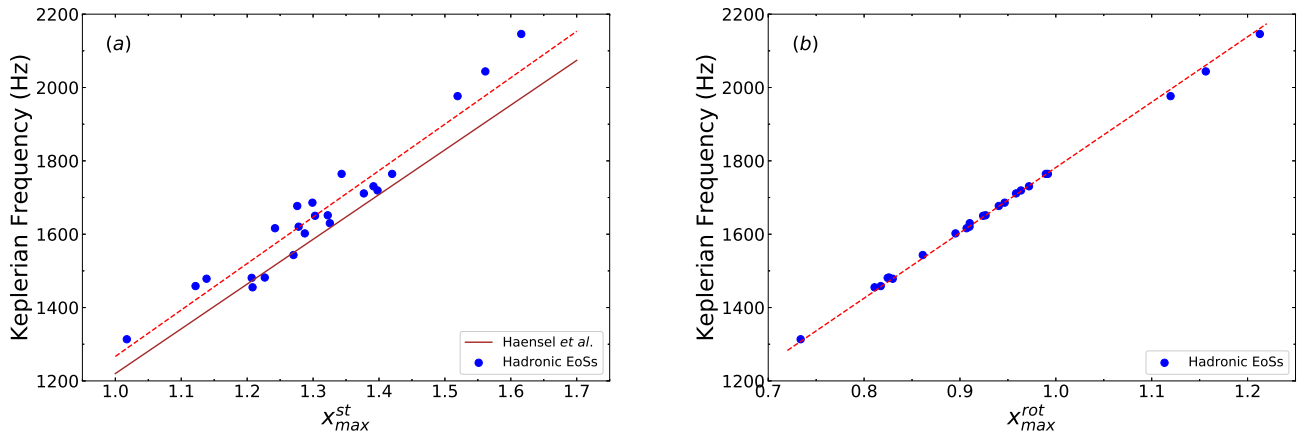


Fig. 1. The Keplerian frequency as a function of the bulk properties of (a) non-rotating and (b) rotating configuration of the 23 EoSs. The brown curve marks the work of Haensel *et al.* [9].

of the results, containing the description of the Keplerian frequency, the moment of inertia, the kerr parameter, the sequences of constant rest mass and the limit on the central energy density. Finally, Section 4 contains the summarize and conclusions of the present study.

2 Models of the equations of state and the rotation

2.1 Equations of state

A large set of EoSs, consistent with the current observed limits on neutron star mass and frequency, is employed in this study [6]. Three categories of models are being used: phenomenological, field theoretical and microscopic. In addition, we have constructed two EoSs, APR-1 and APR-2, based on the MDI model and the microscopic calculations of Akmal *et al.* [7]. As this model can be extended to include temperature, it can be used for future study on proto-neutron star, core-collapse supernova and neutron stars merger.

2.2 Uniform rotation

The equilibrium equations for a rotating neutron star, in the framework of General Relativity, can be described a) by the stationary axisymmetric space-time metric [10]

$$ds^2 = -e^{2\nu} dt^2 + e^{2\psi} (d\phi - \omega dt)^2 + e^{2\mu} (dr^2 + r^2 d\theta^2), \quad (1)$$

where the metric functions ν , ψ , ω and μ depend only on the coordinates r and θ , and b) the matter inside the neutron star. If we neglect sources of non-isotropic stresses, as well as viscous ones and heat transport, then the matter inside the neutron star can be fully described by the stress-energy tensor and modeled as a perfect fluid [10],

$$T^{\alpha\beta} = (\varepsilon + P) u^\alpha u^\beta + P g^{\alpha\beta}, \quad (2)$$

where u^α is the fluid's 4-velocity. The energy density and pressure is denoted as ε and P .

3 Results and discussion

3.1 Keplerian frequency

Similar to the Newtonian physics, the Keplerian frequency may exhibit a relation to the bulk properties of neutron stars. We studied the dependence of the Keplerian frequency on the bulk properties both of non-rotating and maximally rotating with the Keplerian frequency neutron stars, according to [9]

$$f_{max} = C_a \left(\frac{M_{max}^a}{M_\odot} \right)^{1/2} \left(\frac{10 \text{ km}}{R_{max}^a} \right)^{3/2} = C_a x_{max}^a \quad (\text{Hz}), \quad (3)$$

where a takes the form of the corresponding configuration (static, rotating) and the values of C are 1266.68 and 1781.9, respectively. Fig. 1 displays the relation between the quantities under consideration. It is obvious from Fig. 1 that at the maximally rotating configuration, an almost perfect relation holds on. However, the most interesting fact lies with the non-rotating configuration, where a relation between the non-rotating bulk properties and the Keplerian frequency exists [6].

3.2 Moment of inertia and eccentricity

Rotation on compact objects, and especially neutron stars, let us explore more aspects. Between them, there are the moment of inertia and eccentricity, which both of them play important role in pulsar analysis. Moment of inertia quantifies how fast an object can spin while eccentricity inform us about the deformation of the star [6, 11].

Moment of inertia and eccentricity are defined as [6, 11]

$$I = J/\Omega \quad \text{and} \quad \epsilon = \sqrt{1 - \left(\frac{r_p}{r_e} \right)^2}, \quad (4)$$

where J is the angular momentum, Ω the angular velocity, r_p the polar radius and r_e the equatorial radius of the

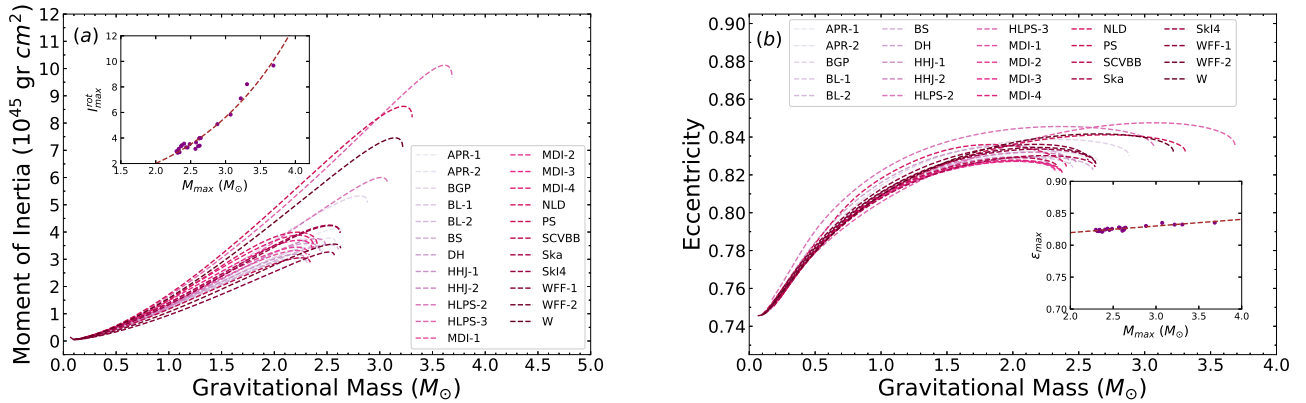


Fig. 2. (a) The moment of inertia and (b) eccentricity as a function of the gravitational mass at the mass-shedding limit. The inner figures represent the data and relations at the maximum mass configuration.

neutron star. As Fig. 2(a) displays the relation between the moment of inertia and the gravitational mass, we observed that moment of inertia, at the maximum mass configuration, is an EoS-dependent property because its behaviour is determined through the specific EoS. However, in Fig. 2(b), where the relation between the eccentricity and the gravitational mass is presented, there is a different approach. Eccentricity, at the maximum mass configuration, is an EoS-independent property. The relations that describe the above properties at maximum mass configuration, are

$$I_{max}^{rot} = -1.568 + 0.883 \exp \left[0.7 \left(\frac{M_{max}^{gm;rot}}{M_{\odot}} \right) \right], \quad (5)$$

$$\epsilon_{max} = 0.799 + 0.01 \left(\frac{M_{max}^{gm;rot}}{M_{\odot}} \right), \quad (6)$$

where Eq. (5) is in units (10^{45} gr cm^2).

3.3 Kerr parameter

Another important quantity for neutron stars is the spin parameter of kerr parameter [6, 11, 12]. In nuclear Astrophysics this parameter defines the upper limit for rotating kerr black holes and it is defined as

$$\mathcal{K} = \frac{cJ}{GM^2}. \quad (7)$$

While this parameter is well-established for black holes, that not the case for neutron stars. In this case, we study the dependence of the kerr parameter on the gravitational mass at the mass-shedding limit as Fig. 3 shows.

From Fig. 3 we concluded that there is a maximum value of the kerr parameter at around 0.75 [6], much lower than the 0.998 [13] for the maximally-rotating Kerr black holes. This constrain may play severe role on the compactness of neutron stars and also can form a criterion to determine the final fate of the collapse of a rotating

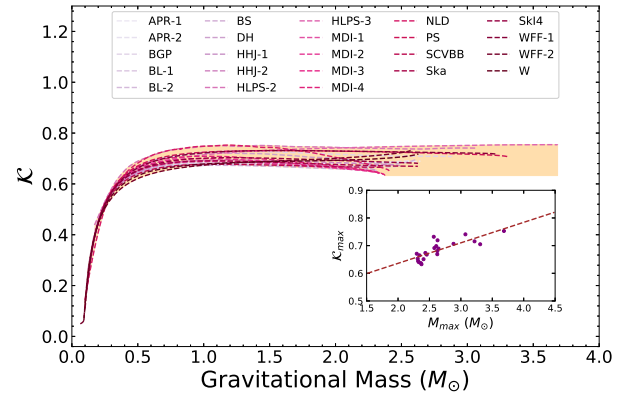


Fig. 3. The kerr parameter as a function of the gravitational mass at the mass-shedding limit. The inner figure represents the data and the relation at the maximum mass configuration.

compact object. The relation that yields at the maximum mass configuration is

$$\mathcal{K}_{max} = 0.488 + 0.074 \left(\frac{M_{max}^{gm;rot}}{M_{\odot}} \right). \quad (8)$$

3.4 Sequences of constant rest mass

The sequences of constant baryon mass are lines (roughly horizontal) that extend from the Keplerian sequence to the non-rotating end point or at the axisymmetric instability limit [14]. While sequences that are below the rest mass value that corresponds to the maximum mass configuration at the non-rotating model are stable and terminate at the non-rotating model sequence, the ones that are above this value are unstable and terminate at the axisymmetric instability limit. The former are called normal sequences and the latter ones, are called supramassive as their mass exceeds the maximum mass of the non-rotating configuration.

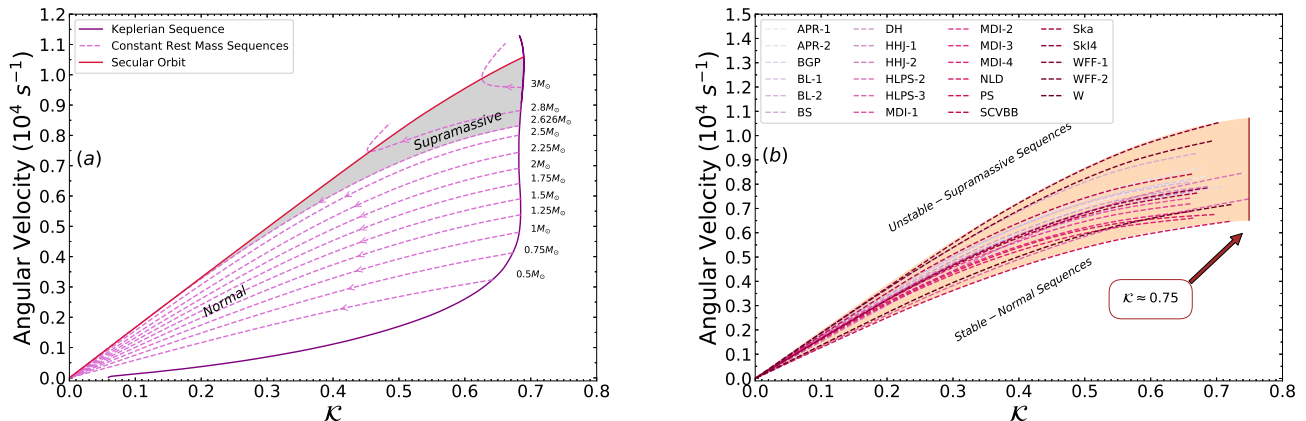


Fig. 4. (a) Normal and supramassive sequences of constant rest mass and (b) the LSRMS as the dependence of the angular velocity on kerr parameter.

In all cases, neutron stars which evolve along normal evolutionary sequences, never spin-up as they lose angular momentum. In contradiction to them, neutron stars on supramassive ones, because their unstable portion is always at higher angular velocity than the stable one, at the same value of angular momentum, must spin-up with angular momentum loss in the neighbourhood of the stability limit. If the neutron star is massive enough, then the evolutionary sequence (supramassive) exhibits an extended region where spin-up is allowed as Fig. 4(a) shows [14]. This effect may provide us an observable precursor to gravitational collapse to a black hole. As a follow up to Fig. 4(a), we have constructed the last stable rest mass sequence (LSRMS) for the set of hadronic EoSs, as Fig. 4(b) shows. This sequence is the one that divides the normal from supramassive sequences. In Fig. 4(b), we present a window (colored area) where the LSRMS can lie and because this sequence is the one that corresponds to the maximum mass configuration at the non-rotating model, this is also the region where the EoS can lie.

3.5 A limit on the central energy density

Analytical solutions provide us with the upper limit on the central energy density inside any compact object. To be more specific, Lattimer and Prakash [8] have proved that Tolman VII solution leads to this upper limit taking under consideration only the non-rotating case of course. In this study, following the work of Lattimer and Prakash [8], we have used the set of realistic EoSs, in order to reproduce their result. Having confirmed that Tolman VII defines the upper limit on central energy density taking into account the non-rotating configuration, we used a similar relation described as

$$\frac{M}{M_\odot} = 4.25 \sqrt{\frac{10^{15} \text{ gr cm}^{-3}}{\varepsilon_c/c^2}}, \quad (9)$$

in order to describe the region which includes also the maximally rotating configuration, as Fig 5 shows [6].

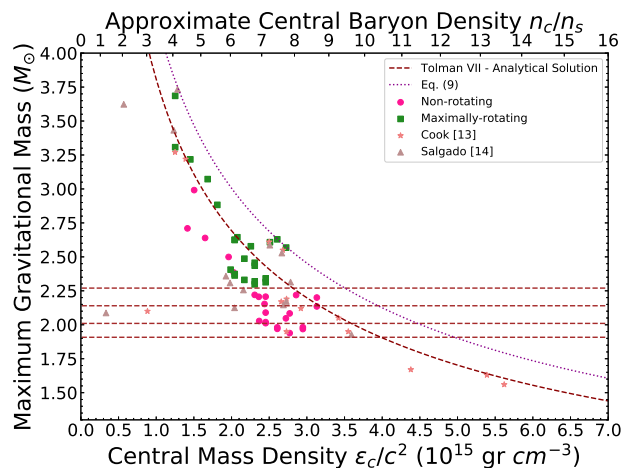


Fig. 5. The maximum gravitational mass as a function of the central mass density and the central baryon density. The non-rotating data are presented with circles and the rotating ones with squares. The data from Cook [14] and Salgado [15] are also presented with the stars and triangles. The Tolman VII analytical solution is marked with the dashed line while the Eq.(8) with the dotted line. The horizontal dashed lines mark the maximum observed neutron star mass.

4 Conclusions

A set of hadronic EoSs have been studied under the assumption of uniform rotation. For the numerical integration of the equilibrium equations, we used the public RNS code by Stergioulas and Friedman [16]. In particular, we have calculated their gravitational mass, moment of inertia, eccentricity and kerr parameter. Relations between these bulk properties have been established and shown in the corresponding figures. We have also studied the normal and supramassive sequences of constant rest mass for a specific EoS (APR-1) and determining the stability region of a neutron star [6].

From an astrophysical point of view, we have established a universal empirical relation between the Keplerian frequency and the bulk properties of both non-rotating and rotating with the Keplerian frequency neutron stars. In addition, we have shown that moment of inertia is an EoS-dependent property as it is highly depending on the employed EoS while eccentricity is an EoS-independent property at the maximum mass configuration. Furthermore, we have computed the maximum possible value of the kerr parameter in neutron stars at 0.75, and concluded that the gravitational collapse of a rotating neutron star, constrained to mass-energy and angular momentum conservation, cannot lead to a maximally-rotating kerr black hole [6, 11]. An important finding is also the LSRMS. This sequence, as it is the one that corresponds to the maximum mass configuration of the non-rotating model, can give us useful insight of the region where the EoS can lie and constrain both the angular velocity and kerr parameter.

The gravitational waves, as the powerful tool to study compact objects such as neutron stars, will provide us with the mass-shedding limit (Keplerian frequency) of these objects. To be more specific, the remnant formed in the immediate aftermath of the GW170817 merger contains sufficient angular momentum to be near its mass-shedding limit [17]. The observational measurement of the Keplerian frequency, along with the theoretical predictions, would provide us with strong constraints on the constitution of the dense nuclear matter.

Acknowledgements

This work was partially supported by the COST action PHAROS (CA16214) and the DAAD Germany-Greece grant ID 57340132.

References

1. Zaven Arzoumanian, Adam Brazier, Sarah Burke-Spolaor, Sydney Chamberlin, Shami Chatterjee, et al. The NANOGrav 11-year Data Set: High-precision Timing of 45 Millisecond Pulsars. *ApJS*, 235:37, 2018.
2. J. Antoniadis, P.C. Freire, N. Wex, T.M. Tauris, R.S. Lynch, et al. A massive pulsar in a compact relativistic binary. *Sci*, 340, 2013.
3. H.T. Cromartie, E. Fonseca, S.M. Ransom, P. B. Demorest, Z. Arzoumanian, et al. Relativistic Shapiro delay measurements of an extremely massive millisecond pulsar. *NatAs*, 2019.
4. M. Linares, T. Shahbaz, and J. Casares. Peering into the Dark Side: Magnesium Lines Establish a Massive Neutron Star in PSR J2215+5135. *ApJ*, 859:54, 2018.
5. Jason W. T. Hessels, Scott M. Ransom, Ingrid H. Stairs, Paulo C. C. Freire, Victoria M. Kaspi, and Fernando Camilo. A radio pulsar spinning at 716 hz. *Science*, 311(5769):1901–1904, 2006.
6. P. S. Koliogiannis and Ch. C. Moustakidis. Effects of the equation of state on the bulk properties of maximally rotating neutron stars. *PhRvC*, 101:015805, Jan 2020.
7. A. Akmal, V.R. Pandharipande, and D.G. Ravenhall. Equation of state of nucleon matter and neutron star structure. *Phys. Rev. C*, 58:1804, 1998.
8. James M. Lattimer and Madappa Prakash. Ultimate energy density of observable cold baryonic matter. *PhRvL*, 94:111101, Mar 2005.
9. Haensel, P., Zdunik, J. L., Bejger, M., and Lattimer, J. M. Keplerian frequency of uniformly rotating neutron stars and strange stars. *A&A*, 502(2):605–610, 2009.
10. V. Paschalidis and N. Stergioulas. Rotating stars in relativity. *LRR*, 20, 2017.
11. F. Cipolletta, C. Cherubini, S. Filippi, J. A. Rueda, and R. Ruffini. Fast rotating neutron stars with realistic nuclear matter equation of state. *PhRvD*, 92:023007, Jul 2015.
12. Ka-Wai Lo and Lap-Ming Lin. The spin parameter of uniformly rotating compact stars. *ApJ*, 728(1):12, jan 2011.
13. Kip S. Thorne. Disk-accretion onto a black hole. ii. evolution of the hole. *ApJ*, 191:507–520, Jul 1974.
14. S.L. Shapiro G.B. Cook and S.A. Teukolsky. Fast rotating neutron stars with realistic nuclear matter equation of state. *ApJ*, 424:823–845, 1994.
15. E. Gourgoulhon M. Salgado, S. Bonazzola and P. Haensel. High precision rotating neutron star models. ii. large sample of neutron star properties. *A&AS*, 108:455, 1994.
16. N. Stergioulas. <http://www.gravity.phys.uwm.edu/rns/>, 1996.
17. James M. Lattimer. Neutron star mass and radius measurements. *Universe*, 5(7), 2019.

Speed of sound bounds in dense matter and its effects on the bulk properties of rapidly rotating neutron stars

Ch. Margaritis¹, P.S. Koliogiannis¹, and Ch.C. Moustakidis^{1,2}

¹ Department of Theoretical Physics/Aristotle University of Thessaloniki, Greece

² Theoretical Astrophysics/Eberhard Karls University of Tübingen, Germany

Abstract. We study the effects of the upper limit of the speed of sound in dense matter on the bulk properties of rapidly rotating (at the Kepler limit) neutron stars. We investigate to what extent the possible predicted (from various theories and conjectures) upper bounds on the speed of sound constrain various key quantities, such as the maximum mass and the corresponding radius, Keplerian frequency, Kerr parameter and moment of inertia. We also explore the critical astrophysical question in which extent the bound of the speed of sound, especially the lower limit $v_s = c/\sqrt{3}$, prevents a neutron star to simulate the bulk properties of a black hole. In any case, useful relations of the mentioned bulk properties with the transition density are derived and compared with the corresponding nonrotating cases.

Key words. Speed of sound; Dense matter; Rotating neutron stars

PACS. 2 6.60.-c, 26.60.Kp, 97.60.Jd

1 Introduction

The main assumption is that the speed of sound in an EoS cannot exceed the speed of light because of the causality. In fact, Hartle in [1] pointed out that causality is not enough to constrain the high density part of the EoS. Recently, the effects of the upper bound of the sound speed in neutron star properties have been studied extensively [24]. In the present work, we employ in addition two upper bounds, the $v_s = c/\sqrt{3}$ and the one originated from the relativistic kinetic theory [5]. The main motivation of the present work is to investigate the possibility to provide some universal constraints on the bulk properties of maximally rotating neutron stars. We also study the constant rest mass sequences of a neutron star in order to provide constraints relative to its collapse to a black hole [6]. Finally, we provide a detailed study about the connection between the minimum period of a rotating neutron star and the maximum neutron star mass of a non-rotating one.

2 Speed of sound bounds, maximum mass configuration and rotating neutron stars

We have constructed the maximum mass configuration by considering the following two structures for the neutron star EoS [7]: (a) maximum angular velocity for known low-density EoS (b) maximum angular velocity from the

relativistic kinetic theory. Both cases are presented in [8]. In case (a), the speed of sound takes the values c and $c/\sqrt{3}$, while in case (b) it is self-constrained in the range $1/3 \leq (v_s/c)^2 \leq 1$. The EoS, that is used, is predicted by the MomentumDependentInteraction (MDI) model in correlation with data from Akmal [9] and predicts the currently observed maximum neutron star masses (for more details, see [6]). The cases which took effect in this study were the ones where the fiducial transition density is $n_{tr} = p_n n_s$, where n_s is the saturation density of symmetric nuclear matter ($n_s = 0.16 fm^{-3}$) and p_n takes the values 1.5, 2, 3, 4, 5. In the specific case where $n_{tr} = 1.5n_s$, when the speed of sound is equal to $c/\sqrt{3}$, then we have the EoS-maxstiff scenario and when the speed of sound is equal to $c/\sqrt{3}$, then we have the EoSminstiff scenario.

In approach (a) the continuity on the EoS is well ensured. However, approach (a), due to its artificial character, does not ensure continuity in the speed of sound at the transition density. In particular, we avoided the discontinuities in the speed of sound appeared at the transition densities by employing a method presented in [10]. We proceeded with the matching of the EOSs on the transition density by considering that, above this value, the speed of sound is parametrized as follows (for more details, see [10]):

$$\frac{v_s}{c} = \left(a - c_1 \exp \left[-\frac{(n - c_2)^2}{w^2} \right] \right)^{1/2}, \quad a = 1, 1/3. \quad (1)$$

Moreover, in the approach (a) we studied the method where discontinuities are presented in the EoS and the one where continuity exhibits based on the previously mentioned method. In approach (b), these effects on the bulk properties of neutron stars at the maximum mass configuration are insignificant.

It has been shown by Friedman et al. [11] that the turning -point method can also be used in the case of uniformly rotating neutron stars. With this consideration, in a constant angular momentum sequence, the condition

$$\frac{\partial M(\mathcal{E}_c, J)}{\partial \mathcal{E}_c} \Big|_{J=\text{constant}} = 0, \quad (2)$$

where \mathcal{E}_c is the energy density in the center of the neutron star and J is the angular momentum, defines the possible maximum mass. For the numerical integration of the equilibrium equations, we used the public RNS code by Stergioulas and Friedman [12].

3 Constraints on the bulk properties

3.1 Gravitational mass and radius

As Fig.1. shows, both in nonrotating and maximally rotating configuration, a reduction on the gravitational mass along the transition density occurs until it reaches a constant value. The dependence of the gravitational mass on the transition density can be described accurately by the formula

$$\frac{M_{\text{max}}}{M_{\odot}} = \alpha_1 \coth \left[\alpha_2 \left(\frac{n_{\text{tr}}}{n_s} \right)^{1/2} \right]. \quad (3)$$

In the case of the equatorial and polar radius as a function of the transition density, while similar dependence with the gravitational mass is presented, the bound $c/\sqrt{3}$ differs. In particular, after $3n_s$ the $c/\sqrt{3}$ case leads to higher values of radius than the other two bounds. The dependence of the equatorial radius on the transition density can be described accurately by the formula

$$\frac{R_{\text{max}}}{\text{km}} = \alpha_3 \coth \left[\alpha_4 \left(\frac{n_{\text{tr}}}{n_s} \right)^{0.8} \right]. \quad (4)$$

In both formulae α_1 , α_2 , α_3 and α_4 are constants, different for each case.

3.2 Keplerian angular velocity

Angular velocity at the maximum mass configuration for the maximally rotating case is an increasing function of the transition density. This effect remains valid only for the bound $c/\sqrt{3}$. In the rest of the cases, it reaches a maximum at $3n_s$ and then decreases along the transition density. In Fig.2., the above behaviour is demonstrated.

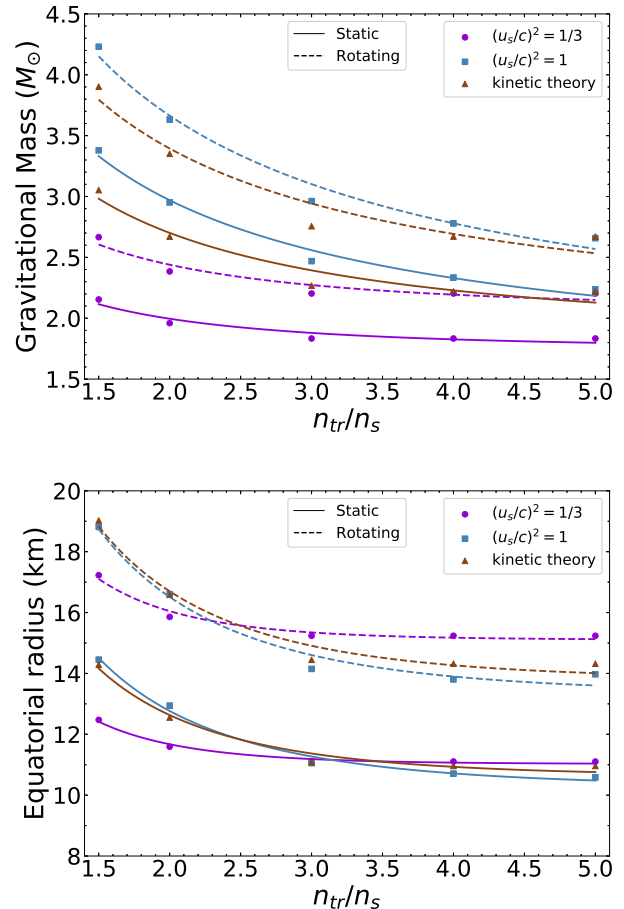


Fig. 1. Dependence of the maximum gravitational mass (up) and the equatorial radius (down) on the transition density for various speed of sound bounds.

3.3 Kerr parameter

The Kerr parameter is important for neutrons stars and, in general, compact objects. The relation which describes the Kerr parameter [6] is

$$\mathcal{K} = \frac{cJ}{GM^2}. \quad (5)$$

The Kerr parameter can lead to possible limits for the compactness on neutron stars and it can be a criterion for determining the final fate of the collapse of a rotating compact star [6]. It follows the mass-density relation as a decreasing function of the transition density (see Fig.2.). The dependence on the transition density can be described accurately by the formula

$$\mathcal{K}_{\text{max}} = \alpha_7 \coth \left[\alpha_8 \left(\frac{n_{\text{tr}}}{n_s} \right)^{1/2} \right], \quad (6)$$

where α_7 and α_8 are the corresponding constants for each case.

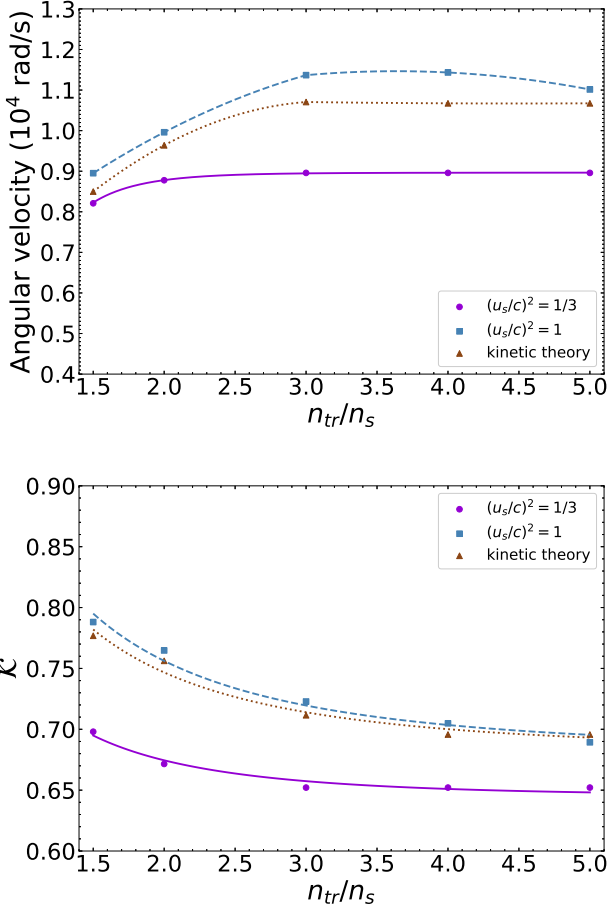


Fig. 2. Dependence of the angular velocity (up) and the Kerr parameter (down) on the transition density for various speed of sound bounds.

3.4 Moment of inertia

One of the most relevant properties in pulsar analysis is the moment of inertia, which can quantify how fast an object can spin with a given angular momentum [6]. In this case too, moment of inertia follows a decreasing trajectory along the transition density until it reaches a constant value (see Fig.3.). The significant meaning of this property appears with the $v_s/c = 1/\sqrt{3}$ bound which leads to much lower values of moment of inertia than the other two. The dependence of the moment of inertia on the transition density can be described accurately by the formula

$$I_{\max} = \alpha_5 \coth \left[\alpha_6 \left(\frac{n_{tr}}{n_s} \right)^{3/2} \right] \quad (10^{45} \text{ gr cm}^2), \quad (7)$$

where α_5 and α_6 are also constants, different for each case.

3.5 Constant rest mass sequences

These sequences describe the time evolution of a neutron star (with a fixed rest mass) created by spinning with its

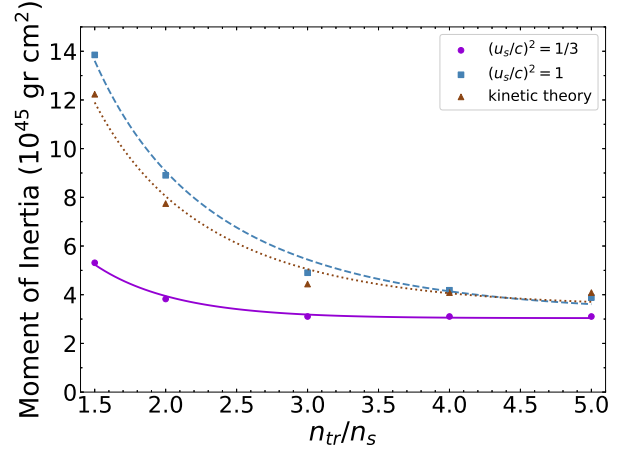


Fig. 3. Dependence of the moment of inertia on the transition density at the maximum mass configuration for the various speed of sound bounds.

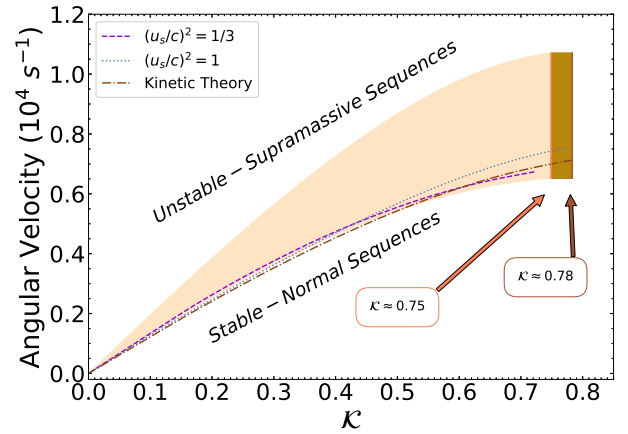


Fig. 4. Last stable rest mass sequence as the dependence of the angular velocity on the Kerr parameter for the various speed of sound bounds at $n_{tr} = 1.5n_s$.

Keplerian velocity. In the case of normal ones, neutron stars eventually losing their angular momentum (for various reasons) and becoming nonrotating as they approach a stable configuration. On the other hand, during the supramassive sequence, neutron stars never approach the stable nonrotating case, and their final fate is to collapse to a black hole.

We plot in Fig.4., the last stable rest mass sequence (LSRMS) for the various bounds at $n_{tr} = 1.5n_s$, which corresponds to the maximum mass configuration at the nonrotating model and defines the upper limit to the stable region. It is remarkable, that the three bounds, define the lower limit on the LSRMS.

3.6 Minimum rotational period

For a given EoS the maximum gravitational mass in the sequence of gravitationally bound neutron stars has the

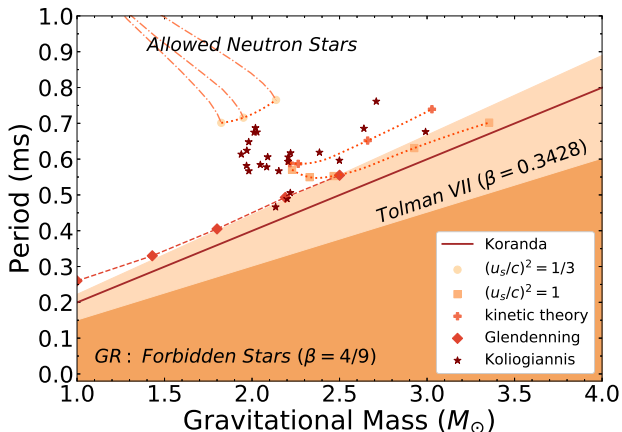


Fig. 5. Minimum rotational period of rotating neutron stars as a function of the mass of the maximum mass spherical star allowed by the EoS of the stellar matter.

minimum Keplerian period. Therefore, we present Fig.5., in order to provide useful constraints on the EoS.

The most striking feature is the constraints imposed by the bound $v_s = c/\sqrt{3}$. Obviously, the use of this bound leads to a significant increase in the minimum period (almost twice the time of the causality limit $v_s = c$) and consequently limits the allowed region. In fact, the allowed region is restricted dramatically by using this bound, also excluding the prediction of all realistic EOSs.

4 Discussion and conclusions

Sequences of both nonrotating and rotating neutron stars with different speed of sound bounds and transition densities have been studied. In this paper we have studied the bulk properties of maximally rotating neutron stars in correlation with the transition density and the gravitational mass. The gravitational mass and radius are decreasing functions along the transition density for all bounds until they reach a constant value. Another interesting effect is provided through the $c/\sqrt{3}$ bound, where the radius exceeds the other two bounds after $3n_s$. The study of the angular velocity showed that, in all cases, after $3n_s$ a decrease is observed, except in $c/\sqrt{3}$ case where it stabilizes after $3n_s$ in a constant value. In the case of the Kerr parameter, the bound c leads to higher values than the other two bounds. At the most extreme configuration studied in this paper, meaning at $1.5n_s$ and bound c , the Kerr parameter reaches a maximum value at around 0.8, which means that the gravitational collapse of a uniformly rotating neutron star, constrained to massenergy and angular momentum conservation, cannot lead to a maximally rotating Kerr black hole [6]. The effects of the speed of sound bounds are enhanced for the moment of inertia, where the decrease is up to 2.5 times between the c and $c/\sqrt{3}$ bound. This can lead to possible constraints on the spin frequency on neutron stars. From the LSRMS sequence it is obvious that the normal region of neutron stars is extended

downwards concerning the angular velocity. The latter one leads us to lower spin frequencies on neutron stars. Furthermore, the minimum rotating period of a neutron star as a function of the spherical gravitational mass has been studied. The bound $c/\sqrt{3}$ significantly limits the allowed area of neutron stars, excluding also a majority of realistic EOSs. This bound can provide strong constraints on the maximum gravitational mass, as well as on the minimum rotating period of neutron stars.

The observational measurement of the Keplerian frequency as well as of the rest bulk properties (mass, radius, Kerr parameter and moment of inertia and etc.), along with the theoretical predictions, would provide us with strong constraints on the highdensity part of the EoS. Moreover, these observations will help also to check the validity of the proposed upper bounds of the speed of sound in dense nuclear matter (for example, see [4]).

5 Acknowledgements

The authors thank Prof. K. Kokkotas for his constructive comments on the preparation of the manuscript, Prof. N. Stergioulas for providing the RNS code and for fruitful discussions and Dr. S. Typel for useful corresponds and discussions. This work was partially supported by the COST action PHAROS (CA16214) and the DAAD GermanyGreece grant ID 57340132.

References

1. J.B. Hartle, Phys. Rep. **46**, (1978) 201.
2. N. Glendenning, *Compact Stars: Nuclear Physics, Particle Physics and General Relativity* (Springer, Berlin 2000)
3. J. M. Lattimer, M. Prakash, D. Masak, and A. Yahil, Astrophys. J. **355**, (1990) 241.
4. J. Alsing, O. H. Silva, and E. Berti, Mon. Not. Roy. Astron. Soc. **478**, (2018) 1377.
5. T. Olson, Phys. Rev. C **63**, (2000) 015802.
6. P. Koliogiannis and C. Moustakidis, Phys. Rev. C **101**, (2020) 015805.
7. Ch. Margaritis, P. Koliogiannis and C. Moustakidis, Phys. Rev. D **101**, (2020) 043023.
8. Ch. C. Moustakidis, T. Gaitanos, Ch. Margaritis, G. A. Lalazissis, Phys. Rev. C **95**, (2017) 045801.
9. A. Akmal, V. Pandharipande, and D. Ravenhall, Phys. Rev. C **58**, (1998) 1804.
10. I. Tews, J. Carlson, S. Gandolfi, and S. Reddy, Astrophys. J. **860**, (2018) 149.
11. J. L. Friedman, J. R. Ipser, and R. D. Sorkin, Astrophys. J. **325**, (1988) 722.
12. N. Stergioulas and J. Friedman, Astrophys. J. **444**, (1995) 1.

Constraints on neutron stars equation of state, from the observation of the tidal deformability of the GW170817 system

A. Kanakis-Pegios¹ and Ch.C. Moustakidis¹

¹Department of Theoretical Physics, Aristotle University of Thessaloniki, 54124 Thessaloniki, Greece

Abstract. The purpose of this work is the study of neutron stars equation of state using constraints on tidal deformability from the multimessenger observation of the binary neutron star event GW170817. Firstly, the mathematical formalism of Tolman-Oppenheimer-Volkov equations is introduced, and then for a variety of equations of state the system is solved numerically, allowing us to determine the mass, the radius, the tidal love number k_2 and the tidal deformability λ of a non-rotating neutron star, each one of them unique for each equation of state. Moreover, for a fixed chirp mass of $\mathcal{M}_c = 1.188M_\odot$ under the assumption that $m_2 < m_1$ (where m_1 is the heavier component mass of the binary), the effective (mass-weighted) tidal deformability $\tilde{\Lambda}$ of the binary system is determined for each equation of state. We consider an upper limit of $\tilde{\Lambda} \leq 800$ (GW170817) and a lower limit of $\tilde{\Lambda} \geq 400$ (AT2017gfo). Also, we construct the $\Lambda_1 - \Lambda_2$ space and we compare the behavior of the equations of state with the most recent LIGO's data. We found out that the most equation of state models provide $\tilde{\Lambda}$ less than the upper limit.

Key words. neutron stars – gw170817 – tidal deformability – equation of state

1 Introduction

On August 17, 2017, the LIGO/VIRGO gravitational-wave detectors network observed a signal of emitted gravitational waves, which was identified as a binary neutron star system. The VIRGO's contribution allowed constraining the sky location of the event, through triangulation-based techniques. The combined data from both LIGO and VIRGO detectors, determined the precise sky position of the source to an area of 28 deg^2 [1]. In the next days and weeks, a strong search begun aiming at the detection of the optical and electromagnetic (EM) counterpart of the event.

Flanagan and Hinderer articulated that binary neutron stars coalescence is one of the most important source for gravitational-wave detectors [2]. One of the goals of neutron stars binaries detections is to obtain information about the nuclear equation of state. For the most part of the inspiral, finite-size effects have a negligible influence on the gravitational-wave signal, therefore only during the last orbits of the inspiral, and especially for gravitational-wave frequencies above a lower limit of 500 Hz, the effect of the internal structure can be seen.

Some of the parameters that can be measured and constrained by the gravitational-wave detectors are the chirp mass \mathcal{M}_c of the binary system and the effective tidal deformability $\tilde{\Lambda}$. In the present work, we compute the mass, the radius and the tidal parameters of a single neutron star using the Tolman-Oppenheimer-Volkov (TOV) equations for a variety of equations of state. Moreover, we use the

constraints on the effective tidal deformability $\tilde{\Lambda}$, that the GW170817 event provided us, both from the gravitational-wave signal and the EM counterpart, in order to study the behavior of each equation of state.

2 Tidal deformation

It has been shown that the orbital motion of a binary neutron stars system produces the emission of gravitational waves, which in turn removes energy and angular momentum from the system [2–4]. This causes the orbits to decrease in radius and increase in frequency, leading to the inspiraling motion of the two compact objects of the binary. During the late phase of the inspiral, the tidal interaction between the two compact bodies has a significant role to their gravitational field and orbital motion. The induced tidal field E_{ij} affects the quadrupole moment Q_{ij} [5]:

$$Q_{ij} = \lambda(m)E_{ij}, \quad (1)$$

where m is the star's mass and λ is the tidal deformability, given by [5]:

$$\lambda = \frac{2}{3} \frac{R^5}{G} k_2, \quad (2)$$

The tidal deformability λ depends on the tidal parameter k_2 , which is called as tidal Love number, and the star's radius R . The dependence on the star's radius means that the smaller the star, the harder to be deformed. The tidal Love number k_2 depends on the structure of the neutron

star, i.e. its mass and the equation of state. This parameter is described by [5,6]:

$$k_2 = \frac{8\beta^5}{5}(1-2\beta)^2[2-y_R+(y_R-1)2\beta] \times \left[2\beta(6-3y_R+3\beta(5y_R-8)) + 4\beta^3(13-11y_R+\beta(3y_R-2)+2\beta^2(1+y_R)) + 3(1-2\beta)^2[2-y_R+2\beta(y_R-1)]\ln(1-2\beta) \right]^{-1}, \quad (3)$$

where $\beta = GM/Rc^2$ is the compactness parameter. The quantity y_R is determined by solving the following differential equation:

$$r \frac{dy(r)}{dr} + y^2(r) + y(r)F(r) + r^2Q(r) = 0, \quad (4)$$

with $y(0) = 2$ and $y_R \equiv y(R)$ [5,6]. The functionals $F(r)$ and $Q(r)$ are defined as [5,6]:

$$F(r) = \left[1 - \frac{4\pi r^2 G}{c^4} (\mathcal{E}(r) - P(r)) \right] \left(1 - \frac{2M(r)G}{rc^2} \right)^{-1}, \quad (5)$$

and

$$r^2Q(r) = \frac{4\pi r^2 G}{c^4} \left[5\mathcal{E}(r) + 9P(r) + \frac{\mathcal{E}(r) + P(r)}{\partial P(r)/\partial \mathcal{E}(r)} \right] \times \left(1 - \frac{2M(r)G}{rc^2} \right)^{-1} - 6 \left(1 - \frac{2M(r)G}{rc^2} \right)^{-1} - \frac{4M^2(r)G^2}{r^2c^4} \left(1 + \frac{4\pi r^3 P(r)}{M(r)c^2} \right)^2 \times \left(1 - \frac{2M(r)G}{rc^2} \right)^{-2}. \quad (6)$$

The numerical integration of the previous equations, combined with the well known TOV equations, provide us the mass M , the radius R and the parameter y_R . Hence, the compactness parameter β and the tidal Love number k_2 can be determined for each equation of state, leading to the computation of λ .

Fig.1 shows the M-R diagram for all the equations of state that we used in our study. In Fig.2 the tidal deformability λ of an isolated and non-rotating neutron star is shown. In general, one can observe that the more stiff equations of state provide bigger values of tidal deformability. To be more specific, the tidal deformability λ depends mainly on the 5th order of the star's radius (see Eq.(2)). Therefore, equations of state with bigger radius lead to higher values of tidal deformation, nevertheless the high mass values that some equations of state predict (e.g. the equation of state HLPS-2 provide small values of tidal deformability even if its maximum mass is higher than other equations of state).

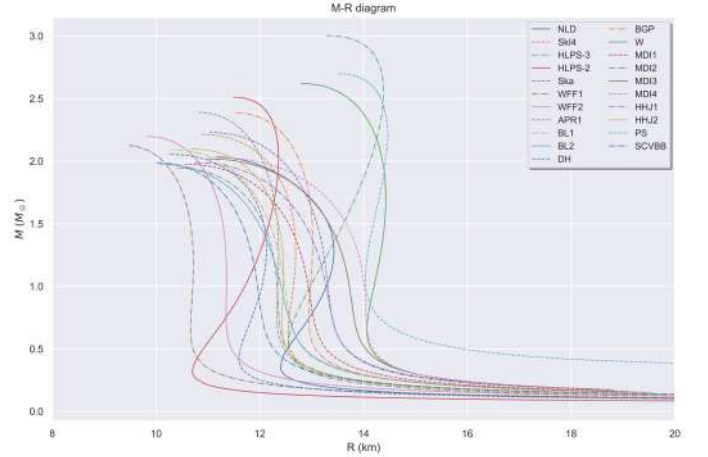


Fig. 1. Mass vs radius for an isolated neutron star and a variety of equations of state.

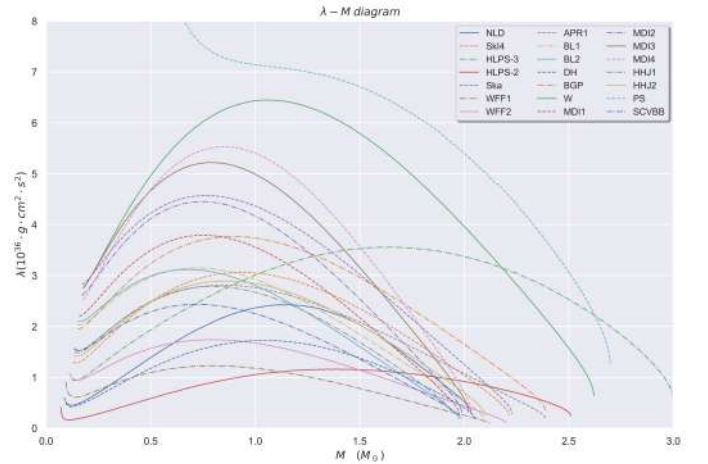


Fig. 2. Tidal deformability vs mass for an isolated neutron star and a variety of equations of state.

3 Binary tidal deformability

As it was mentioned before, the tidal deformability affects the late phase of evolution for a binary neutron star system. One of the system's parameters that can be well measured is the chirp mass \mathcal{M}_c , which is a combination of the masses of the two component stars [1]. Its expression is given below [1]:

$$\mathcal{M}_c = \frac{(m_1 m_2)^{3/5}}{(m_1 + m_2)^{1/5}} = \frac{q^{3/5}}{(1+q)^{1/5}} m_1, \quad (7)$$

where $q = m_2/m_1$, with $m_2 \leq m_1 \rightarrow q \leq 1$, is the binary mass ratio.

Moreover, the combined tidal effects of two neutron stars in circular orbits are given by an effective average of the quadrupole responses, known as effective tidal deformability, which form is given by [5,7]:

$$\tilde{\lambda} = \frac{1}{26} \left[\frac{m_1 + 12m_2}{m_1} \lambda_1 + \frac{m_2 + 12m_1}{m_2} \lambda_2 \right]. \quad (8)$$

The Eq.(8) can be rewritten so that the effective tidal deformability would be a dimensionless quantity [8]:

$$\tilde{\Lambda} = \frac{16}{13} \frac{(12q+1)A_1 + (12+q)q^4 A_2}{(1+q)^5}, \quad (9)$$

where $\Lambda = \lambda/M^5 = \frac{2}{3}k_2 \left(\frac{c^2 R}{GM}\right)^5$ is the dimensionless tidal deformability of a single neutron star.

The gravitational-wave detectors provide tight constraints on the effective tidal deformability $\tilde{\Lambda}$. Especially, for the GW170817 event, the LIGO/VIRGO collaboration estimated an upper limit on $\tilde{\Lambda}$, $\tilde{\Lambda} \leq 800$ [1]. Nevertheless, a more recent analysis lowers this upper bound. In our studied we used the initial estimation. The exact value of chirp mass estimated to be $\mathcal{M}_c = 1.188 M_\odot$ with $q \in (0.7, 1.0)$ [1]. The mass range for the heavier component star is $m_1 \in (1.36, 1.60) M_\odot$ and for the lighter one $m_2 \in (1.17, 1.36) M_\odot$. In our study we used the proposed estimations of LIGO, but for a wider range for q , so that $q \in (0.4, 1.0)$. By using Eq.(9) in combination with the \mathcal{M}_c and q on can determine the $\tilde{\Lambda}$ (see Fig.3 below).

Under this assumption, the dimensionless tidal deformability can be rewritten as:

$$\Lambda \simeq \alpha \beta^{-6}, \quad (10)$$

where α estimated to be $\alpha = 0.0039 \pm 0.0007$ for the GW170817 event [10]. This value is valid in the mass range $1.1 M_\odot \leq m \leq 1.6 M_\odot$, almost identical to the GW170817 one (for the low-spin case). Soumi De *et al.* articulated that the range of stellar radii in the mass range of interest for GW170817 is small [8]. Therefore, one can consider that $R_1 \simeq R_2 \simeq \hat{R}$. Hence, by using Eq.(10), we obtain [8, 10]:

$$A_1 = q^6 A_2. \quad (11)$$

By substituting the Eq.(11) with Eq.(9) we obtain that [8]:

$$A_1(\tilde{\Lambda}, q) = \frac{13}{16} \tilde{\Lambda} \frac{q^2(1+q)^4}{12q^2 - 11q + 12} \quad (12)$$

$$A_2(\tilde{\Lambda}, q) = q^{-6} A_1.$$

When the two component stars have equal masses, i.e. the binary mass ratio equals to unity $q = 1$, then $\tilde{\Lambda} = A_1 = A_2$. Therefore, for a given mass range, one can determine the value of $\tilde{\Lambda}$ when $q = 1$ (in our case this happens when $m_1 = m_2 = 1.36 M_\odot$). Subsequently, by treating the $\tilde{\Lambda}$ as a constant, for a specific mass range, the dimensionless tidal deformability of each component star can be derived from Eq.(12). Hence, the $A_1 - A_2$ space can be constructed (see Fig.4 below).

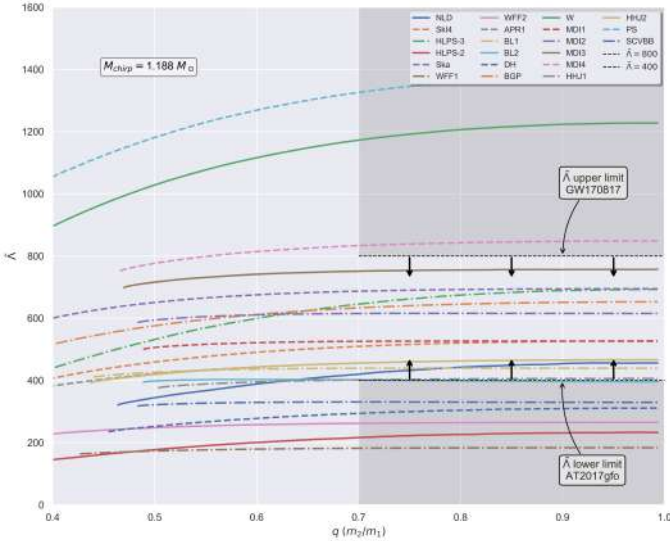


Fig. 3. $\tilde{\Lambda} - q$ for $q \in (0.4, 1.0)$ and $\mathcal{M}_c = 1.188 M_\odot$. The shaded grey area corresponds to the excluded regions from the GW170817 event, both from the gravitational-wave counterpart and the electromagnetic one [1,9], which are indicated with arrows.

Fig.3 shows the effective tidal deformability $\tilde{\Lambda}$ as a function of the binary mass ratio q . One can observe that the more stiff equations of state provide high values for $\tilde{\Lambda}$, in some cases even above the upper bound of 800. On the other hand, the more soft equations of state lead in general to smaller values of $\tilde{\Lambda}$. The lower bound of $\tilde{\Lambda} \geq 400$, which is extracted from the EM counterpart of the event, excludes the softer equations of state. We note that the exact value of the lower bound is still under investigation [9].

Lattimer *et al.* pointed out that for neutron stars with $m \geq 1 M_\odot$, the k_2 parameter varies roughly as β^{-1} [8,10].

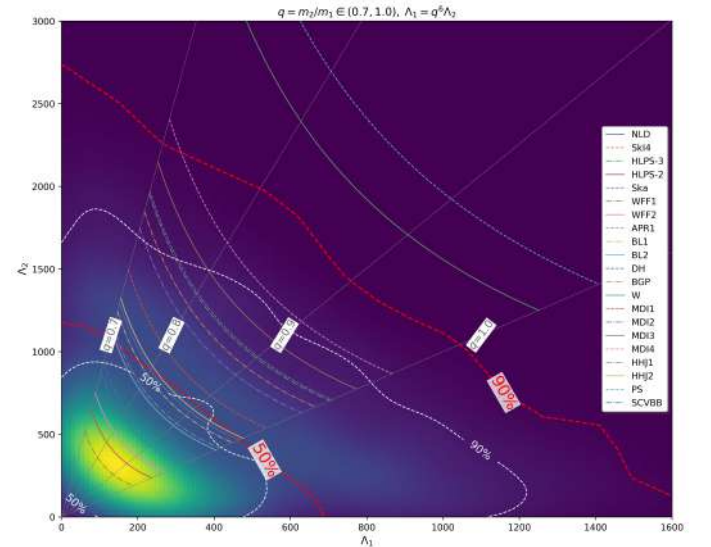


Fig. 4. $A_1 - A_2$ space for a variety of equations of state. The red (white) contours corresponds to the initial (more recent) LIGO's estimation [1,11,12], for both 50% and 90% credible regions.

Fig.4 shows the $A_1 - A_2$ space for all the equations of state that we used in our study. Similar to Fig.3, the more stiff equations of state provide values of tidal deformability beyond the upper confidence limit of 90%. On the other

hand, the more soft equations of state provide small values of Λ_i . This is due to the dependence of Λ to the 5th order of R . Therefore, the GW170817 event favors more compact neutron stars.

4 Discussion

The equations of state that we used in our analysis are consistent with the observational constraints on the maximum mass of neutron stars and reproduce a neutron star of $2 M_\odot$. In the first part of our work, we studied the mass, the radius and the tidal parameters for a single neutron star. The main remark is that in general the more stiff equations of state predict bigger values for the tidal deformability λ . In addition, we observed the significant role of the radius affecting the tidal deformability, both in a single neutron star and in the binary case. Moreover, we studied the binary tidal parameters, especially the effective tidal deformability $\tilde{\Lambda}$. In our approach we used the estimations of the LIGO's analysis regarding to the parameters of our interest. The GW170817 provided a strong constraint on the upper limit of $\tilde{\Lambda}$, while a lower limit on $\tilde{\Lambda}$ is useful to impose additional constraints. In this case, we used a value derived from the EM counterpart of the signal. The upper limit on the $\tilde{\Lambda}$ led to the exclusion of the most stiff equations of state. Also, by the studying of $\Lambda_1 - \Lambda_2$ space one can observe that the GW170817 event favors more compact neutron stars. We note that the detection of a binary neutron stars merger and the constraints that it brought to the equation of state, it's only the beginning of a new era and further detections of future events will provide even more constraints on the equation of state and broaden our knowledge about the neutron stars structure and characteristics.

5 Acknowledgments

The authors thank Prof. K. Kokkotas for his constructive comments on the preparation of the manuscript. This work was partially supported by the COST action PHAROS (CA16214) and the DAAD Germany-Greece grant ID 57340132.

References

1. B.P. Abbott *et al.*, Phys. Rev. Lett. **119**, 161101 (2017).
2. E.E. Flanagan and T. Hinderer, Phys. Rev. D **77**, 021502 (2008).
3. T. Binnington and E. Poisson, Phys. Rev. D **80**, 084018 (2009).
4. T. Hinderer, Astrophys. J. **677**, 1216 (2008).
5. Ch. C. Moustakidis, T. Gaitanos, Ch. Margaritis and G. A. Lalazassis, Phys. Rev. C **95**, 045801 (2017).
6. S. Postnikov, M. Prakash, and J. M. Lattimer, Phys. Rev. D **82**, 024016 (2010).
7. T. Hinderer, B. D. Lackey, R. N. Lang and J. S. Read, Phys. Rev. D **81**, 123016 (2010).
8. S. De et al. , Phys.Rev. Lett. **121**, 091102 (2018).
9. D. Radice, A. Perego, F. Zappa, S. Bernuzzi, Astrophys. J. **852**, L29 (2018).
10. T. Zhao, J.M. Lattimer, Phys. Rev. D **98**, 063020 (2018).
11. B. P. Abbott et al., Phys. Rev. Lett. **121**, 161101 (2018).
12. B. P. Abbott et al., Physical Review X **9**, 011001 (2019).

Study of Momentum Distributions of Projectile Fragments from Heavy-ion Peripheral Collisions at 15 MeV/nucleon

S. Koulouris^a, G.A. Souliotis^{a,*}, I. Dimitropoulos^a, K. Palli^a,
M. Veselsky^b, A. Bonasera^{c,d}

^a *Laboratory of Physical Chemistry, Department of Chemistry, National and
Kapodistrian University of Athens, Athens, Greece*

^b *Institute of Physics, Slovak Academy of Sciences, Bratislava, Slovakia*

^c *Cyclotron Institute, Texas A&M University, College Station, Texas, USA*

^d *Laboratori Nazionali del Sud, INFN, Catania, Italy*

* *Corresponding author. Email: soulioti@chem.uoa.gr*

Abstract

This paper presents our recent efforts to study the momentum distributions as well as the production of neutron-rich rare isotopes with heavy-ion beams in the energy region of 15 MeV/nucleon. We present experimental cross sections of neutron-rich nuclides from collisions of a ⁸⁶Kr (15 MeV/nucleon) beam with ⁶⁴Ni and ⁵⁸Ni targets. Experimental data were obtained from the previous work of our group with the MARS mass spectrometer at the Cyclotron Institute of Texas A&M University. The study of momentum distributions is a new research activity and is expected to shed light on details of the reaction mechanism. The momentum, as a measure of the energy dissipation of a process, can provide important information on which mechanism ultimately dominates the production of the fragments of interest. We will present the momentum distributions of neutron-rich nuclides produced from collisions of the ⁸⁶Kr (15 MeV/nucleon) beam with the ⁶⁴Ni target.

1 Introduction

During almost a century since the dawn of nuclear physics as an interdisciplinary but also a distinct field in science, approximately one half of the theoretically estimated 7000 bound nuclei have been produced and thoroughly investigated [1]. Nuclei far away from the line of beta stability, are not present

in nature and have to be prepared in laboratory using appropriate nuclear reactions and separation techniques [2]. The exploration of the nuclear landscape toward the neutron drip-line is currently one of the major efforts in nuclear physics research [3–5]. The investigation of neutron-rich nuclei offers the possibility to elucidate important astrophysical nucleosynthesis processes, most notably the rapid neutron capture process (r-process), which is responsible for half the abundance of the stable neutron-rich nuclides heavier than iron [7–9]. A novel approach to produce neutron-rich nuclides is for the projectile nucleus to capture neutrons from the target. Such a possibility is offered by reactions of nucleon exchange at beam energies from the Coulomb barrier [10] to the Fermi energy (20–40 MeV/nucleon) [11]. Detailed experimental data in this broad energy range are scarce at present [12,13]. In multinucleon transfer and deep-inelastic reactions near the Coulomb barrier [13], the low velocities of the fragments and the wide angular and ionic charge state distributions may limit the collection efficiency for the most neutron-rich products. However, the reactions in the Fermi energy regime combine the advantages of both low-energy (i.e., near and above the Coulomb barrier) and high-energy (i.e., above 100 MeV/nucleon) reactions. At this energy, the interaction of the projectile with the target enhances the N/Z of the fragments, while the velocities are high enough to allow efficient in-flight collection and separation. The Fermi energy regime is in fact, a link between dissipative processes observed at low-energy reactions, dominated by mean-field considerations, and high energy collisions for which nucleon-nucleon collisions play an important role [14,15]. In this contribution, we present experimental mass distributions of projectile fragments with $Z = 33 - 40$ produced from the reaction ^{86}Kr (15 MeV/nucleon) with ^{64}Ni and ^{58}Ni targets and also the momentum distributions of various products of the reaction ^{86}Kr (15 MeV/nucleon) with ^{64}Ni .

2 Outline of Results and Comparisons

A detailed presentation of previously obtained experimental results appear in [15–18] in which the mass spectrometric measurements of production cross sections of neutron-rich projectile fragments from the reactions of a 15 MeV/nucleon ^{86}Kr beam with $^{64,58}\text{Ni}$ targets are given.

In Fig. 1, we present the extracted production cross sections for each isotope of the elements with $Z = 33-40$ from the reactions ^{86}Kr (15 MeV/nucleon) with ^{64}Ni and ^{58}Ni [15]. Solid circles correspond to the first reaction and the open ones to the latter, respectively. As expected, the yields of fragments from the reaction $^{86}\text{Kr} + ^{64}\text{Ni}$, are generally larger than the ones of the reaction $^{86}\text{Kr} + ^{58}\text{Ni}$ due to the relative neutron deficiency of the second target. Firstly we point out that for fragments close to the projectile (e.g., $Z = 34, 35$) neutron pickup products are observed in both cases with up to six neutrons picked up from

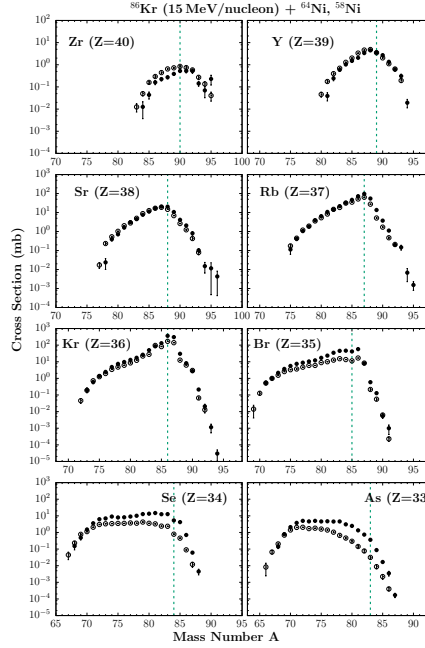


Fig. 1. (Color online) Experimental mass distributions (symbols) of elements $Z = 33$ – 40 from the reactions of ^{86}Kr (15 MeV/nucleon) with ^{64}Ni and ^{58}Ni [15]. The data are shown by solid circles for $^{86}\text{Kr} + ^{64}\text{Ni}$ and open circles for $^{86}\text{Kr} + ^{58}\text{Ni}$. The green line indicates the starting point of neutron pickup.

the target. As for the Kr isotopes (with $Z = 36$), we notice the pickup of up to seven neutrons from the target. We observe the production of multinucleon transfer products that picked up several protons and neutrons from the target. Interestingly, in the case of Rb ($Z = 37$) and Sr ($Z = 38$), we notice the pickup of up to eight neutrons from the target. These encouraging results, in addition to the trend of modern research activity towards the production of heavier than the projectile neutron-rich nuclei in the field of intermediate energies [19–21] led us to study the momentum distributions of these trans-projectile isotopes, which will be presented by our team in our next contribution. Understanding the details of the production mechanism of these trans-projectile isotopes is of great importance for the application of such reactions in the production of neutron-rich isotopes of heavy elements [22]. The observable of momentum, is in fact a measure of the energy dissipation caused by the interaction of the projectile-target binary system, and thus can provide important information on which mechanism ultimately dominates the production of the fragments of interest. The general feature of the momentum distributions, as expected, is the presence of two regions: a) a quasielastic peak that corresponds to direct processes, and b) a broad region, located at lower values of P/A (momentum per nucleon) that corresponds to deep inelastic processes and multinucleon transfers. Each frame of the momentum distributions corresponds to a specific isotope produced by the reaction.

In Fig. 2, the momentum distributions of three isotopes of Kr ($Z = 36$) from

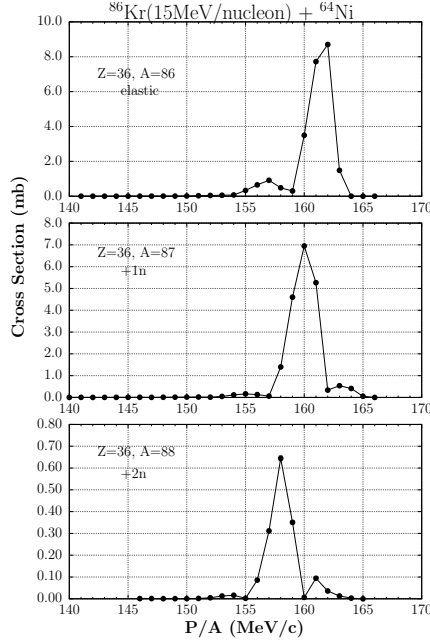


Fig. 2. (Color online) Momentum distributions depicting the elastic channel (^{86}Kr) and the products of the pickup of up to two neutrons from the target. The data are shown by solid circles.

the reaction ^{86}Kr (15 MeV/nucleon) with ^{64}Ni are presented. Firstly we notice a quasielastic peak at a P/A value of 163 MeV/c at the elastic channel. However, kinematic calculations carried out by our team, based on the classical two-body kinematics, point out that a ^{86}Kr beam of 15 MeV/nucleon should yield $P/A = 167.1$ MeV/c. So this quasielastic peak is a strong indication of ^{86}Kr fragments, that are not purely elastic, as they were produced from primary excited fragments, which were finally de-excited via nucleon evaporation, leading to ^{86}Kr secondary fragments. Moreover, we observe by the distributions of ^{87}Kr , ^{88}Kr (+1n, +2n) that the further pickup of neutrons from the target, leads to considerable dissipation of the produced fragment. In other words, the peaks at the distributions are located at lower values of P/A .

In Fig. 3, we present the momentum distributions of ^{87}Rb , ^{88}Sr , ^{89}Y and ^{90}Zr , which are the products of the capture of up to four protons from the target. We observe that the experimental data of the proton pickup products yield broader distributions in comparison to the neutron pickup products that were examined in Fig.2. This observation stresses that these final products, are a result of multinucleon transfer from the target. Also, due to the fact that the peaks of these distributions are located in much lower values of P/A , we can point out that the proton pickup leads to a greater dissipation of the system.

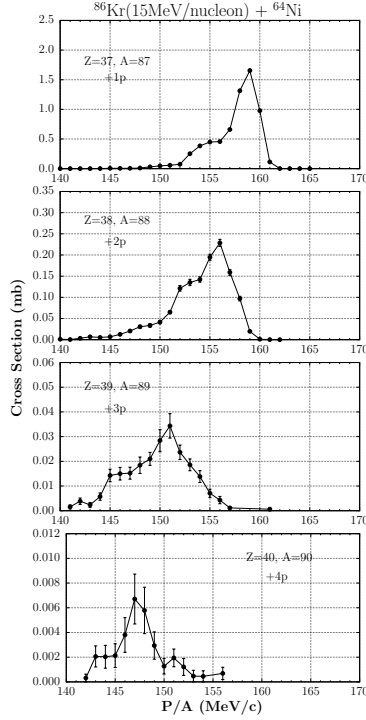


Fig. 3. (Color online) Momentum distributions of the products of the pickup of up to four protons by the projectile. The data are shown by solid circles.

3 Summary and Conclusions

We presented recent efforts to study the production of neutron-rich rare isotopes from heavy-ion peripheral collisions at 15 MeV/nucleon. We presented experimental production cross sections of neutron-rich nuclides from collisions of a ^{86}Kr (15 MeV/nucleon) beam with ^{64}Ni and ^{58}Ni targets. As expected, the yields of fragments from the reaction with the neutron-rich target ^{64}Ni , are generally larger relative to those from the reaction with the neutron-poor ^{58}Ni .

In parallel, we presented the momentum distributions of specific projectile fragments that were produced by the reaction ^{86}Kr (15 MeV/nucleon) + ^{64}Ni . It is a novel activity as there is limited research worldwide in the kinematic study of reactions in the Fermi energy region through the observable of momentum. In the near future, we will present momentum distributions of trans-projectile fragments, in which will be included not only experimental data, but also calculations carried out by our team, using the microscopic CoMD model [23,24] for the primary interaction stage combined with the deexcitation code GEMINI [25]. We conclude that the study of momentum distributions may lead us to a better understanding of the reaction mechanism at beam energies near the Fermi energy. Thus, a more effective exploitation of nuclear reactions in this regime in order to access extremely neutron-rich isotopes toward the

r-process path and the neutron drip-line can be achieved.

References

- [1] J. Erler et al, *Nature* **486**, 509 (2011).
- [2] Y. Blumenfeld, T. Nilsson, P.V. Duppen, *Phys. Scr. T* **152**, 014203 (2013).
- [3] J. Äystö, W. Nazarewicz, M. Pfützner, C. Signorini, eds, Proceedings of the Fifth International Conference on Exotic Nuclei and Atomic Masses (ENAM'08), Ryn, Poland, September 7–13 (2008); *Eur. Phys. J. A* **42** (2009).
- [4] V.I. Zagrebaev, W. Greiner, *Phys. Rev. C* **83**, 044618 (2011).
- [5] T.L. Lang et al., *Phys. Rev. Lett.* **124**, 062502 (2020).
- [6] G.G. Adamian et al., *Eur. Phys. J. A* **56**:47 (2020).
- [7] M. Arnould, S. Goriely, *Prog. Part. Nucl. Phys.* **112**, 103766 (2020).
- [8] K. Langanke and M. Wiescher, *Rep. Prog. Phys.* **64**, 1657 (2001).
- [9] H.-T. Lanka, K. Langanke, A. Marek, G. Martinez-Pinedo and B. Müller, *Phys. Rep.* **442**, 38 (2007).
- [10] L. Corradi, G. Pollarolo, S. Szilner, *J. Phys. G* **36**, 113101 (2009).
- [11] G. A. Souliotis et al., *Phys. Lett. B* **543**, 163 (2002).
- [12] G. A. Souliotis et al., *Nucl. Instrum. Methods B* **204** 166 (2003).
- [13] G. A. Souliotis et al., *Nucl. Instrum. Methods B* **266**, 4692 (2008).
- [14] B. Borderie, M.F. Rivet, L. Tassan-Got, *Ann. Phys. Fr.*, 15:4 pp. 287-390 (1990).
- [15] G. A. Souliotis et al., *Phys. Rev. C* **84**, 064607 (2011).
- [16] P.N. Fountas, G.A. Souliotis, M. Veselsky and A. Bonasera, *Phys. Rev. C* **90**, 064613 (2014).
- [17] N. Vonta, G.A. Souliotis et al., *Phys. Rev. C* **92**, 064611 (2016).
- [18] A. Papageorgiou, G.A. Souliotis et al., *Journal of Physics G* **45**, 095105 (2018).
- [19] V. Zagrebaev, W. Greiner, *Phys. Rev. C* **83**, 044618 (2011).
- [20] X. Jiang, N. Wang, *Front. Phys.* **8**:38 (2020).
- [21] W.D. Loveland, *Front. Phys.* **7**:23 (2019).
- [22] J. Dvorak et al., *Nucl Instrum. Methods Phys. Res., Sect. A* (2011).
- [23] M. Papa et al., *Phys. Rev. C* **64**, 024612 (2001).
- [24] M. Papa, T. Maruyama, and A. Bonasera, *J. Comput. Phys.* **208**, 403 (2005).
- [25] R. Charity et al., *Nucl. Phys. A* **483**, 371 (1988).

Study of the production mechanism of projectile fragments of the nuclear reaction ^{40}Ar (15 MeV/nucleon) with ^{64}Ni

I. Dimitropoulos^a, G.A. Souliotis^{a,*}, S. Koulouris^a, K. Palli^a,
M. Veselsky^c, A. Bonasera^{d,e}

^a *Laboratory of Physical Chemistry, Department of Chemistry, National and Kapodistrian University of Athens, Athens, Greece*

^c *Institute of Physics, Slovak Academy of Sciences, Bratislava, Slovakia*

^d *Cyclotron Institute, Texas A&M University, College Station, Texas, USA*

^e *Laboratori Nazionali del Sud, INFN, Catania, Italy*

* *Corresponding author. Email: soulioti@chem.uoa.gr*

Abstract

This paper presents our recent study on the production mechanism of neutron-rich isotopes. The main subject of our research is the momentum distributions of projectile fragments from the peripheral reaction $^{40}\text{Ar} + ^{64}\text{Ni}$ with energy beam 15 MeV/A. We compared experimental cross section data of neutron-rich nuclides from collisions of a ^{40}Ar (15 MeV/nucleon) beam with ^{58}Ni , ^{64}Ni targets. We also studied the experimental data of the momentum distributions from the same reactions. In the future, we plan to make calculations for more isotopes with the phenomenological DIT model and the microscopic constrained molecular dynamic (CoMD) model. The deexcitation of the hot projectile fragments will be performed with the statistical code Gemini. We conclude that the reaction mechanism at beam energies below the Fermi energy offer an effective route to access extremely neutron-rich rare isotopes for nuclear structure or reaction studies.

1 Introduction

The study of the chart of the nuclides toward the astrophysical r-process path and the neutron drip-line continues to receive special attention by the nuclear physics community (see, e.g., [1,2]). Moreover, the efficient production of very neutron-rich nuclides constitutes a central issue in current and upcoming rare isotope beam facilities (see, e.g., [3–5]). The reactions in the Fermi

energy regime (15–35 MeV/nucleon) combine the advantages of both low-energy (i.e., near and above the Coulomb barrier) and high-energy (i.e., above 100 MeV/nucleon) reactions. At this energy, the interaction of the projectile with the target enhances the N/Z of the fragments, while the velocities are high enough to allow efficient in-flight collection and separation. In this article, we present experimental cross section data from the reactions ^{40}Ar (15 MeV/nucleon) beam with ^{58}Ni , ^{64}Ni targets, which have been published in previous work of our research team [8]. We also present the momentum distributions from the same reactions, which is a new route of research for us.

2 Outline of Experimental Method and Data

Experimental data on neutron rich nuclide production with a beam of ^{40}Ar (15 MeV/nucleon) were obtained at the Cyclotron Institute of Texas A&M University, in parallel to a series of measurements with a ^{86}Kr (15 MeV/nucleon) beam already published in [6]. A preliminary version of the ^{40}Ar data has already been presented in [7]. The experimental setup has been presented in detail in [6]. For completeness, we give a brief overview of the experimental methods here. A 15 MeV/nucleon $^{40}\text{Ar}^{9+}$ beam hit targets of ^{64}Ni and ^{58}Ni with thickness of 2 mg cm^2 . Projectile fragments were collected and identified using the MARS recoil separator applying the techniques developed and documented in [6]. The ^{40}Ar beam was send on the primary target location of MARS with an angle of 4° with respect to the optical axis of the separator and projectile fragments were collected in the polar angular range of $2.2^\circ - 5.5^\circ$ (in a solid angle of 4.0 msr). After interaction with the target, the fragments traversed a parallel-plate avalanche counter (PPAC) at the intermediate image location (for position, magnetic rigidity and START-time information) and then they were focused at the end of the separator passing through a second PPAC (for image-size and STOP-time information). Finally the fragments were collected in a Si detector telescope. Following standard techniques of magnetic rigidity, energy-loss, residual energy and time-of-flight, the atomic number Z, the mass number A, the velocity and the ionic charge of the fragments were obtained on an event-by-event basis. Data were obtained in a series of successive magnetic rigidity settings of the spectrometer in the range 1.1-1.5 Tm. We note that this magnetic rigidity range did not fully cover the neutron-deficient side of the product distributions which extends down to 0.8 Tm according to our calculations. (The neutron-deficient isotopes with incomplete magnetic rigidity coverage lie to the left of the thin solid lines in figure 1.)

In Fig. 1, we present the experimental mass distributions of elements with $Z = 13-20$ of the reactions $^{40}\text{Ar}(15\text{ MeV/nucleon})+^{58}\text{Ni}$, ^{64}Ni . As we can see the reaction with the target ^{64}Ni produce more neutron rich isotopes. Also the

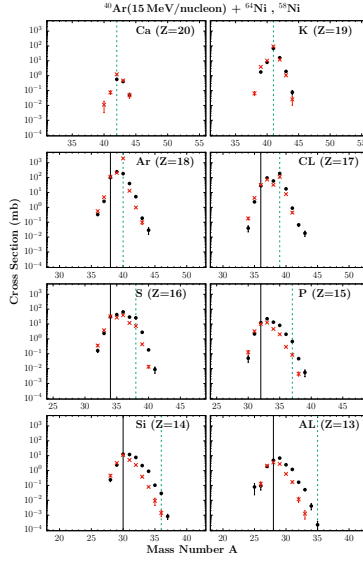


Fig. 1. (Color online) Experimental mass distributions of elements with $Z = 13-20$ observed in the reactions $^{40}\text{Ar}(15 \text{ MeV/nucleon}) + ^{58}\text{Ni}$ (red crosses), ^{64}Ni (black circles).

rate of cross section is much bigger. In each diagram, right of the green line the neutron pick-up process starts.

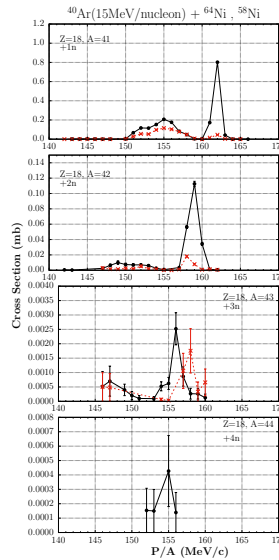


Fig. 2. (Color online) Experimental momentum distributions from the reactions $^{40}\text{Ar}(15 \text{ MeV/nucleon}) + ^{58}\text{Ni}$ (red line), ^{64}Ni (black line). The four boxes describe the addition of one to four neutrons, respectively.

In Fig.2,3, we present the experimental momentum distributions of the same reactions. At the diagrams is obvious that the two reactions have similar mechanisms and the cross section is much bigger in the case of ^{64}Ni as target. Most of the diagrams have one main peak and a secondary peak.

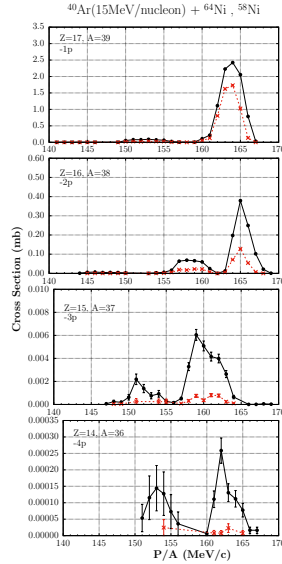


Fig. 3. (Color online) Experimental momentum distributions from the reactions $^{40}\text{Ar}(15 \text{ MeV/nucleon}) + ^{58}\text{Ni}$ (red line), ^{64}Ni (black line). The four boxes describe the removal of one to four protons, respectively.

3 Summary and Conclusions

We presented recent efforts to study the momentum distributions of neutron-rich isotopes with beams in the energy of 15 MeV/nucleon. The study of this diagrams will offer a lot of information of the reaction mechanism. Combined with the calculations that we plan to do with the DIT and CoMD models, we will take a step forward for the understanding the energy region below the Fermi energy and over the Coulomb barrier. We believe that our current understanding of the reaction mechanism at beam energies below the Fermi energy suggests that such nuclear reactions, involving peripheral nucleon exchange, can be exploited as a novel and effective route to access neutron-rich isotopes. Therefore, future experiments in several accelerator facilities can be planned that will enable a variety of nuclear structure and nuclear reaction studies in unexplored regions of the nuclear chart.

References

- [1] J. Erler et al, Nature **486**, 509 (2011).
- [2] J. Äystö, W. Nazarewicz, M. Pfützner, C. Signorini, eds, Proceedings of the Fifth International Conference on Exotic Nuclei and Atomic Masses (ENAM'08), Ryn, Poland, September 7–13 (2008); Eur. Phys. J. A **42** (2009).
- [3] D. F. Geesaman, C. K. Gelbke, R. V. F. Janssens, B. M. Sherrill, Ann. Rev. Nucl. Part. Sci. **56**, 53 (2006)
- [4] K. Tshoo, Y. K. Kim, Y. K. Kwon et al, Nucl. Instrum. Methods B **317**, 242 (2013).
- [5] K. Tshoo, H. Chae, J. Park, J.Y. Moon, Y.K. Kwon, G.A. Souliotis et al, Nucl. Instrum. Methods B **376**, 188 (2016).
- [6] G. A. Souliotis et al., Phys. Rev. C **84**, 064607 (2011).
- [7] G. A. Souliotis 2009 Progress in Research Cyclotron Institute, Texas A&M University
- [8] A. Papageorgiou, G.A. Souliotis et al., Journal of Physics G **45**, 095105 (2018).

COMPARATIVE DOSIMETRIC RADIOTHERAPY ANALYSIS IN RECTAL CANCER

Giagtzis Smaragdi^{1,2}, Sofka Vasiliki^{1,2}, Stoulos, Stylianos², Makridou Anna¹, Mponiou
Konstantina³, Iliopoulou Chrysoula³, Charalampidou Martha³

¹Medical Physics Department, Anticancer Theageneio Hospital

²Aristotle University of Thessaloniki

³Radiation Oncology Department, Anticancer Theageneio

Radiation therapy is an effective and safety method of treating tumors. The use of preoperative radiotherapy in locally advanced rectal cancer may increase total survival and reduce the local recurrence. The aim of this study is the comparative dosimetric analysis in four different radiotherapy techniques, 3DCRT (3D Conformal Radiation Therapy), IMRT (Intensity Modulated Radiotherapy) with three and four fields, and VMAT (Volumetric Modulated Arc Therapy) in rectal cancer.

- Handbook of Radiotherapy Physics, P. Mayles, A. Nahum, J.C. Rosenwald, Taylor and Francis Group, New York, London
- Radiation Physics for Medical Physicists, E.B. Podgorsak Springer, Montreal, Canada